Microlensing and the Search for Extrasolar Planets

DISSERTATION

Presented in Partial Fulfillment of the Requirements for

the Degree Doctor of Philosophy in the

Graduate School of The Ohio State University

By

B. Scott Gaudi, M.S.

*****

The Ohio State University

2000

Dissertation Committee:

Professor Andrew Gould, Adviser

Professor David H. Weinberg

Professor Darren DePoy

Approved by

Adviser
Astronomy Graduate Program

ABSTRACT

One of the first steps in determining the frequency of life outside the solar system is the determination of the frequency of extrasolar planets. Microlensing is a potentially powerful tool that is currently being used to accomplish this goal. I develop and apply a method of drawing inferences about the presence of companions to stars in our Galaxy using microlensing observations.

Planets reveal themselves in microlensing events as short-duration deviations to the primary light curve. I present an algorithm which can be used to search for such deviations in an observed light curve, and to quantify the efficiency of that light curve to the detection of planets. This algorithm is conceptually simple, computationally straightforward, and has the advantage that it automatically incorporates the actual sampling, photometric precision, and monitored duration of individual light curves, thus making it less prone to the biases that may arise when using simplified models of observational conditions. I test this algorithm using artificial datasets, and address complications associated with applying it to real datasets.

I then use this algorithm to search for the signature of planets in the dataset of microlensing event OGLE-1998-BUL-14 acquired by the PLANET collaboration. I find that the light curve of OGLE-1998-BUL-14 is consistent with a single lens to within observational uncertainties. I find that the detection efficiency to a Jovian analog was $\sim 60\%$, thereby demonstrating that such datasets are sensitive to planetary companions.

Finally, I analyze five years of microlensing data from PLANET, searching for planetary companions. I construct a well-defined sample of 44 intensively monitored events, in which I search for planetary perturbations over a densely sampled region of parameter space spanning two decades in mass and separation. I find no viable planetary candidates. This null result implies that, at 95% confidence, $< 25\%$ of M-dwarfs in the Galactic bulge have Jupiter mass companions between 1.5 and 4 AU, and $< 45\%$ have Jupiter mass companions between 1 and 7 AU. These are the first significant limits on planetary companions to M-dwarfs.

To my parents,
and Heather.

ACKNOWLEDGMENTS

The number of people who deserve to be acknowledged here is probably larger than the number of planets that will ever be found by microlensing. As you shall see, it is certainly larger than the number that have already been found. So, I'll begin with an apology to those who I forgot to thank. Next in line is, of course, my parents, without whom I wouldn't be so many things, confident in my own abilities being the most important. They taught me to believe I could accomplish anything I set my mind to, and furthermore that I had better accomplish everything I was capable of. And to my dear Heather: what can I say? You know.

Various faculty members have contributed to my scientific growth during the five years I've spent at Ohio State. David Weinberg has always been an enthusiastic supporter of me and my work, he taught me some essential aspects of careful research, taught me to try to figure the answer out for myself, not to mention warning me of the dangers of *a posteriori* statistics. Pat Osmer is an amazing chair, his vigilance and concern brought an essential aspect of humanity to the department. Darren DePoy, one of my 'surrogate' advisors, taught me almost everything I know about astronomical observations. I would also like to thank him for our scientific, pseudo-scientific, and completely non-scientific conversations, and for being a friend. A special thanks are in order to Rick Pogge, who worked tirelessly and rapidly to prepare the data which is analyzed in this thesis. Thanks to Jerry Newsom, Barbara Ryden, Kris Sellgren, and Don Terndrup, all of whom taught me a thing or two, and helped to make my stay at Ohio State more enjoyable.

I have had the pleasure to work and become friends with many terrific graduate students at Ohio State. Cheongho Han guided me through the first few terrifying months of being at Ohio State and working with Andy, without him, I don't think I would have lasted. Many thanks to Paul Martini for constantly raising the bar. Andreas Berlind and Alberto Conti have been true friends, and made the graduate student experience infinitely more enjoyable. My gratitude to Andy Stephens, who was always willing to drop everything and help when I had a problem, despite my constant harassment.

Many thanks to my fellow members of the PLANET collaboration for working so hard to collect and reduce the truly amazing data that I had the pleasure and privilege of analyzing. Of course, none of this work would have been possible without the alerts provided by the EROS, MACHO, and OGLE collaborations. Their dedication and commitment to the field should be a lesson for us all. Special thanks to Penny Sackett, my other 'surrogate' advisor, for keeping me grounded, forcing me to be honest, and encouraging a healthy amount of skepticism. Also, thanks to Roeland van der Marel, for giving me thoughtful and careful job advice, and for saving my Hubble Fellowship application from the late pile.

Numerous others have contributed to keeping me sane and appropriately distracted during my stint as a graduate student. To Mikey, Phil, Mike, Neil, Rick, Dennis, Mark, Jimmy, and all the other friends and companions I've acquired along the way: thank you.

And finally, my advisor, Andy Gould. The nine months I spent in his office were the most intense, educational, and productive times I have had. If I can claim to have learned anything during my stay here, it is because of him. More than anything else, he taught my *how* to the think about a problem, how to dig down to its essential roots and thus solve it. He is simultaneously the most intense, enthusiastic, intelligent, thoughtful, bizarre, annoying, giving, frustrating, pushy, and inspiring person I have ever met. I may have been able to choose an easier adviser; I could not have chosen a better one.

VITA

February 19, 1974	Born – Beruit, Lebanon.
1995	B.S., Astrophysics, Michigan State University.
1995 - 1998	Teaching and Research Assistant, The Ohio State University.
1997	M.S., Astronomy, The Ohio State University.
1999 - present	Presidential Fellow, The Ohio State University.

PUBLICATIONS

Research Publications

1. B. Scott Gaudi and Andrew Gould, "Satellite Parallaxes of Lensing Events Towards the Galactic Bulge", ApJ, 477, 152 (1997).
2. B. Scott Gaudi and Andrew Gould, "Detection Rates for Close Binaries Via Microlensing", ApJ, 482, 83 (1997).
3. B. Scott Gaudi and Andrew Gould, "Planet Parameters in Microlensing Events", ApJ, 486, 85 (1997).
4. Andrew Gould and B. Scott Gaudi, "Femtolens Imaging of a Quasar Central Engine Using a Dwarf Star Telescope", ApJ, 486, 687 (1997).
5. B. Scott Gaudi, Richard M. Naber, and Penny D. Sackett, "Microlensing by Multiple Planets in High-Magnification Events", ApJ, 502, L33 (1998).
6. B. Scott Gaudi, "Distinguishing Between Binary Source and Planetary Microlensing Perturbations", ApJ, 506, 533 (1998).
7. Michael D. Albrow et al., "The Relative Lens-Source Proper Motion in MACHO 98-SMC-1", ApJ, 512, 672 (1999).
8. B. Scott Gaudi and Andrew Gould, "Spectrophotometric Resolution of Stellar Atmospheres with Microlensing", ApJ, 513, 619 (1999).
9. Michael D. Albrow et al., "A Complete Set of Solutions for Caustic-Crossing Binary Microlensing Events", ApJ, 522, 1022 (1999).

10. B. Scott Gaudi and Penny D. Sackett, "Detection Efficiencies of Microlensing Datasets to Stellar and Planetary Companions", ApJ, 528, 56 (2000).
11. C. Afonso et al, "Combined Analysis of the Binary-Lens Caustic-Crossing Event MACHO 98-SMC-1", ApJ, 532, 340 (2000).
12. Michael D. Albrow et al., "Detection of Rotation in a Binary Microlens: PLANET Photometry of MACHO 97-BLG-41", ApJ, 534, 894 (2000).
13. Michael D. Albrow et al., "Limits on Stellar and Planetary Companions in Microlensing Event OGLE-1998-BUL-14", ApJ, 535, 176 (2000).
14. David S. Graff and B. Scott Gaudi, "Direct Detection of Giant Close-In Planets Around the Source Stars of Caustic-Crossing Microlensing Events", ApJ, 538, L133 (2000).
15. B. Scott Gaudi, "Planetary Transits Toward the Galactic Bulge", ApJ, 539, L59 (2000).
16. Michael D. Albrow et al., "PLANET Observations of Microlensing Event OGLE-1999-BUL-23: Limb Darkening Measurement of the Source Star", ApJ, submitted.
17. Michael D. Albrow et al., "Limits on the Abundance of Galactic Planets From Five Years of PLANET Observations", ApJL, submitted.

FIELDS OF STUDY

Major Field: Astronomy

Table of Contents

List of Tables

List of Figures

Chapter 1

Introduction

"Is there life out there?" It is one of the most fundamental human questions, the topic of countless pages of writing, countless good and bad movies, and countless late-night conversations. The answer to this question has boundless philosophical implications, and the reasons for our fascination with the question themselves probably go a long way toward explaining human behavior. We as scientists, however, are so far from answering this question that we find it almost laughable, and some regard the pursuit of the answer as uninteresting, or worse, unscientific. But clearly it is not, it is just a hard question.

The first step to answering this question is to access the frequency of extrasolar planets. Unfortunately, finding extrasolar planets is extraordinarily difficult, due to their small mass and size in comparison to the stars they orbit. By almost every astronomical ruler, the signatures that indicate the presence of planets are incredibly tiny. For instance, a Jupiter-like planet orbiting a star like the sun induces a radial velocity of ten *meters* per second. A Jupiter-mass planet orbiting a sunlike star at 10 parsecs would induce a wobble in the position of the star of less than one *millionth* of the angular size of the moon.

Undaunted by these small numbers, astronomers searched for extrasolar planets for many years. Without success. However, the discovery of a massive planet orbiting the star 51 Peg in 1995 (Mayor & Queloz, 1995) heralded the beginning of a new age in the search for extrasolar planets. Since this discovery, the field has grown almost exponentially. The number of known extrasolar planets is now nearly 50, with new planets being discovered every few months.

Around the same time, another subfield in astronomy began to receive significant attention: microlensing. Microlensing is the term given to the phenomenon of the deflection of light from a distant star by the gravitational field of an intervening object. The intervening object magnifies, or "lenses" the light from the distant star for a period of a few weeks, thus revealing its presence in a characteristic way (a "microlensing event"). Since the microlensing effect relies only on the mass of the intervening object, it can reveal the existence of objects that emit no light whatsoever. This led Paczyński (1986) to suggest that microlensing could be used to detect dark matter in the halo of our Galaxy. At first sight, the suggestion seemed preposterous: the probability that any given star is being microlensed by an intervening star at any given time is one in a million. Therefore, in order to see *just one* microlensing event, a million stars must be monitored simultaneously. As hard as this sounds, the real situation is much worse: stars vary all the time for many different reasons, the vast majority of which have nothing to do with microlensing. Also, in order to monitor so many stars at one time, the searches must performed toward targets with a large surface density of stars. This makes distinguishing between individual stars very difficult. Furthermore, microlensing events only occur once, so there is no possibility of repeating the observations. In other words, searching for a microlensing event is like searching for the proverbial needle in a haystack, except that there is only one chance to find the needle, the search must be carried out from a hundred yards away, and the haystack is also full of things that look a lot like needles, but aren't. Undaunted by these difficulties, two groups, MACHO and EROS, began monitoring stars towards the Large Magellanic Clouds (LMC) to try to find these microlensing events. In 1992, the first events were discovered (Alcock et al., 1993; Aubourg et al., 1993), thus initiating the field of microlensing. To date, over 500 microlensing events have been detected, and microlensing is now being used to study many different astrophysical phenomenon, such as stellar atmospheres, black holes, mass functions, stellar rotation, and binary systems.

Given that finding extrasolar planets is difficult, and given that microlensing is difficult, it would appear to be pure lunacy to attempt to use microlensing to search for planets. Yet this is exactly what was proposed by Mao & Paczyński (1991). The difficulty with using microlensing to find planets lies not in finding the events, other collaborations have been enormously successful at doing this, but in obtaining the accurate, densely sampled, and continuous coverage needed to detect and characterize the short time scale deviations to the primary microlensing that are the signatures of planets. Undaunted by these difficulties, in 1995, the PLANET, GMAN, and MPS collaborations began intensively monitoring microlensing events from several sites spread throughout the southern hemisphere with the express aim of detecting planets.

That was five years ago. And yet, no planets have been found with microlensing. This apparent failure is, in fact, not due to insufficient gumption or diligence, but rather an indication that planets are not very common. The purpose of this thesis is to prove that assertion, and to quantify exactly what is meant by "not very common."

In Chapter 2, I develop a method of systematically searching for planets in observed microlensing light curves, and calculating the detection efficiency of these light curves to planetary companions. Such a method is required in order to draw robust and quantitative statistical inferences about planetary companions. The method is conceptually simple, computationally efficient, and convenient in that is condenses all the information about planetary companions in individual light curves into one two-dimensional function. It has the advantage that it explicitly takes into account the sampling, photometric precision, and monitoring duration of the event, thus making it less prone to biases that may result from using idealized models of observational conditions. I test the robustness of the method by applying it to artificial datasets, and give specific suggestions for dealing with the practical difficulties of applying it to real datasets.

I apply this method to the PLANET dataset of the microlensing event OGLE-1998-BUL-14 in Chapter 3. The dataset consists of 600 data points, the majority of which was taken over a three month period. The median sampling rate during this period is ~ 1 hour, and the 1σ scatter is $\sim 5\%$, making it an excellent event to search for the signatures of a planetary companion orbiting the primary lens. I find that the observed light curve is completely consistent with a single lens (no planet) to within the observational uncertainties. Using the method described in Chapter 2, I calculate the detection efficiency of OGLE-1998-BUL-14 to planetary companions. I find that a companion of mass > 10 Jupiter masses is ruled out for separations between one and 7 AU, and the detection efficiency to a companion with the mass and separation of Jupiter was $\sim 60\%$.

In Chapter 4, I analyze five years of PLANET photometry of microlensing events toward the Galactic bulge for the presence of planets. Using strict event selection criterion, I construct a well-defined sample of 44 intensively monitored events. Again using the method presented in Chapter 2, I search for planetary perturbations in these events over a densely sampled region of parameter space spanning two decades in mass and separation. I find no viable planetary candidates. Using a model of the mass, velocity and spatial distribution of bulge lenses, I infer that the majority of our lenses are likely M dwarfs in the Galactic bulge. Using this inference, I conclude that $< 33\%$ of M-dwarfs in the Galactic bulge have Jupiter mass companions between 1.5 and 4 AU, and $< 45\%$ have 3-Jupiter mass companions between 1 and 7 AU, the first significant limits on planetary companions to M-dwarfs.

Each of these chapters were written as separate papers, and have been, or soon will be, published in the Astrophysical Journal. Chapter 2 was written in collaboration with Penny Sackett, and appeared as Gaudi & Sackett (2000). Chapter 3 was written with the PLANET collaboration, and appeared as Albrow et al. (2000b). Chapter 4 was also written with the PLANET collaboration, and will soon be submitted to the

Astrophysical Journal. There exists significant redundancy between these chapters, however I have chosen to leave them as they are so they can be read as separate entities.

Chapter 2

Detection Efficiencies of Microlensing Datasets

2.1. Introduction

Microlensing was proposed in 1986 by Paczyński as a method to detect compact baryonic dark matter in the halo of our Galaxy, but before the first events were discovered (Alcock et al., 1993; Aubourg et al., 1993; Udalski et al., 1993), Mao & Paczyński (1991) had already noted that it might be possible to detect planetary companions of the primary microlenses. The basic idea is simple: when a compact object, such as a star or massive dark object, passes near the line of sight to a distant source, the source is magnified. This magnification is depends (only) on the angular separation of the lens and source. Since the lens, source, and observer are all in relative motion, the magnification will be time-variable, creating a "microlensing event." Companions to the primary lens can be detected via the distortions they create in the light curve generated by the primary lens. The nature of the distortion depends on the mass ratio and angular separation of the two components.

As a planet search technique, microlensing offers unique advantages. Since microlensing is caused the gravitational field (i.e., mass) of the lenses, it is not limited to the study of nearby or indeed luminous objects, and thus can be used to search for planetary companions around typical Galactic stars at distances of many kiloparsecs. As a consequence, a nearly unlimited number of dwarf stars are available to serve as gravitational microlenses and potential search candidates. This advantage is linked to the primary drawback of microlensing planetary searches: most follow-up studies will be difficult due to the faintness of the stars serving as typical lenses. This drawback is compounded by the irrepeatability of specific microlensing observations; lensing of a particular source by a particular lens is a singular occurrence. Nevertheless, the robust statistics on the nature of planetary systems many kiloparsecs distant and the complementary nature of the information about discovered systems microlensing can provide make it an important tool in the cadre being assembled to study extra-solar planets (Sackett, 1999a). Furthermore, microlensing planet searches are relatively inexpensive, requiring only several dedicated 1-meter class telescopes. Microlensing is the only technique currently capable of routinely discovering planets like our own Jupiter, and the only ground-based method capable, in principle, of detecting distant terrestrial-mass planets, though this will require substantial enhancements over existing capabilities (Bennett & Rhie, 1996; Peale, 1997; Sackett, 1997)).

Current microlensing survey teams have sampling rates that are too large ($\sim$day) and/or photometric accuracies that are too poor ($\sim 5\%$) to detect and characterize the perturbations caused by planets, but the nearly 100 real-time electronic alerts of on-going bulge events that they provide annually have become the primary targets for newly-formed microlensing planet searches. These new 'monitoring teams' (PLANET, Albrow et al. 1997, 1998; GMAN, Alcock et al. 1997; MPS, Rhie et al. 1999b) have formed with the express purpose of executing the nearly continuous temporal coverage and high photometric precision on real-time microlensing alerts necessary to detect deviations from the generic light curve of the sort expected from planetary and other microlensing anomalies (see e.g. Albrow et al. (1998)). The PLANET collaboration in particular has now monitored nearly 100 microlensing events with varying degrees of photometric sampling and precision (often $\sim$hourly with $\sim$2% photometry over the largest magnification regions); such existing datasets may already place interesting constraints on the frequency of stellar binaries and planetary systems.

Like all planet search techniques, microlensing is not 100% efficient, due to both intrinsic and observational limitations. The efficiency with which a given dataset will reveal the presence of a companion to the primary microlens must be quantified before it can be used to constrain the frequency and properties of extra-solar planetary systems. Quantification of detection efficiencies of any kind can be a difficult and tedious process: the intrinsic limitations of the method must be identified and combined with the actual observational limitations. The detection efficiency may depend on hidden or unmeasurable parameters; these must be identified and properly quantified in order to avoid biasing the final conclusions. Despite a substantial body of work addressing the likely planet detection efficiency of idealized microlensing programs, no methods have yet been proposed for calculating the efficiency of observed datasets to lensing binaries.

Here we present an algorithm for computing the detection efficiency to lensing binaries that is specific to individual observed microlensing light curves. By directly imposing the actual observational limitations as a constraint, the approach is less prone to the biases that may arise when using simplified models of observational conditions. Furthermore, the method is simple to implement and computationally inexpensive, since it involves direct integration over unknown quantities rather than Monte Carlo simulations commonly used to calculate detection efficiencies of idealized observing programs. We apply this method to simulated datasets in order to explore how the detection efficiency depends on intrinsic and observational effects.

We also explore possible biases that may be introduced into the inferred efficiency of individual events to planet detection if the size of the source and the fraction of unresolved light ('blending') are ill-constrained.

We begin by reviewing the relevant formalism for microlensing by single and double stars in § 2.2. In § 2.3, we provide a general overview of the connection between detection efficiency and the mass ratio, angular separation and impact parameter of the event. We outline the unique difficulties in calculating the detection efficiency for observed events in § 2.4, and define detection and detection efficiency, as used throughout this work. Our algorithm for computing detection efficiencies is described in § 2.5, and in § 2.6 we apply this algorithm to simulated data in order to access the effects of different detection criterion, finite source size, and blending. Suggestions for addressing complications associated with determining accurate detection efficiencies of observed microlensing datasets are given in § 2.7. We summarize and conclude in § 2.8.

2.2. Relevant Formalism for Single and Double Microlenses

2.2.1. Single lenses

The time-variable flux observed from a microlensed star is

$$F(t) = F_0[A(t) + f_{\rm B}] \quad , \tag{2.1}$$

where F_0 is the unlensed flux of the star, $f_{\rm B}$ is the ratio of any unresolved, unlensed background light to F_0 (the 'blend fraction'), and $A(t)$ is the magnification. The magnification of A_0 of a point source by a point lens can be written as

$$A_0 = \frac{u^2+2}{u(u^2+4)^{1/2}} \quad . \tag{2.2}$$

Here u is the instantaneous angular separation of the source and the lens in units of the angular Einstein ring radius $\theta_{\rm E}$ of the lens, a degenerate combination of the lens mass and and distances defined by

$$\theta_{\rm E} \equiv \left[\frac{4GM}{c^2}\frac{D_{LS}}{D_{OL}\,D_{OS}}\right]^{1/2} \sim 260\,\mu{\rm as}\left(\frac{M}{0.2M_\odot}\right)^{1/2} , \tag{2.3}$$

where M is the mass of the lens, and $D_{\rm LS}$, $D_{\rm OS}$, $D_{\rm OL}$ are the lens-source, observer-source, and observer-lens distances, respectively. For the scaling relation on the far right of equation (2.3), we have assumed $D_{\rm OL} = 6$ kpc and $D_{\rm OS} = 8$ kpc. Note that for $u \to 0$, $A_0 \to 1/u$. Since the source, lens, and observer are all in relative motion, u will be a function of time. For rectilinear motion,

$$u(t) = \left[\left(\frac{t - t_0}{t_{\rm E}}\right)^2 + u_{\rm min}^2\right]^{1/2}, \tag{2.4}$$

where t_0 is the time of maximum magnification, $u_{\rm min}$ is the minimum angular separation, or impact parameter, of the event in units of $\theta_{\rm E}$, and $t_{\rm E}$ is a characteristic time scale of the event, the Einstein time, defined by

$$t_{\rm E} = \frac{\theta_{\rm E} D_{\rm OL}}{v_\perp} \sim 30 \text{ days} \left(\frac{M}{0.2 M_\odot}\right)^{1/2}. \tag{2.5}$$

Here $v_\perp$ is the transverse velocity of the lens relative to the observer-source line-of-sight. For the scaling relation on the far right of equation (2.5), we have assumed $D_{\rm OL} = 6$ kpc, $D_{\rm OS} = 8$ kpc, and $v_\perp = 100 \text{ km s}^{-1}$.

A point-lens point-source (PSPL) light curve is thus a function of five parameters, t_0, $t_{\rm E}$, $u_{\rm min}$, F_0, and $f_{\rm B}$. Unless the lens is luminous, the parameters F_0 and $f_{\rm B}$ depend only on the source and its environment. Their distributions depend on the luminosity functions of the observed sources and any blended light. The parameters t_0 and $u_{\rm min}$ are purely geometrical. Since the distribution of t_0 is flat and its value has no effect on the analysis of detection efficiencies, we will hereafter set $t_0 = 0$. The intrinsic distribution of $u_{\rm min}$ is also flat, but the observed distribution has an upper limit set by the detection threshold of the survey teams. If the lens is not contributing significantly to the blended light, only the characteristic time $t_{\rm E}$ contains physical information about the lens itself. Its intrinsic distribution is set by the lens masses and spatial distribution of the lenses and sources; the observed distribution of $t_{\rm E}$ depends on the temporal sampling of the microlensing campaigns.

An example of a point-lens light curve with $t_0 = 15$ days, $t_{\rm E} = 30$ days, $u_{\rm min} = 0.5$, $F_0 = 1$, and $f_{\rm B} = 0$ is shown as the dotted line in the top panel of Figure 2.1.

2.2.2. Binary lenses

A primary lens with an orbiting companion is described by the formalism of binary lenses. The flux is still expressed by equation (2.1), but the magnification can no longer be calculated analytically. Instead, the lens equation describing the mapping from the source plane (η, ξ) to the image plane (x, y) must be solved numerically. Following Witt (1990), we write the lens equation for two masses with fractional mass m_1 and m_2 located at positions z_1 and z_2 in terms of the complex coordinates $\zeta \equiv \eta + i\xi$ and $z \equiv x + iy$,

$$\zeta = z + \frac{m_1}{\bar{z}_1 - \bar{z}} + \frac{m_2}{\bar{z}_2 - \bar{z}} \quad . \tag{2.6}$$

Here all distances are in units of $\theta_{\rm E}$. The mapping is described completely by two parameters, the instantaneous angular separation of the two components in units of $\theta_{\rm E}$, $b = |z_1 - z_2|$, and the mass ratio of the system, $q = m_2/m_1$. Without loss of generality, we will assume that $m_2 \leq m_1$, so that $q \leq 1$. Equation (2.6) is equivalent to a fifth-order complex polynomial in z, which can be solved by the usual techniques. Each source position produces either three or five images. The magnification A_j of each image j is inversely proportional to the determinant of the Jacobian of the lens mapping, evaluated at that image position,

$$A_j = \left.\frac{1}{|\mathrm{det}J|}\right|_{z=z_j} , \quad \mathrm{det}J = 1 - \frac{\partial\zeta}{\partial\bar{z}}\overline{\frac{\partial\zeta}{\partial\bar{z}}}. \tag{2.7}$$

The total magnification is given by the sum of the individual magnifications, $A = \sum_j A_j$. The set of source positions for which the magnification is formally infinite, given by the condition $\mathrm{det}J = 0$, defines a set of closed curves called caustics. Depending on the values of b and q, a binary lens may have one, two, or three caustics; the multiplicity of images changes by two as the source crosses a caustic.

A static, point-source binary-lens light curve is a function of eight parameters. Two are identical to the point-lens case, F_0 and $f_{\rm B}$. The equation for $t_{\rm E}$ (and $\theta_{\rm E}$) retains the same form, but the choice of the fiducial mass M is arbitrary and can refer to the total mass of the binary or the mass of one of the components. For binaries, $u_{\rm min}$ refers to the minimum angular separation (in units of $\theta_{\rm E}$) between the source and the origin of the binary system. The choice of origin is also arbitrary; popular choices are the position of center of mass, the position of one of the masses, or the midpoint between the two. Equation (2.4) still holds for static binaries, so that t_0 is the time at which $u = u_{\rm min}$, but for binary lenses this need not be the time of maximum magnification. The mapping parameters b and q, and the angle θ on the sky between source trajectory and the binary axis, are the final three binary lens parameters. In the case of a single lens, the lensing geometry is azimuthally symmetric, and θ is completely degenerate for any measured light curve.

The value of $u_{\rm min}$ has a large effect on the detection efficiency of a given light curve to lens binarity; smaller $u_{\rm min}$ events generally have higher efficiency. The Einstein time scale $t_{\rm E}$ affects the detection efficiencies in that shorter time scale events will, in general, be less densely sampled by monitoring teams than longer time scale events. Blending complicates matters due to the ambiguity between light curves with different combinations of $u_{\rm min}$ and blend fraction $f_{\rm B}$ (Woźniak & Pacyński 1997), which can lead to ill-determined detection efficiencies if the blend fraction is poorly constrained (§ 2.6.3).

The magnification patterns of close binaries ($b \ll 1$), wide binaries ($b \gg 1$), and binaries with small mass ratios ($q \ll 1$), can be written as mathematical perturbations to the single lens pattern (Dominik, 1999b); the light curves they produce can be mistaken for those due to a single lens for a majority of source trajectories. The fractional deviation δ, which is defined by

$$\delta(t) \equiv \frac{A(t) - A_0(t)}{A(t)} \ , \tag{2.8}$$

where $A(t)$ is the binary-lens magnification and $A_0(t)$ is the magnification of the best-fit single-lens model, quantifies the degree to which a binary-lens light curve deviates from a best-fit single lens model as a function of time.

The best-fit single lens model need not have the same parameters t_0, $t_{\rm E}$ and $u_{\rm min}$ as the underlying binary and will vary depending on the size and duration of the deviation, which is determined by the source trajectory θ and the binary-lens parameters (b, q). The top panel of Figure 2.1 shows a light curve for binary system with $q = 0.01$ and $b = 1.0$, and two single-lens light curves: one assuming that the parameters $t_{\rm E}, t_0, u_{\rm min}$ are the same as in the underlying system, and the other the best-fit single lens curve. In this particular instance, the difference between the two single-lens curves is not large, although this is not universally true (see § 2.6.1). The bottom panel shows the fractional deviation of the binary light curve from both single-lens light curves. In this example, the deviation is appreciable ($\delta > 1\%$) for a large fraction of the light curve, but is large ($\delta > 5\%$) for only ~ 5 days, underscoring the need for high photometric precision in microlensing planet searches.

2.3. Qualitative Effects of the Intrinsic Binary Parameters

In addition to its dependence on observational parameters, the detection efficiency of a given light curve will be a strong function of the intrinsic mass ratio q, the instantaneous binary separation b of the lens system, the angle of the source trajectory with respect to the binary axis, θ, and the impact parameter of the event, $u_{\rm min}$.

To illustrate these dependences, we calculate δ as a function source position (ξ, η) for a grid of b and q values. Since the best-fit single lens light curve, and therefore δ, depends on the exact trajectory, we must adopt heuristic approximations in order to display these qualitative results in a single plot of δ contours. For $b \leq 1.0$ and all q, we choose $u_{\rm min}$ to be the minimum projected separation from the center-of-mass, and normalize $t_{\rm E}$ to the total mass of the binary. For $b > 1.0$ and $q \leq 10^{-1}$, we choose $u_{\rm min}$ to be the minimum separation from the more massive lens component, and normalize $t_{\rm E}$ to this component as well. For $q = 1$ and $b = 1.5$ we choose $u_{\rm min}$ to be the minimum projected separation from the center-of-mass, and normalize $t_{\rm E}$ to the total mass of the binary. Finally, for $q = 1$ and $b \geq 2.0$, we choose $u_{\rm min}$ to be the minimum separation from one of the components, and normalize $t_{\rm E}$ to the same component. These choices were made in order to approximate the transition between close and wide binaries and minimize the deviation *globally*. Since this qualitative example does not use best-fit single lens parameters, δ will be overestimated in all cases; we discuss this effect fully in § 2.6.1. To cover the full range of parameter space for which the detection efficiency is high, we choose 5 values of q, logarithmically spaced between 1.0 and 10^{-4}, and $b = 0.2$, 0.6, 1.0, 1.5, 2.0, and 3.0. The results are shown in Figure 2.2, where contours of $\delta = \pm 0.01$ and ± 0.05 are plotted with the caustics ($\delta = \infty$). Light curves are one-dimensional cuts through these diagrams. Since current survey programs rarely alert on-going events with $u_{\rm min} \gtrsim 1$, only trajectories that pass within $\theta_{\rm E}$ (circles in Figure 2.2) of the primary lens will be observed by the monitoring teams.

In Figure 2.3, light curves resulting from the sample trajectory in Figure 2.2 are displayed. This trajectory is rather typical, with $u_{\rm min} = 0.5$ and a randomly chosen angle θ. While for $q = 1.0$ and 10^{-1}, most trajectories will exhibit considerable ($\delta \geq 0.05$) deviations, for $q \lesssim 10^{-2}$, the magnitude of the deviation will depend strongly on the value of the θ. For example, although the light curve in Figure 2.3 for $q = 10^{-3}$ and $b = 0.6$ exhibits no significant deviation, inspection of Figure 2.2 reveals that a trajectory with the same impact parameter but $\theta \sim 90^\circ$ would be likely to have larger δ. This illustrates why a calculation of the detection efficiency of a non-anomalous light curve must involve an integration over θ, which is degenerate in the single-lens case. Figures 2.2 and 2.3 also illustrate why the detection efficiency of a light curve depends strongly on its $u_{\rm min}$. The sample trajectory for $q = 10^{-3}$ and $b = 1.0$, for example, does not deviate more than $\delta \sim 0.05$, yet almost all trajectories with smaller $u_{\rm min}$ would exhibit much larger deviations.

Several conclusions can be drawn from inspection of Figures 2.2 and 2.3. First, for $q \sim 1$ and $0.2 \lesssim b \lesssim 3.0$, nearly *all* trajectories have deviations $\delta > 5\%$. Second, for all separations b, events with $u_{\rm min} \lesssim 0.1$ will have a much higher detection efficiency than larger $u_{\rm min}$ events. Third, for small mass ratios ($q \lesssim 10^{-2}$), it is likely that only a small fraction of detected events will exhibit caustic crossings, since, for these mass ratios, the area covered by the caustics is considerably smaller than the area covered by the $\delta = \pm 0.05$ contours. Finally, for small q, detection efficiencies for light curves with typical impact parameters will be substantial only for companions with separations $0.6 \lesssim b \lesssim 1.6$, commonly referred to as the 'Lensing Zone'.

2.4. Motivation and Definitions

2.4.1. Efficiencies for Observed Microlensing Events

All light curves contain information about the presence of companions around Galactic lenses: obviously anomalous light curves signal the possible presence of a companion while light curves without a detectable anomaly signal the possible absence of (certain types of) companions. With observed datasets, both statements are probabilistic: the presence or absence a particular type of lensing companion in a particular system can only be made with a certain degree of confidence. Ultimately, we seek a method to characterize this probability consistently for all light curves, whether obviously anomalous or not, so that the complete dataset can be used to constrain the distribution of planets and other companions in orbit around Galactic lenses.

Because most microlensing light curves do not show obvious anomalies indicative of companions, we begin here by quantifying the extent to which an apparently non-anomalous light curve can be taken as a sign that planetary companions of a given mass ratio q and projected separation b are truly absent in the microlensing system under consideration. The absence of an observed planetary anomaly may be due to insufficient sampling, photometric precision, or monitoring duration, rather than the absence of a planet. This means that the efficiency of detection must be computed separately for each event. Intrinsic parameters, such as source trajectory, source size, and blending, may also serve to 'hide' the planetary anomaly from the observer, and must be disentangled from observational effects both to compute detection efficiencies of individual datasets and to formulate future observing strategies which will maximize the detection probability.

Previous studies of detection probabilities of idealized microlensing planet searches, which adopted simplifying assumptions such as uniform sampling and uniform distributions of $u_{\rm min}$ (Mao & Paczyński, 1991; Gould & Loeb, 1992; Bolatto & Falco, 1993; Bennett & Rhie, 1996; Di Stefano & Scalzo, 1999a,b; Griest & Safizadeh, 1998)) are not applicable to the situation confronted by a researcher wishing to use an actual database of microlensing light curves to draw inferences about possible lensing companions. While these studies sought to determine what one might expect to learn from microlensing experiments, we seek to determine what can be learned form the experiments (after they have been done). There are several essential differences between these two questions. First, observed light curves are irregularly sampled, each with its own and usually varying photometric precision. Second, only the post-alert portion of the light curve is available to current monitoring teams, resulting in differences in the monitored phase of each event. Third, the intrinsic impact parameter distribution of the events is altered by choices made by both the discovery and monitoring teams; the actual distribution cannot be assumed to be uniform over any interval. Finally, as pointed out by Griest & Safizadeh (1998), when comparing a binary-lens model to a single-lens model, the binary lens fit must be compared to the best-fit single lens model for a given light curve, not to a single-lens model in which the companion has been removed, because the true lensing parameters are unknown (see Fig. 2.1). Previous studies that did not use the best-fit single-lens model as the null hypothesis when calculating detection probabilities for idealized searches have overestimated the true detection probability (§ 2.6.1). These differences motivate the detection criteria and method of calculating detection efficiencies for actual datasets presented in this chapter.

2.4.2. Detection and Detection Efficiency

Before we can begin to quantify the detection efficiency, $\epsilon_i(b,q)$, of a lensing binary with microlensing parameters b,q using light curve ℓ_i, we must define the meaning of 'detection.' Here, we will consider a planetary companion to a lens to be 'detected' in light curve ℓ_i if some combination of the intrinsic binary parameters b,q and θ produces a substantially better fit (characterized by $\Delta\chi^2$) to the observed light curve than the best-fit single lens model. In making the comparison, the parameters $t_0, t_{\rm E}, F_0, u_{\rm min}$ and $f_{\rm B}$ are allowed to vary to achieve the best fit in both the binary and single lens models. The meaning of 'substantially better fit' can be adjusted by altering the threshold value of $\Delta\chi^2_{\rm thresh}$ that $\Delta\chi^2 = \chi^2_{\rm best\,single} - \chi^2_{\rm best\,binary}$ must exceed.

Since here we consider only light curves that are not obviously discrepant from PSPL (by the criterion above), the angle θ between the source trajectory and binary axis is degenerate, and can be assumed to be drawn from a random distribution over the full range $0 < \theta \leq 2\pi$. By *detection efficiency*, $\epsilon_i(b,q)$, we will mean the probability that an actual planetary companion with mass ratio q and instantaneous angular separation b would be 'detected' by the criterion above in a given *observed* light curve ℓ_i, assuming a random source trajectory. Only a subset of source trajectory angles will produce detections by this criterion. The efficiency incorporates both the intrinsic sensitivity of the observations to a given anomaly and the probability that such an anomaly occurs for random source trajectories. An efficiency $\epsilon_i(b,q)$ of zero implies that a lensing companion with characteristics b and q would always escape detection with these observations; $\epsilon_i(b,q) = 1$ implies that the companions would always be detected (if present) with data of this type and quality regardless of source trajectory through the magnification pattern. This efficiency can then be used to place a confidence level on the *non-detection* of b, q binary anomalies in a given light curve.

2.5. Description of the Algorithm

An schematic of our basic algorithm is displayed in Figure 2.4. The top panel shows a simulated light curve, which for the moment we use as a stand-in for an observed light curve. (For details on how this curve was generated, see § 2.6.1) For simplicity, we assume that the baseline flux is known perfectly ($F_0 = 1$) and that the event is not blended ($f_{\mathrm{B}} = 0$). We fit a restricted PSPL model with the three remaining free parameters $t_{\mathrm{E}}, u_{\mathrm{min}}, t_0$ to this 'observed' light curve, and obtain a χ^2 per degree of freedom of $\chi^2_\nu \equiv \chi^2/\mathrm{dof} = 288/300 = 0.96$, with best-fit parameters ($t_{\mathrm{E}} = 15\,\mathrm{days}, u_{\mathrm{min}} = 0.3, t_0 = 15.0$). This value of χ^2_ν indicates that the observed light curve is consistent with the PSPL model. In order to calculate the efficiency function $\epsilon(b,q)$ for this event, we must determine what fraction of all possible light curves arising from a $b - q$ binary lens is *incompatible* with the observed light curve. The middle panel of Figure 2.4 shows contours of constant δ for a binary with $q = 10^{-3}$ and $b = 1.5$, and a sample trajectory with $u_{\mathrm{min}} = 0.3$ and angle $\theta = 120°$ between the trajectory and the binary axis. Since this source path does not cross any regions of significant deviation, the corresponding observed light curve would be consistent with PSPL within the precision of typical monitoring photometry. Light curves resulting from some other trajectories with other values of θ would be inconsistent with the observed light curve. In order to determine the incompatibility of a $b - q$ binary lens model with the observed light curve as function θ, for each fixed θ we find the best-fit binary-lens light curve, leaving $u_{\mathrm{min}}, t_{\mathrm{E}}$ and t_0 as free parameters. We then calculate $\Delta\chi^2(b,q,\theta)$, the difference in χ^2 between the best-fit binary-lens light curve and the best-fit single lens light curve as a function of θ. The bottom panel of Figure 2.4 shows $\Delta\chi^2$ as a function of θ for a binary with $q = 10^{-3}$ and $b = 1.5$. Since only a small fraction of all possible trajectories would give rise to binary-lens light curves that are statistically incompatible with the data, the detection efficiency of this light curve is small for this parameter combination. Quantitatively, the detection efficiency is simply the fraction of all possible trajectories ($0 \le \theta \le 2\pi$), for which $\Delta\chi^2(b,q,\theta) > \Delta\chi^2_{\rm thresh}$,

$$\epsilon(b,q) \equiv \frac{1}{2\pi}\int_0^{2\pi} {\rm d}\theta\ \Theta[\Delta\chi^2(b,q,\theta) - \Delta\chi^2_{\rm thresh}], \tag{2.9}$$

where $\Theta[x]$ is a step function. For the event depicted in Figure 2.4, $\epsilon = 5\%$ for $b = 1.5$ and $q = 10^{-3}$ and a detection criterion of $\Delta\chi^2_{\rm thresh} = 225$. This process must then be repeated for all q and b, and then for all light curves that are consistent with the point-lens model.

For Gaussian errors, χ^2 is the best measure of goodness-of-fit, and the significance of the detection can be altered by adjusting $\Delta\chi^2_{\rm thresh}$, the minimum $\Delta\chi^2$ between the best-fit single and binary lens models required for a detection. The choice of $\Delta\chi^2_{\rm thresh}$ required for a 'detection' is arbitrary (as is any criterion for detection), but it should be kept in mind that error distributions for actual monitored events are far from Gaussian, and usually contain systematic errors with unrecognized correlations at the few percent level. In light of this, we choose rather conservative detection criteria, $\Delta\chi^2_{\rm thresh} > 100$. For such high criteria, the exact form of the error distribution is unlikely to have a substantial effect on the detection efficiency. The choice of the appropriate detection criterion for realistic error distributions will likely depend sensitively on, and be determined by, the actual error distributions themselves. We return to this point with a discussion of the dependence of detection efficiencies on the detection threshold in § 2.6.1.

The basic steps of our method to calculate the detection efficiency of non-anomalous events to binary lenses are summarized below. With the appropriate modifications, a similar algorithm can be applied to the analysis of detection efficiency for *any* microlensing anomaly, including those due to binary sources, lens rotation and parallax effects.

(1) Fit each event with a single lens model by minimizing χ^2 (or some other suitable goodness-of-fit estimator). Evaluate χ^2 for this model.

(2) Hold the angular separation and mass ratio (b, q) fixed. For each source trajectory θ, find the binary lens model that best fits the observed light curve, leaving $t_{\rm E}, t_0$, and $u_{\rm min}$ as free parameters. Evaluate the difference $\Delta\chi^2(b,q,\theta)$ between the single-lens and binary-lens fits.

(3) Find the fraction of all binary-lens fits for the given (b, q) that satisfy the detection criterion (e.g. $\Delta\chi^2 > \Delta\chi^2_{\rm thresh}$). This is the detection efficiency $\epsilon(b, q)$ for this event for the assumed separation and mass ratio.

(4) Repeat items (2) and (3) for all (b, q). This gives the detection efficiency for the ith event as a function of b and q, $\epsilon_i(b, q)$.

(5) Repeat items (1)-(4) for all events.

The steps itemized above assume that the baseline flux F_0 is known perfectly, and that the event is not blended, ($f_{\rm B} = 0$). In reality, one must always fit for the baseline flux F_0 and blend parameter $f_{\rm B}$. Including F_0 and $f_{\rm B}$ in the fitting procedures can have a strong effect on the computed detection efficiency of the resulting light curve. Similarly, the algorithmic outline above assumes that the source can be treated as point-like. Including finite source sizes can also have a significant effect on the inferred detection efficiency of a given event. In order to obtain an accurate estimate of the detection efficiency, these effects must be included in the fitting procedure, and either the light curve itself or other data used to constrain the blending and finite source size parameters. However, in order to clearly delineate the effects of blending, finite source size, and the choice of the detection criterion, we will first assume that the baseline flux is known perfectly, the blending is negligible, and the source can be approximated as a point-like. The effects of detection criterion, finite source size and blending on the detection efficiency $\epsilon(b, q)$ are then explored separately in §§ 2.6.1, 2.6.2 and 2.6.3, respectively.

The detection efficiencies calculated in the prescribed way for non-anomalous events can be used in several ways: (1) to place quantitative constraints on the absence of planets of certain b, q in non-anomalous lensing event; (2) to estimate the average detection efficiency $\epsilon(b, q)$ for a given dataset; (3) to estimate $\epsilon(b, q)$ for hypothetical datasets as a guide to future observational programs, and (4) as a proxy for the detection efficiency of observed anomalous events, for which additional challenges exist (see discussion in § 2.7.4).

2.6. Application to Simulated Data

In order to explore more fully the effect of the parameters $u_{\rm min}$, b, q, and detection criterion on the detection efficiency, and to test the robustness of the algorithm, we simulate light curves and calculate their detection efficiency $\epsilon(b, q)$.

Each simulated event is assumed to be alerted at $A = 1.54$ (the smallest amplification that the MACHO team will alert, see Alcock et al. 1997b), and then continuously observed at uniform intervals of $t_{\rm E}/200$ until either $t_{\rm E}$ after the peak or $3t_{\rm E}$ after the peak. A more realistic light curve would contain gaps due to bad weather or other observing conditions. In order to isolate as much as possible the intrinsic dependencies of the detection efficiency, we use uniform sampling, and also assume here $f_{\rm B} = 0$ and $F_0 = 1$. At each observation, a residual is drawn from a Gaussian distribution with $\sigma = \sigma_0 A_0$, where $\sigma_0 = 1\%$ or 2%, and A_0 is given by Equation (2.2). These parameters are roughly consistent with the best sampling and photometric accuracy of the PLANET collaboration (Albrow et al., 1998). Hereafter, all results will be for light curves with $\sigma_0 = 2\%$ and observations until $t_{\rm E}$ unless otherwise noted. Three values of the impact parameter, $u_{\rm min} = 0.5$, 0.3, and 0.1, are investigated.

For each light curve, we calculate $\epsilon(b, q)$ using steps (2-4) in § 2.5. When fitting the binary, we employ a downhill-simplex method (Press et al., 1992), which usually converges quickly and robustly to the minimum. The fitted single-lens parameters are used as an initial guess, since best-fit binary parameters are typically close to the single-lens values for small mass ratios q.

Since the fitting procedure can be computationally expensive, we sample θ only at intervals of $2\pi/100$; our efficiencies are thus limited to a resolution of $\Delta\epsilon = 0.01$. Although one would like to sample the (b, q) plane as densely as possible, we are again limited by computational expense. Since planetary events are the primary interest of most monitoring collaborations, and nearly equal mass binaries ($10^{-1} \leq q \leq 1.0$) will have $\epsilon \sim 100\%$ in the Lensing Zone anyway, we choose to restrict our attention to $q \leq 10^{-2}$. Furthermore, the effect of finite source sizes and blending, which we wish to investigate, will be substantially less dramatic for $q \gtrsim 10^{-1}$ than for lower mass-ratio systems. We choose three mass ratios: $q = 10^{-2}$, 10^{-3} and 10^{-4}. Using a different detection algorithm, Bennett & Rhie (1996) found detection probabilities of ~2% for $q = 10^{-5}$. Since this is comparable to our resolution $\Delta\epsilon = 0.01$, we will not extend our analysis to mass ratios smaller than $q = 10^{-4}$. We calculate ϵ from $b = 0.2$ to 2.0 at intervals of 0.2, and then again at $b = 3.0$.

2.6.1. Basic Results

Previous explorations of planetary microlensing detection probabilities have *not* used the best-fit binary lens light curve, which is computationally expensive to compute. Holding $t_{\rm E}$, t_0 and $u_{\rm min}$ fixed will cause one to overestimate the detection efficiency in two ways. First, for large mass ratios $q \gtrsim 10^{-2}$, the secondary cannot simply be treated as a perturbation to the primary light curve. The presence of the secondary will have a significant effect on the global (averaged over all trajectories) values of the best-fit parameters. For example, a close ($b \ll 1$) equal mass binary will have a time scale that is a factor of $2^{1/2}$ larger than an otherwise identical wide ($b \gg 1$) binary. Second, for small mass ratios $q \lesssim 10^{-3}$, the majority of the detection efficiency will arise from relatively small, $\delta \lesssim 10\%$, deviations. These deviations can be suppressed below the detection criterion if the fit is allowed to adjust to compensate for them (Griest & Safizadeh, 1998). In order to facilitate comparison between our results and previous calculations, and to gauge the error induced by holding the parameters $t_{\rm E}$, t_0, and $u_{\rm min}$ fixed when calculating the difference between binary-lens and single-lens magnifications, we have also calculated $\epsilon(b,q)$ without finding the best-fit binary, assuming instead that $t_{\rm E}$, t_0 and $u_{\rm min}$ are the same for the binary and single lens fits. For $b \leq 1$, we choose the center-of-mass as the origin of the binary; for $b > 1$, we choose the position of the primary.

In Figure 2.5 the detection efficiency $\epsilon(b,q)$ is displayed as a function of the dimensionless angular separation b, for the three different impact parameters ($u_{\rm min} = 0.1, 0.3$, and 0.5) and mass ratios ($q = 10^{-2}, 10^{-3}$, and 10^{-4}) we investigated. We show $\epsilon(b,q)$ calculated using different detection criteria: $\Delta\chi^2_{\rm thresh} = 100$, $\Delta\chi^2_{\rm thresh} = 225$, and the criterion that the trajectory must cross a caustic in order to be detected. Also shown is $\epsilon(b,q)$ for $\Delta\chi^2_{\rm thresh} = 225$ without fitting the binary light curve.

Figure 2.5 illustrates several points. First, the difference between the detection efficiency calculated using the two different thresholds, $\Delta\chi^2_{\rm thresh} = 225$ and 100, is small and approximately constant at $\Delta\epsilon \sim 0.05$ over most of the parameter space considered. However, since the magnitude of $\epsilon(b,q)$ decreases with decreasing mass ratio q, the fractional difference increases. The exact choice of $\Delta\chi^2_{\rm thresh}$ thus has little effect on $\epsilon(b,q)$ for deviations well above the detection threshold. For perturbations near the detection limit, however, such as those arising from companions with mass ratio $q = 10^{-4}$, the detection efficiency can vary by a factor of two depending on the choice of detection criterion. Second, the error induced by not using the best-fit binary lens light curve can be substantial for $q = 10^{-2}$, because such companions cause significant anomalies over a large fraction of the light curve so that the parameters of the best fit binary- and single-lens models can differ dramatically. This is especially true for high magnification events with $b > 1$, for which the fractional deviation δ from the best single-lens model depends critically on the choice of the binary origin, which can be significantly different from the primary lens position depending on the value of b. The error induced is also large for $q = 10^{-4}$, because these deviations are very near the detection limit. For $q = 10^{-3}$, the deviations caused by the companion can be treated as a perturbation to the primary light curve, and are well above the detection limit, minimizing the effect of not using the best-fit binary; we caution, however, that this is unlikely to be true for all realizations of realistic sampling. We conclude that one can avoid fitting the binary lens light curve for mass ratios $q \lesssim 10^{-3}$ only if the deviations are well above the detection limit of the observed light curve. Finally, as noted by Gould & Loeb (1992), we find that caustic crossing events are likely to comprise only a small fraction of all detected events. This is especially important because non-caustic crossing events are more prone to degeneracies and thus the most difficult to characterize (Gaudi & Gould, 1997; Gaudi, 1998).

To quantify the effects of the various detection criteria and impact parameters on $\epsilon(b,q)$, we tabulate in Table 2.1 average detection efficiencies $\epsilon_{\rm LZ}(q)$ for the curves in Figure 2.5 integrated over the Lensing Zone (where the detection efficiency is the highest), $0.6 \le b \le 1.6$,

$$\epsilon_{\rm LZ}(q) \equiv \int_{0.6}^{1.6} {\rm d}b\, \epsilon(b,q) \ . \tag{2.10}$$

The accuracy of these results are limited by the fact that we sample $\epsilon(b,q)$ only at intervals of $\Delta b = 0.2$ in this zone. For any given event, however, the results are more secure, so that comparisons between $\epsilon_{\rm LZ}$ for ($u_{\rm min} = 0.1, q = 10^{-2}$) and ($u_{\rm min} = 0.1, q = 10^{-3}$) should be more reliable than comparisons between ($u_{\rm min} = 0.1, q = 10^{-2}$) and ($u_{\rm min} = 0.3, q = 10^{-2}$). Table 2.1 illustrates that the fractional error induced by not fitting the binary light curve is smallest for $q = 10^{-3}$, $\lesssim 15\%$. For $q = 10^{-2}$ and $q = 10^{-4}$ however, the error can be considerably larger, $\sim 20\%$ for $u_{\rm min} = 0.3$ and $q = 10^{-2}$, and $\sim 30\%$ for $u_{\rm min} = 0.5$ and $q = 10^{-4}$. The fractional difference in $\epsilon_{\rm LZ}$ between $\Delta\chi^2_{\rm thresh} = 100$ and 225 can be substantial, especially for $q = 10^{-4}$, where it is always greater than 50%. Finally, caustic crossing anomalies comprise a relatively small fraction of the total events, representing at most 35% of the integrated detection efficiency, and decrease in importance for large impact parameters and smaller mass ratio.

If all lensing primaries have planets distributed uniformly in b, the numbers in Table 2.1 represent the fraction of all events with the given $u_{\rm min}$ that would exhibit detectable deviations with the given q and $0.6 \le b \le 1.6$. For larger mass ratio companions with $q = 10^{-2}$, the detectable fraction is quite large, $\epsilon_{\rm LZ}(q) \gtrsim 30\%$, and remains substantial, $\epsilon_{\rm LZ}(q) \gtrsim 10\%$, even for "Jovian" companions with $q = 10^{-3}$. For small companions with $q = 10^{-4}$, however, the detectable lensing zone fraction drops significantly below 10% in all cases, although the exact numbers are somewhat uncertain due to the poor sampling in b. We conclude that microlensing will be able to place strong constraints on the frequency of double lenses with $q \gtrsim 10^{-2}$ and mild constraints on systems with $q = 10^{-3}$ companions, but will be unable to meaningfully constrain systems with $q \lesssim 10^{-4}$, unless the sampling and photometric precision are significantly better than those assumed in these simulations.

2.6.2. Finite Source Effects

The results in § 2.6.1 were calculated under the assumption that the microlensed source was point-like, so that the magnification of the source is infinite at the caustics. The magnification $A_{\rm fs}$ of a source with finite size is given by the integral of the point-source magnification over the face of the star,

$$A_{\rm fs}(t) = \frac{\int {\rm d}^2r\, A(t;\mathbf{r}) I(\mathbf{r})}{\int {\rm d}^2 r\, I(\mathbf{r})} \ , \tag{2.11}$$

and is equivalent to the intensity-weighted area of the images (numerator) divided by the intensity-weighted area of the unlensed source (denominator). Here $I(\mathbf{r})$ is the intensity profile of the source. The finite size of the source smoothes and broadens the discontinuous jumps in magnification near caustics by an amount that depends on the angular size of the source, θ_*, in units of $\theta_{\rm E}$,

$$\rho_* \equiv \frac{\theta_*}{\theta_{\rm E}} = \frac{R_*}{R_E}\frac{D_{\rm OL}}{D_{\rm OS}} = 0.03\left(\frac{M}{0.2 M_\odot}\right)^{1/2}\left(\frac{R_*}{10 R_\odot}\right) \ , \tag{2.12}$$

where R_* is the physical size of the star. For the scaling relation on the right of equation (2.12), a lens distance of $D_{\rm OL} = 6$ kpc and a source distance of $D_{\rm OS} = 8$ kpc has been assumed. For a given ρ_*, uniform sources ($I =$ constant) will have a larger effect on the magnification than limb-darkened sources. Since we are interested primarily in the magnitude of the effect that finite sources will have on the detection efficiency, we will assume a (less-realistic) uniform source profile, which also increases computational speed.

Since the caustic of a point lens is a single point at the center of the lens ($u = 0$), the magnification of a finite source will differ from that of a point source only when the source approaches the center of the lens, $u_{\rm min} \sim \rho_*$. For typical sources and lenses, $\rho_* \ll 1$ (c.f. equation (2.12)), so that for single lenses finite source effects are noticeable only in high magnification events ($u_{\rm min} \ll 1$), for which $A \sim u^{-1}$ (equation (2.2)). Assuming a uniform source, the single lens magnification can be found analytically in this limit (Schneider, Ehlers, & Falco, 1992),

$$A_{\rm fs,0}(t) = A_0(t)\mathcal{B}[z(t)], \tag{2.13}$$

where

$$\mathcal{B}(z) = \begin{cases} \frac{4}{\pi} E(z) & z \le 1 \\ \frac{4}{\pi} z\left[E(1/z) - (1 - z^{-2}) K(1/z)\right] & z \ge 1 \end{cases} \ . \tag{2.14}$$

Here K and E are the complete elliptic integrals of the first and second kind, and $z \equiv u/\rho_*$.

For a binary lens, the finite size of the source affects the magnification whenever the source approaches a caustic or, more precisely, wherever the second derivative of the magnification is large. As can be seen in Figure 2.2, for binaries with $q \sim 1$ much of the region inside the Einstein ring satisfies this condition: caustic approaches and crossings will be common. On the other hand, the results of § 2.6.1 indicate that caustic crossings make up only a small fraction of all detectable events for binaries with mass ratios consistent with planetary systems ($q \lesssim 10^{-2}$). Nevertheless, as can be seen from Figure 2.2, in order to produce a detectable deviation, trajectories must pass close to caustics, where the gradient of the magnification is large and finite source effects are non-negligible. Finite source magnifications for binary lenses cannot be found analytically. Numerical integration of the point source magnification over the face of the star is difficult, as the divergent magnification near caustics causes the results to depend critically on the integration grid size. A more robust method is to compute the total area of all images and then divide by this area by that of the source to find the magnification of the finite source at that position. Numerous methods have been suggested; we will integrate over the boundary of the images (Kayser & Schramm, 1988; Gould & Gaucherel, 1997; Dominik, 1998). For alternative methods, see Bennett & Rhie (1996), Wambsganss (1997), and Griest & Safizadeh (1998).

Effect on Finite Sources on the Detection Efficiency

What is relevant to this discussion is not the difference between the finite source and point source magnification, but the effects of finite source size on the determination of the detection efficiency ϵ. For nearly equal-mass binaries ($q \gtrsim 10^{-1}$), the magnification may be altered considerably by finite source effects without substantially altering ϵ. This can be seen by comparing the size of the deviations (δ) in the $q = 1.0$ and $q = 10^{-1}$ panels of Figure 2.2 to the size of a large source ($\rho_* = 0.03$). For mass ratios as small as $q \lesssim 10^{-3}$, however, the size of the δ structures is comparable to that of a large source, and finite source effects are important to a proper determination of the detection efficiency ϵ. Roughly speaking, finite source effects become important whenever the source size becomes comparable to the Einstein ring of the companion, $\theta_* \gtrsim \theta_p = q^{1/2}\theta_{\rm E}$, or,

$$\rho_* \gtrsim q^{1/2}. \tag{2.15}$$

This criterion is satisfied at $\rho_* \simeq 0.1$ for $q \simeq 10^{-2}$, whereas for $q \sim 10^{-3}$ source sizes $\rho_* \gtrsim 0.03$ will begin to seriously affect ϵ. Since the largest sources routinely monitored in the Galactic bulge are clump giants, with $\rho_* \simeq 0.03$, finite source effects will be negligible for $q > 10^{-3}$, but must be considered for smaller mass ratios.

Although the magnitude of the perturbation will always be suppressed in the presence of a finite source, it will also be broadened. Finite sources thus have competing effects on the detection efficiency ϵ: ϵ is decreased because previously significant deviations are suppressed below the detection threshold, but increased for those trajectories for which the limb of the star grazes a caustic (or high magnification area) yielding a significant deviation where no significant deviation would have occurred for a point source. The net result of these two competing effects will depend on the specific value of q and b.

Contours of constant fractional deviation δ of a binary from a single lens magnification, are illustrated in Figure 2.6 for both a point source and a finite source. We choose $\rho_* = 0.03$, a relatively large source, and $q = 10^{-4}$, the smallest mass ratio we consider, in order to present a scenario in which the source size will have an extreme effect. For the finite-source cases, the fractional deviation is computed with respect to a *finite-source* point-lens magnification, as given by equation (2.13). Figure 2.6 clearly demonstrates that, for this mass ratio and source size, the differences between the point and finite source magnification are dramatic. Both the shape and size of the δ-contours are altered considerably.

As can be seen from Figure 2.6, planetary perturbations with $b < 1$ are qualitatively different than those with $b > 1$ (Gould & Loeb 1992; Gaudi & Gould 1997; Wambsganss 1997). Consider the case $b = 0.8$: the perturbation is substantially depressed by the finite source and the $\delta = 5\%$ contours have nearly disappeared. This is because, for $b < 1$, regions of constant positive and negative deviation are closely spaced and of nearly equal area so that the smoothing induced by a large source tends to cause a cancellation leaving a deviation that is nearly zero (Bennett & Rhie, 1996; Gould & Gaucherel, 1997). The effect is even more prominent for $b \sim 1$, where the regions of positive and negative deviation are especially closely spaced (Bennett & Rhie 1996). Obviously, for these two parameter combinations, the planet is unlikely to be detected and $\epsilon \to 0$. For $b > 1$, regions of positive deviation encompass considerably more area than those of negative deviation (at a fixed value of $|\delta| \gtrsim 5\%$), and the cancellation is less dramatic. As a result, $\epsilon(b > 1)$ will be less affected by finite sources than $\epsilon(b \leq 1)$. In both cases, the perturbations caused by the central caustic (near $\zeta = 0, \eta = 0$) have dropped below $\delta = 1\%$. Central caustics are an important channel to planet detection in high magnification events; detection efficiencies for these events will be highly sensitive to ρ_* (Griest & Safizadeh, 1998). Fortunately, this is a class of events for which ρ_* can often be measured.

In Figure 2.7, the light curves resulting from the trajectories shown in Figure 2.6 are displayed. The trajectories were chosen to create a significant point source fractional deviation, but are otherwise representative. Dramatic cancellation can be seen in the light curves for $b = 0.8$ and $b = 1.0$. For $b = 1.2$, the deviation is substantially suppressed but is also broader. For photometry of sufficient precision, the detection efficiency ϵ for this parameter combination will actually be *increased*.

To make a quantitative comparison, we have calculated ϵ in the same manner and for the same parameters as in § 2.6.1, but now compare the simulated light curves to the best-fit finite source binary light curves with $\rho_* = 0.03$. The results with a detection criterion $\Delta\chi^2_{\text{thresh}} = 225$ are shown in Figure 2.8, along with the corresponding point source efficiencies from Figure 2.5. In agreement with the estimate from equation (2.15), the detection efficiency ϵ for $q = 10^{-2}$ companions is hardly affected. For $q = 10^{-3}$ and separations $b < 1$, ϵ is similar to or smaller than finite source efficiencies, but for wider separations $b > 1$, ϵ can be either somewhat smaller or somewhat *larger* due to the finite source size. The difference is dramatic for $q = 10^{-4}$: source sizes corresponding to bulge giants always yield efficiencies $\lesssim 1\%$. As in § 2.6.1, we calculate lensing zone efficiencies ϵ_{LZ} (equation (2.10)); the results are shown in Table 2.2. We conclude that finite source sizes have negligible effect on ϵ for $q \gtrsim 10^{-2}$, but sources as large as bulge giants ($\rho_* \simeq 0.03$) can have a dramatic effect for smaller companions, either increasing or decreasing ϵ ($q \simeq 10^{-3}$), or wiping out the detection efficiency completely ($q \lesssim 10^{-4}$).

Unfortunately, for individual events, the value of ρ_* is very poorly constrained. While it is possible to estimate the physical size of the source from its color and magnitude, this cannot be translated to the dimensionless projected size ρ_* if the value of θ_{E} remains unknown. The detection efficiency ϵ for most events could be in error therefore by many tens of percent (c.f. Figure 2.8 and Table 2.2). We discuss method of dealing with this difficulty in § 2.7.2.

2.6.3. Blending

A microlensing event is blended whenever unresolved, unlensed background light contributes significantly to the observed baseline flux of the source star (i.e. $f_{\text{B}} \neq 0$). From equation (2.1), the observed magnification in the presence of blending, A_{B}, is related to the true magnification by,

$$A_{\text{B}} = (1 + f_{\text{B}})^{-1}(A + f_{\text{B}}) \ , \tag{2.16}$$

where f_{B} is the ratio of the blend flux to the true lensed source flux.

Blending will have two effects on the detection efficiency. The first is a suppression of the deviation caused by the binary. From equation (2.16) and equation (2.1), it is straightforward to show that the fractional deviation in the presence of a blend, $\delta_{\rm B}$, is related to the true fractional deviation by,

$$\delta_{\rm B} = \delta \left(1 + \frac{f_{\rm B}}{A_0}\right)^{-1} \quad . \tag{2.17}$$

As before, A_0 is the magnification of the best-fit PSPL light curve. Note that equation (2.17) applies to any anomaly that produces a deviation from the standard PSPL light curve, including parallax, binary source, and finite source effects. Since A_0 is a function of time, the magnitude of the suppression will also be a function of time, such that deviations occurring closer to the peak ($u \sim u_{\rm min}$) will be less suppressed than those occurring near the beginning and end of the event. Figure 2.9 shows the ratio $\delta_{\rm B}/\delta$ as a function of the angular separation u of the lens and source, for three values of $f_{\rm B}$ corresponding to relatively mild blending, $f_{\rm B} < 1$. Anomalies occurring near the peak of high magnification events ($u \sim 0$) will be only slightly suppressed (Griest & Safizadeh, 1998), while repeating events caused by wide binaries (Di Stefano & Mao 1996; Di Stefano & Scalzo 1999b) can be suppressed by as much as $(1 + f_{\rm B})^{-1}$. Overall, the amplitude of the suppression for mild blending is relatively small, $\delta_{\rm B}/\delta \leq (1 + f_{\rm B})^{-1}$, and thus will not have a large effect on the detection efficiencies for binaries with mass ratios $q \geq 10^{-2}$ for which the fractional deviations are usually large. For mass ratios consistent with planets, $q \leq 10^{-3}$, however, a substantial fraction of detected events will have maximum fractional deviation $\delta_{\rm max} \lesssim 0.1$ so that even a suppression of ~ 0.5 can have a significant effect on planetary detection efficiencies.

The second effect that blending has on detection efficiencies is to alter the presumed distribution of $u_{\rm min}$ in observed events. The intrinsic distribution of $u_{\rm min}$ is flat up to the magnification threshold set for detection by the survey teams (e.g., $A > 1.34$ corresponds to $u_{\rm min} < 1$). This threshold is calculated in real time near the beginning of the event when a robust determination of blending is not possible. Consequently, the magnification of the event at any time is assumed to be the total flux divided by the baseline flux, $A_{\rm B} = (1 + f_{\rm B})^{-1}(A + f_{\rm B})$, which is less than the true magnification A for all non-zero blending values. Thus, in the presence of blending, an event will require a larger magnification and thus smaller intrinsic $u_{\rm min}$ in order to pass the detection criterion, which is *per force* applied to the observed quantity $A_{\rm B}$ (see Alcock et al. 1997 for an example and discussion). Since the intrinsic detection efficiency is larger for smaller impact parameters (see § 2.6.1 and Figure 2.5), the blended event will be more sensitive to the presence of planets than would be calculated for a $u_{\rm min}$ based on the (erroneous) assumption that $f_{\rm B} = 0$. Blending thus affects binary detection efficiency in two competing ways: the efficiency is decreased by suppressing the amplitude of observed deviations, while at the same time it is increased due to the skewing of the observed $u_{\rm min}$ distribution to smaller values. The net effect on the detection efficiencies will depend on the values of b and q and vary on an event-by-event basis.

Clearly, blending must be considered when calculating binary and planetary detection efficiencies. Since blending effects are relatively easy to quantify, this poses no serious complication as long as the blending parameter, $f_{\rm B}$, can be accurately determined for individual events. Unfortunately, as discussed by Woźniak & Paczynksi (1997), blending can be extremely difficult to determine for individual observed light curves, due to the serious correlations in the parameters $F_0, t_{\rm E}, u_{\rm min}$ and $f_{\rm B}$ in the presence of blending. The degeneracy is especially severe in two regimes. In the 'spike' regime, defined by $f_{\rm B} \gg 1$ and $u_{\rm min} \ll 1$, $t_{\rm E}$ and $u_{\rm min}$ cannot be measured separately and only the degenerate combination $t_{\rm E}/u_{\rm min}$ is measurable (Gould, 1996). This regime is most important in severely crowded fields, such as those towards M31. The second regime, defined by large impact parameter ($u_{\rm min} \gtrsim 0.5$) events with modest blending $f_{\rm B} < 1$, is more common in bulge fields, and thus the focus of our current attention.

Effect on Blending on the Detection Eqfficiency

In order to illustrate the difficulty in quantifying the fraction of blended light, we calculate the range of allowed values inferred for $f_{\rm B}$ from fits to our fiducial simulated light curves (i.e., observations from alert until $t_{\rm E}$, 2% errors, and *no blending*). Fixing $f_{\rm B}$ at some value, we find the best fit to a point-lens model allowing the parameters $u_{\rm min}, t_{\rm E}, t_0$, and F_0 to vary. We then compute $\Delta\chi^2$ between this fit and that assuming $f_{\rm B} = 0$. The resulting $\Delta\chi^2$ as a function of $f_{\rm B}$ is shown in Figure 2.10. For $u_{\rm min} = 0.1$ and $u_{\rm min} = 0.3$, the degeneracy is not severe; the 3σ allowed ranges in $f_{\rm B}$ are $f_{\rm B} \leq 0.125$ and $f_{\rm B} \leq 0.45$, respectively. For $u_{\rm min} = 0.5$, the blend fraction is almost completely unconstrained because for large $u_{\rm min}$ events constraints on blending arise mostly from the combination of information from the wings ($|t - t_0| \sim t_{\rm E}$) of the event and the baseline ($|t - t_0| \gg t_{\rm E}$). Thus, without a baseline measurement, the value of F_0 can be arbitrarily adjusted to compensate for large values of $f_{\rm B}$ without significantly affecting the fit. With this in mind, we have also computed the same $\Delta\chi^2$ statistic for a simulated light curve with observations from alert until $3t_{\rm E}$. Here the blending is much better constrained, $f_{\rm B} \leq 0.27$, with additional improvement if the errors are reduced by half, in which case $f_{\rm B} \leq 0.15$. Since the majority of the constraint comes from sampling the wings and baseline of the light curve, it would be more efficient for monitoring teams to concentrate on more, rather than better, measurements.

The right panels of Figure 2.10 demonstrate how an inaccurately-determined blend fraction can affect the determination of $u_{\rm min}$ and thus the detection efficiency ϵ. Here we show the ratio between the value of $u_{\rm min}$ determined by assuming a constant blend fraction $f_{\rm B}$, $u_{\rm min,f}$, and the true value $u_{\rm min}$. The value of $u_{\rm min}$ deduced for blend fractions between $f_{\rm B} = 0$ to $f_{\rm B} = 0.4$ can vary by nearly 50% resulting in quite different inferred detection efficiencies (c.f. Figure 2.5). To quantify this, we have calculated ϵ as a function of $f_{\rm B}$ for an extreme example, $u_{\rm min} = 0.5$ and observations from alert until $1 t_{\rm E}$. The procedure for calculating ϵ is the same, except now $f_{\rm B}$ is fixed at an assumed value and F_0 is included as a free parameter in both the single lens and binary lens fits. The results are shown in Figure 2.11, where we plot $\epsilon(q = 10^{-2})$ as a function of b for $f_{\rm B} = 0$ (same as Figure 2.5), 0.2, 0.4, and 0.6. Recall that all these blend fractions are statistically indistinguishable for this light curve. The differences in ϵ are dramatic. The suppression of binary anomalies induced by blending of $f_{\rm B} = 0$ and 0.2 causes a drop in detection efficiency for separations $b \lesssim 0.6$ and $b \gtrsim 1.6$. Inside the Lensing Zone, however, the net effect is a dramatic increase in ϵ due to the lower value of $u_{\rm min}$ required to produce the observed light curve for increasing $f_{\rm B}$. This can be appreciated best by examination of Table 2.3, which tabulates $\epsilon_{\rm LZ}$ as a function of $f_{\rm B}$. To the extent that these values of $f_{\rm B}$ cannot be distinguished from one another by the light curve alone, they are all equally likely, and thus ϵ can be quite uncertain.

Blending can give rise to a serious uncertainty in derived detection efficiencies but, unlike finite source size, the blend fraction can be determined with sufficient accuracy for most events. To do so, however, requires precise measurements by the monitoring teams during the wings of the event and at baseline. Without a reasonable quantification of the blend fraction, the detection efficiency of individual events will be very uncertain.

2.7. Application to Observed Data

In previous sections, we used simulated data to explore several effects that can influence significantly the determination of the detection efficiency ϵ of individual light curves, including detection criteria (§ 2.6.1), finite source size (§ 2.6.2), and blending (§ 2.6.3). These effects are often difficult to quantify in observed data, for which sampling and photometric precision is likely to vary on an event-by-event basis, and with observing conditions and microlensing phase for individual events. Furthermore, real-time observational decisions may alter (increase) the sampling of clearly anomalous events from that of apparently non-anomalous PSPL events.

2.7.1. Variable Sampling and Photometric Precision

Since the algorithm we presented in § 2.5 uses the observed light curve, and thus the observed sampling and photometric uncertainties associated with each event, irregular sampling and variable precision are taken into account explicitly in the determination of the detection efficiency ϵ. The efficiencies based on simulated data presented in previous sections to illustrate general principles will not be strictly applicable to observed microlensing events, for which weather and other considerations prevent continuous monitoring with a sampling of $t_{\rm E}/200$. In general, the effect of reduced or incomplete sampling will be to lower detection efficiencies. For extremely long events, or those (including very short) events alerted post-peak by the survey teams, substantial portions of the light curve will have no (dense) monitoring at all, and the effects on the detection efficiency can be quite devastating. In such partially-monitored light curves, the PSPL fit parameters ($u_{\rm min}, t_{\rm E}, t_0, F_0$ and $f_{\rm B}$) will be very uncertain, and in extreme cases almost completely unconstrained. Since the detection efficiency depends on these parameters, the resulting uncertainty in ϵ will be quite large. Unless additional information is available (e.g. from the survey teams) to constrain the fit, these data will add almost nothing to our knowledge of the abundance of planets since their detection efficiency cannot be reliably quantified.

For Gaussian, uncorrelated errors, the χ^2 statistic can be used as a measure of goodness-of-fit. Real measurement uncertainties are seldom truly Gaussian, especially in crowded microlensing fields where systematic effects associated with seeing, scattered light, and detector characteristics become increasingly important. Uncertainties on individual data points are often taken to be the formal errors reported by the PSF-fitting algorithms of photometric reduction packages like DoPhot (Schechter, Mateo, & Saha, 1993), which often underestimate the true scatter (Albrow et al., 1998). Image subtraction techniques (Tomaney & Crotts, 1996; Alard & Lupton, 1998) may alleviate some of these difficulties, but for the moment are too cumbersome and slow to implement for multi-site, real-time reduction of large fields and thus have not yet been implemented by monitoring teams. An empirical correction to account for the correlation of measured photometric magnitude with the FWHM of the point spread function often results in a more Gaussian error distribution whose average magnitude corresponds more closely to the formal DoPhot-reported error (Naber, private communication; Albrow et al. 2000b). As long as the detection criterion $\Delta\chi^2_{\rm thresh}$ is maintained at a suitably high value (§ 2.6.1), the exact error distribution is likely to have little effect on the computed efficiency ϵ. Remaining doubts can be assuaged by attaching the observed error distribution derived from constant stars to simulated PSPL light curves to calibrate both the 'false alarm rate' and efficiency of true detections with a given $\Delta\chi^2_{\rm thresh}$ criterion.

2.7.2. Finite Source Effects

Finite source effects pose a significant challenge to the robust determination of the detection efficiency ϵ because the dimensionless source size, ρ_* is unknown a priori. As we have shown in § 2.6.2, the finite size of the source should have negligible effect on ϵ for $q \gtrsim 10^{-2}$ but can have a significant effect for $q \lesssim 10^{-3}$. Thus, without additional information about ρ_*, ϵ can be determined robustly only for $q \gtrsim 10^{-2}$, which is unsatisfactory for microlensing monitoring programs whose primary goal is to learn about small mass-ratio systems. A first-order estimate for ρ_* could be obtained by measuring the angular size of the source, θ_*, and assuming that the relative proper motion of the lens, $\mu = v_\perp / D_{\mathrm{OL}}$, is equal to the mean relative proper motion $\langle \mu \rangle$ for all lenses toward the bulge. The dimensionless size of the source would then be given by

$$\rho_* \approx \frac{\theta_*}{\langle \mu \rangle \, t_{\mathrm{E}}} \; . \tag{2.18}$$

The angular size of the source can be estimated by its color and magnitude, or by obtaining a precise spectral type through more resource-intensive spectroscopy. Unfortunately, the value of $\langle \mu \rangle$ depends on the assumed velocity and spatial distribution of the lenses. Moreover, even within a given model, the distribution of μ is wide, having a variance of a factor of ~ 3 and long tails toward higher and lower values (Han & Gould, 1995). The true value of μ thus could differ substantially from $\langle \mu \rangle$, leading to a large error in ϵ for individual events. When averaged over many events, these errors should approximately cancel, but current monitoring programs are very far from this regime, especially for *anomalous* events.

A somewhat better estimate for the effect of ρ_* on detection efficiencies could be made as follows. Assume that an event has measured time scale t_{E} and angular source size θ_*. For an assumed model of lens distances and velocities, the expected distribution of proper motions, $\mathcal{G}_i(\mu)$, can be computed. The individual detection efficiency can then be approximated as,

$$\epsilon_i(b, q) = \int_{\mu_{\mathrm{min}}}^{\mu_{\mathrm{max}}} \mathrm{d}\mu \, \epsilon_i(b, q; \rho_*) \mathcal{G}_i(\mu) \; , \tag{2.19}$$

where $\rho_* = \theta_* / \mu t_{\mathrm{E}}$, μ_{max} is the maximum proper motion allowed by the observed light curve, and μ_{min} is some reasonable lower limit. This model-dependent estimate of the detection efficiency should be more accurate whenever finite source effects are large, but it is time consuming to compute because $\epsilon(b, q)$ must be determined for many ρ_*.

Ideally, one would like to determine ρ_* directly for each individual lens. This can be done by measuring μ from single-color light curves for only $\sim 5\%$ of events (Gould, 1994; Witt, 1995), namely those with high peak magnification. With both optical and infrared photometry, ρ_* could be determined for approximately twice as many events (Gould & Welch, 1996; Witt, 1995). If the lens is luminous, one could measure the proper motion of the lens directly using accurate astrometry and a high resolution instrument, such as HST (Gaudi & Gould, 1997). This will not be possible for all events, however, and requires a long temporal baseline. The angular Einstein ring radius $\theta_{\rm E}$ can be determined directly by measuring the centroid shift of the two unresolved images created by the lens. As the lens passes across the line of sight to the source, these two images move and change magnification. The centroid of these two images traces out an ellipse who size is $\sim \theta_{\rm E}$ (Walker, 1995), thus requiring an an astrometric accuracy considerably smaller than 1 mas. Preliminary studies have shown that SIM, with its planned 4μas accuracy, should be able to measure $\theta_{\rm E}$ reliably for almost all known microlenses toward the galactic bulge (Boden et al., 1998a; Jeong, Han & Park, 1999; Dominik & Sahu, 1999; Gould & Salim, 1999). Ground-based interferometers currently being developed, such as the Keck Testbed Interferometer, should be able to measure $\theta_{\rm E}$ for a smaller, but substantial, fraction of events (Boden et al., 1998a). Measurements of this kind would require coordination and cooperation between microlensing and astrometric communities, but the results would be well worth the effort.

In summary, if microlensing monitoring teams can make use of other resources, such as HST and SIM, the best method of dealing with finite source size effects is simply to measure the dimensionless source size ρ_* for each individual event directly. In the absence of these options, the effect of finite source size on ϵ must rely on statistical and model-dependent estimates of the distribution of ρ_*.

2.7.3. Blending

As discussed in § 2.7, the accurate determination of the blending, $f_{\rm B}$, in individual light curves is essential to the accurate determination of the detection efficiency. Precise measurements during the wings of the event and at baseline can allow the quantification of $f_{\rm B}$, but may not always be possible: bad weather may prevent wing measurements in some events and the faintness of the source star may preclude precise baseline measurements in others. Improved or alternate methods of quantifying blending would be beneficial; several have already been suggested.

Since the blending problem arises mainly because the PSFs of individual stars are blended together in crowded microlensing fields, simply improving the spatial resolution of the observations eliminates or reduces the blended light in most cases. The resolution needed is roughly that of HST (Han, 1997), for which only a modest use of resources is required. Nevertheless, even the resolution of HST will be insufficient to resolve any blended light that might arise from the lens itself or unresolved companions to the lens or source. Blending caused either by the lens or unrelated projected stars near the source or lens will generally cause a color shift in the combined light as the source is magnified during the course of the event (Griest & Hu, 1992; Buchalter & Kamionkowski, 1996). Since most stars in the bulge have nearly the same color, the color shift is expected to be small and difficult to measure. Alternatively, the blend fraction can be quantified by measuring the centroid shift of the blended PSF during the course of the event[1] (Goldberg & Woźniak, 1998; Goldberg, 1998). Blend fractions can be reliably determined in this way only for heavily blended, high-magnification events (Han, Jeong, & Kim, 1998) in which the centroid shift is prominent. Finally, improvement can be made through the use of image subtraction rather than the usual PSF-fitting photometry. Image subtraction reveals only the time-variable flux, $\Delta F = F_0[A(t) - 1]$, so that constant sources of blended light are removed. Although image subtraction does not remove the correlations between fitted parameters that make blending problematic, it is useful since photometric uncertainties are generally near the photon noise limit (Tomaney & Crotts, 1996; Alard & Lupton, 1998), which allows better discrimination between subtle differences in blended light curves.

2.7.4. Anomalous Events

If solar systems like our own are not atypical, dense, precise photometric monitoring will eventually result in the detection of anomalous events consistent with planetary perturbations. The algorithm of § 2.5 can be used to place direct limits on planetary systems in non-anomalous events and give meaning to the large number of null results now in hand, but what of the detection efficiency of events in which planetary anomalies are actually observed?

By the detection efficiency $\epsilon_i(b, q)$ of an anomalous event, we mean, by analogy with the definition for non-anomalous events given in § 2.4, the probability that a lensing companion with parameters b, q would be detected in light curve i (using the *same*

[1] This is not to be confused with the $\mathcal{O}(1\,\mathrm{mas})$ centroid shift caused by the motion and variable magnification of the two images created during a microlensing event. The centroid shift due to blending is $\sim d(A_{\rm B} - 1)/A_{\rm B}$, where d is the separation of the blended sources and $A_{\rm B}$ is the observed (blended) magnification. Since d is of order the resolution, 1", this centroid shift is measurable using current ground-based observations.

$\Delta\chi^2_{\rm thresh}$ criterion) after integrating over source trajectory angles θ. In principle, if the parameters $t_0, t_{\rm E}, u_{\rm min}, F_0$ and $f_{\rm B}$ can be well-determined in a binary fit that meets the $\Delta\chi^2_{\rm thresh}$ criterion, $\epsilon(b,q)$ can be calculated in a manner similar to that presented in § 2.5. A PSPL light curve with these parameters can be generated with the *actual sampling and photometric errors* of the observed event and the method of § 2.5 applied for the b, q combination that produced the best-fit 'detected' binary.

Several difficulties inherent to anomalous light curves must be addressed. First, for large mass ratio ($q \gtrsim 10^{-2}$), the source trajectory θ may actually be constrained by the light curve itself, but in a way that is partially degenerate with other fitting parameters. Second, even for small mass ratios, i.e., true planetary anomalies, the parameters $t_0, t_{\rm E}, u_{\rm min}, F_0$ and $f_{\rm B}$ may not be well-constrained, though of course this difficulty is present for non-anomalous events as well. Third, the anomaly, if large, may produce changes in magnification significant enough to alter the photometric precision obtained at the phase of the perturbation. Most planetary anomalies will have rather gentle changes in magnification (Figure 2.3) so that this effect may not be severe for $q \lesssim 10^{-3}$. Fourth, if detected real time, observer intervention may alter the photometric sampling in a way that is also phase-dependent (i.e. higher sampling after the anomaly detection than before). These last two possibilities present difficulties when integrating the corresponding PSPL light curve over source trajectory θ, since the altered sampling and photometric errors will not correspond to the phase of actual anomalies for most choices of θ.

One approach to handling this increased sampling at the phase of the anomaly is to resample the 'post-anomaly' portion of the light curve in a manner that is consistent with what would have been the sampling had the anomaly gone unnoticed. (Determining how to do this in the presence of weather and other observing facts-of-life may not be trivial). Both the initial test of binarity and the procedure to determine the detection efficiency would then be performed with the sparser, resampled light curve. The full dataset would be used only to refine the best-fit parameters. Alternatively, a Bayesian approach to analyzing the full dataset (anomalous and non-anomalous) could be employed, which addresses many of the special difficulties posed by anomalous events (Sackett, 1999b).

2.8. Conclusion

In this chapter, we have presented and tested a method to calculate the detection efficiency of microlensing datasets to stellar and planetary lensing companions. This method is conceptually simple, direct, and not excessively time consuming. The final result, $\epsilon(b,q)$, conveniently summarizes the efficiency of a given dataset in revealing binary lensing systems with any mass ratio q and dimensionless separation b. This efficiency can then be used to evaluate the likelihood that any given model of planetary systems would give rise to the observed dataset.

The algorithm that we have presented has several advantages. First, by working directly with measured light curves, it makes few assumptions, and explicitly takes into account the dependence of the efficiency on the sampling, photometric precision, monitoring duration, and impact parameter of the events. Second, it is computationally efficient, involving direct integration over only one unknown parameter, the angle of the trajectory. Finally, it is convenient, incorporating all information into one two-dimensional function, $\epsilon(b, q)$, which can then be used to evaluate the likelihood of any model of planetary systems. Note that in order to draw inferences about planetary companions with absolute mass m_p (in $M_\odot$) and orbital radius a (in AU), additional assumptions or information must be brought to bear on the distribution of lens masses and distances. Integrations over orbital phase and inclination then must be performed to deproject the instantaneous angular separation b into a probabilistic distribution function for orbital radius a.

Some caveats must be noted. First, the method assumes that the primary lensing parameters $t_0, t_{\rm E}, u_{\rm min}, F_0$ and $f_{\rm B}$ are well-constrained by the light curve, while emphasizing that ϵ is poorly known in the absence of such constraints. Possible altered sampling and photometric precision of anomalous events may necessitate a resampling of the corresponding light curve or the assumption that the efficiency of anomalous events is equal to the average efficiency of the normal events. Resampling is not an efficient use of all the data, and for individual events the average efficiency of non-anomalous events is likely to be a rather poor proxy for ϵ_i. Finally, the algorithm implicitly assumes that the efficiency is independent of the planetary system model (e.g., the effect of multiple planets is ignored).

We have also applied our method to simulated light curves in order to explore the dependence of binary detection efficiency on the impact parameter of the event, the choice of the detection criterion, neglecting to fit comparison binary curves separately, finite source effects, and blending. Our conclusions are as follows:

(1) Most of the efficiency of microlensing datasets to detecting planetary anomalies results from non-caustic crossing events.

(2) The detection efficiency is strongly dependent on the impact parameter $u_{\rm min}$ of the event. This implies that combined detection efficiencies will depend strongly on the actual distribution of impact parameters of the monitored events.

(3) For mass ratios $q \geq 10^{-2}$, the inferred detection efficiency ϵ is robust to changes in the detection criterion $\Delta\chi^2_{\rm thresh}$. For smaller mass ratios $q \sim 10^{-4}$ near the detection limit, different choices of $\Delta\chi^2_{\rm thresh}$ can lead to differences in ϵ of a factor of two.

(4) In order to obtain accurate detection efficiencies, the binary lens light curve must be fit separately unless the mass ratio is small ($q \lesssim 10^{-3}$) and the deviations are well above the detection limit (which may be difficult to satisfy simultaneously).

(5) Finite source effects are negligible for $q \gtrsim 10^{-2}$, can either increase or decrease ϵ for $q \simeq 10^{-3}$, and can be devastating for $q \lesssim 10^{-4}$, at least for the large dimensionless source sizes ($\rho_* \gtrsim 0.03$) that are typical of bulge giants.

(6) The detection efficiency is very sensitive to the fraction of blended light, primarily due to item (2) above; higher blend fractions imply smaller impact parameters for detection, and smaller impact parameters have higher intrinsic detection efficiencies. This fact, combined with the degeneracy in the blend fraction that exists between poorly/inaccurately sampled blended light curves means that *monitoring teams should make every effort to quantify the blend fractions in every monitored light curve.*

The final result of applying this method to an observed data set is the integrated detection efficiency, $\epsilon(b, q)$. This result should be regarded as a primary outcome of microlensing monitoring teams conducting planet searches; it incorporates all the information from the observations, and is essential for establishing any conclusions about the abundance and nature of Galactic planetary systems.

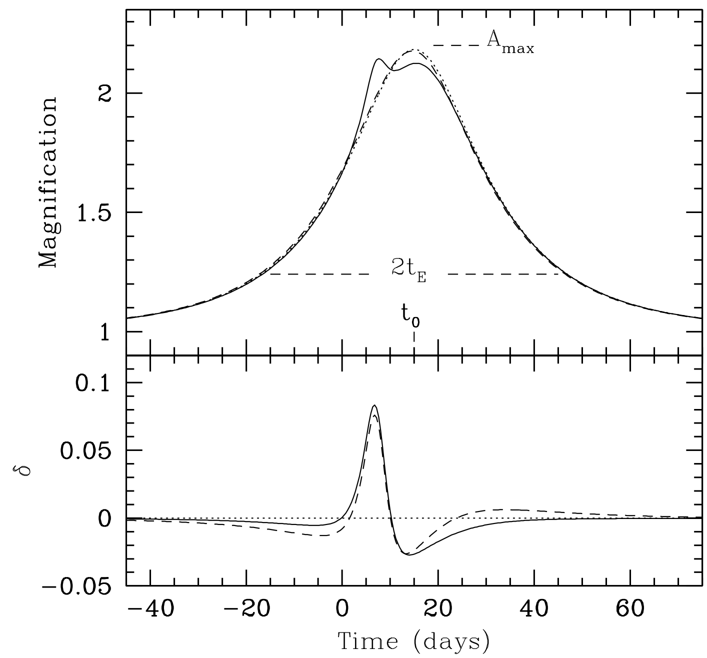

Fig. 2.1.— Top panel: Magnification as a function of time in days for a microlensing event with (solid curve) and without (dotted curve) the presence of a companion with mass ratio $q = 10^{-2}$. The event has an Einstein time scale of $t_{\rm E} = 30$ days and minimum impact parameter in units of the Einstein ring radius of $u_{\rm min} = 0.5$. The single lens curve reaches a maximum magnification of $A_{\rm max} = 2.2$ at a time $t_0 = 15$ days. The binary lens curve was generated assuming that the source trajectory makes angle $\theta = 300^\circ$ with respect to the binary axis. Also shown is the best single-lens fit to the binary-lens light curve (dashed curve). Bottom panel: The fractional deviation δ of the binary-lens light curve from the single-lens light curve with parameters $t_{\rm E} = 30$ days, $u_{\rm min} = 0.5, t_0 = 15$ days (solid curve) and from the best fit single-lens light curve (dashed curve).

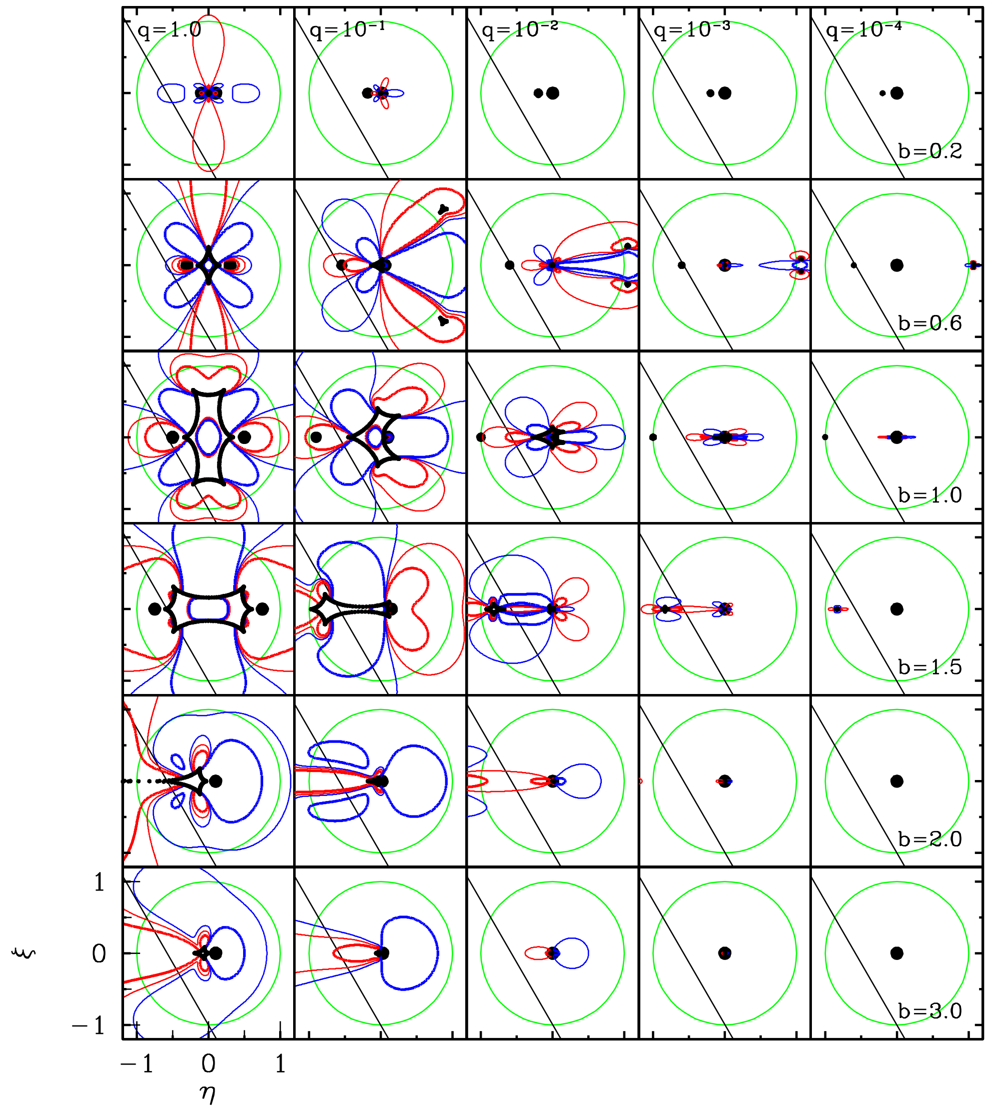

Fig. 2.2.— Contours of fractional deviation δ, for binary separations $b = 0.2, 0.6, 1.0, 1.5, 2.0,\ 3.0$ and mass ratios $q = 1.0, 10^{-1}, 10^{-2}, 10^{-3},\ 10^{-4}$, as a function of position in the source plane in units of the Einstein ring radius of the binary, (η, ξ). The red contours are $\delta = +0.01, +0.05$ (thin and heavy lines), the blue contours are $\delta = -0.01, -0.05$ (thin and heavy lines), and the heavy black lines are the caustics, $\delta = \infty$. The green circle is the Einstein ring. Black dots mark the positions of the lensing masses. The thin straight line is a trajectory with $u_{min} = 0.5$ and $\theta = 300$. Light curves for these trajectories are shown in Figure 2.3.

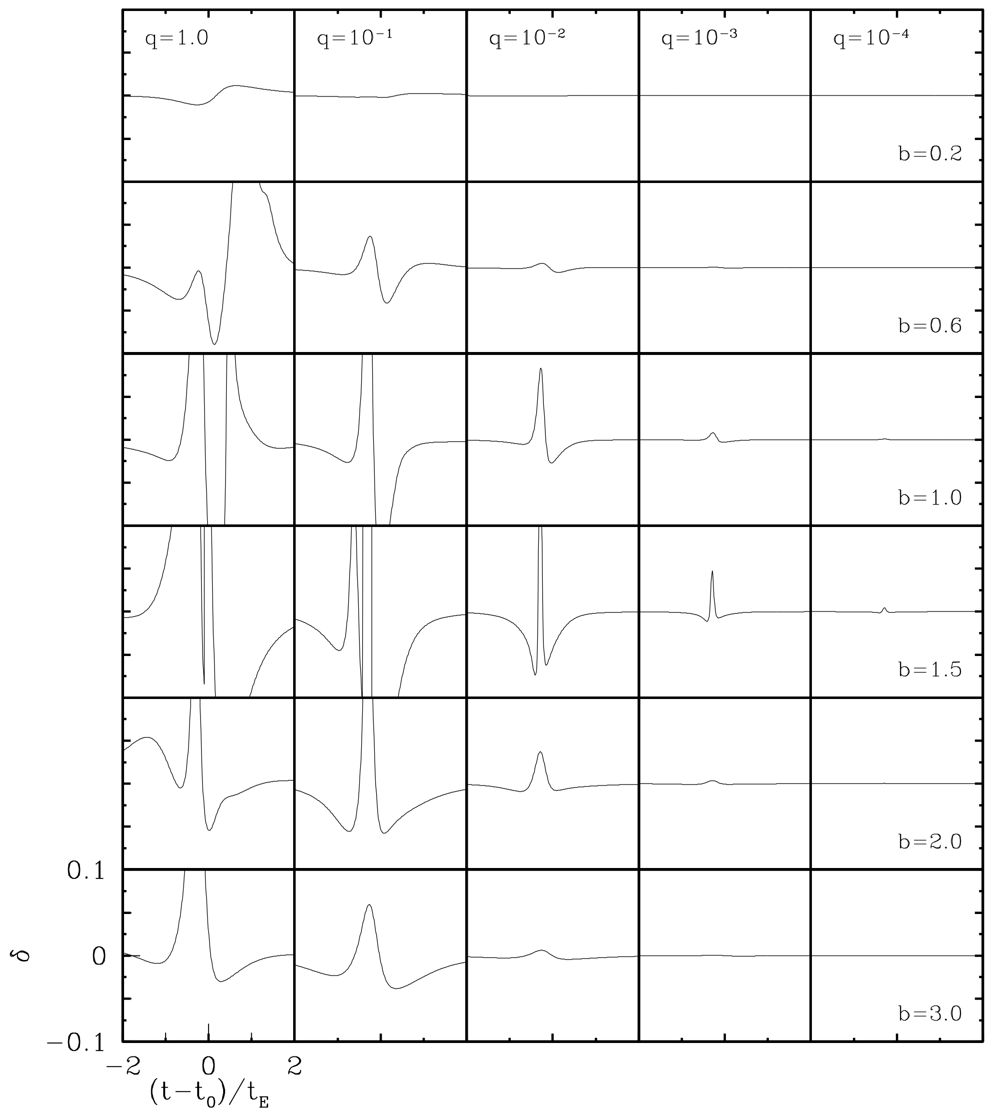

Fig. 2.3.— The fractional deviation, δ, from the single-lens light curve as function of time from the peak of the single lens light curve, t_0, in units of the Einstein ring crossing time $t_{\rm E}$, for the trajectories shown in Figure 2.2.

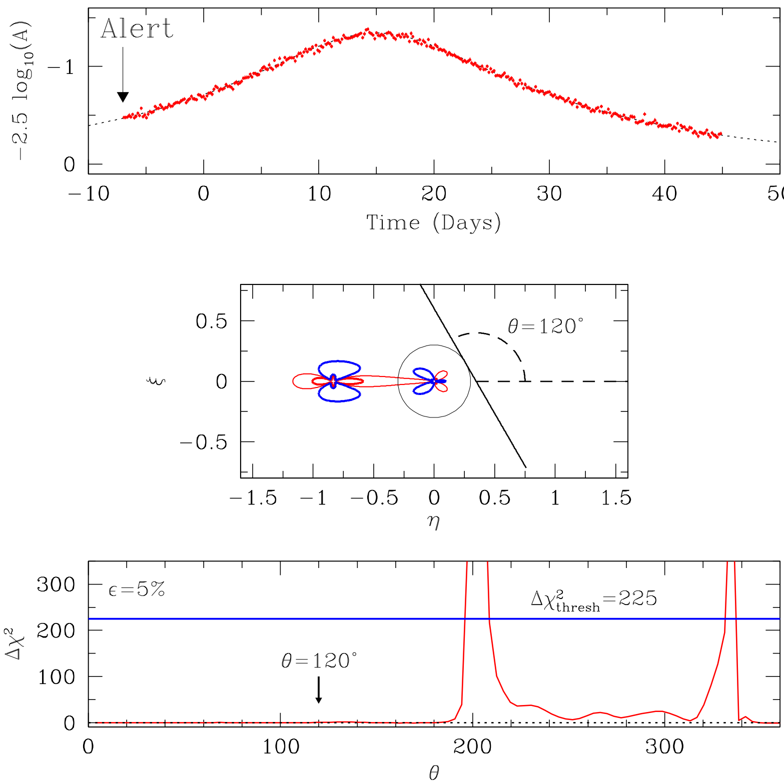

Fig. 2.4.— Top panel: The difference in magnitude, $-2.5\ \log_{10}(A)$, as a function of time for a simulated microlensing event with photometric precision of 2% and with uniform sampling at the rate $t_{\rm E}/200$ from alert until $t_{\rm E}$. The dotted line shows the best-fit point-source point-lens (PSPL) event, which has parameters $t_{\rm E} = 15$ days, $u_{\rm min} = 0.5, t_0 = 15$ days. Middle panel: Contours of constant fractional deviation δ from the single-lens magnification, as a function of source position in units of the Einstein ring radius (η, ξ). The solid line shows a trajectory with $u_{\rm min} = 0.5$ and $\theta = 120°$. The contours are the same as in Figure 2.2. Bottom panel: The difference in χ^2 between the best-fit binary-lens light curve with $b = 1.5$ and $q = 10^{-3}$ and the best-fit PSPL light curve, as a function of θ. The horizontal line indicates a detection threshold of $\Delta\chi^2_{\rm thresh} = 225$. The detection efficiency ϵ of the light curve in the top panel to companions with $b = 1.5$ and $q = 10^{-3}$ is the fraction of all possible trajectories for which $\Delta\chi^2 > \Delta\chi^2_{\rm thresh}$. In this case, $\epsilon = 5\%$.

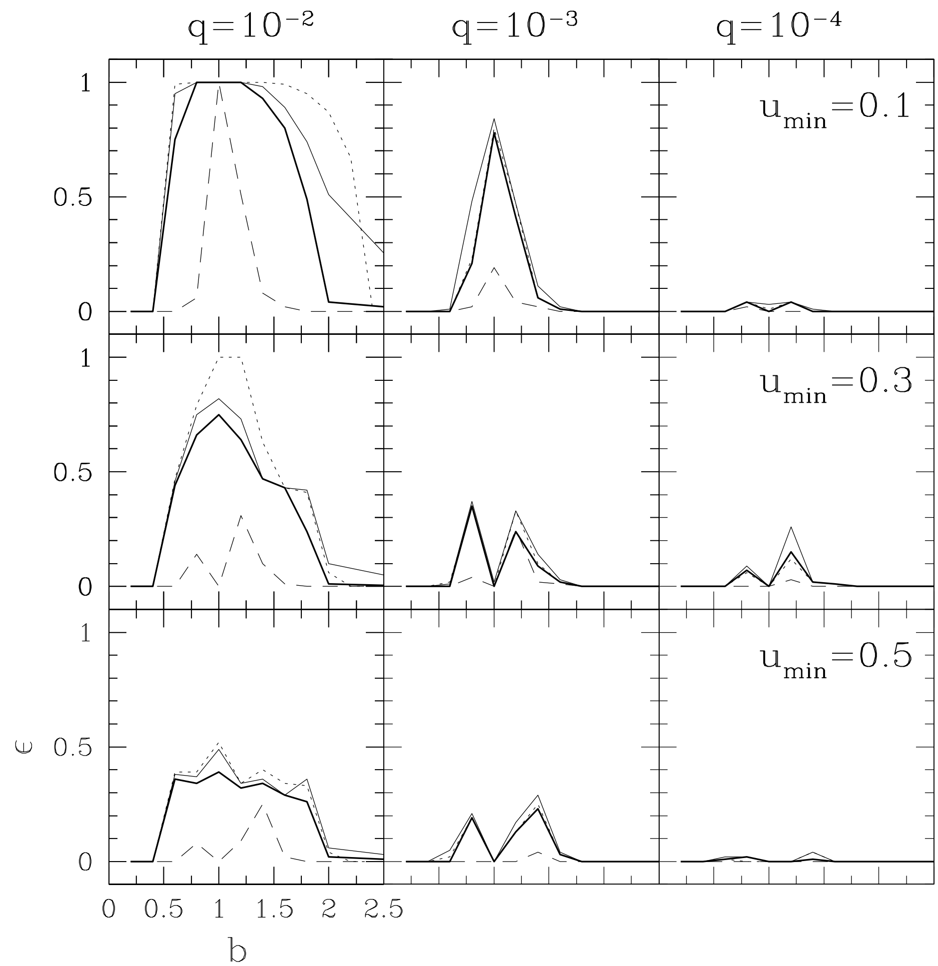

Fig. 2.5.— The detection efficiency, $\epsilon(b, q)$ as a function of the instantaneous separation of the binary, b for three different mass ratios ($q = 10^{-2}, 10^{-3}$, and 10^{-4}) and impact parameters ($u_{\rm min} = 0.1, 0.3$, and 0.5). Three detection criteria are shown: $\Delta\chi^2 > 225$ (thick solid line), $\Delta\chi^2 > 100$ (thin solid line), and caustic crossing (dashed line). The efficiency ϵ using $\Delta\chi^2 > 225$, but without fitting the binary-lens light curve, is also shown (dotted line). Throughout it is assumed that the events are sampled uniformly with 2% photometry at the rate $t_{\rm E}/200$ from alert to $t_{\rm E}$. See § 2.6.

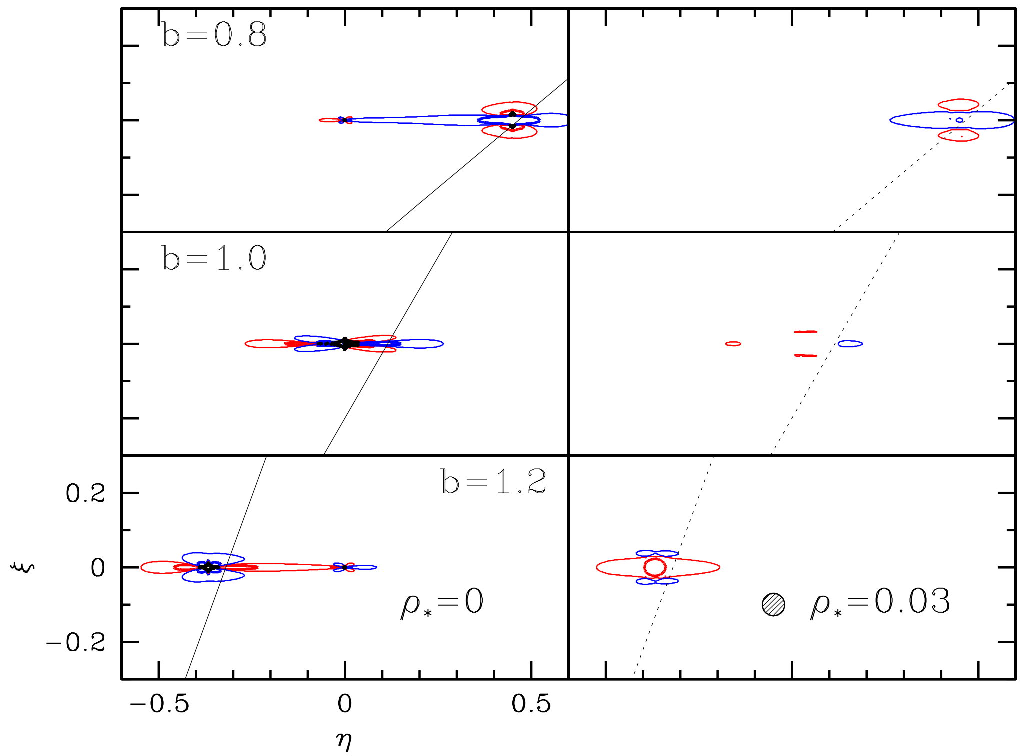

Fig. 2.6.— Contours of constant fractional deviation, δ, from the single-lens magnification for a point-source (left panels) and source with radius $\rho_* = 0.03$ (right panels), as a function of source position in units of the Einstein ring radius, (η, ξ), for mass ratio $q = 10^{-4}$ and dimensionless separations $b = 0.8, 1.0, 1.2$. The contours are the same as in Figure 2.2. The light curves arising from the sample trajectories (solid and dotted straight lines) are shown in Figure 2.7.

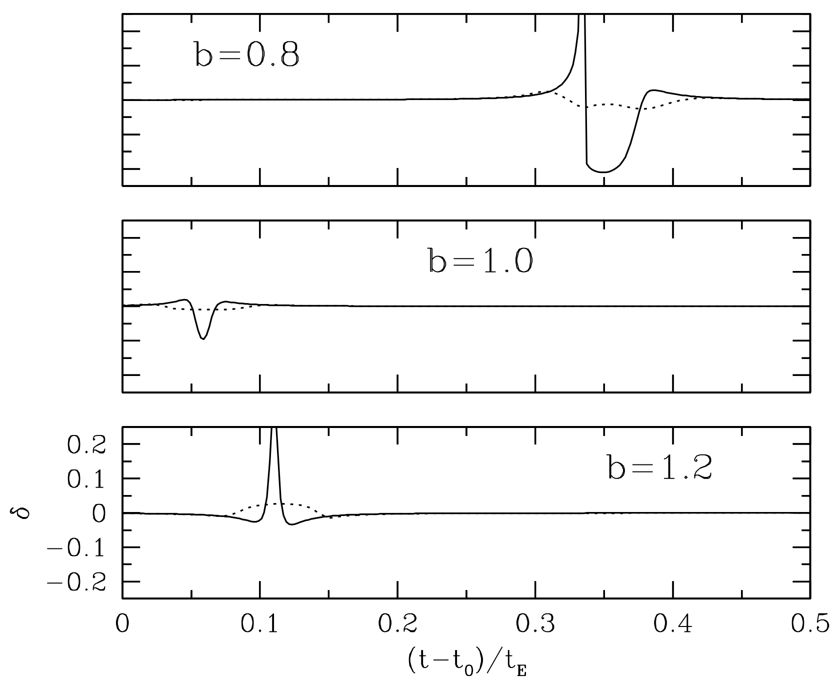

Fig. 2.7.— The fractional deviation, δ, from the single-lens light curve as function of time from the peak of the single lens light curve, t_0, in units of the Einstein ring crossing time $t_{\rm E}$, for the trajectories shown in Figure 2.6. The solid line is for a point-source, and the dotted lines are for a source of radius $\rho_* = 0.03$.

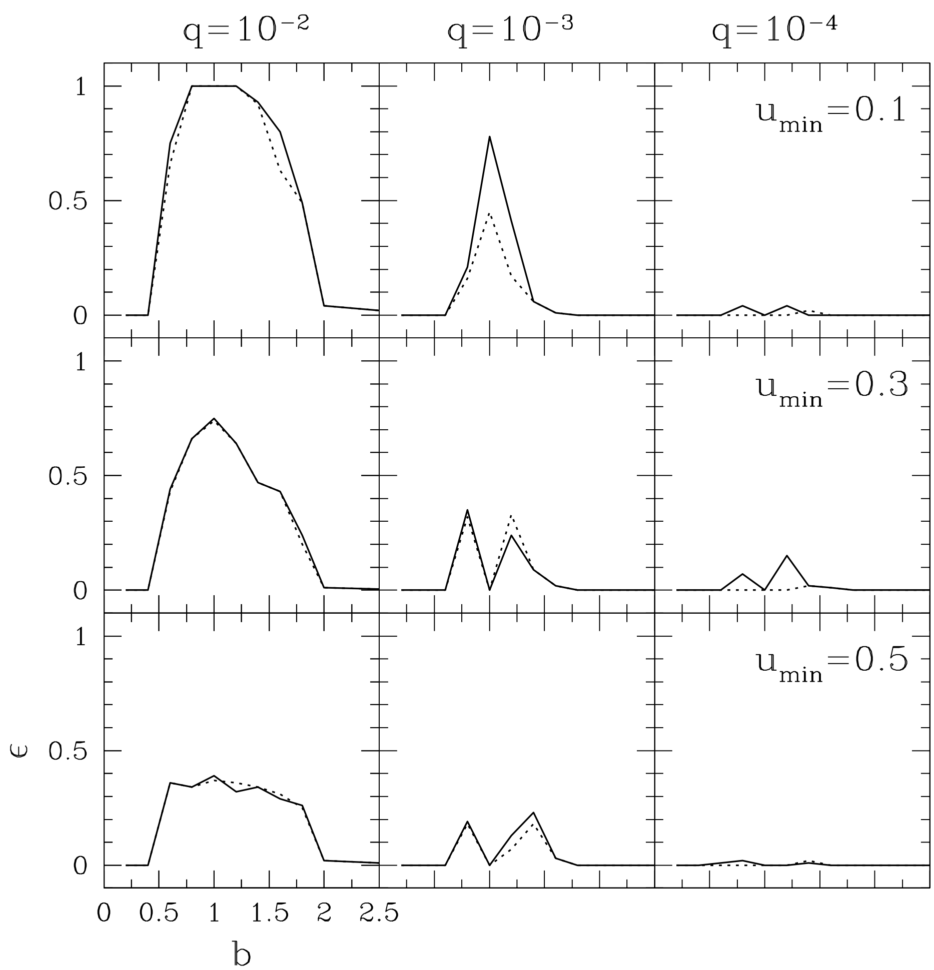

Fig. 2.8.— The detection efficiency ϵ as a function of the dimensionless separation of the binary, b, for three different mass ratios q and three events with different minimum impact parameter $u_{\rm min}$. The solid line is ϵ for a point-source and a detection criterion $\Delta\chi^2 > 225$; the dotted line is ϵ using the same detection criterion for a source of radius $\rho_* = 0.03$. It is assumed that the events are sampled uniformly with 2% photometry at the rate $t_{\rm E}/200$ from alert to $t_{\rm E}$.

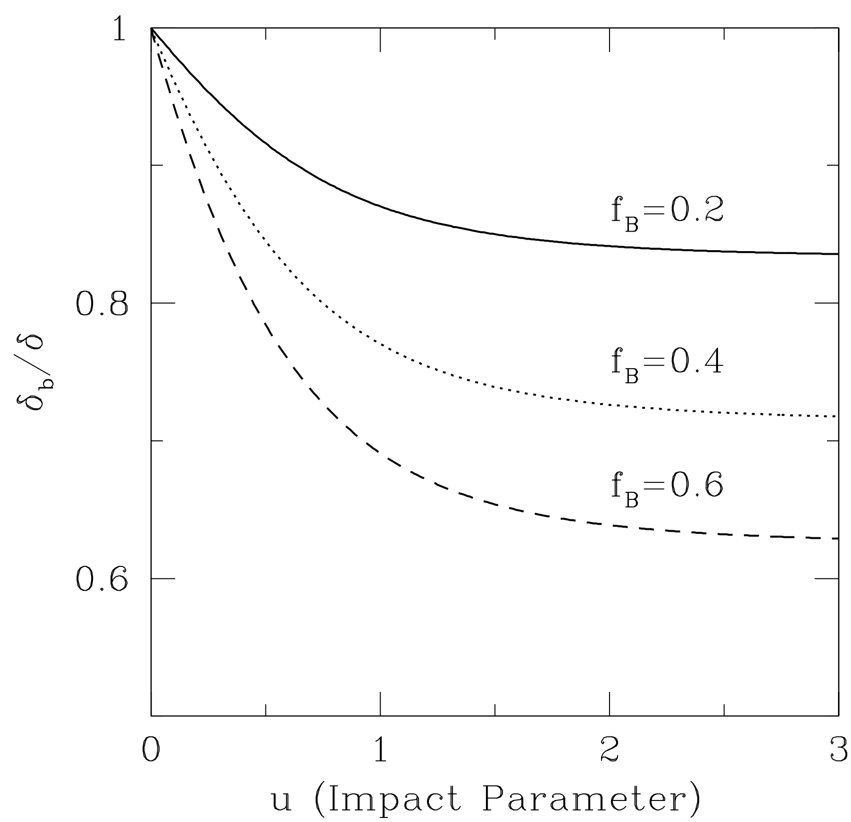

Fig. 2.9.— Ratio of blended δ_B to true fractional deviation δ, as a function of impact parameter u for three different blend fractions, f_B. Microlensing events are generally alerted when $u < 1$.

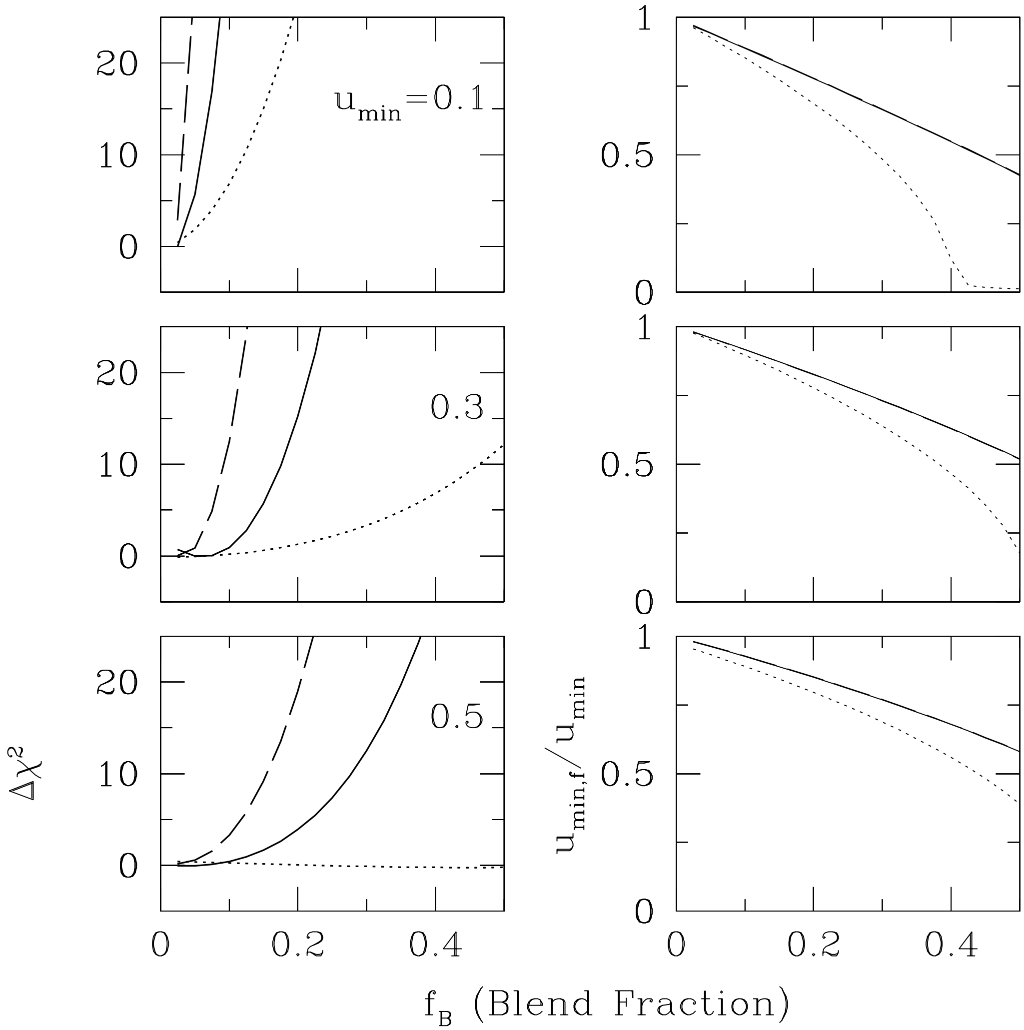

Fig. 2.10.— Left panels: The difference in χ^2 between a point-lens fit with no blending and one with the blend fraction held fixed at f_{B}, for observations from alert ($A = 1.54$) until $t = t_{\mathrm{E}}$ (dotted line) and from alert until $t = 3t_{\mathrm{E}}$ (solid line). The effect of improving the photometric precision by a factor two while monitoring to $t = 3t_{\mathrm{E}}$ is also shown (long-dashed line). Right panels: The ratio of the fitted value of u_{min} to the true value of u_{min} as a function of the blend fraction. Line types are the same as the left panels; the long-dashed line is coincident with the solid line.

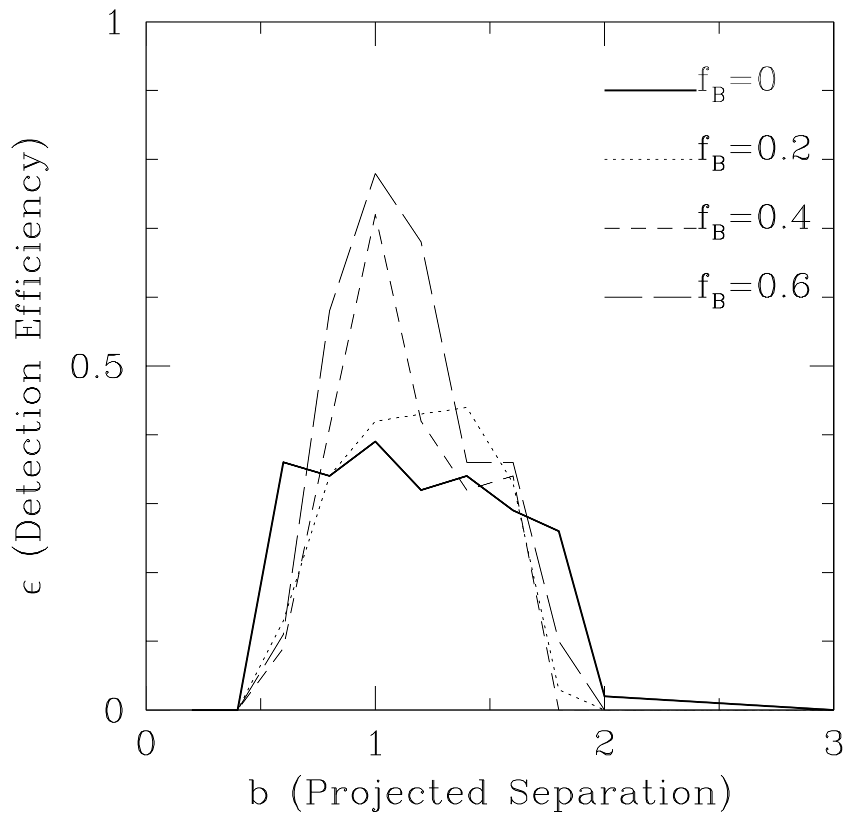

Fig. 2.11.— The detection efficiency ϵ as a function of the dimensionless separation of the binary, b, for mass ratio $q = 10^{-2}$ and four different blend fractions $f_{\rm B}$ for an event with 2% photometry, uniform sampling from alert until $t_{\rm E}$ at the rate $t_{\rm E}/200$, and minimum impact parameter $u_{\rm min} = 0.5$.

u_{min}	q	$\Delta\chi^2_{\rm thresh} = 100$	$\Delta\chi^2_{\rm thresh} = 225$	C.C.	$\Delta\chi^2_{\rm thresh} = 225$ w/o fit
0.1	10^{-2}	98%	94	33	100
	10^{-3}	38	30	5	31
	10^{-4}	5	2	0	2
0.3	10^{-2}	64	60	11	77
	10^{-3}	18	14	6	16
	10^{-4}	8	5	1	4
0.5	10^{-2}	38	34	9	40
	10^{-3}	14	11	1	12
	10^{-4}	1	1	0	1

Table 2.1: Lensing Zone Detection Efficiencies $\epsilon_{\rm LZ}(q)$: Point Source

u_{min}	q	Point Source	$\rho_* = 0.003$
0.1	10^{-2}	94%	91
	10^{-3}	30	17
	10^{-4}	2	0
0.3	10^{-2}	60	59
	10^{-3}	14	15
	10^{-4}	5	1
0.5	10^{-2}	34	35
	10^{-3}	11	9
	10^{-4}	1	0

Table 2.2: Lensing Zone Detection Efficiencies $\epsilon_{\rm LZ}(q)$, $\Delta\chi^2_{\rm thresh} = 225$: Finite Source

$f_{\rm B}$	$u_{min,f}$	$\epsilon_{\rm LZ}$
0.0	0.50	34%
0.1	0.44	33
0.2	0.40	37
0.3	0.34	40
0.4	0.28	42
0.5	0.19	57
0.6	0.02	53

Table 2.3: Lensing Zone Detection Efficiencies $\epsilon_{\rm LZ}(q = 10^{-2})$, $\Delta\chi^2_{\rm thresh} = 225$: Blending

Chapter 3

Limits on Companions in OGLE-1998-BUL-14

3.1. Introduction

Mao & Paczyński (1991) first suggested that planets could be detected in microlensing events; Gould & Loeb (1992) pointed out that if all stars had Jupiter-mass planets with separations near 5 AU, then $\sim 20\%$ of the microlensing events should exhibit detectable planetary deviations, provided that events were monitored frequently and with moderately high precision. Current microlensing discovery teams do not generally sample frequently or precisely enough to detect the short-lived perturbations caused by planets. However, since these collaborations reduce their data in real time, they are able to issue 'alerts,' notification of ongoing microlensing events detected before the peak magnification. Prompted by this alert capability, several other groups have formed to monitor alerted microlensing events more closely (GMAN, Alcock et al. 1997; PLANET, Albrow et al. 1998; MPS, Rhie et al. 1999a). Since only a handful of alerted events are in progress at any given time, they can be monitored with the fine temporal sampling and photometric precision required to discover planetary perturbations. In particular, the PLANET (Probing Lensing Anomalies NETwork) collaboration has access to four telescopes that are roughly equally-spaced in longitude, and thus can monitor microlensing events almost continuously, weather permitting.

Over the last five years, PLANET has monitored over 100 events with varying degrees of sampling and photometric precision. Here we present photometry and analysis of one such event, OGLE-1998-BUL-14, the 14th event alerted by the OGLE collaboration toward the Galactic bulge in 1998. The total PLANET data set for this event consists of 600 data points, the majority of which was taken during a 3 month period starting 1 May 1998. The median sampling interval during this interval is about 1 hour, with no gaps greater than 4 days. The photometric precision near the peak of the event, where the sensitivity to planets is highest, is 1.5%. These characteristics, combined with the high maximum magnification of OGLE-1998-BUL-14 make our data set highly sensitive to planetary perturbations. The PLANET data for the event are consistent with a generic point-source point-lens (PSPL) model. The excellent photometry and dense sampling also allow us to place stringent constraints on possible stellar and planetary companions. We also place limits on parallax effects arising from the motion of the Earth, deviations arising from the finite size of the source, and the amount of blended light from the lens itself. These limits are then translated into limits on the mass of the lens. We find that, despite the excellent coverage and photometry of OGLE-1998-BUL-14, the limits on the mass of the lens are very weak. This indicates that it will in general be quite difficult to obtain interesting constraints on the masses of the lenses giving rise to microlensing events from photometric data alone.

Our study is similar to that done by the MPS and MOA collaborations on the microlensing event MACHO-1998-BLG-35 (Rhie et al., 1999b), which was a higher maximum magnification event ($A_{\rm max} \sim 75$) than OGLE-1998-BUL-14. We compare the limits on companions for OGLE-1998-BUL-14 to those for MACHO-1998-BLG-35 directly in § 3.5.2.

A brief introduction to the theory of microlensing is given in § 3.2. The observations and data are presented in § 3.3. In § 3.4, we discuss known systematic effects in crowded-field photometry and our method of correcting for them, and fit the data to a PSPL model. In § 3.5, we search for the kinds of deviations from the PSPL model that would arise from companions to the primary lens. Finding none, we calculate the detection efficiency of OGLE-1998-BUL-14 light curve to companions as a function of the mass ratio and angular separation of the companion, and use this efficiency to place limits on possible companions to the primary lens. In § 3.6, we use several considerations to constrain the mass of the primary lens. In § 3.7, we convert from mass ratio and angular separation to mass and physical separation of the companion using an assumption of the mass and distance to the primary lens, and compare the OGLE-1998-BUL-14 detection efficiencies to other methods of detecting extrasolar planets. We conclude in § 3.8.

3.2. Basic Microlensing

The flux of a microlensing event is given by

$$F(t) = F_{\mathrm{S}} A(t) + F_{\mathrm{B}}, \tag{3.1}$$

where F_{S} is the unlensed flux of the source, $A(t)$ is the magnification as a function of time, and F_{B} is the flux of unresolved stars not being lensed, which may include light from the lens itself. For a PSPL model, the magnification is

$$A[u(t)] = \frac{u^2(t) + 2}{u(t)\sqrt{u^2(t) + 4}}, \tag{3.2}$$

where $u(t)$ is the angular separation of the source and the lens in units of the angular Einstein radius θ_{E} defined by

$$\theta_{\mathrm{E}} \equiv \left[\frac{4GM}{c^2}\frac{D_{\mathrm{LS}}}{D_{\mathrm{L}}\,D_{\mathrm{S}}}\right]^{1/2} \sim 480\,\mu\mathrm{as}\left(\frac{M}{M_\odot}\right)^{1/2}, \tag{3.3}$$

where M is the mass of the lens, and D_{LS}, D_{S}, D_{L} are the lens-source, observer-source, and observer-lens distances, respectively. This corresponds to a physical distance at the lens plane of

$$r_{\rm E} = \theta_{\rm E} D_{\rm L} \sim 3 \text{ AU} \left(\frac{M}{M_\odot}\right)^{1/2} . \tag{3.4}$$

For the scaling relation on the far right of equations (3.3) and (3.4), we have assumed $D_{\rm S} = 8$ kpc and $D_{\rm L} = 6.5$ kpc, typical distances to the lens and source for microlensing events toward the bulge. For rectilinear motion,

$$u(t) = \left[\left(\frac{t - t_0}{t_{\rm E}}\right)^2 + u_0^2\right]^{1/2} , \tag{3.5}$$

where t_0 is the time of maximum magnification, u_0 is the minimum impact parameter of the event in units of $\theta_{\rm E}$, and $t_{\rm E}$ is the Einstein time scale, a characteristic time scale of the event defined by

$$t_{\rm E} \equiv \frac{\theta_{\rm E} D_{\rm L}}{v} \sim 40 \text{ days} \left(\frac{M}{M_\odot}\right)^{1/2} . \tag{3.6}$$

Here v is the transverse velocity of the lens relative to the observer-source line-of-sight. For the scaling relation on the far right of equation (3.6) we have assumed a transverse velocity of $v = 130 \text{ km s}^{-1}$, and we have again assumed $D_{\rm L} = 6.5$ kpc and $D_{\rm S} = 8$ kpc.

A PSPL fit to an observed data set is a function of $3 + 2N_l$ parameters: $t_{\rm E}$, u_0, t_0, and one source flux $F_{\rm S}$ and one blend flux $F_{\rm B}$ for each of N_l light curves taken in different sites or in different bands.

3.3. Observations

PLANET observations of OGLE-1998-BUL-14 were taken in two broad-band filters at five sites using seven different detectors. The five sites are the CTIO 0.9m and the Yale-CTIO 1m in Chile, the SAAO 1m in South Africa, the Canopus 1m in Tasmania, and the Perth 0.6m near Perth, Australia. Canopus data prior to $\mathrm{HJD}' \equiv \mathrm{HJD} - 2450000.0 = 975.0$ were taken with a different detector than those taken afterwards; we will refer to these data sets as Canopus A ($\mathrm{HJD}' < 975.0$) and Canopus B ($\mathrm{HJD}' > 975.0$), respectively. SAAO data were taken in three segments: during the period from $\mathrm{HJD}' = 976.0$ to $\mathrm{HJD}' = 980.0$, a different detector was used than prior to $\mathrm{HJD}' = 976.0$ or after $\mathrm{HJD}' = 980.0$, when the original detector was reinstalled on the telescope. Since different detectors have different characteristics that can affect the photometry, we will treat these as independent light curves. In addition, because the SAAO data prior to $\mathrm{HJD}' = 976.0$ and after $\mathrm{HJD}' = 980.0$ are substantially offset photometrically despite being taken with the same telescope, detector and filters, these are also treated as independent light curves. We refer to these as SAAO A ($\mathrm{HJD}' > 976.0$), SAAO B ($976.0 \leq \mathrm{HJD}' \leq 980.0$) and SAAO C ($\mathrm{HJD}' \geq 980.0$). All independent light curves have both I and V band photometry, except for the CTIO 0.9m and Canopus B data, which do not have V-band photometry.

The entire data set consists of 461 I-band and 139 V-band data points forming a total of 14 independent light curves. The number of data points per light curve is given in Table 3.1. The data were reduced using DoPHOT (Schechter, Mateo, & Saha, 1993), and reference stars were chosen to optimize photometry at each individual site. For details concerning the reduction, see Albrow et al. (1998).

The PLANET data set for OGLE-1998-BUL-14 is one of the best sampled light curves to date. Over 95% of the measurements were taken during a 3.3 month time period from $\mathrm{HJD}' = 945.0$ to $\mathrm{HJD}' = 1045.0$, corresponding to times $-0.2t_{\mathrm{E}}$ before the peak until $2t_{\mathrm{E}}$ after the peak. In Figure 3.1, we show the distribution of sampling intervals (time between successive measurements) in hours for the cleaned PLANET OGLE-1998-BUL-14 dataset. The median sampling interval is about 1 hour, or 10^{-3} of the Einstein ring crossing time. Furthermore, there are very few gaps greater than 1 day.

Our primary results are based solely on PLANET data. We use the publically-available OGLE data set[1] for OGLE-1998-BUL-14 only to test our PSPL model and to derive a parallax-based constraint on the lens mass. The OGLE data set consists of 159 data points taken in the standard I filter with the 1.3 Warsaw Telescope in Chile: 125 baseline points were taken prior to $\mathrm{HJD}' = 800$ when the source was not being lensed, and the remaining 34 points taken during the course of the event. For more information on the OGLE project and the Early Warning System, which is used to alert microlensing events toward the Galactic bulge, see Udalski, Kubiak, & Szymański (1997), and Udalski et al. (1994).

3.4. Correcting for Known Systematic Effects

Along with the usual reduction procedures, we take additional steps to optimize the data quality before analyzing the light curve of OGLE-1998-BUL-14. Since planetary perturbations are expected to often have small amplitudes, it is essential that any low-level systematic deviations caused by observational effects be minimized in order to avoid spurious detections. Such effects can be quite common in crowded-field photometry. We describe in turn several systematic effects and our procedures to remove them.

Light curves of constant stars in our fields often display residuals from the mean value for the star that are correlated with seeing (or more specifically, image quality as measured by the FWHM of point sources), and occasionally with the sky background as well. These correlations seem to be a generic feature of crowded-field DoPHOT photometry, and presumably are present at some level in all light curves. We find that the magnitude (and sign) of the correlation depends on the site and detector, being quite strong for some data sets and almost completely absent in others. Typically, these

[1]http://www.astrouw.edu.pl/~ftp/ogle/ogle2/ews/ews.html

correlations with the seeing and background are linear in flux and hence approximately linear in magnitudes, and are below 10%. Such correlations inflate the overall scatter in typical light curves by about a factor of two, diminishing the recognizability of subtle deviations. The correlation with FWHM can be especially dangerous: coherent deviations of order a few percent are seen on nightly time scales, partly due to the correlation between seeing and airmass. Such deviations can easily mimic low amplitude perturbations caused by small-mass planetary companions.

Based on studies of constant stars in crowded fields, Albrow et al. (1998) found that formal DoPHOT errors typically underestimate the true photometric uncertainties by a factor of $1.5 - 2$. Using the formal DoPHOT errors for our analysis would therefore overestimate the significance of any anomaly being studied. Furthermore, observed error distributions are not Gaussian, with long tails toward larger values, primarily due to the seeing and background systematics described above. These distributions are poorly represented by the formal DoPHOT errors. Thus, when not corrected for systematics, many light curves have more large ($> 3\sigma$) outliers than would be expected from a Gaussian distribution. While it may be tempting simply to eliminate these outliers from the data set, such an approach could be dangerous since an isolated outlier could, in principle, be due to a short-duration deviation caused by a planetary companion. Unfortunately, in many cases the cause of the outliers is not known and nearly-simultaneous photometry that in principle could be used to discriminate real deviations from poor-quality data is not available.

Our approach is to apply a correction to the entire dataset prior to the analysis, as we now describe. We fit the entire data set to a preliminary PSPL model, including seeing and background correlation terms, so that for each observed light curve our model takes the form,

$$m_{\mathrm{pred},i} = m_{\mathrm{PSPL}}(t_i) + \eta\theta_i + \zeta b_i. \tag{3.7}$$

Here $m_{\mathrm{pred},i}$ is the predicted flux in magnitudes, m_{PSPL} is the flux in magnitudes due to the PSPL magnification (Eq. 3.1) at time t_i, η is the slope of the seeing correlation, θ_i is the DoPHOT-reported full-width half-maximum of the PSF of the ith data point, ζ is the slope of the correlation with background flux, and b_i is the DoPHOT-reported background of the ith data point. In general, the specific model used to correct for seeing and background systematics is not important, provided that the model parameters are not strongly correlated with η and ζ. For most of the deviations we will be considering in this chapter, i.e. those arising from nearly equal mass binary lenses, parallax, and finite source effects, model parameters are nearly uncorrelated with η and ζ. However, deviations caused by small mass ratio companions can occur over the course of several hours, and thus these deviations can be highly correlated with variations in seeing. Since these binary-lens models will not have the benefit of the additional fit parameters (η, ζ), the significance of any short-duration deviation will be overestimated. We will return to this point in § 3.5.2.

We fit the model in the following way. We choose trial values for t_{E}, u_0, and t_0. This gives a prediction for the PSPL magnification as a function of time $A(t)$. The two parameters F_{S} and F_{B} are then determined by performing a linear fit to the flux. This gives the PSPL flux $m_{\mathrm{PSPL}}(t_i)$. Finally, the parameters η and ζ are determined by performing a linear fit in magnitudes. The final χ^2 for the trial model with parameters $(t_{\mathrm{E}}, t_0, u_0, F_{\mathrm{S}}, F_{\mathrm{B}}, \eta, \zeta)$ is then evaluated in magnitudes and the values of these parameters that minimize χ^2 are then found using a downhill-simplex method (Press et al., 1992). Using the final values of η and ζ, the data are corrected for the seeing and background systematics. This preliminary PSPL fit produces $\chi^2 \sim 2000$ for 569 degrees-of-freedom (dof). Since no gross deviations from a PSPL light curve are apparent in the data, the high χ^2/dof is an indication that the DoPHOT errors are underestimating the true error, in this case by a factor of ~ 2. Some of this inflated χ^2 arises from a few highly-deviant outliers. Furthermore, different light curves have scatter that are underestimated by different amounts. For these reasons, simply scaling all the errors by a factor that forces χ^2/dof to be unity would not be appropriate. We therefore adopt the following procedure. Using the preliminary model, we first find the largest $> 3\sigma$ outlier and reject it. We recompute χ^2 for each light curve, and then rescale the errors in the individual light curves by a factor that forces the χ^2/N_i for each light curve to be equal to unity, where N_i is the number of measurements in light curve i. All the errors are then scaled with an overall factor to force χ^2/dof for the entire data set to unity. This light curve is then refit to the model in equation (3.7), removing any residual seeing and background correlations. We iterate this process, successively removing the largest 3σ outlier, rescaling the errors, and refitting the light curve, until no further 3σ outliers remain, and the fit has converged. The final scaling factors are given in Table 3.1. We find a total of five outliers that deviate from the final model by more than $> 3\sigma$. At the final step, we form two data sets. For the first data set, we reintroduce the $> 3\sigma$ outliers, but with errors scaled by the same factor as their parent light curves; we will refer to this as the "cleaned" PLANET data set. The second data set does not contain the outliers; we refer to this as the "super-cleaned" PLANET data set. Finally, for some analyses, we combine the OGLE and super-cleaned PLANET data sets, scaling the OGLE errors by 2.01 so as to force χ^2/d.o.f. to unity. We will refer to this as the OGLE+PLANET super-cleaned data set.

We now fit these corrected data sets to a PSPL model with parameters $t_{\rm E}, t_0, u_0, F_{\rm S}, F_{\rm B}$ (Eq. 3.1). For the PLANET datasets, there are 14 light curves, and thus the fit is a function of 31 parameters. Including OGLE data increases to the number of parameters by two. For the cleaned PLANET data set we find fit parameters and formal 1σ errors determined from the linearized covariance matrix of $t_{\rm E} = (39.6 \pm 1.1)$ days, $u_0 = 0.0643 \pm 0.0002$, $t_0 = 956.016 \pm 0.005$. The fit parameters for the super-cleaned PLANET data set and the OGLE+PLANET super-cleaned data set are the same within the errors. The parameters and formal 1σ errors for all three fits are summarized in Table 3.1, along with the blend fractions $g \equiv F_{\rm B}/F_{\rm S}$ for each light curve. The OGLE+PLANET dataset is shown in Figure 3.2, while the cleaned PLANET light curve and the best-fit PSPL model are shown in Figure 3.3, along with the residuals from the model.

In Figure 3.4 we show the distribution of residuals of the cleaned PLANET dataset from the best-fit PSPL model divided by their respective (rescaled) errors, along with a Gaussian of unit variance. Other than a few outliers, the two distributions are very similar, indicating that our errors are nearly Gaussian distributed. In order to illustrate the importance of including the seeing and background corrections, we also show the distribution of residuals divided by their respective rescaled errors before these corrections. The uncorrected data have a broader distribution with a median value that is systematically offset from zero; the entire distribution is highly non-Gaussian.

In Figure 3.5 we show the residuals of the cleaned PLANET dataset from the PSPL model as a function of the predicted magnitude of the model. The photometry in I is excellent; the 1σ scatter for $I < 16$ is 1.5%; while the scatter for the entire I dataset is 4%. The scatter is approximately 2.5 times larger in V; however this constitutes only 20% of the entire dataset.

3.5. Limits on Companions to the Lens

The excellent coverage and high-quality photometry, combined with the fact that OGLE-1998-BUL-14 was a high-magnification event, make this an excellent candidate for the detection of planetary perturbations. Direct examination of the light curve and residuals reveals no obvious planetary signatures, and, in fact, no obvious deviations from the PSPL model of any kind. However, since the deviations could be quite subtle, it is important that the light curve be searched systematically for any deviations. If no significant deviations are found, the good photometry and excellent coverage can be used to place limits on the kinds of companions to the lens that could be present. To do this, we must calculate the detection efficiency of the OGLE-1998-BUL-14 light curve to companions.

3.5.1. Detection Efficiency of OGLE-1998-BUL-14 to Companions

The efficiency ϵ of a particular microlensing light curve to the detection of a binary system depends sensitively on two quantities: the the mass ratio of the system, q, and the angular separation d in units of $\theta_{\rm E}$. The efficiency $\epsilon(d,q)$ tends to zero when $q \to 0$, $d \to 0$, or $d \to \infty$ (i.e. when the companion has a low mass compared to the primary, or is very close or very far from the primary). We simultaneously search for planetary deviations and calculate the detection efficiency for OGLE-1998-BUL-14 using a method proposed by Gaudi & Sackett (2000). We briefly review the steps below.

(1) The OGLE-1998-BUL-14 light curve is fit with a PSPL model by minimizing χ^2. The resulting χ^2 for this model is labelled $\chi^2_{\rm PSPL}$.

(2) Holding d and q fixed, the binary lens model that best fits the observed light curve is found for each source trajectory α, leaving the 31 parameters $(t_{\rm E}, u_0, t_0, 14 \times F_{\rm S}, 14 \times F_{\rm B})$ as free parameters. The difference $\Delta\chi^2(d,q,\alpha) \equiv \chi^2(d,q,\alpha) - \chi^2_{\rm PSPL}$ is evaluated.

(3a) All parameter combinations (d,q,α) yielding $\Delta\chi^2(d,q,\alpha) < \Delta\chi^2_{\rm flag}$ are flagged for further study as possible detections, where $\Delta\chi^2_{\rm flag}$ is some reasonable detection criterion.

(3b) The fraction of all binary-lens fits for the given (d,q) that satisfy the criterion $\Delta\chi^2 > \Delta\chi^2_{\rm thresh}$ in computed, where $\Delta\chi^2_{\rm thresh}$ is a rejection criterion. The detection efficiency $\epsilon(d,q)$ of the data set for the assumed separation and mass ratio,

$$\epsilon(d,q) \equiv \frac{1}{2\pi}\int_0^{2\pi} \mathrm{d}\alpha\ \Theta[\Delta\chi^2(d,q,\alpha) - \Delta\chi^2_{\mathrm{thresh}}], \tag{3.8}$$

where $\Theta[x]$ is a step function, is then computed. Note that α is uniformly distributed.

(4) Items (2) and (3) are repeated for a grid of (d,q) values. This gives the detection efficiency $\epsilon(d,q)$ for OGLE-1998-BUL-14 as a function of d and q, and also all binary-lens parameters (d,q,α) that give rise to significantly better fits to the light curve than the PSPL model.

(5) The parameter combinations found in step (3a) are then used as initial guesses for our binary-lens χ^2 minimization routine, leaving all 34 parameters as free parameters, in order to find the minimum χ^2 and best-fit parameters for this local minimum.

We search for binary-lens fits and calculate $\epsilon(d,q)$ for $0 \leq d \leq 4$ and $0 \geq \log(q) \geq -5$ at intervals of 0.1 in d and 0.5 in $\log(q)$. Since the search is performed on a grid of (d,q,α) and the grid points are unlikely to be situated exactly on local minima, it important that $|\Delta\chi^2_{\mathrm{flag}}|$ be sufficiently low so that all probable fits are found. We chose $\Delta\chi^2_{\mathrm{flag}} = -9$ for our flagging criterion, and find only three combinations of d and q for which $\Delta\chi^2 < \Delta\chi^2_{\mathrm{flag}}$. Minimizing χ^2 in the neighborhood of these trial solutions reveals that the best-fit parameters are quite close to the initial parameters, and χ^2 decreases minimally. The absolute best-fit binary lens to OGLE-1998-BUL-14 has a $\chi^2 = 720.6$, or $\Delta\chi^2 = -9.2$. Since this is well below our threshold for detection of $\Delta\chi^2 = -50$, we do not claim a detection. Indeed, even a naive calculation based on Gaussian statistics and three additional parameters to describe the companion yields a chance probability of 2.7% for $\Delta\chi^2 \leq -9.2$, which cannot be considered a detection at even the 3-sigma level.

In fact, the probability of a random fluctuation of this magnitude is substantially higher than 2.7%. First, since we are including outlier points in the search, χ^2 should be renormalized by the number of degrees of freedom, which would imply $\Delta\chi^2 = -7.2$ for which the chance probability with three additional parameters is 6.7%. However, the chance probability of a false planet detection is substantially higher than this. Moreover, it cannot be computed from a χ^2 table and would have to be determined by Monte Carlo simulation. To understand why, consider one of the planetary models we found that fits OGLE-1998-BUL-14 with $\Delta\chi^2 = -7.2$. The "success" of this model is basically driven by 15 points clustered within 1 day whose mean lies $\sim 0.6\%$ above the PSPL model. The chance for such a deviation *on this particular day* is $\sim \exp(\Delta\chi^2/2)/(2\pi|\Delta\chi^2|)^{1/2} = 0.4\%$. Since there are a total of ~ 600 data points, there is a similar probability for such a fluctuation on each of $600/15 = 40$ time intervals. Hence, the total probability is $1 - (1 - 0.004)^{40} \sim 15\%$. In fact, the probability is somewhat higher still because we have taken account of only 15-point clusters and not larger or smaller clusters that could also mimic a planet.

In any event, we have set our detection threshold substantially higher than would be warranted solely to avoid chance statistical fluctuations. This conservative approach is motivated by concern over unrecognized systematics which, experience has taught us, often give rise to spurious detections of formally high significance. We therefore conclude that the light curve of OGLE-1998-BUL-14 is consistent with a single lens within the uncertainties.

3.5.2. Resulting Constraints on Companions

The detection efficiency at a given (d, q) is the probability that a companion of separation d and mass ratio q would have produced a deviation inconsistent (in the sense of $\Delta\chi^2 > \Delta\chi^2_{\rm thresh}$) with the observed OGLE-1998-BUL-14 light curve. If no deviations are seen, companions with (d, q) can be ruled out at a significance level of $\epsilon(d, q)$. The choice of the rejection threshold $\Delta\chi^2_{\rm thresh}$ can have a significant effect on the resulting detection efficiency, especially for low thresholds and mass ratios $q \lesssim 10^{-3}$ (Gaudi & Sackett, 2000). We choose to be conservative, and adopt $\Delta\chi^2_{\rm thresh} = 50$ as our fiducial threshold. For comparison, we also show the results for $\Delta\chi^2_{\rm thresh} = 25$ and $\Delta\chi^2_{\rm thresh} = 100$.

The binary-lens detection efficiency of OGLE-1998-BUL-14 as a function of the mass ratio q and angular separation d is shown in Figure 3.6. The darkest shading denotes those parameter combinations (d, q) for which $\epsilon > 95\%$, and thus are excluded at the 95% significance level from lying above the rejection criterion. Table 3.2 shows the range of angular separations d that are excluded by our OGLE-1998-BUL-14 data set for several mass ratios and the three different rejection thresholds, $\Delta\chi^2_{\rm thresh} = 25, 50,$ and 100. For $q \gtrsim 10^{-1.5}$, $\epsilon = 100\%$ out to the largest separation for which we calculate ϵ, namely $d = 4.0$. For these mass ratios $d = 4$ is thus a lower limit to the excluded range; the upper end of the excluded range is likely to be considerably larger. We find that any companion to the primary lens with mass ratio $q \gtrsim 10^{-2}$ and angular separation $0.4 \leq d \leq 2.4$ is excluded by the data, that is, such a companion would produce deviations at the $\Delta\chi^2 > 100$ level that are not observed.

Note that these limits apply to individual companions only, not to systems of companions. Implicit in our calculation of $\epsilon(d, q)$ is the assumption that multiple planets affect the magnification structure of the lens, and therefore the deviation from the single-lens magnification, in an independent way. This assumption is likely to break down in regions near the central caustic when more than one planet is in the lensing zone (Gaudi, Naber, & Sackett, 1998). In this case, the efficiencies calculated using the method of Gaudi & Sackett (2000) will be in error by an amount that will depend on the relative mass ratios, orientations, and projected separations of the two companions. Since OGLE-1998-BUL-14 is a high-magnification event, and most of the constraints come from portions of the light curve near the peak of the event (i.e. where the central caustic is probed), our results are only strictly valid for single planets. A full investigation of the effect of multiple planets of ϵ is beyond the scope of this thesis. We expect, however, that the planet detection efficiencies for multiple Jovian planetary systems may actually be higher than for single planets near the peak of OGLE-1998-BUL-14, since the region of anomalous magnification near the central caustic generally occupies a larger fraction of the Einstein ring when two planets are present (Gaudi, Naber, & Sackett, 1998).

It is interesting to compare the limits on companions to the primary lens of OGLE-1998-BUL-14 to those for the primary lens of MACHO-98-BLG-35 derived by the MPS/MOA collaborations (Rhie et al., 1999b). MACHO-98-BLG-35 was a higher magnification event ($A_{\rm max} \sim 75$) than OGLE-1998-BUL-14 ($A_{\rm max} \sim 16$). Since higher magnification events have higher intrinsic detection efficiencies (Griest & Safizadeh, 1998; Gaudi & Sackett, 2000), one would expect, for similar sampling and photometric precision, the limits on companions to be more stringent for MACHO-98-BLG-35. However, although the photometric precision obtained by MPS/MOA on MACHO-98-BLG-35 is similar to that for OGLE-1998-BUL-14 ($\sim$ few percent), the sampling of MACHO-98-BLG-35 (in terms of fraction of the time scale $t_{\rm E}$) is poorer, due primarily to the fact that MACHO-98-BLG-35 was a shorter time scale event. Although Rhie et al. (1999b) used a slightly different method to calculate $\epsilon(d,q)$ than that suggested by Gaudi & Sackett (2000), and used a different rejection criterion ($\Delta\chi^2_{\rm thresh} = 40$), we can make a rough comparison between their resulting detection efficiencies shown in their Figure 7 with ours for $\Delta\chi^2_{\rm thresh} = 50$ shown in the middle panel of Figure 3.6. We see that the detection efficiencies to companions are everywhere higher for MACHO-98-BLG-35 than for OGLE-1998-BUL-14. This indicates that, when the peak of the event can be measured, maximum magnification is a more important factor than sampling in determining the constraining power (and hence the ability to detect companions) in an observed microlensing event.

In Figure 3.7 we show the detection efficiency averaged over the lensing zone (where the detection efficiency is the highest), $0.6 \leq d \leq 1.6$,

$$\epsilon_{\rm LZ}(q) \equiv \int_{0.6}^{1.6} \epsilon(d,q)\ {\rm d}d\ , \tag{3.9}$$

for mass ratios $0 \leq q \leq 10^{-5}$. The lensing zone detection efficiencies for several representative mass ratios are tabulated in Table 3.3. For a planetary model in which companions have angular separations distributed uniformly throughout the lensing zone, $\epsilon_{\rm LZ}$ represents the probability that a companion of mass ratio q would have been detected with the OGLE-1998-BUL-14 data set. These probabilities are quite high: for example, the detection efficiency for a companion of mass ratio $q \gtrsim 10^{-3}$ in the lensing zone of the OGLE-1998-BUL-14 primary is $\gtrsim 80\%$.

For this analysis, we have assumed that the source can be treated as point-like. Finite source effects will have a substantial effect on $\epsilon(d,q)$ if the angular size of source $\rho_* \equiv \theta_*/\theta_{\rm E}$ is comparable to the Einstein ring radius of the companion, $\theta_{\rm p} = \theta_{\rm E} q^{1/2}$ (Gaudi & Sackett, 2000). Any planetary deviations will be broadened but reduced in amplitude for $\rho_* \gtrsim q^{1/2}$. For OGLE-1998-BUL-14, no finite source size effects were detected, thus we can place an upper limit on ρ_*. As we show in the § 3.6.2, the 3σ limit is $\rho_* \leq 0.062$. Thus the detection efficiencies calculated above are strictly valid only for $q \gtrsim 10^{-2.5}$. However, for typical lens parameters, ρ_* is likely to be considerably smaller, $\rho_* \sim 0.01$. Statistically, we thus expect the results to be valid for $q \gtrsim 10^{-4}$. For mass ratios less than this, the detection efficiencies calculating using a point source may be overestimated by tens of percent (Gaudi & Sackett, 2000).

Poorly-constrained blend fractions can also induce substantial uncertainties in the derived detection efficiencies, due to the correlation between blending and impact parameter u_0 (Gaudi & Sackett, 2000). Fortunately, blending is easier to constrain in high-magnification events. Indeed, due to the high magnification of OGLE-1998-BUL-14 and the dense and precise photometry, the blend fraction of the event, and therefore u_0, are quite well constrained. The fractional error in u_0 is $< 1\%$ and should contribute negligibly to the uncertainty in $\epsilon(d, q)$.

When fitting for the binary-lens model, we did not include seeing and background correlation terms (§ 3.4). Although the proper approach would be to include these terms in all binary-lens fits (and indeed, all fits in general), the computational cost is prohibitive. Since these terms were included in the PSPL fit, this implies that $\Delta\chi^2$ between the binary-lens fit and single-lens fit may be overestimated if the deviations from the PSPL fit due to the binary lens are highly correlated with either the seeing or background. This is generally not a problem for background correlations because the systematic deviations arising from the long time scale changes in the background are unlikely to be confused with deviations caused by companions. However seeing correlations are more insidious, because the short-time scale deviations caused by low mass ratio companions could be confused with systematic deviations arising from the nightly seeing changes in a poorly sampled light curve. Consider a deviation from the PSPL light curve that is perfectly correlated with the seeing. It can be shown that the fractional error in χ^2 one makes by not including the seeing correlation in the binary lens fit is $\Delta\chi^2/\chi^2 \sim N_\delta/N_{\rm tot}$, where N_δ is the number of deviant data points and $N_{\rm tot}$ is the total number of data points in the light curve. For uniformly sampled data, this is simply the ratio of the time scale of the perturbation t_δ to the total duration of observations. For planetary microlensing, $t_\delta \sim q^{1/2} t_{\rm E}$, and thus $\Delta\chi^2/\chi^2 \sim q^{1/2}$. Thus for small mass ratios, $q < 10^{-3}$, the fractional error in χ^2 is small $\lesssim 3\%$. For $q > 10^{-3}$, the companions produce coherent deviations that last many days, and thus cannot be correlated with the seeing. We therefore conclude that neglecting the seeing and background correlations does not result in seriously overestimated detection efficiencies.

3.6. Limits on the Mass of the Lens

In the previous section, we placed limits on possible companions to the primary lens responsible for the microlensing event OGLE-1998-BUL-14 by calculating the detection efficiency as a function of the mass ratio q and angular separation d between the primary and secondary in units of the angular Einstein ring of the system. Although limits on the mass ratio are interesting in their own right, what is of interest ultimately are limits on the mass of the companion, $M_{\rm p}$, and the physical orbital separation of the companion, a. In order to translate limits on q and d into limits on $M_{\rm p}$ and a, one must know the mass of the primary lens, M, and its distance $D_{\rm L}$, and the orbital phase and inclination of the system.

Unfortunately it is not generally possible to measure the mass and distance to the lens. The only parameter one can measure from a generic single lens event that contains information about the lens is the time scale $t_{\rm E}$, a degenerate combination of the mass M, distance $D_{\rm L}$, and transverse velocity v of the lens (c.f. Eq. 3.6). However, detection of various higher order effects, such as parallax or finite source effects, enables one to extract additional information and partially break this degeneracy. In the following subsections, we search for signatures of these effects in the light curve of OGLE-1998-BUL-14. Other than a marginal detection of a parallax asymmetry, we do not detect either of these effects, and use their absence to exclude regions of the $(M, D_{\rm L})$ plane. In addition, we place a limit on the amount of light emitted from the lens itself, and translate this into a limit on the lens mass. As we show, despite the excellent photometry and coverage of OGLE-1998-BUL-14, the limits on these higher order effects are not very stringent, and do not translate into strong constraints on the mass of the lens.

The analysis uses the super-cleaned PLANET data set since, as opposed to planetary perturbations, the effects we are searching for here induce subtle deviations with time scales of many days, and therefore cannot be described by a isolated large outliers. Using the super-cleaned data set (which does not include these outliers) will provide more robust and reliable limits. For the parallax analysis only we use the OGLE+PLANET cleaned data set in order to have a more secure description of the total baseline flux.

3.6.1. Parallax Limits

The motion of the Earth around the Sun induces departures from rectilinear motion in the path of the lens relative to the Earth-source line-of-sight and thus alters the formula for the angular separation $u(t)$ as a function of time. This phenomenon is commonly referred to as parallax, and in general gives rise to light curves that deviate from the standard PSPL model (Gould, 1992; Alcock et al., 1995). The magnitude of the deviation depends on the time of year when the event peaks, the angle ϕ of the lens trajectory with respect to the north ecliptic pole, and the transverse velocity $\tilde{\mathbf{v}} \equiv \mathbf{v}(D_{\mathrm{S}}/D_{\mathrm{LS}})$ of the lens projected onto the observer plane.

If the time scale of the event is short compared to the period of the Earth's orbit, the Earth's acceleration can be approximated as constant over the course of the event. In this case, the angular separation can be written as (Gould, Miralda-Escudé, & Bahcall, 1994),

$$u(t) = \left[\xi^2 + u_0^2\right]^{1/2}, \quad \xi \equiv \tau + \frac{1}{2}\kappa t_{\mathrm{E}} \tau^2, \tag{3.10}$$

where $\tau \equiv (t - t_0)/t_{\mathrm{E}}$. The asymmetry parameter κ is given by,

$$\kappa = \Omega_{\oplus} \frac{v_{\oplus}}{\tilde{v}} \sin\lambda \sin\phi, \tag{3.11}$$

where $\Omega_{\oplus} = 2\pi\ \mathrm{yr}^{-1}$, $v_{\oplus} \simeq 30\ \mathrm{km\,s}^{-1}$ is the linear speed of the Earth around the Sun, and λ is the angle between the source and Sun at the time of maximum magnification.

In the case of OGLE-1998-BUL-14, $\sin\lambda \sim 0.5$. Implicit in equation (3.11) is the approximation that the source is in the Galactic plane. Thus, for short-time scale events one can measure only the degenerate combination $\tilde{v}/\sin\phi$.

We fit our OGLE-1998-BUL-14 light curve data with the parallax asymmetry model above and find an improvement of $\Delta\chi^2 = 4.4$ for 1 extra dof over the standard PSPL model, corresponding to a $\sim 2\sigma$ detection of an asymmetry. We find a best-fit value of $\kappa = 6.1 \pm 3.6 \times 10^{-4}$ (1σ), corresponding to

$$\frac{\tilde{v}}{\sin\phi} = (420 \pm 250)\ \mathrm{km\,s^{-1}} \quad (1\sigma). \tag{3.12}$$

This detection is not particularly useful for our purposes, however, not only because it is merely a 2σ detection, but also because the direction of lens motion is unknown.

In order to obtain a constraint on $\tilde{v}$ that is independent of ϕ, we must use the form for $u(t)$ that includes the full two-dimensional $(\tilde{v}, \phi)$ parallax information (Alcock et al., 1995). Given that the detection of asymmetry was marginal, it is not surprising that we are unable to obtain independent constraints on $\tilde{v}$ and ϕ. Calculating χ^2 as a function of $\tilde{v}$, and letting all other parameters (including ϕ) vary, we recover the detection of the parallax asymmetry for $\tilde{v} \gtrsim 30\ \mathrm{km\,s^{-1}}$. For $\tilde{v} \lesssim 30\ \mathrm{km\,s^{-1}}$, however, $\tilde{v}$ becomes comparable to the Earth's velocity. For these small velocities, the component of the Earth's velocity perpendicular to the motion of the lens becomes significant, and the light curve begins to deviate appreciably from the PSPL model, in a manner that is inconsistent with the observations for all values of ϕ. This produces a lower limit to the projected velocity that is independent of ϕ,

$$\tilde{v} > 28.5\ \mathrm{km\,s^{-1}} \quad (3\sigma). \tag{3.13}$$

We can combine this limit with the time scale of the event to give a lower limit to the lens mass as a function of the relative lens distance,

$$M(x) > 6.7 \times 10^{-3} M_\odot \frac{1-x}{x} \quad (\text{Parallax}, 3\sigma) \tag{3.14}$$

where $x \equiv D_\mathrm{L}/D_\mathrm{S}$. This limit is shown in Figure 3.8.

For bulge self-lensing, both lens and source belong to a population with approximately isotropic velocity distributions, producing no preferred direction for the transverse velocity, v, and thus no preferred value for ϕ. For disk lenses, however, there is a preferred direction for ϕ due to Galactic rotation, in which case we would obtain a stronger limit on $\tilde{v}$. Unfortunately, we do not know a priori whether the lens is in the bulge or disk. We will therefore adopt the conservative assumption that there is no preferred direction for v, and use the limit given in equation (3.14).

3.6.2. Finite Source Limit

A point-lens transiting the face of a source will resolve it, creating a distortion in the magnification that deviates from the form given in equation (3.2). A detection of this distortion gives a measurement of the angular size of the source, θ_*, in units of the angular Einstein ring radius, $\rho_* = \theta_*/\theta_\mathrm{E}$ (Gould, 1994; Nemiroff & Wickramasinghe, 1994; Witt & Mao, 1994). The requirement for such finite source effects to be detectable is that the impact parameter of the event must be comparable to or smaller than the dimensionless source size, $u_0 \lesssim \rho_*$. No such finite-source deviations are apparent in the light curve of OGLE-1998-BUL-14. This implies an upper limit to the dimensionless source size of $\rho_* \lesssim 0.06$. For a more exact limit, we calculate χ^2 as a function of ρ_*, leaving all other parameters free to vary, and find that

$$\rho_* < 0.062 \quad (3\sigma). \tag{3.15}$$

In calculating this limit, we have assumed a uniform surface brightness profile for the source. Using a more realistic, but model-dependent, limb-darkened profile weakens this limit slightly.

In order to convert this upper limit on ρ_* into a lower limit on $\theta_{\rm E}$, we must know the angular size of the source, θ_*, which can be estimated from its $(V-I)$ color and I magnitude. Figure 3.9 shows the calibrated dereddened color magnitude diagram (CMD) for OGLE-1998-BUL-14 field from Yale-CTIO 1m data. The stars in the OGLE-1998-BUL-14 field were calibrated relative to observations of 9 standard stars in Landolt (1992), measured several times during the night of 14 August 1998 at the Yale-CTIO 1m telescope in the same V and I filters used for the observations of the microlensing event. Extinction and color correction terms were derived in the normal manner. Comparison with similar measurements on other nights suggests the accuracy of the calibration is ~ 0.02 mag. We fit the distribution of I magnitudes and $(V-I)$ colors of the observed clump to the model of Stanek (1995). We then determined the $\mathrm{E}(V-I)$ and A_I by comparing our fitted clump magnitude and color to the dereddened $I_{\rm cl,0}$ and $(V-I)_{\rm cl,0}$ of the clump for the bulge as determined by Paczyński & Stanek (1998). We find $\mathrm{E}(V-I) = 1.56$ and $A_I = 2.16$. Using the PSPL fit and Yale-CTIO standards, we determine the calibrated, dereddened color and magnitude of the microlensed source to be $I_0 = 14.73 \pm 0.03$ and $(V-I)_0 = 1.23 \pm 0.08$, where the errors reflect the calibration and model uncertainties added in quadrature. From its position on the CMD, Figure 3.9, we conclude that OGLE-1998-BUL-14 is likely to be a clump giant or a RGB star.

To obtain an estimate of the source radius, θ_*, we use the empirical color-surface brightness relationship for giant stars derived by van Belle (1999), which we rewrite as

$$\theta_* = 6.0\ \mu\text{as}\ 10^{-0.2(V-16)+0.5[(V-I)-1.2]}, \tag{3.16}$$

where we have assumed the relationship $(V - K) = 2.2(V - I)$, derived from Bertelli et al. (1994) isochrones. For our parameters, we find $\theta_* = 6.3\mu$as. An uncertainty in the extinction δA_V leads to an uncertainty in the angular size of $\delta\theta_*/\theta_* \sim -0.16\ \delta A_\mathrm{V}$, where the coefficient depends on the temperature of the source (Albrow et al., 1999), which we have assumed to be $T = 5000$ K. We estimate the uncertainty in the extinction to be $\delta A_\mathrm{V} \sim 0.15$, based on the dispersion of the clump, resulting in an uncertainty of $\sim 2\%$ in θ_*. The 3% uncertainty in the I-magnitude of the source leads to an additional uncertainty of $\sim 1\%$ in θ_*; the 8% uncertainty in the color leads to an uncertainty of $\sim 6\%$ in θ_*. Adding these in quadrature, we find $\theta_* = (6.3 \pm 0.4)\ \mu$as.

Adopting this value for the angular size of the source, we can now translate the limit on ρ_* (Eq. 3.15) directly to a limit on the angular Einstein ring radius,

$$\theta_\mathrm{E} > 100\ \mu\mathrm{as} \qquad (3\sigma). \tag{3.17}$$

Since θ_E depends only on the lens mass and distance and on the distance to the source, this limit can be written in terms of a limit of the lens mass as a function of the relative lens distance,

$$M(x) > 1.0 \times 10^{-2} M_\odot \frac{x}{1-x} \qquad (\mathrm{Finite\ Source}, 3\sigma) \tag{3.18}$$

We combine the parallax limit (Eq. 3.14) and the finite source limit (Eq. 3.18) to obtain a lower limit to the lens mass $M > 8.3 \times 10^{-3} M_\odot$, which occurs at $x = 3.55$. This lower limit is indicated in Figure 3.8.

3.6.3. Luminous Lens Limit

If the lens of OGLE-1998-BUL-14 is a main-sequence star, it emits light. Although the angular separation between the lens and source is much too small for the lens to be resolved, additional light from the lens could, in principle, alter the shape of the light curve (c.f. Eq. 3.1). For most microlensing events, degeneracies between the fit parameters make it difficult to constrain accurately the amount of blended light, and thus any light that may be arising from the lens itself. Fortunately, the good photometry, complete coverage, and small u_0 of OGLE-1998-BUL-14 enable the blend fraction to be constrained quite tightly, allowing us to place an interesting upper limit on the blended light emitted by the lens.

To do this, we rewrite the flux of any unresolved light as $F_{\rm B} = F_{\rm U} + F_{\rm L}$, where $F_{\rm L}$ is the flux of the lens, and $F_{\rm U}$ is the flux of any additional unresolved source. Equation 3.1 is then

$$F(t) = F_{\rm S}A(t) + F_{\rm U} + F_{\rm L}. \tag{3.19}$$

We assume that the I-band flux of the lens is the same for all the I-band light curves, and similarly that the V-band flux is the same for all the V-band light curves. This is a reasonable assumption, since all the observatories use the same I and V filters, and because the lens and source will be unresolved for all observatories. However, due to differences in pixel size and image quality, we must allow additional unresolved light, $F_{\rm U}$ not associated with the lens or source to vary from site to site. We then compute χ^2 as a function of $F_{\rm L}$, allowing the other parameters to vary, and imposing the constraint that $F_{\rm B}$ always be positive. For $F_{\rm L} \ll F_{\rm S}$, $\Delta\chi^2$ between the fit with and without a luminous lens is small. However, as $F_{\rm L}$ increases, $\Delta\chi^2$ rises because $F_{\rm U}$ must be negative to match the observations, which is unphysical. In this way we find the minimum I-band magnitude of the lens that is consistent with our observations to be

$$I_{\rm L} > \begin{cases} 21.69 - (V-I) & \text{if } (V-I) \leq 1.75 \\ 19.94 & \text{if } (V-I) \geq 1.75 \end{cases}, \tag{3.20}$$

where the limit is 3σ. Note that this limit is not dereddened since the lens may have less extinction than the mean extinction toward the OGLE-1998-BUL-14 field. For reference, the dereddened limit is shown in Figure 3.9, assuming the reddening to the lens is the same as for the OGLE-1998-BUL-14 field.

In order to convert this limit on lens light into a limit on the lens mass as a function of its distance, we must adopt a relationship between mass and I and V magnitude. For this purpose, we use the solar metallicity Bertelli et al. (1994) theoretical isochrones for $M > 0.6\ M_\odot$, the solar metallicity Yale isochrones (Demarque et al., 1996) for $0.35\ M_\odot \leq M \leq 0.6\ M_\odot$, and extrapolate the Yale isochrones using a 2nd order polynomial for $0 \leq M \leq 0.35\ M_\odot$. We assume that the dust is distributed uniformly between the observer and 1.5 kpc, with a total reddening at 1.5 kpc equal to the mean reddening of the OGLE-1998-BUL-14 field, $\mathrm{E}(V-I) = 1.56$ and $A_I = 2.16$. For all distances between 0 and 8 kpc, we find the largest mass that is consistent with the apparent magnitude limit (Eq. 3.20). This mass-distance limit is shown in Figure 3.8. It can be adequately represented by,

$$\log[M(x)] < 0.8 + 0.07x - 0.75x^{-0.2} \qquad (\mathrm{Luminous\ Lens}, 3\sigma) \tag{3.21}$$

Varying the age, metallicity, or dust distribution within reasonable limits changes the mass limit at any distance by $\lesssim 0.2$ dex.

If the lens is a main-sequence star, the largest mass consistent with the lack of appreciable light in the light curve of OGLE-1998-BUL-14 is $M \sim 1.3\ M_\odot$ which occurs when $D_\mathrm{L} \sim 8$ kpc ($x = 1$). Thus the lens must be a G dwarf or later. Of course, the lens may not be a main sequence star. Gould (1999) estimates that $\sim 80\%$ of events detected toward the bulge are due to main-sequence lenses. The remaining 20% are due to stellar remnants, i.e. as white dwarfs, neutron stars, or black holes. If the lens is such a remnant, it would not obey the mass-luminosity relationship used to find the limit in equation (3.21). However, white dwarfs and neutron stars have masses of

$M_{\rm WD} \sim 0.6\ M_{\odot}$ and $M_{\rm NS} \sim 1.35\ M_{\odot}$, and so automatically satisfy this limit for nearly all likely distances to the lens. Thus the vast majority (99%) of lenses will satisfy the limit in equation (3.21).

3.6.4. Combined Limits

The limits on the mass and distance to the lens set in the previous subsections are, for the most part, model independent. Unfortunately, they are also not very stringent. Even with the assumption that the lens is a main-sequence star, the allowed regions in the $(M, D_{\rm L})$ plane are quite large, spanning two orders of magnitude in mass, $0.01\ M_{\odot} \lesssim M \lesssim 1.3\ M_{\odot}$, and nearly the entire range in distance, $0.5\ {\rm kpc} \lesssim D_{\rm L} \lesssim 8\ {\rm kpc}$. Our analysis indicates that, even with excellent coverage and good photometry, it will be quite difficult to routinely obtain stringent limits on the mass and distance to the lens for most events based on photometry alone.

It has been shown by Dominik (1998) how probability densities for physical quantities of the lens system can be derived under the assumption of statistical distributions of the mass spectrum, the mass density, and the transverse velocity. Rather than doing this, we will simply note that if the lens is in the bulge ($6\ {\rm kpc} \lesssim D_{\rm L} \lesssim 8\ {\rm kpc}$), and has a typical transverse velocity for bulge self-lensing events ($v \sim 100\ {\rm km\,s^{-1}}$), then the measured $t_{\rm E}$ implies that it is likely to have a mass near the upper end of the allowed range. However, we cannot rule out that the lens is moving slowly, and therefore that the mass is quite small.

3.7. Discussion

3.7.1. The Detection Efficiency as a Function of Mass and Separation

In order to convert the limits on companions in the $q - d$ plane to limits on companions in the $M_{\rm p} - a$ plane, we need estimates of the mass and distance to the lens. However, as we demonstrated in § 3.6, it is quite difficult to obtain stringent limits on these quantities from photometric data alone. For illustrative purposes, therefore, we will simply assume that the lens is a G dwarf and adopt $M = M_{\odot}$, and a lens distance of 6.5 kpc, so that $r_{\rm E} = 3.1$ AU. We stress, however, that this choice is somewhat arbitrary, and that the lens mass may be smaller by two orders of magnitude.

Since microlensing is only sensitive to the instantaneous angular separation, d, we must first convolve the detection efficiency $\epsilon(d)$ with the distribution of d for a given semi-major axis a. To do this we integrate over all random inclinations and orbital phases, assuming circular orbits. This distribution is given explicitly in Gould & Loeb (1992). Convolving the resulting distribution with $\epsilon(d)$ gives the detection efficiency as a function of mass ratio and physical (three dimensional) separation in units of $r_{\rm E}$. We then use the values of M and $r_{\rm E}$ above to convert to $\epsilon(q, a/r_{\rm E})$ to the desired detection efficiency $\epsilon(M_{\rm p}, a)$ as a function of the mass and true orbital separation of the companion in AU.

This detection efficiency $\epsilon(M_{\rm p}, a)$ as a function of physical parameters for our assumed primary lens ($M = M_{\odot}$ and $D_{\rm L} = 6.5$ kpc) is shown in Figure 3.10, for our fiducial rejection threshold of $\Delta\chi^2_{\rm thresh} = 50$. Stellar companions to the primary lens of OGLE-1998-BUL-14 with separations between ~ 2 AU and 11 AU, (the largest separation for which we calculate ϵ) are excluded. Although we cannot exclude a Jupiter-mass companion at any separation, we have a $\sim 80\%$ chance of detecting such a companion at 3 AU. The detection efficiency for OGLE-1998-BUL-14 is $> 25\%$ at

$a = 3$ AU for all companion masses $M_{\rm p} > 0.03\ M_{\rm J}$. We find that we had a $\sim 60\%$ chance of detecting a companion with the mass and separation of Jupiter ($M_{\rm p} = M_{\rm J}$ and $a = 5.2$ AU), and a $\sim 5\%$ chance of detecting a companion with the mass and separation of Saturn ($M_{\rm p} = 0.3\ M_{\rm J}$ and $a = 9.5$ AU) in the light curve of OGLE-1998-BUL-14.

Thus, although Jupiter analogs cannot be ruled out in OGLE-1998-BUL-14, the detection efficiencies are high enough that future non-detections in several events with similar quality will be sufficient to place meaningful constraints on their abundance.

3.7.2. Comparison with Other Methods

How do the OGLE-1998-BUL-14 efficiencies compare to planet detection via other methods? In Figure 3.10 we show the radial velocity detection limit on $M_{\rm p} \sin i$ for a solar mass primary as a function of the semi-major axis for a velocity amplitude of $K = 20$ m s^{-1}, which is the limit found for the majority of the stars in the Lick Planet Search (Cumming, Marcy, & Butler, 1999). Although we show this limit for the full range of a, in reality the detection sensitivity extends only to $a \lesssim 5$ AU due to the finite duration of radial-velocity planet searches and the fact that one needs to observe a significant fraction of an orbital period. The limit rises dramatically for $a \gtrsim 5$ AU because the period of the companion becomes larger than the duration of the observations. In addition, we plot in Figure 3.10 the $M_{\rm p} \sin i$ and a for planetary candidates detected in the Lick survey. Radial velocity searches clearly probe a different region of parameter space than microlensing, in particular, smaller separations. Note, however, that our OGLE-1998-BUL-14 data set gives us a $> 75\%$ chance of detecting analogs to two of these extrasolar planets: the third companion to Upsilon And and the companion to 14 Her. Although the efficiency is low, we do have sensitivity to planets with masses as small as $\sim 0.01 M_{\rm J}$, considerably smaller than can be detected via radial velocity methods.

For comparison, we also show in Figure 3.10 the astrometric detection limit on $M_{\rm p}$ for a $M_\odot$ primary at 10 pc, for an astrometric accuracy of $\sigma_{\rm A} = 1$ mas. For an astrometric campaign of 11 years, this limit extends to ~ 5 AU. Such an astrometric campaign ($\sigma_{\rm A} = 1$ mas, $P = 11$ years), would be sensitive to companions similar to those excluded in our analysis of OGLE-1998-BUL-14. The proposed Space Interferometry Mission (SIM) promises ~ 4 μas astrometric accuracy, which would permit the detection of considerably smaller mass companions.

3.8. Conclusion

We have presented the PLANET photometric data set, consisting of 461 I-band and 139 V-band measurements, for the microlensing event OGLE-1998-BUL-14. The median sampling interval of one hour, RMS scatter of 1.5% over the peak, and high magnification of OGLE-1998-BUL-14 make this data set especially sensitive to the presence of lensing companions. Within our photometric uncertainties, the data set is consistent with a single lens.

Our analysis indicates that no companions with mass ratios $q > 0.01$ and instantaneous projected separations $0.4 < d < 2.4$ are present. Assuming a solar-mass primary, this mass ratio range includes known stellar binaries and super Jupiters ($M_{\rm p} = 10$ $M_{\rm J}$). Less massive companions and those at larger or smaller separations are excluded with less significance. Massive companions with $q \gtrsim 10^{-1.5}$ can be excluded for projected separations at least as large as 4 $r_{\rm E}$.

The absence of strong parallax, proper motion, or lens light detections allows us to constrain the mass of the lens to 0.01 $M_\odot \lesssim M \lesssim 1.3$ $M_\odot$. Assuming a solar-type lens with $M = M_\odot$ at a distance $D_{\rm L} = 6.5$ kpc, the Einstein ring radius of the primary corresponds to $r_{\rm E} = 3.1$ AU. Using this value, the PLANET light curve has efficiencies of 60% and 5% for Jupiter and Saturn analogs, respectively, and a greater than $> 75\%$ efficiency for companions like those in the Upsilon And and 14 Her systems. Planets with $M_{\rm p} > 10\ M_{\rm J}$ and true orbital separations 1.2 AU $< a <$ 7.4 AU are excluded, assuming these fiducial primary lens parameters.

In performing our analysis, we have considered the systematic effects of (1) correlations between our photometry and image quality and sky background; (2) underestimated error bars; (3) finite source size; and (4) poorly-constrained blending. We find that the DoPHOT-reported uncertainties underestimate the true scatter, and that the residuals from the best-fit model are significantly correlated with image quality and background. Applying a simple linear correction term, rescaling the uncertainties, and eliminating five non-sequential outliers, however, results in a Gaussian error distribution yielding $\chi^2/{\rm dof} = 1$ for a point-source point-lens fit. This allowed us to proceed with a χ^2-analysis to find the portion of projected separation-mass ratio (d-q) binary parameter space excluded by our data. We estimate that non-zero source size is unlikely to significantly affect our results for $q \gtrsim 10^{-4}$ and almost certainly not for $q \gtrsim 10^{-2.5}$. Blending (and thus the true impact parameter) is well constrained for OGLE-1998-BUL-14 by our data set, and thus has a negligible effect on our conclusions.

Our data set for this microlensing event is sensitive to planets occupying a different range of parameter space than current planet searches by other techniques. In particular, super-Jupiters ($M_{\rm p} \simeq 10\ M_{\rm J}$) can be ruled out as companions to the stellar-mass lens of OGLE-1998-BUL-14 at distances of several AU, larger than those probed by more sensitive – but relatively recently commenced – radial velocity and astrometric searches.

It is not possible to derive general inferences about the abundance and characteristics of binary or planetary systems from observations of any single system. Nevertheless, our results for OGLE-1998-BUL-14 clearly demonstrate the ability of microlensing to contribute to our knowledge of Jovian planets several AU from their parent stars, and

– if data of high enough quality can be collected for a large enough number of events – to the search for and study of planets of much smaller mass as well. The analysis presented here for OGLE-1998-BUL-14 represents the first step in the larger task of performing a combined analysis of the growing PLANET data base of frequently and precisely monitored microlensing light curves. When completed, statistical inferences can be drawn about the frequency and distribution of stellar and Jovian companions to stellar lenses in the Galaxy.

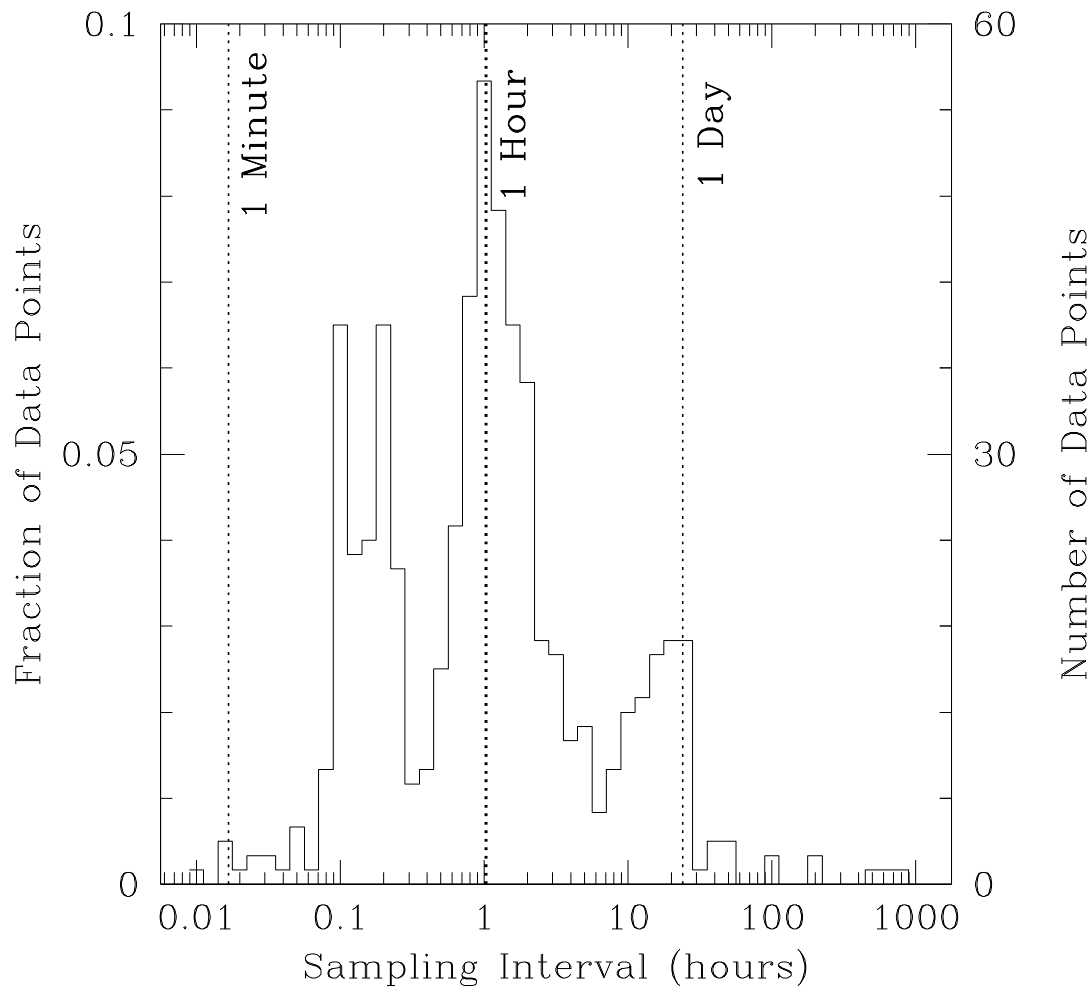

Fig. 3.1.— Histogram of the distribution of sampling intervals (time between successive measurements) in hours for the OGLE-1998-BUL-14 dataset. The median sampling interval is about 1 hour.

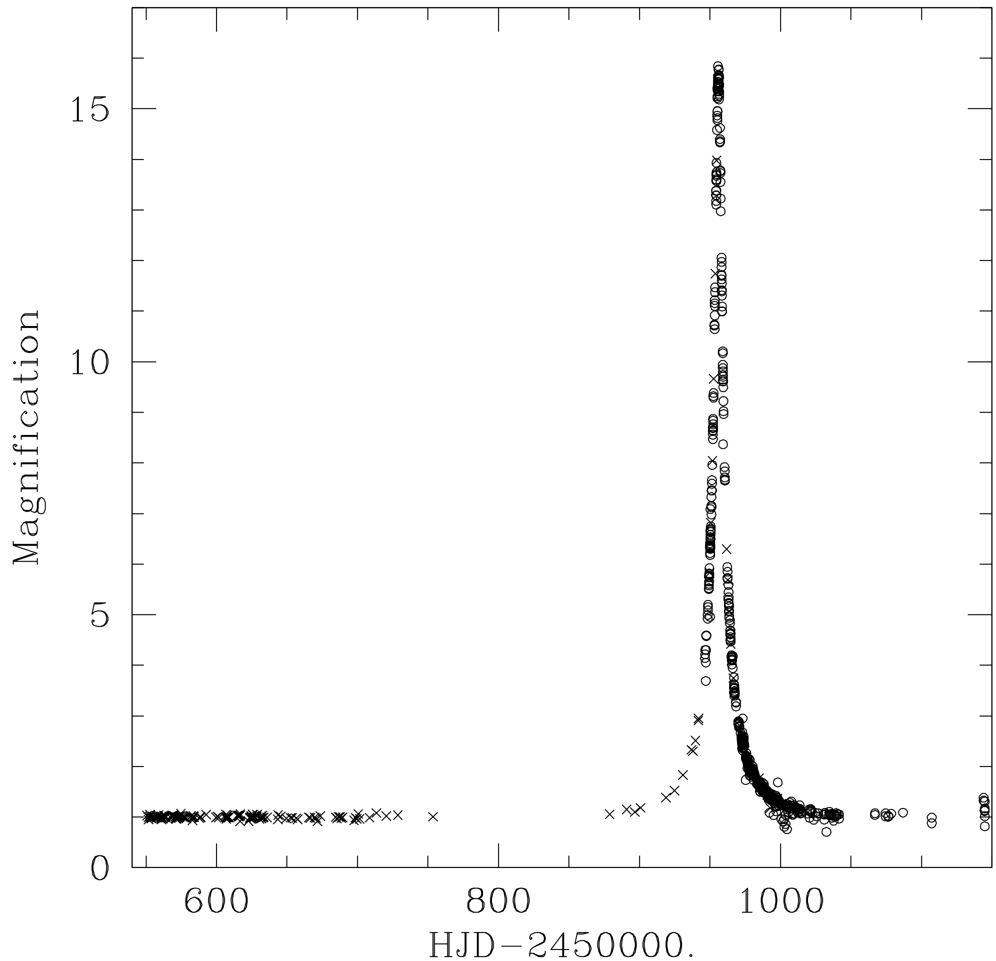

Fig. 3.2.— The combined PLANET (open circles) and OGLE (crosses) light curves for OGLE-1998-BUL-14. In order to show all data on the same figure, we have plotted the total magnification for each light curve, which is given by $A = (F - F_{\rm B})/F_{\rm S}$, where F is the observed flux, and $F_{\rm S}$ and $F_{\rm B}$ are the source and blended fluxes derived by fitting the data to a PSPL model, respectively. All data prior to $\mathrm{HJD}' \equiv \mathrm{HJD} - 2450000 \simeq 940$ are from OGLE; the majority of the data after $\mathrm{HJD}' = 940$ are from PLANET.

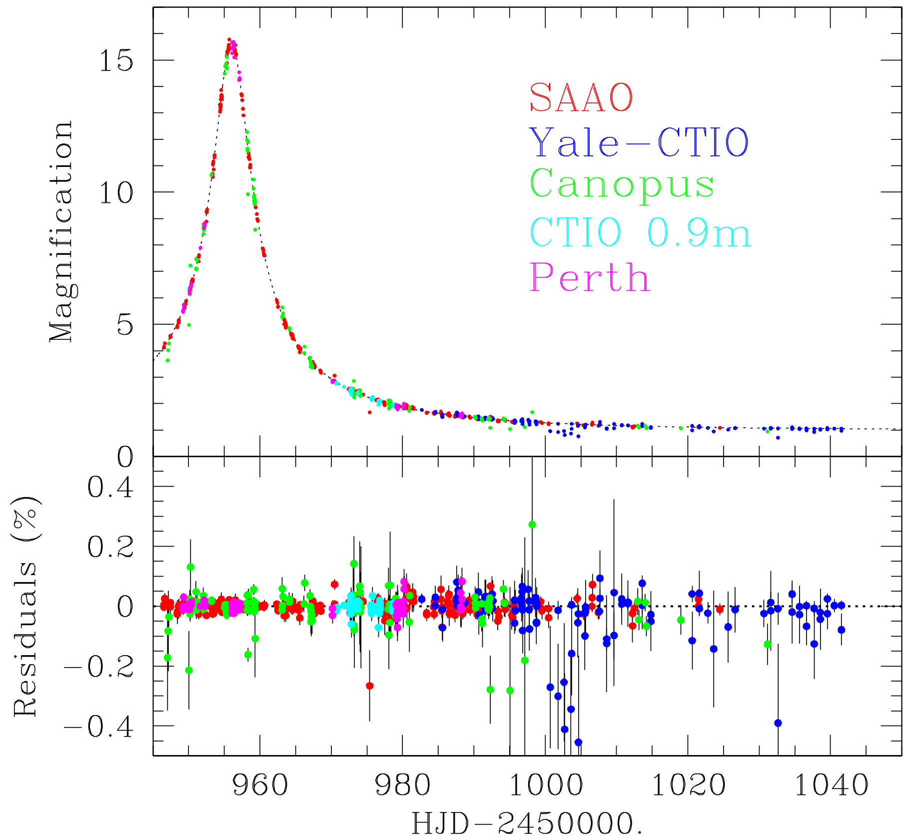

Fig. 3.3.— Top Panel: The cleaned PLANET data for OGLE-1998-BUL-14. As in Figure 3.1, the magnification $A = (F - F_{\rm B})/F_{\rm S}$ is plotted. Only PLANET data prior to HJD$'$ = 1050, constituting $\sim$ 95% of the complete PLANET data set are shown. The dashed line indicates the best-fit PSPL model, which has a time scale $t_{\rm E} = 40$ days, and a minimum impact parameter $u_0 = 0.064$, corresponding to a maximum magnification of $A_{\rm max} \sim 16$. The entire data set consists of 461 I-band and 139 V-band data points, the majority of which was taken between HJD$' \simeq 950$ to HJD$' \simeq 1040$. The median sampling interval during this time span is about 1 hour, or $10^{-3} t_{\rm E}$, with no gaps greater than four days. The data are from the Yale-CTIO 1m, South African Astronomical Observatory 1m, the Perth 0.6m, the Canopus 1m, and the CTIO 0.9m. Bottom Panel: Residuals from the best-fit PSPL model.

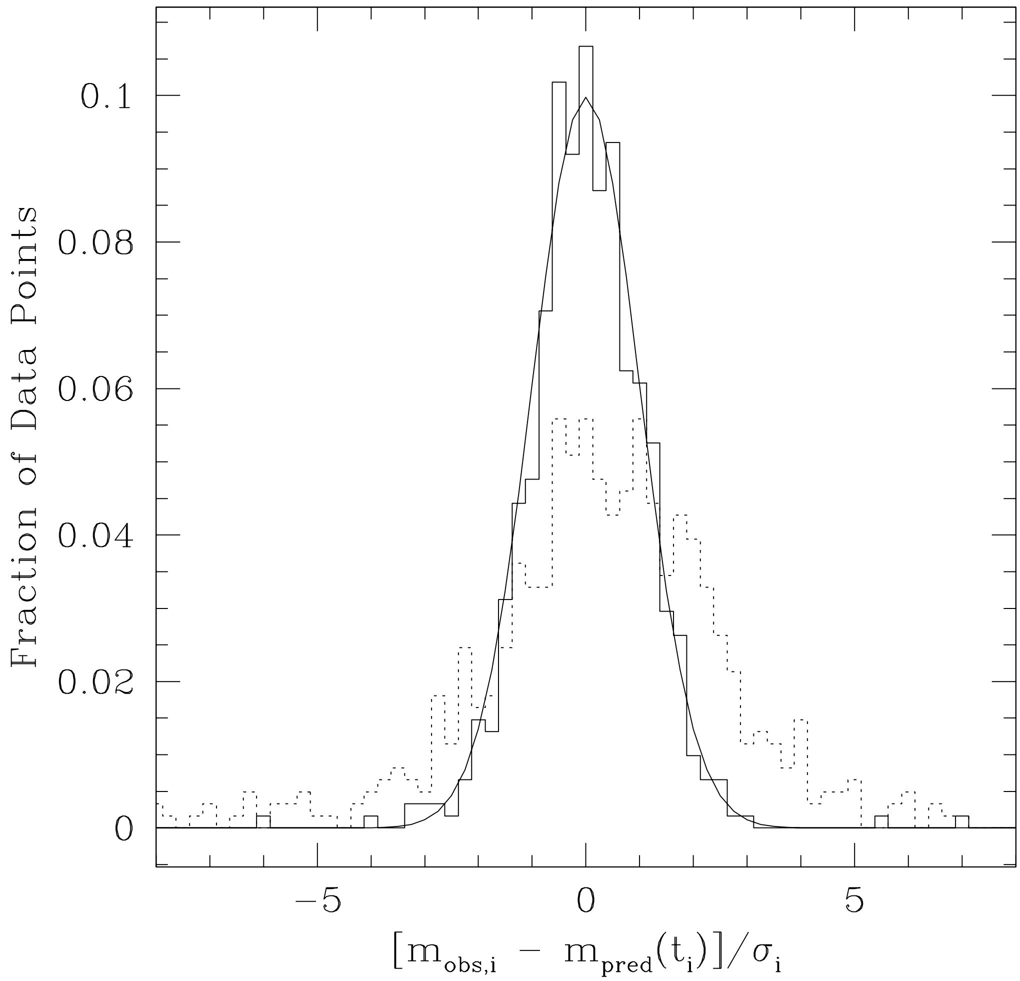

Fig. 3.4.— The histograms show the distributions of the residuals of the individual data points from the best-fit PSPL model, divided by their respective errors, before correction for seeing and background systematics (dashed histogram) and after correction (solid histogram). The solid curve is a Gaussian of unit variance.

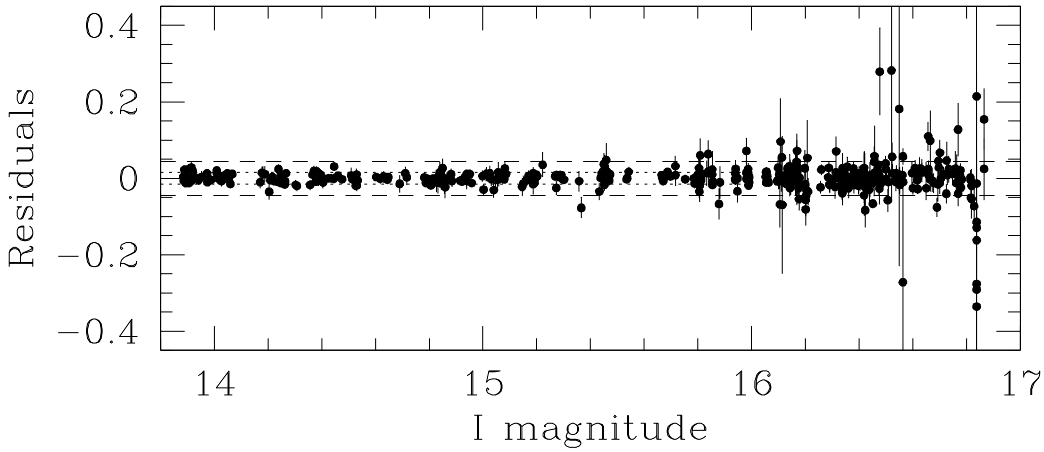

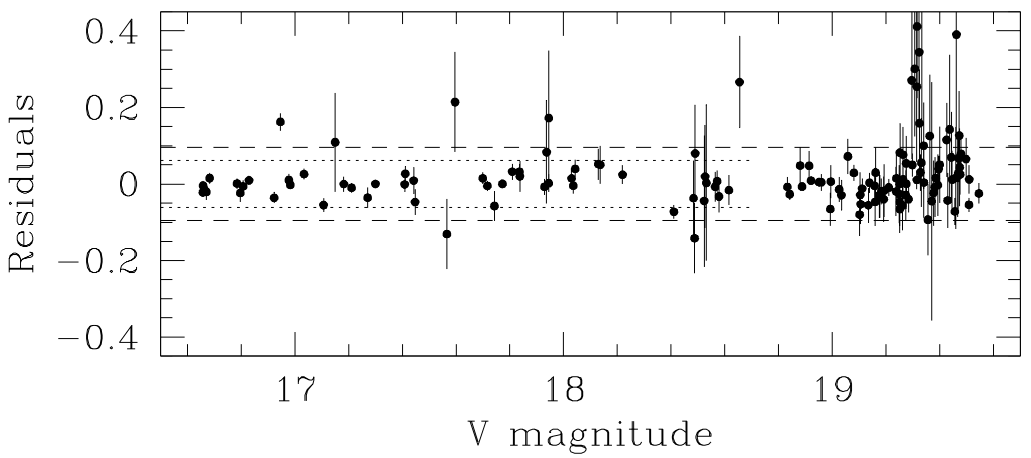

Fig. 3.5.— The points with error bars are the residuals (in magnitudes) of the OGLE-1998-BUL-14 data points from the best-fit PSPL model as a function of the magnitude predicted by the model. We show the residuals separately for the I-band dataset (top panel) and the V-band dataset (bottom panel). The 1σ scatter for the entire I-band data set, as denoted by the dashed line, is $\sim 4\%$, whereas the scatter for all points with $I < 16$ is 1.5% (dotted line). The 1σ scatter for the V-band data set is $\sim 10\%$ (entire data set), and $\sim 7\%$ ($V < 18.7$).

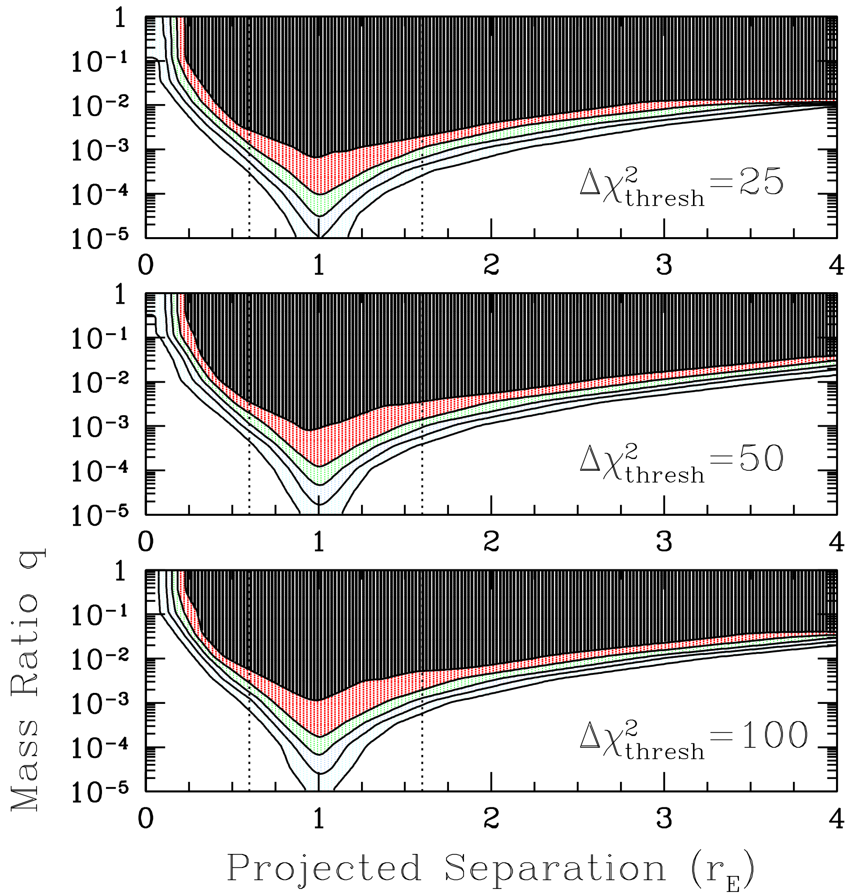

Fig. 3.6.— The solid black lines are contours of constant detection efficiency, $\epsilon(d, q)$, for all PLANET OGLE-1998-BUL-14 data, shown for projected separations d between the primary and companion in units of the Einstein ring radius, of $0 < d < 4$, and mass ratios between the primary and companion, q, of $0 > \log(q) > -5.0$. The contours mark $\epsilon = 5\%$ (outer contour), 25%, 50%, 75%, and 95% (inner contour). The vertical dotted lines indicate the boundaries of the lensing zone, $0.6 \leq d \leq 1.6$. The region of (d, q) parameter space shaded in black is excluded by the observations at the 95% significance level. The panels are the results for different rejection criteria, $\Delta\chi^2_{\rm thresh} = 25$ (top), 50 (middle), 100 (bottom). A mass ratio of $q = 10^{-2}$ corresponds to the mass ratio between a $10M_J$ planet and a G dwarf. For this mass ratio, a companion with projected separation $0.4 \leq d \leq 2.4$ is excluded at the 95% significance level for all our rejection criterion. This corresponds to a range of instantaneous projected separations in physical units of 1.2 to 7.4 AU, assuming a G dwarf primary at 6.5 kpc.

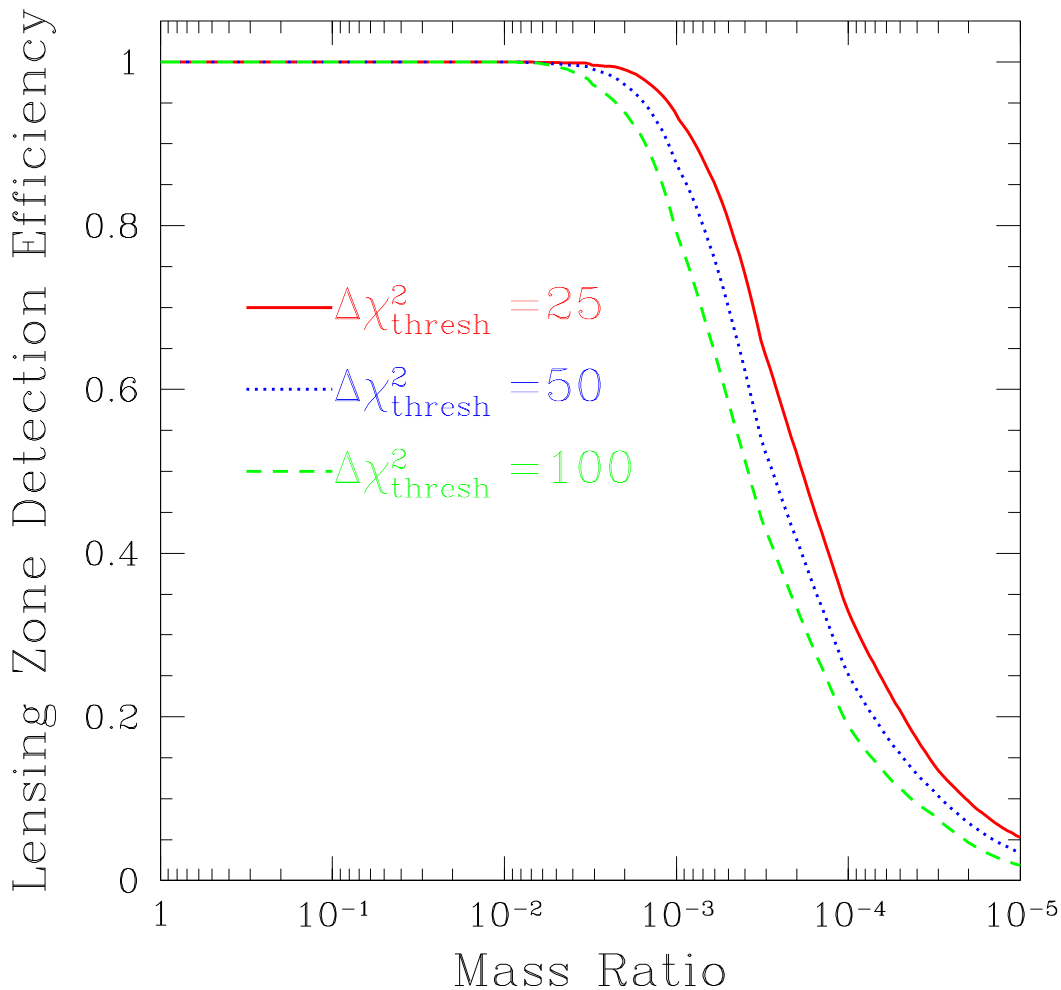

Fig. 3.7.— The detection efficiency of PLANET OGLE-1998-BUL-14 data to a companion averaged over the lensing zone, $0.6 \leq d \leq 1.6$, as a function of the mass ratio q between the primary and the companion. We show the lensing zone detection efficiency for three different rejection thresholds, $\Delta\chi^2_{\rm thresh} = 25$ (solid), 50 (dotted), and 100 (dashed).

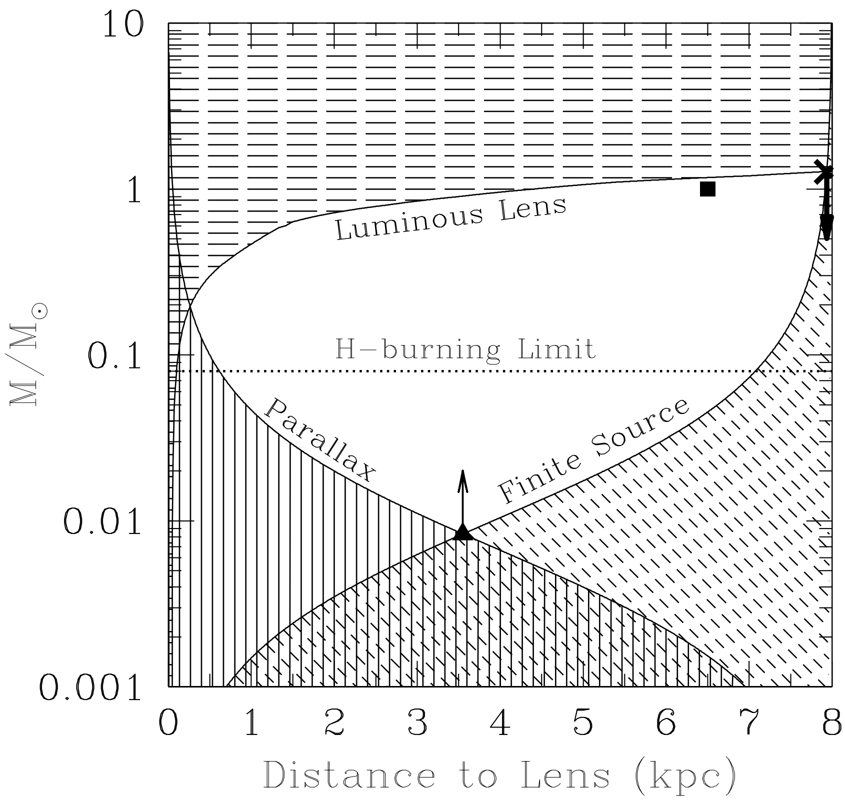

Fig. 3.8.— Excluded regions for the lens mass and distance based on the lack of second-order signatures in the light curve of OGLE-1998-BUL-14. The solid lines show 3σ upper or lower limits to the mass of the lens in solar masses $M/M_\odot$ as a function of the distance of the lens in kpc for a source distance of 8 kpc. The solid hatching shows the excluded region from the lack of parallax effects. The short-dashed hatching shows the region excluded by the lack of finite source effects. Combining the finite source and parallax limits, we obtain a lower limit to the mass, which is shown as the triangle. The long-dashed hatching shows the region excluded if the lens is a main-sequence star; the upper limit to the lens mass is shown as a cross. The dotted horizontal line is the hydrogen-burning limit. Our adopted lens mass $M = M_\odot$ and distance $D_{\rm L} = 8$ kpc are shown as the square.

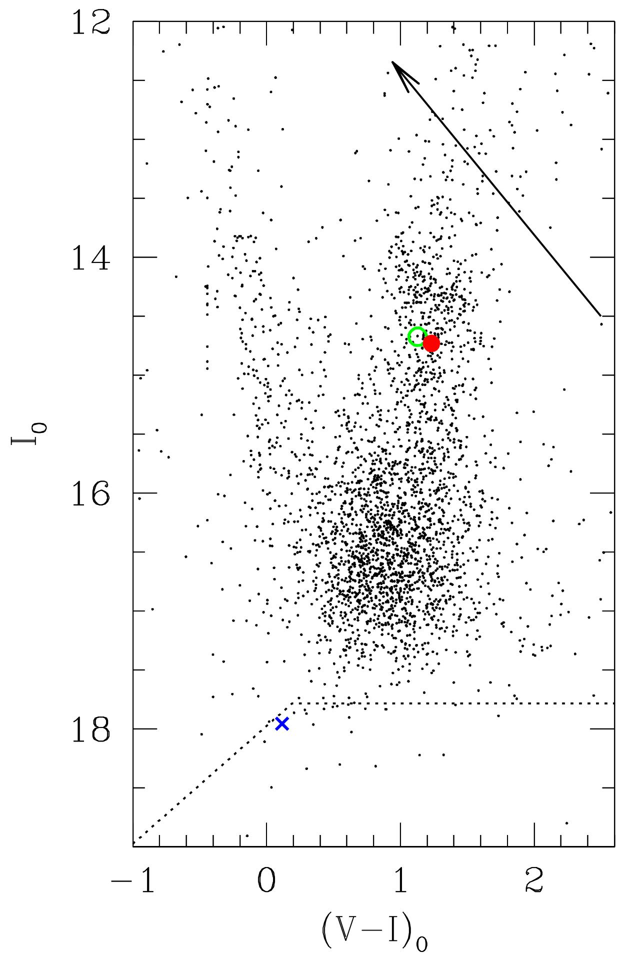

Fig. 3.9.— Calibrated, dereddened color-magnitude diagram for the field centered on OGLE-1998-BUL-14 from Yale-CTIO 1m data. The mean reddening for the field is A_I and E($V-I$)=1.56, determined from the mean I magnitude and $V-I$ color of the clump. The arrow shows the direction and magnitude of the dereddening vector. The open circle shows the dereddened position of the unmagnified source, which is composed of the microlensed source (filled circle) and an unresolved blended star (cross). The dotted line shows the 3σ upper limit to the dereddened I magnitude of the lens, assuming the extinction to the lens is the same as the OGLE-1998-BUL-14 field.

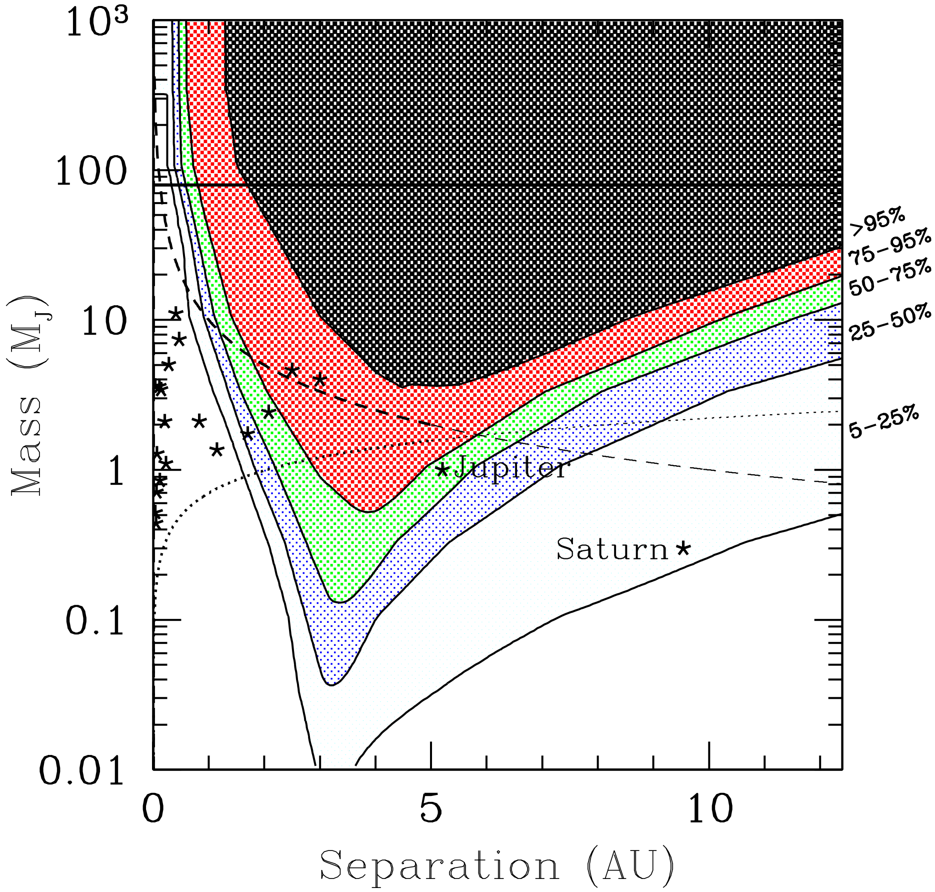

Fig. 3.10.— Example detection efficiencies for the PLANET data set of OGLE-1998-BUL-14 as a function of the mass and orbital separation of the companion assuming a primary lens mass of $M_{\odot}$ and Einstein ring radius of $r_{\rm E} = 3.1$ AU. The contours are the same as in Figure 3.6. In order to convert from mass ratio and projected separation to mass and physical separation, we have averaged over orbital phase and inclination (assuming circular orbits). Jupiter and Saturn are marked with stars, as are the extrasolar planets discovered with radial velocity techniques. The horizontal line marks the hydrogen-burning limit. The dotted line shows the radial-velocity detection limit for an accuracy of 20 ms^{-1} and a primary mass of $M_{\odot}$. The dashed line is the astrometric detection limit for an accuracy of 1 mas and a primary of mass $M_{\odot}$ at 10 pc.

Filter	Site	Number of Points	$\sigma/\sigma_{\mathrm{DoP}}$[a]
I	CTIO 0.9m	48	1.55
	Perth	50	1.00
	Canopus A	60	1.78
	Canopus B	47	2.25
	Yale	56	1.83
	SAAO A	113	1.43
	SAAO B	20	1.43
	SAAO C	67	1.42
	Total PLANET I	461	–
V	Perth	4	0.08
	Canopus A	20	1.77
	Yale	56	1.85
	SAAO A	33	1.38
	SAAO B	6	0.94
	SAAO C	20	0.88
	Total PLANET V	139	–
	Total PLANET I+V	600	–
I	OGLE	159	2.01
	Total PLANET+OGLE	754	–

Table 3.1: Number of Data Points and Error Scaling Factors

[a]The scaling factor for the DoPHOT reported errors.

		PLANET CL[a]	PLANET SC[b]	OGLE+PL SC[c]
t_0		956.016±0.005	956.011±0.005	956.011±0.005
$t_{\rm E}$		39.6±1.1	40.0±1.2	40.0±0.58
u_0		0.0643±0.0002	0.0639±0.0002	0.0639±0.0002
g_I	CTIO 0.9m	0.16±0.05	0.17±0.05	0.17±0.04
	Perth	0.00±0.03	0.00±0.03	0.00±0.02
	Canopus A	0.03±0.04	0.04±0.04	0.04±0.04
	Canopus B	0.14±0.05	0.14±0.05	0.14±0.04
	Yale	0.03±0.03	0.05±0.03	0.04±0.02
	SAAO A	0.18±0.03	0.17±0.03	0.17±0.02
	SAAO B	0.00±0.11	0.00±0.11	0.00±0.10
	SAAO C	0.06±0.03	0.06±0.03	0.06±0.03
	OGLE	–	–	0.06±0.01
g_V	Perth	0.14±0.03	0.15±0.03	0.15±0.02
	Canopus A	0.47±0.13	0.20±0.13	0.20±0.13
	Yale	0.12±0.08	0.13±0.08	0.13±0.07
	SAAO A	0.30±0.05	0.23±0.05	0.23±0.04
	SAAO B	0.00±0.33	0.00±0.33	0.00±0.33
	SAAO C	0.00±0.07	0.00±0.07	0.00±0.07
χ^2		729.7	565.3	720.9
# points		600	595	595+159=754
χ^2/d.o.f.		1.28	1.00	1.00

Table 3.2: Point-source Point-lens Fit Parameters

[a] PLANET "cleaned" data set; includes all data.

[b] PLANET "super-cleaned" data set; does not include outliers with residuals $\geq 3\sigma$.

[c] Combined PLANET "super-cleaned" and OGLE data sets.

Mass Ratio	$\Delta\chi^2_{\rm thresh} = 25$	$\Delta\chi^2_{\rm thresh} = 50$	$\Delta\chi^2_{\rm thresh} = 100$
$10^{0.0}$	0.19–4][a]	0.19–4]	0.19–4]
$10^{-0.5}$	0.19–4]	0.19–4]	0.19–4]
$10^{-1.0}$	0.19–4]	0.26–4]	0.28–4]
$10^{-1.5}$	0.28–4]	0.29–3.86	0.29–3.48
$10^{-2.0}$	0.38–2.87	0.39–2.63	0.40–2.37
$10^{-2.5}$	0.50–1.96	0.57–1.73	0.67–1.51
$10^{-3.0}$	0.82–1.27	0.85–1.20	0.88–1.05

Table 3.3: Excluded Separations

[a]Bracket indicates that companions are excluded at the largest separation we calculate.

Mass Ratio	$\Delta\chi^2 = 25$	$\Delta\chi^2 = 50$	$\Delta\chi^2 = 100$
$10^{0.0}$	1.00	1.00	1.00
$10^{-0.5}$	1.00	1.00	1.00
$10^{-1.0}$	1.00	1.00	1.00
$10^{-1.5}$	1.00	1.00	1.00
$10^{-2.0}$	1.00	1.00	1.00
$10^{-2.5}$	1.00	0.99	0.98
$10^{-3.0}$	0.94	0.87	0.80
$10^{-3.5}$	0.66	0.54	0.44
$10^{-4.0}$	0.33	0.24	0.19
$10^{-4.5}$	0.14	0.11	0.08
$10^{-5.0}$	0.05	0.03	0.02

Table 3.4: Lensing Zone Detection Efficiencies

Chapter 4

Constraints from 5 Years of PLANET Photometry

4.1. Introduction

The discovery in 1995 of a massive planet orbiting 51 Peg (Mayor & Queloz, 1995), followed by the discovery of several more planets orbiting nearby dwarf stars using the same radial velocity technique (see Marcy & Butler 1998 and references therein) has focussed both public and scientific attention on the search for extra-solar planets and the experimental and theoretical progress being made in developing other viable detection techniques.

Due to their small mass and size, extra-solar planets are difficult to find. Proposed detection methods can be subdivided into direct and indirect techniques. Direct methods rely on the detection of the reflected light of the parent star, and are exceedingly challenging due to the extremely small flux expected from the planet, which is overwhelmed by stray light from the star itself (Angel & Woolf, 1997). Some direct imaging searches have already been performed (Boden et al., 1998b), but the future of this method lies in the construction and launching of a space-based interferometer (Woolf & Angel, 1998).

Astrometric, radial velocity and occultation measurements can be used to detect the presence of a planet indirectly. Astrometric detection relies on the measurement of the wobble of the stellar centroid caused by the motion of the star around the center-of-mass of the planet-star system, and yields the mass ratio of the planet-star system. Many attempts to find extra-solar planets in this way have been made, but the measurements are difficult and the detections remain controversial; planned space-based missions astrometric missions such as the Full-Sky Astrometric Mapping Explorer (FAME) and the Space Interferometry Mission (SIM) are expected to be enormously more successful (Lindegren & Perryman, 1996). Occultation methods use very accurate photometry of the parent star to detect the small decrease in flux ($\lesssim 1\%$) caused by a planet transiting the face of the star (Hale & Doyle, 1994). Occultation searches are currently being carried out (Deeg et al., 1998; Brown & Charbonneau, 2000; Borucki et al., 1999), with important new limits being placed on planetary companions in 47 Tuc (Gilliland et al., 2000). Recently, one of the extrasolar planets detected via radial velocity surveys was also found to transit if parent star, yielding a measurement of the mass, distance and density of the companion (Charbonneau et al., 2000; Henry et al., 2000). Spaced-based missions are being planned to increase the sensitivity to small-mass planets (Deleuil et al., 1997; Borucki et al., 1997). By far the most successful indirect method for discovering planets has been the Doppler technique, which employs extraordinarily precise radial velocity measurements of nearby stars to detect Doppler shifts caused by orbiting planets. Several teams have monitored nearby stars with the aim of detecting the Doppler signal of orbiting planets (McMillan et al., 1993; Mayor & Queloz, 1995; Butler et al., 1996; Cochran et al., 1997; Noyes et al., 1997; Vogt et al., 2000). To date these groups combined have discovered over 30 extra-solar planets using this technique, with new planetary companions being announced every few months (Marcy, Cochran & Mayor, 2000). Several exciting discoveries using radial velocity technique include the first detection of an extrasolar planetary system (Butler et al., 1999), and the detection of planets with mass below that of Saturn (Marcy, Butler, & Vogt, 2000).

These detection techniques are complementary to one another both in terms of their sensitivity to planetary mass and orbital separations and the specific physical quantities of the planetary system that they measure. All share two distinct advantages: the experiments are repeatable and, due to their reliance on flux measurements of the parent star or the planet itself, they are sensitive to stars in the solar neighborhood where follow-up studies can be most easily pursued. For example, spectroscopic follow-up studies may enable the detection of molecules commonly thought to be indicative of life, such as water, carbon dioxide, and ozone (Woolf & Angel, 1998). This advantage is linked to a common drawback: the searches can be conducted only on a limited number of nearby stars. Without substantial developments in technology beyond what is currently available, these methods are unlikely to detect planets orbiting stars more distant than $\sim$1 kpc, and are thus unable to address questions about the nature of planetary systems beyond the immediate solar neighborhood. In addition, most of the methods (astrometry, radial velocity and occulation) can only probe companions with orbital periods smaller than the duration of the experiment. Furthermore, most are fundamentally restricted to massive planets; of the proposed and currently implemented methods, only space-based interferometric imaging and transit searches are expected to be sensitive to Earth-mass planets.

A Galactic microlensing event occurs when a massive, compact object (the lens) passes near to our line-of-sight to a more distant star (the source). If the lens, observer, and source are perfectly aligned, then the lens images the source into a ring, called the Einstein ring, which has angular radius of

$$\theta_{\mathrm{E}} = \sqrt{\frac{4GM}{c^2}\frac{\pi_{\mathrm{rel}}}{\mathrm{AU}}} \sim 320\mu\mathrm{as}\left(\frac{M}{0.3\ M_{\odot}}\right)^{1/2}, \tag{4.1}$$

where M is the mass of the lens, and π_{rel} is the relative source-lens parallax, i.e,

$$\pi_{\mathrm{rel}} = \frac{1}{D_{\mathrm{L}}} - \frac{1}{D_{\mathrm{S}}}, \tag{4.2}$$

where $D_{\rm L}$ and $D_{\rm S}$ are the distances to the lens and source, respectively. Note that $\theta_{\rm E}$ corresponds to a physical distance at the lens of,

$$r_{\rm E} = \theta_{\rm E} D_{\rm L} \simeq 2\ {\rm AU} \left(\frac{M}{0.3\ M_\odot}\right)^{1/2}. \tag{4.3}$$

If the lens is not perfectly aligned with the line-of-sight, then the lens splits the source into two images. The separation of these images is $\mathcal{O}(\theta_{\rm E})$ and hence unresolvable. However, the source is also magnified by the lens, by an amount that depends on the angular separation between the lens and source in units of $\theta_{\rm E}$. Since the lens, observer, and source are all in relative motion, this magnification is a function of time: a 'microlensing event.' The time scale for such an event is

$$t_{\rm E} = \frac{\theta_{\rm E}}{\mu_{\rm rel}} \simeq 20\ {\rm days} \left(\frac{M}{0.3\ M_\odot}\right)^{1/2}, \tag{4.4}$$

where $\mu_{\rm rel}$ is the relative lens-source proper motion, and we have assumed $\mu_{\rm rel} = 25\ {\rm km\,s^{-1}\ kpc^{-1}}$, which is typical for events toward the Galactic bulge.

If the primary lens has a planetary companion, and the position of this companion happens to be in the path of one of the two images created during the primary event, then the planet will perturb the light from this image, creating a deviation from the primary light curve. The duration of the deviation, $t_{\rm p}$, is roughly the time it takes the source to cross the Einstein ring of the planet, $\theta_{\rm p}$. From equation (4.1), $\theta_{\rm p} = (m_{\rm p}/M)^{1/2}\theta_{\rm E}$, where $m_{\rm p}$ is the mass of the planet. Therefore, from equation (4.4), $t_{\rm p} = (m_{\rm p}/M)^{1/2} t_{\rm E}$, or

$$t_{\rm p} = \sqrt{q}\, t_{\rm E} \tag{4.5}$$

where $q \equiv m_{\rm p}/M$ is the mass ratio of the system. For a Jupiter/Sun mass ratio ($q \simeq 10^{-3}$), the perturbation time scale is $\mathcal{O}$(day). Since the perturbation time scale is considerably less than $t_{\rm E}$, the majority of the light curve will be indistinguishable from a single lens. Hence the signature of the planet orbiting the primary lens is a short-duration deviation atop an otherwise normal single lens curve.

Microlensing overcomes many of the disadvantages of more traditional methods of searching for planets. First, because the method relies on the mass (and not light) of the system, planets can be searched for around stars with distances of many kiloparsecs. Second, the sensitivity can, in principle, be extended down to Earth-mass planets (Bennett & Rhie, 1996). Third, a nearly infinite number of parent stars can be searched and finally, orbital separations of many AU can be probed immediately, without having to wait for a full orbital period. The primary disadvantages of microlensing searches for planets are that the measurements are not repeatable and there is little hope for follow-up study of the systems.

Mao & Paczyński (1991) first suggested that microlensing might be used to find extrasolar planets. Their ideas were expanded upon by Gould & Loeb (1992), who in particular noted that if all stars had Jupiter-mass planets at distances of $\sim \theta_{\rm E}$, then $\sim 15\%$ of all microlensing events should exhibit planetary perturbations. Gould & Loeb (1992) also note that the detection probability will be highest for planets with projected separations lying within $[0.6 - 1.6]\theta_{\rm E}$ of the primary, the "lensing zone." Since these two seminal papers, the theoretical basis of planetary microlensing has developed rapidly. Numerous authors have studied detection probabilities and observing strategies incorporating a variety of new effects (Bolatto & Falco, 1993; Bennett & Rhie, 1996; Peale, 1997; Sackett, 1997; Griest & Safizadeh, 1998; Gaudi, Naber, & Sackett, 1998; Di Stefano & Scalzo, 1999a,b). Notably, Bennett & Rhie (1996) found that the detection probability for Earth-mass planets was appreciable ($\sim 2\%$), and Griest & Safizadeh (1998) found that, for high magnification events, the detection probability can be nearly 100% for Jovian planets in the lensing zone. Gaudi & Gould (1997), Gaudi (1998) and Gaudi & Sackett (2000) all discussed extracting information from observed microlensing events. In particular, Gaudi & Sackett (2000) developed a method to calculate the detection efficiency of observed datasets to planetary companions, which we will be employing extensively here. Planetary microlensing has been placed in the global context of binary lensing by Dominik (1999b), and studied via perturbative analysis by Bozza (1999, 2000a,b).

On the observational front, progress has been somewhat slower. This is primarily due to the fact that the survey collaborations that discover microlensing events toward the Galactic bulge, EROS (Afonso et al., 2001), MACHO (Alcock et al., 1997), and OGLE (Udalski et al., 2000), have sampling rates that are of order or smaller than the planetary perturbation time scale. However, soon after these searches commenced, these collaborations developed the capability to recognize microlensing events in real time (Alcock et al., 1996; Udalski et al., 1994), thus allowing them to alert the public of ongoing events. In response to this potential, several "follow-up" collaborations were formed, GMAN (Alcock et al., 1997), PLANET, (Albrow et al., 1998) and MPS, (Rhie et al., 1999a) with the express purpose of intensively monitoring these alerted events in order to search for deviations from the nominal point-source point-lens (PSPL) light curve, and in particular the short duration signatures of planets. The feasibility of such a monitoring campaign was conclusively demonstrated in the 1995 pilot season of PLANET (Albrow et al., 1998), during which we achieved ~ 2 hour sampling and few percent photometry on several concurrent bulge microlensing events. The first observational results from these collaborations in the context of planets came from the Rhie et al. (1999b) who used their observations of the high-magnification event MACHO 98-BLG-35 to rule out Jovian companions to the primary microlens for a large range of separations. We performed a similar study of OGLE-1998-BUL-14 (Albrow et al., 2000b), demonstrating that companions with mass $> 10\ M_{\rm Jup}$ were ruled out for separations $1-7$ AU. Our detection efficiency for this event was $\sim 60\%$ for a companion with the mass and separation of Jupiter, thereby demonstrating that a combined analysis of many event of similar quality would place interesting constraints on Jovian analogs. The first claimed detection of an extrasolar planet using microlensing was made by Bennett et al. (1999). Based on their anylsis of event MACHO 97-BLG-41, they claimed to have discovered a $\sim 3\ M_{\rm Jup}$ mass planet orbiting a binary star system. Our analysis of our own (independent) data set demonstrated that the event was explainable by a rotating binary lens, and did not require the existence of a planet (Albrow et al., 2000a).

Thus, despite the excellent prospects for detecting planets with microlensing, and after more than 5 years of intensive monitoring of microlensing events, no viable planetary candidates have been found. As these null results accumulate, the obvious conclusion becomes inescapable: the planets we are searching for must not be common. Here we quantify this conclusion. We analyze 5 years of PLANET photometry of microlensing events toward the bulge for the presence of planets orbiting the primary microlenses. We use strict event criterion to construct a well-defined subsample of events. Employing analysis techniques presented in Gaudi & Sackett (2000) and applied in Albrow et al. (2000b), we search for the signals of planets in these events. We find none. Using this null result, taking into account the detection efficiencies to planetary companions for each event, we derive a statistical upper limit to the fraction of primary microlenses with a companion. Since most of the events in our sample are likely due to normal stars in the Galactic bulge, we therefore place limits on the fraction of stars in the bulge with planets.

We describe our observations, data reduction and post-processing in § 4.2. In § 4.3, we present a qualitative discussion of our event sample, categorize this sample, and present circumstantial evidence that planetary deviations are not seen in our data. We define and apply our event selection criteria in § 4.4; this section also includes a description of how our events are fitted with a PSPL model. We summarize the characteristics of our final sample of events in § 4.5. In § 4.6, we describe our algorithm for searching for planetary perturbations (§ 4.6.1) as well as various nuances in its implementation. We describe our detections (or lack thereof) in § 4.6.2 and our detection efficiencies in § 4.6.3. Our method of correcting for finite source effect is discussed in § 4.7, and we derive our upper limits in § 4.8. We interpret our results in § 4.9, compare our results to other constraints on extrasolar planets in § 4.10, and summaries and conclude in § 4.11. Appendix A lists our excluded anomalous events, Appendix B discusses parallax contamination, and Appendix C discusses the efficiency of high-magnification events to planets near the Einstein ring.

This chapter is quite long, and some of the discussion is technical, and not of interest to all readers. Those who want to simply understand the basic reasons why we conclude there are no planets and understand our resulting upper limits on companions should read § 4.3, and §§4.8-4.11. Those who want only the upper limits and their implications should read §§ 4.10 and 4.11. Those who just want the answer should examine Figures 4.13 and 4.14. A brief summary of these results is given in Albrow et al. (2001b).

4.2. Observations, Data Reduction, and Post-Processing

Details of the observations, detectors, telescopes, and primary data reduction will be presented elsewhere (Albrow et al., 2001d). Here we will simply summarize the essential aspects of the observations and primary data reduction, and only discuss our post-processing in detail.

The photometry of the microlensing events presented and analyzed here was taken over four years starting from June of 1995 and ending in December 1999, with a few scattered baseline points taken in early in 2000. These data were taken with six different telescopes: the CTIO 0.9m, Yale-CTIO 1m, and Dutch 0.91m in Chile, the SAAO 1m in South Africa, the Perth 0.6m near Perth, Australia, and the Canopus 1m in Tasmania. Measurements were taken in the broadband filters V and I using a total of 11 different detectors.

The data were reduced as follows. Images were taken and flat-fielded in the usual way. These images were then photometered with the DoPHOT package (Schechter, Mateo, & Saha, 1993): a high-quality image was chosen for each field, which was then used to find all the objects on the frame. From this "template" image, the geometrical transformations were found for all the other frames. Fixed-position photometry was then performed on all the objects in all the frames. The time-series photometry of all the objects found on the original template image was then archived using specialized software designed specifically for this task. This software enables the determination of relative photometry using arbitrary reference stars. Note that each site and detector adopted a unique template image for each event, this making automatic photometric alignment of light curves from different observatories and detectors difficult or impossible, since all objects in the archive are not common. We will therefore treat each light curve for each site, detector and filter as independent. The number of independent light curves for each event ranges from one to twelve. For the majority of the events, the V-band data were reduced with the I-band template, since, in general, the signal-to-noise is considerably higher in I-band and more objects are detected, thus improving the subsequent photometry.

Once the photometry of all objects in the microlensing target fields were archived, we performed various post-reduction procedures to optimize the data quality. The light curves of the microlensing source stars were extracted using reference stars chosen in a uniform manner. Four to ten reference stars were chosen that were close to the microlensing source star (typically within 30") and exhibited to obvious brightness variations. In practice, the ratio of the mean DoPHOT-reported error in the measurements of each reference star to standard deviation all of the measurements of the star was approximately unity, with no significant systematic trend over the entire set of observations. Generally, the mean DoPHOT-reported error in a single measurement of a reference star was 0.01 mag. Reference stars were selected for each independent light curve, although typically the set of reference stars was similar for all observations of a particular event. The final number of reference stars varies between 5 and 10. Only those points on the microlensing event light curve with DoPHOT types[1] 11 or 13, and data points DoPHOT-reported errors < 0.4 mags were kept. Further data points were rejected based on unreliable reference star photometry as follows. For each reference star, the error-weighted mean was determined. Then, the point that deviated most from the mean was removed. The errors of the remaining points were scaled to force the χ^2 per degree of freedom (d.o.f.) for the reference star light curve to one. The error-weighted mean was then recomputed, and the entire process repeated until no $> 3\ \sigma$ outliers remained. The outliers were reintroduced with error scalings determined from their parent light curves. Then, for each data point in the microlensing light curve, the χ^2 of all the reference stars were summed. If this χ^2 was larger than 4 times the number of reference stars, the data point was discarded. After this procedure, individual light curves were then examined. If the light curves displayed behavior that was grossly inconsistent with other light curves of the same microlensing event, they were discarded. In general, this procedure eliminated light curves for which the microlensing target was too faint to be detected on the template image. In addition, individual light curves with less than 10 points were eliminated. Since at least 3 parameters are needed to fit each light curve (see § 4.4), light curves with fewer than 10 points contain very little information. Finally, a small number ($\lesssim 10$) of individual data points were removed by hand. These data points were clearly highly discrepant with other photometry taken nearly simultaneously, and were invariably taken under extreme seeing and/or background conditions.

---

[1]DoPHOT types rate the quality of the photometry. DoPHOT type 11 indicates a "perfect" star, whereas DoPHOT type 13 indicates a blend of two close stars. From our experience, all other DoPHOT types often provide unreliable or suspect photometry.

4.3. General Considerations

During the 1995-1999 seasons, PLANET relied on alerts from three survey teams, EROS (98-99), MACHO (95-99), and OGLE (95; 98-99). During these five years, many hundreds of events were alerted by all three collaborations. Often, there are too many to follow at one time, and PLANET must decide real-time which alerts to follow, and which to ignore. Since the event parameters are typically not well known and data for the event is sometimes not available from the survey teams, it is impossible to set forth a set of rigid guidelines for the selection of alerts. The entire process is necessarily organic: the decisions are primarily made by one (but not always the same) member of the collaboration, and secondarily by the observers at the telescopes, and are based on such considerations as the predicted maximum magnification and time scale of the event, the brightness and crowding conditions of the source, and the number and quality of other events currently being followed. Clearly this selection procedure impossible to quantify, and therefore our final compilation of events does not represent a well-defined sample. Inclusion of all events may therefore introduce biases. These can be partially alleviated by imposing a posteriori cuts on our events, arriving at a well-defined sample for analysis. However, there remain some selection effects in both the sample of events alerted by the survey teams and the sample of events we choose to follow. For example, as we show in § 4.5, our events have a longer median time scale than the parent population of microlensing events. Although these selection effects could in principle bias our conclusions, in practice the biases are probably quite minor, since the reasons an event was or was not alerted and/or monitored (i.e. crowding conditions and/or brightness of the source, number of concurrent events, maximum magnification) are not related to the presence or absence of a planetary signal in the light curve. The one exception to this is the microlensing time scale. One might imagine that, since our sample is biased against longer time scale events, that we are, in fact, probing higher mass lenses. In fact, as we show in §4.9, it is more likely that we are preferentially selecting slower, not more massive, lenses. Furthermore, this is not necessarily a bias, per se, as long as we take care to specify the population of primary lenses around which we are searching for planets. Thus, provided that our a postiori cuts are also not related to the presence or absence of planetary anomalies in the light curves, this should provide a relatively unbiased sample of events.

In general, microlensing events can roughly be divided into five categories. These are:

(1) Apparently normal PSPL events.

(2) Events that deviate from the PSPL form in a way not associated with binary lensing (i.e. finite source effects, parallax, and binary source events).

(3) Events deviating in a way from the PSPL form in a manner that indicates a nearly equal-mass binary lens.

(4) Events for which the photometry and/or sampling is too poor to draw any definitive conclusions about the nature of the lensing system.

(5) Events deviating in a way from the PSPL form in a manner indicating the presence of a small mass ratio (i.e. planetary) companion to the primary lens.

For the most part, events can be cleanly placed into these categories by eye, without the need of detailed modeling or analysis. Events in the first category are just that: normal events that follow the PSPL form without significant deviations. Events in the second category betray themselves with either gross deviations or secondary indicators. For instance, parallax anomalies are nearly always associated with long (>100 day) event, while finite source effect deviations always occur near the peak of the light curve, and are associated with large sources. Nearly equal mass binary lenses (category 3) are also nearly always immediately recognizable: they are typically associated with caustic crossings and global deviations from the PSPL form. Events in the fourth category are the most plentiful: they consist of events with a very small number of points ($\lesssim 20$) and poor photometry. Finally, events in category 5 are characterized by a short-duration deviation superimposed on an otherwise normal PSPL light curve. Of course, in some cases the issue is more subtle, and the interpretation of the event is not so clear. For example, not all nearly equal-mass binary-lens events exhibit caustic crossings, and some subset could be mistaken for binary-source or even parallax events. In general, however, most other deviations from the PSPL form are easily distinguishable from planetary deviations, with two caveats. First, there is no clear division between "nearly equal mass-ratio" and "small mass ratio" binary lenses: if the mass ratio distribution of binary lenses were, e.g. uniform between $q = 10^{-5}$ and $q = 1$, one would expect grossly deviant light curves, light curves with short-duration deviations, and everything in between. In practice, however, this does not appear to be the case, as we discuss below. Second, there exists a class of binary-source events that can mimic the short-duration deviations caused by planetary companions (Gaudi, 1998). Detections of short-duration anomalies must therefore be scrutinized for this possibility.

All of the 126 Galactic bulge[2] microlensing events for which PLANET has acquired data during the 1995-1999 seasons are listed in Table 4.1. A cursory inspection of these events reveals that $\sim 25\%$ clearly belong in category (1), $\sim 3\%$ clearly belong in category (2), $\sim 8\%$ clearly belong in category (3), and $\sim 40\%$ clearly belong in category (4). The remaining $\sim 25\%$ are marginal events that could be placed in either category (1) or (4). However, no events clearly belong to the last category, i.e. *there are no events that are clearly consistent with a low mass-ratio companion.* We can immediately draw several conclusions from this fact. First, the mass ratio distribution is likely not uniformly distributed between equal mass and small mass ratios: we do not see a continuous

[2]We exclude events toward the Magellanic Clouds and the spiral arms.

distribution in the time scale of deviations with respect to the parent light curve time scale. Second, planetary companions are probably not common. For the remainder of the chapter, we will use strict event criteria and sophisticated methods of analysis to try to justify and quantify these statements. We will carefully search our microlensing light curves for planetary deviations, calculate the efficiency of these light curves to the planetary companions, and consider various secondary effects and possible complications. As we show, however, what may seem to be rather large leaps-of-faith based on a simple cursory examination of the data, are, in fact, quite robust conclusions.

4.4. Event Selection

Our selection criteria are designed to mimic the categorization presented in the previous section (§4.3). The goal of these criteria is to provide a clean sample of events for which we can reliably search for planetary deviations and robustly quantify the efficiency for detection of such companions. Such criteria are also necessary so that future samples of events (and possibly future detections) can be analyzed in a similar manner, and thus combined with the results presented here. Note that any arbitrary rejection criterion is valid, *as long as the criterion is not related the presence or absence of a planet in the light curve.*

We first list our adopted rejection criteria, and then describe the criteria and the procedure to implement them below. There are three criteria:

(1) Non-planetary anomalies (including parallax, finite source, binary sources, and binaries of mass ratio > 0.01) are rejected.

(2) Events for which every individual light curve has less than 20 points are rejected.

(3) Events for which the fractional error in the fitted impact impact parameter is $> 50\%$

are rejected.

The original sample of 126 events along with an indication of which events were cut and why is tabulated in Table 4.1. The first criterion eliminates 17 events, the second 31 events, and the third eliminates 32 events, for a final sample of 43 events.

We are confident that the anomalous events we have rejected in criterion (1) are, in fact, non-planetary in origin, based on our own analyses, analyses in the published literature, and a variety of secondary indicators. Descriptions of each of these events and the reasons why we believe the anomaly to be non-planetary in origin are given in Appendix A.

We will be fitting the microlensing events to the model,

$$F(t_i) = F_{\mathrm{S},j} A(t_i) + F_{\mathrm{B,j}} + \eta_j[\theta(t_i) - \theta_{0,j}] \tag{4.6}$$

where $A(t_i)$ is the magnification at time t_i; $F_{\mathrm{S},j}$ and $F_{rmB,j}$ are the source and blend fluxes for light curve j. The last term is included to account for the correlation of the flux with seeing that we observe in all of our photometry, see Albrow et al. (2000b). Here η_j is the slope of the seeing correlation, $\theta(t_i)$ is the FWHM of the PSF at time t_i, and θ_0 is the error-weighted mean FWHM of all observations in light curve j. For a single lens, the magnification is given by,

$$A_0[u(t)] = \frac{u^2(t)+2}{u(t)\sqrt{u^2(t)+4}}; \qquad u^2(t) = \tau^2 + u_0^2, \tag{4.7}$$

where τ is the "normalized time,"

$$\tau \equiv \frac{t - t_0}{t_{\mathrm{E}}}. \tag{4.8}$$

Here t_0 is the time of maximum magnification, t_{E} is the time scale of the event, and u_0 is the minimum angular separation between the lens and source in units of θ_{E} (the impact parameter). A single lens fit to an observed light curve is thus a function of $3 + 3N_l$ parameters: $t_{\rm E}$, u_0, t_0, and one source flux $F_{{\rm S},j}$, blend flux $F_{{\rm B},j}$, and seeing correlation slope η_j for each of N_l independent light curves. For a binary lens, one must also include the mass ratio of the two components, q, the binary separation d in units of $\theta_{\rm E}$, and the angle of the source trajectory with respect to the binary axis, α, increasing the number of parameters by 3. Thus for a event to contain more information than the number of free parameters, at least one observatory must have at least 9+1=10 data points. Of course, in order for the fit to be well-constrained, considerably more data points than fit parameters are needed. We therefore impose criterion (2): if no independent light curve has at least 20 data points, the event is rejected. The number 20 is somewhat arbitrary, however the exact choice has little effect on our conclusions: there exists a natural break such that the majority of events are well above this criterion, and those few events that are near the cut have little sensitivity to planetary perturbations.

All the events that pass criterion (2) are fit to a PSPL model (Eqns. 4.6 and 4.7). At this stage, we also incorporate MACHO and/or OGLE data into the fit, when available[3]. To fit the PSPL model, we combine a downhill-simplex minimization routine AMOEBA (Press et al., 1992) with linear least-squares fitting. Each trial combination of the parameters $(t_{\rm E}, t_{\rm E}, u0)$ immediately yields a prediction for $A_0(t)$. The flux is then just a linear combination of $F_{{\rm S},j}$, $F_{{\rm B},j}$ and η_j (Eq. 4.6). The best fit parameters $a_i = (F_{{\rm S},1}, F_{{\rm B},1}, \eta_1, F_{{\rm S},2}, F_{{\rm B},2}, \eta_2, ...)$ can then be found by forming,

$$b_{ij} = \sum_k \frac{1}{\sigma_k^2} \frac{\partial F(t_k)}{\partial a_i} \frac{\partial F(t_k)}{\partial a_j}, \qquad c_{ij} = b_{ij}^{-1}, \qquad d_i = \sum_k \frac{F_k}{\sigma_k^2} \frac{\partial F(t_k)}{\partial a_i}, \tag{4.9}$$

where the index k refers to a single observation, the sum is over all observations and F_k

[3]MACHO data is available for those events alerted by MACHO in 1999, along with a few events originally alerted by OGLE. OGLE data is available for events alerted by OGLE in 1998-99, along with a few events alerted by MACHO during these years.

represents the observed flux at time t_k. The parameter combination a_i which minimizes χ^2 is then,

$$a_i = \sum_j c_{ij} d_i. \tag{4.10}$$

Occasionally, the values of $F_{\mathrm{B},j}$ obtained from this procedure are negative. If $F_{\mathrm{B},j}$ is negative by more than its error, we apply a constraint to $c_{i,j}$ to force $F_{\mathrm{B},j} = 0$. Finally, we AMOEBA to find the values of $(t_{\mathrm{E}}, t_{\mathrm{E}}, u_0)$ that minimize χ^2. Note that since neither MACHO nor OGLE report seeing values, we do not correct their data for seeing correlations.

We know from experience (Albrow et al., 1998, 2000b) that the DoPHOT-reported errors are typically underestimated by a factor of ~ 1.5. Naively adopting the DoPHOT-reported errors would thus lead one to underestimate the error on fitted parameters, and overestimate the significance of any detection. However, simply scaling all errors by a factor to force $\chi^2/d.o.f.$ to unity is also not appropriate, as we find that our photometry contains usually significantly more large ($> 3\sigma$) outliers than would be expected from a Gaussian distribution (Albrow et al., 2000b,c). Furthermore, independent light curves from different site and filters typically have different error scalings. Therefore we adopt the following iterative procedure, similar to that used in Albrow et al. (2000b). We first fit the entire dataset to a PSPL model in the manner explained above. We then find the largest $> 3\sigma$ outlier, and reject it. The then renormalize the errors on each individual light curve to force $\chi^2/d.o.f.$ to be equal to unity for that light curves. We then refit the PSPL form, find the largest $> 3\sigma$ outlier, etc. This process is iterated into no other $> 3\sigma$ are found, and the fit converges. The outliers are then reintroduced, with error scalings appropriate to their parent light curves. We typically find 3 to 6 $> 3\sigma$ outliers in the PLANET data and OGLE data, and a larger number for MACHO data (which include significantly more data points). The median error scaling for PLANET data is 1.4, with 90% of our data having scalings between 0.8 and 2.8. The errors reported by

OGLE are typically quite close to correct (error scalings of ~ 1.1), while MACHO errors are typically overestimated (error scalings of ~ 0.8).

Once the best-fit PSPL model is found, we determine the errors on the model parameters by forming $c_{i,j}$ as in equation (4.9), except that now the parameters are $a_i = (t_0, t_{\rm E}, u_0, F_{\rm S,1}, F_{\rm B,1}, \eta_1, F_{\rm S,2}, F_{\rm B,2}, \eta_2, ...)$, i.e. we have included $t_{\rm E}$, t_0, and u_0. The error in parameter a_i is then simply $\delta a_i = \sqrt{c_{i,i}}$. Note that to be conservative, we include the outliers to determine the errors. Of particular interest is the error in the impact parameter. As discussed by Griest & Safizadeh (1998), the sensitivity of a light curve to planetary companions is strongly dependent on u_0 such that events with small u_0 (large maximum magnification) have considerably higher sensitivity to planets than events with larger u_0. Poor knowledge of u_0 therefore translates directly into poor knowledge of the sensitivity of the event to planets (Gaudi & Sackett, 2000). Furthermore, since for blended PSPL fits, u_0 and $t_{\rm E}$ are highly correlated, a large error in u_0 implies a large error in $t_{\rm E}$. For a planetary perturbation, the projected separation d is a function of the observables $(t_{0,\rm p} - t_0)/t_E$, where $t_{0,\rm p}$ is the time of the planetary perturbation, while the mass ratio is $q \sim t_p/t_{\rm E}$ (Gould & Loeb, 1992; Gaudi & Gould, 1997), where t_p is the duration of the perturbation. Therefore a detection of planet in an event with poorly constrained u_0 would be highly ambiguous, as the neither the projected separation d nor the mass ratio q would be well-constrained.

Figure 4.1 shows the fractional error in the impact parameter, $\delta u_0/u_0$ versus u_0 for all events that passed selection criterion (2). Examination of the distribution of fractional error in u_0 for these events reveals a large clump of events with small fractional error; many scattered, smoothly distributed events with larger errors, and a natural break in the distribution of errors at $\delta u_0/u_0 = 50\%$. We therefore adopt $\delta u_0/u_0 = 50\%$ for our final event cut. The exact choice for the cut on $\delta u_0/u_0$ has little effect on our conclusions, as we discuss in § 4.6.3, events with $\delta u_0/u_0 \gtrsim 30\%$ typically have low detection efficiencies. There are four main types of events for which u_0 is poorly-constrained. These are events for which the data only cover one side (usually the falling side) of the event, events for which no baseline information is available, events which are highly blended, and events which have an intrinsically low maximum magnification. Thus by imposing a cut on $\delta u_0/u_0$, we eliminate all low magnification events; the event with largest impact parameter in our final sample has $u_0 = 0.61$. Note that the majority of events which fail the cut on $\delta u_0/u_0$ fall into the first two classes; emphasizing the need for coverage of the peak and baseline information. In particular, without MACHO and OGLE data, many more events would not have passed this last cut, and our final sample of event would have been considerably smaller.

After imposing cuts 1 (non-planetary anomalies), 2 (data quantity), and 3 (error in impact parameter), we are left with a sample of 43 events. The light curves for these events are shown in Figure 4.2. In order to be able to show all independent light curves (which in general have different $F_{\rm S}$, $F_{\rm B}$, and seeing correlation corrections), we plot the magnification, which is obtain by solving equation (4.6) for $A_0(t)$. Rather than show the magnification as a function of true time, we show the magnification as a function of time normalized time τ. When plotted this way, perturbations arising from a given q would have the same duration on all plots. Thus the sensitivity of different light curves to companions can be compared directly. In the next section, we describe the properties of these events, paying particular attention to those properties relevant to the detection of planetary anomalies.

4.5. Event Characteristics

The parameters t_0, $t_{\rm E}$, and u_0 and respective 1σ errors for the final event sample is tabulated in Table 4.2, along with the fractional error in u_0. The impact parameter is important in that the sensitivity of an event to planetary companions depends strongly on u_0 (Gaudi & Sackett, 2000) and thus the exact distribution of u_0 determines are overall sensitivity. The time scale is important in that the population of lenses we are probing is determined from the distribution of $t_{\rm E}$. Also, in § 4.7, we will use $t_{\rm E}$ to estimate the effect of finite sources on planetary detection efficiencies and therefore the effect on our final conclusions. For the current analysis, the parameter t_0 is of no interest.

In Figure 4.3, we plot u_0 against $t_{\rm E}$ for our event sample, revealing no obvious correlation between u_0 and $t_{\rm E}$. This lack of correlation between $t_{\rm E}$ and u_0 implies that the lenses that give rise to the events with the most sensitivity to planets comprise a sample that is unbiased with respect to the entire sample of lenses. Given this, we can then inspect the distributions of u_0 and $t_{\rm E}$ independently.

In Figure 4.3 we show the differential and cumulative distributions $t_{\rm E}$. The median time scale of our events is ~ 40 days, about a factor of two higher than the median time scale for events found by the MACHO and OGLE teams toward the Galactic bulge (Alcock et al., 1997; Udalski et al., 2000). This is likely a selection effect caused by the fact that longer time scale events are more likely to be alerted before peak magnification, and thus are more likely to be chosen by us as targets for follow-up photometry. This is compounded by the fact that we are less likely to get good coverage of the peak of short time scale events, even if they are alerted pre-peak. Events with poor or absent peak coverage will therefore fail our selection criterion of $< 50\%$ fractional error in u_0. As we discuss in § 4.9, this selection effect mainly results in a bias toward slower lenses.

We also show in Figure 4.3 the differential and cumulative distributions of u_0. The median u_0 is ~ 0.2, and the fraction of high-magnification ($A_{\rm max} > 10$) events is $\sim 30\%$. As it is a purely random quantity, the intrinsic distribution of u_0 is uniform. The observed distribution of u_0, however, is clearly not uniform. This is due to a combination of various selection effects. First, faint events are more likely to be detected (and hence alerted) by the survey teams if they have a larger maximum magnification (Alcock et al., 1997; Udalski et al., 2000). Since there are more fainter stars than brighter stars, this results in a bias toward smaller impact parameters with respect to a uniform distribution. Second, since events with smaller impact parameters are also more sensitive to planets, we preferentially follow and sample high-magnification events. This bias does not affect our conclusions, since the value u_0 is unrelated to the presence or absence of a planetary companion. However, as emphasized by Gaudi & Sackett (2000), it does imply that in order to accurately determine the overall sensitivity of an ensemble of light curves to planetary companions, the actual distribution of observed u_0 must be used.

Since one of the primary goals of PLANET it to obtain very dense sampling of microlensing events, it is interesting examine how well this goal has been achieved. In Figure 4.4, we show the distribution of sampling intervals (the time between successive exposures of a given event). Three peaks are revealed. The first is at ~ 6 minutes, which is our typical exposure time of 5 minutes plus 1 minute of overhead time; this peak is dominated by events that are followed continuously and also pairs of V-I data points. The second is at ~ 1.5 hours, our fiducial sampling interval. The final peak is at 1 day, and arises primarily from samplings of the wings and baselines of light curves. The median sampling interval is ~ 1.5 hours, with 90% of all data points being taken within 1 minute and 1 day of one another. What is of particular relevance to the detection of planets is the sampling interval in units of $t_{\rm E}$; this is also shown in Figure 4.4. Assuming that at least 10 data points are needed on a planetary perturbation for detection, then the sampling interval needed to detect a companion of mass ratio q is approximately,

$$\Delta t = 3 \times 10^{-3} t_{\rm E} \sqrt{\frac{q}{10^{-3}}}. \tag{4.11}$$

Using this formula and comparing to Figure 4.4, we find that (80%, 65%, 45%, 25%) of our data has sufficient sampling to detect companions of mass ratio $(10^{-2}, 10^{-3}, 10^{-4}, 10^{-5})$. Thus we expect the majority of our data to have some sufficient sampling to detect companions with mass ratios $\gtrsim 10^{-4}$.

The sensitivity of a given light curve to planetary companions is primarily determined by three factors: the photometric error, the temporal sampling, and the impact parameter. In Figure 4.5, we plot the median photometric error, $\sigma_{\rm med}$, versus the median sampling interval, $\Delta t_{\rm med}$ for all events, indicating which are high-magnification ($A_{\rm max} > 10$) events. These are also tabulated in Table 4.3. High magnification events that occupy the lower left quadrant of this figure will have the highest sensitivity to planetary companions. Of the 13 high-magnification events, all have sufficiently small median sampling intervals to detect $q = 10^{-2}$ companions, we therefore expect our sensitivity to such to companions to be quite high. Two high-magnification events have sufficient sampling rates to detect companions with $q = 10^{-5}$; however, for companions as small as this, excellent photometry ($\lesssim 2\%$) is required along with excellent sampling to have significant efficiency for detection (Bennett & Rhie, 1996). No events satisfy both of these requirements ($\sigma_{\rm med} < 2\%$ and $\Delta t_{\rm med} < 10^{-3.5}$). We therefore choose to restrict our attention to $q \geq 10^{-4}$.

It is clear from considering of the number of high-magnification events, and the sampling rate and photometric accuracy of the events that our sample should be quite sensitive to planetary companions, especially those with $q \gtrsim 10^{-3}$. This fact, combined with the fact that no planetary-like perturbations are clearly evident in the light curves, is an indication that planetary companions are probably not common. In the following sections, we strengthen and quantify this statement.

4.6. Search for Detections and Detection Efficiencies

Although a cursory inspection of Figure 4.2 reveals no obvious candidate planetary perturbations, such perturbations could be quite subtle, and thus missed by eye. Furthermore, the significance of the lack of planetary perturbations must be quantified. Specifically, the sensitivity of the light curves to the presence of putative planetary companions, i.e. the detection efficiency, must be determined. Here we use the method of simultaneously searching for planetary signatures in and determining the detection efficiency of individual events suggested by Gaudi & Sackett (2000), and applied to microlensing event OGLE-1998-BUL-14 by Albrow et al. (2000b). We will briefly review the algorithm here, but point the reader to these two papers for a more thorough discussion of the basis of the method and its application.

4.6.1. Algorithm

Of the $6 + 3 \times N_l$ parameters (see § 4.4) in a point source binary microlensing fit, $3 + 3 \times N_l$ have analogs in the PSPL fit: $t_{\rm E}$, u_0, t_0 and one $F_{\rm S}$, $F_{\rm B}$, and η for each of N_l independent light curves. The parameters $t_{\rm E}$, u_0 and t_0 have different meanings in the binary-lens model than in the PSPL model, and depend on the choice of the origin of the binary-lens and the reference mass. For small mass-ratio binaries, however, if one chooses the origin to be the location of the primary lens, and normalize to the mass of the primary, then the values of these parameters will be quite similar in a binary-lens and single-lens fit to a light curve. The 3 parameters not explicit in the PSPL fit are the mass ratio q, the projected separation d, and the angle of the source relative to the binary-lens axis α. While q and d are interesting in that they are related to the physical nature of the planet-star system, the angle α a nuisance parameter that it of no physical interest. It is a random geometric parameter and therefore uniformly distributed. However, the value of α does has a significant effect on the amplitude and duration of the planetary perturbation. Thus, some values of α lead to detectable perturbations to the PSPL model, while others do not. Marginalization over α for a given binary lens specified by (q, d) therefore determines the geometric detection efficiency $\epsilon_i(d, q)$ for event i and such a planetary system. Repeating this process for all (q, d) pairs of interest yields the efficiency for all systems. This is the basis of the method of determining the detection efficiency for individual events suggested by Gaudi & Sackett (2000).

Operationally, the procedure to systematically search for planetary signatures and determine ϵ_i for each event is as follows:

(1) Fit event i to the PSPL model, obtaining $\chi^2_{\rm PSPL}$ (§ 4.4).

(2) Holding d and q fixed, the binary-lens model that best fits light curve i is found for some source trajectory α, leaving the $3 + 3 \times N_l$ parameters $(t_{\rm E}, u_0, t_0, N_l \times F_{\rm S}, N_l \times F_{\rm B}, N_l \times \eta)$ as free parameters. This yields $\chi^2(d,q,\alpha)$.

(3) Repeat item (2) for all source trajectories $0 \leq \alpha < 2\pi$.

(4) Evaluate the difference in χ^2 between the binary and PSPL fits: $\Delta\chi^2(d,q,\alpha) = \chi^2(d,q,\alpha) - \chi^2_{\rm PSPL}$. Compare this to some threshold value $\Delta\chi^2_{\rm thresh}$:

  (a) If $\Delta\chi^2(d,q,\alpha) < -\Delta\chi^2_{\rm thresh}$, then we tentatively conclude we have a detected a planet with parameters d, q, α.

  (b) If $\Delta\chi^2(d,q,\alpha) > \Delta\chi^2_{\rm thresh}$ then the geometry (d,q,α) is excluded.

(5) The detection efficiency $\epsilon_i(d,q)$ of event i for the assumed separation and mass ratio is then,

$$\epsilon(d,q) \equiv \frac{1}{2\pi}\int_0^{2\pi} {\rm d}\alpha \; \Theta[\Delta\chi^2(d,q,\alpha) - \Delta\chi^2_{\rm thresh}], \tag{4.12}$$

where $\Theta[x]$ is a step function

(6) Steps (2)-(5) are repeated for a grid of (d,q) values. This gives the detection efficiency $\epsilon(d,q)$ for event i as a function of d and q, and also all binary-lens parameters (d,q,α) that give rise to significantly better fits to the event than the PSPL model.

(7) Steps (1)-(6) are repeated for all 43 events.

For item (2), we find the parameters $(t_{\rm E}, u_0, t_0, N_l \times F_{\rm S}, N_l \times F_{\rm B}, N_l \times \eta)$ that minimize χ^2 in the same way as the PSPL fit: we choose trial values of $(t_{\rm E}, u_0, t_0)$ which (along with the values of d, q, α) immediately yields the binary-lens magnification[4] as a function of time, $A_{\rm B}(t)$. This is then used to find the least-squares solution for the other parameters, and the resultant χ^2. The downhill-simplex routine is the used find the combination of parameters $(t_{\rm E}, u_0, t_0)$ which minimize χ^2. See § 4.4. The procedure is slightly more complicated for those events for MACHO and/or OGLE data was used for the PSPL fit, as we discuss below.

Although this procedure is conceptually simple and appears straightforward, there are some subtle details that must be addressed before implementation. Specifically, these are the photometric errors adopted for the events, the inclusion of MACHO/OGLE photometry, the grid size and spacing for the binary-lens parameters b, q, and α, the method by which the binary-lens magnification is evaluated, and the choice of the detection threshold $\Delta\chi^2_{\rm thresh}$.

Choice of Dataset

As we discussed in § 4.4, the errors reported by DoPHOT are typically underestimated by a factor of ~ 1.5; adopting such errors would both overestimate the significance of any planetary detections, and overestimate the detection efficiency. Furthermore, since events can have error scaling factors that differ by a factor of three, even the relative significances for different events would not be secure. Ideally, one would like to determine the magnitude of the photometric errors without reference to any

[4]For an explanation of how to calculate the binary-lens magnification, see Witt (1990).

model. Unfortunately, this is in general not possible, since the error depends strongly on the local crowding conditions of the microlensing source object. Therefore, in order to put all events on the same footing and try to arrive at the best possible estimate of the significance of planetary detections and detection efficiencies, we will adopt the error scaling factors as determined in the PSPL fit (see § 4.4) for the light curves input into the algorithm. We typically find that, after scaling the errors in this way, the error distributions are nearly Gaussian, with the exception of a handful of large $> 3\sigma$ outliers (Albrow et al., 2000c).

If the PSPL model is truly the "correct" model, this procedure is perfectly valid, and does not bias the results in any way. However, if the light curve actually deviates from the PSPL model, this procedure will overestimate the error scaling factors, and thus *underestimate* the significance of the anomaly. Assuming that binary-lens model is correct, then it is straightforward to show that the true difference in χ^2, which we will label $\Delta\chi^2_0$, is related to the $\Delta\chi^2$ evaluated assuming the PSPL fit is correct by,

$$\Delta\chi^2_0 = \Delta\chi^2 \left(1 + \frac{\Delta\chi^2}{d.o.f.}\right)^{-1}, \tag{4.13}$$

where $d.o.f.$ is the number of degrees-of-freedom of the event. Thus for an event with ~ 300 data points and $\Delta\chi^2_0 = 60$, using the errors determined from the PSPL fit would lead us to underestimate the "true" $\Delta\chi^2$ by 20%. For events with a small number of $d.o.f.$, this underestimate can formally be as large as 100%. This would seem to argue that the values of χ^2 computed in all fits (PSPL and binary) should be renormalized by the best-fit model (PSPL or binary). However, there are several reasons we feel this not appropriate. First, for any fit, χ^2 is typically *not* dominated by the number of $d.o.f.$: there typically exists a handful of large outliers that contribute a significant fraction of the evaluated χ^2. Thus, in reality $d.o.f.$ should be replaced by $\chi^2_{\rm binary}$ in equation (4.13), which is typically larger by ~ 100, thus reducing the overestimate considerably. Furthermore, renormalizing χ^2 in this way would give extra weight to binary-lens models that "succeed" by fitting isolated many σ outliers, and preferentially so for events with a small number of data points, where χ^2 is dominated by such outliers. The smaller the number of data points, the more difficult it is to objectively judge the reality of such fits, despite the fact that common sense dictates that planets can not be "detected" based on isolated outliers. We will therefore adopt the conservative choice of using the errors determined with reference to the PSPL model.

Including MACHO/OGLE Data

As we discussed in § 4.4, for some events, we include MACHO and/or OGLE data in order to better constrain u_0. This is necessary in order to robustly determine ϵ_i for some events for which our data are poorly sampled near the peak or do not have baseline information. However, as we do not have access to the raw data, nor do we know the details of the data reduction procedures, we have no way of independently judging the quality of the MACHO or OGLE photometry. Furthermore, we do we have access to the seeing values for these data, and hence cannot correct for the seeing correlations that can often mimic low-amplitude planetary deviations. Thus any planetary "signal" discovered using this photometry would be difficult to to interpret, and the reality of this signal would be impossible to determine. Therefore, while we would like to use these data to constrain the global parameters $t_{\rm E}$, t_0 and u_0, we do not want to use these data in either the search for planetary signatures or the calculation of the efficiency. We accomplish these somewhat contradictory goals in the following manner.

All the information on the parameters $t_{\rm E}$, t_0, u_0 and their covariances with the other parameters is contained within the covariance matrix c_{ij} and the vector d_{ij} as determined from the PSPL fit with all parameters (see § 4.4 and Eq. 4.9). Therefore, we simply need to extract the information provided by the MACHO/OGLE data and apply it to the binary-lens fit with only PLANET data. First we calculate the covariance matrix c_{ij} of the best-fit parameters $a_i = (t_0, t_{\rm E}, u_0, F_{\rm S,1}, F_{\rm B,1}, \eta_1, F_{\rm S,2}, F_{\rm B,2}, \eta_2, ...)$ as determined by the PSPL fit to all (MACHO+OGLE+PLANET) data. Note that this is identical to the procedure used in § 4.4 to calculate the errors of a_i. We then restrict c_{ij} and a_i to the parameters $F_{{\rm S},l}, F_{{\rm B},l}, \eta_l$ for PLANET data. We call these restricted quantities $c_{ij}^{\rm MOP}$ and $a_i^{\rm MOP}$. Next we calculate the covariance matrix $c_{ij}^{\rm P}$ of the best-fit parameters $a_i^{\rm P}$ determined from the PSPL fit to only PLANET data, again restricting these quantities to the parameters $F_{{\rm S},l}, F_{{\rm B},l}, \eta_l$. Finally, we form the matrix and vector,

$$b_{ij}^{\rm MOP} = \left(c_{ij}^{\rm MOP}\right)^{-1} \qquad d_i^{\rm MOP} = \sum_j b_{ij}^{\rm MOP} a_i^{\rm MOP}, \tag{4.14}$$

and similarly for $b_{ij}^{\rm P}$ and $d_i^{\rm P}$. Finally, we calculate,

$$b_{ij}^{\rm MO} = b_{ij}^{\rm MOP} - b_{ij}^{\rm P} \qquad d_i^{\rm MO} = d_i^{\rm MOP} - d_i^{\rm P}. \tag{4.15}$$

The resultant matrix $b_{ij}^{\rm MO}$ and vector $d_i^{\rm MO}$ contain only the information on $t_{\rm E}, t_{\rm E}, u_0$ and the parameters $F_{{\rm S},l}, F_{{\rm B},l}, \eta_l$ for PLANET data provided by the MACHO/OGLE data. We then use these two quantities to constrain the binary-lens fits using only PLANET data in the following manner. For each trial $t_{\rm E}, t_0, u_0$, we compute $b_{i,j}$ and d_i for the quantities $F_{{\rm S},l}, F_{{\rm B},l}, \eta_l$ using only PLANET data. We add to these the constraints from MACHO/OGLE, i.e. we form,

$$b_{ij}^{\rm const} = b_{ij} + b_{ij}^{\rm MO} \qquad d_i^{\rm const} = d_i + d_i^{\rm MO}. \tag{4.16}$$

These are then used to find the best-fit parameters $a_i = (F_{\rm S,1}, F_{\rm B,1}, \eta_1, F_{\rm S,2}, F_{\rm B,2}, \eta_2, ...)$ via equation (4.10). The χ_0^2 of the resultant fit is then evaluated. We add to this χ^2 a contribution,

$$\chi^2_{\rm MO} = \sum_{ij} \delta a_i b_{ij}^{\rm MO} \delta a_j \tag{4.17}$$

where $c_{ij}^{\rm MO} = (b_{ij}^{\rm MO})^{-1}$ and

$$\delta a_i = a_i - a_i^{\rm MO}, \qquad a_i^{\rm MO} = \sum_j c_{ij}^{\rm MO} d_i^{\rm MO}. \tag{4.18}$$

This contribution to χ^2 is a penalty for violating the constraints from MACHO/OGLE data. The remainder of the fitting procedure is as before: this χ^2 is then used by the downhill-simplex routine AMOEBA to find the parameters t_0, u_0 and $t_{\rm E}$ that minimize χ^2 for the particular d, q, α binary-lens geometry.

Grid of Binary-Lens Parameters

There are several factors that dictate our choice of grid size and spacing in the b, q, α parameter space. First, the grid spacing must be dense enough that any possible planetary signals are not missed, and dense enough that our error in ϵ_i is not dominated by sampling errors. Second, the grid must cover the full range of parameter space where we significant sensitivity. Finally, the computation must be able to be performed in a reasonable amount of time.

We restrict our attention to $10^{-2} \le q \le 10^{-4}$. The upper end of this range is dictated by the fact that we are primarily interested in planetary companions, and also because our procedure for finding binary-lens fits fails for events which are grossly deviant from the PSPL form. In fact, finding all satisfactory fits to such binary-lens light curves is quite difficult (see Mao & Di Stefano 1995; Di Stefano & Perna 1998; Albrow et al. 1999c). Furthermore, while it is clear that none of our light curves display clear evidence for binaries with $q \lesssim 10^{-2}$, this is not true for $q \gtrsim 10^{-2}$ (see § 4.3). We have clearly detected binaries in this range. Incorporating such binaries into the analysis would entail finding *all* possible fits to these observed binaries *and* calculating the efficiency of all other events. Although such a study is interesting in its own right, it is quite an undertaking, and beyond the scope of this thesis. The lower end of the range of mass ratios we test is dictated by the fact that we are unlikely to have significant sensitivity below $q = 10^{-4}$ (§ 4.5). Since, for small q, the effect of the planet decreases as $q^{1/2}$, we choose to sample q at equally spaced logarithmic intervals of 0.25.

Based on numerous studies (Gould & Loeb, 1992; Di Stefano & Mao, 1996; Bennett & Rhie, 1996; Gaudi & Gould, 1997; Griest & Safizadeh, 1998; Rhie et al., 1999b; Albrow et al., 2000b) it is known that the planetary detection probability is largest in the "Lensing Zone," $0.6 \leq d \leq 1.6$, and is negligible for $d \lesssim 0.1$ and $d \gtrsim 10$. Furthermore, for $q \ll 1$, planetary perturbations betray a $d \rightarrow d^{-1}$ symmetry (Griest & Safizadeh, 1998; Dominik, 1999b). Therefore, we sample d at $0.1, 0.2, ..., 0.9, 1.0$, and also the inverse of these values, for a full range of $0.1 \leq d \leq 10$.

Finally, in order to avoid missing any possible planetary signals, we choose a variable step size for α that depends on q. The size of the region of significant perturbation is $\sim q^{1/2}$, and thus the perturbation caused by a planet at $d = 1$ would cover an opening angle with respect to the center of the primary lens of $\sim q^{1/2}$. Therefore in order to sample the perturbed region at least twice, we choose a step size of,

$$\Delta\alpha = \frac{\sqrt{q}}{2}. \tag{4.19}$$

For a total of $4\pi q^{-1/2} \sim 400(q/10^{-3})^{-1/2}$ integrations per d, q pair.

Magnification Maps

With the grid size and spacing described in 4.6.1, we perform a total of 8.8×10^4 binary-lens fits to each event, for a grand total for all 43 events of 3.9×10^6 fits. Each fit requires at least 50 evaluations of the binary-lens magnification light curve to converge, for a total of more than 100 million binary-lens light curve evaluations. Clearly, given this large number of evaluations, and the fact that many of the calculations are redundant, re-evaluating the magnification for each data point of each event is both prohibitive and inefficient. We therefore choose to first create magnification maps for each of the d, q grid points, and interpolate between these maps to evaluate the binary-lens magnification. We create maps that cover source positions $-2 \leq x \leq 2$ and $-2 \leq y \leq 2$. For source positions outside this range, we use the PSPL magnification. Note that this means that we are implicitly assuming that we are not sensitive to the planetary caustics of companions with separations $d \lesssim 0.4$ and $d \gtrsim 2.4$ (although we are still sensitive to such planets via the central caustic). This is not a severe problem, however, since very few of our light curves have data beyond $2t_{\rm E}$ (see Figure 4.2), excepting baseline points. We sample the source position at intervals of $2 \times 10^{-3}\theta_{\rm E}$, which is typically smaller than or of order the sampling interval of our events (§ 4.5). We have performed numerous tests comparing fits using these maps and fits using the exact binary-lens magnification, and find that using the maps introduces an error of $\Delta\chi^2 \lesssim 2$, which is far below any of our thresholds $\Delta\chi^2_{\rm thresh}$. Typically, efficiencies determined using these maps are in error by $\lesssim 1\%$. We have also inserted planetary deviations into selected light curves, and confirm that these "detections" are recovered when the maps are used to evaluate the magnification.

Choice of Detection Threshold

Ideally, one would like to choose the detection threshold $\Delta\chi^2_{\rm thresh}$ a priori, without reference to the results of the binary-lens fits. Specifically, one would like to be able to determine the probability $P(\Delta\chi^2)$ of obtaining a given $\Delta\chi^2$ by chance, and then choose a probability threshold for detection, say $P = 0.01$. Naively, one might expect that the probably of getting a certain value of $\Delta\chi^2$ is simply given by the probability of getting

$\Delta\chi^2$ with three extra parameters from Gaussian statistics,

$$P(\Delta\chi^2) = (2\pi)^{-1/2} \int_{\Delta\chi^2}^{\infty} \mathrm{d}x x^{1/2} \mathrm{e}^{-x/2}. \quad (4.20)$$

However, this formula fails for several reasons. First, most events contain large outliers that are not described by Gaussian statistics. Second, and more importantly, such a naive calculation fails to take into account the fact that many independent trial binary-lens fits to the datasets are being performed, thereby effectively increasing the difference in the number of degrees-of-freedom between the binary and single lens models. In other words, while the success of a single binary lens model is given by equation (4.20) in the limit of Gaussian errors, the success of *any* binary-lens model is not. Unfortunately, the effect of this increase in the effective number of degrees-of-freedom on the probability cannot be accessed analytically, and must be determined via a Monte Carlo simulation. This would entail generating many different realizations of synthetic events with sampling and errors drawn from the sampling and error distributions of each of the 43 events in our sample. The algorithm in § 4.6.1 would then need to be performed on each of these synthetic events, in order to determine the mapping $P(\Delta\chi^2)$ for each event. Given that each event requires 8.8×10^4 binary-lens fits, this is clearly impossible. We will therefore use the distribution of $\Delta\chi^2$ from the actual events to choose $\Delta\chi^2_{\rm thresh}$, as described in the next section.

4.6.2. "Detections"

We have performed the algorithm presented in § 4.6.1 for all 43 events in our final sample. For each event, we find the absolute minimum $\Delta\chi^2_{\rm min}$ from this procedure. The distribution of these $\Delta\chi^2_{\rm min}$ is shown in Figure 4.6. If all the events harbored planets, we would expect a roughly uniform distribution in $\Delta\chi^2$. If some fraction of events harbored planets, then we would expect a large "clump" of small $\Delta\chi^2_{\rm min}$ obtained from single events through statistical fluctuations, and then a few scattered instances of large $\Delta\chi^2_{\rm min}$ from those events with companions. In fact, this is roughly what is seen; most of the events have $\Delta\chi^2_{\rm min} \gtrsim 60$, with only two events, MACHO 99-BLG-18 and OGLE-1999-BUL-36, having $\Delta\chi^2_{\rm min} \leq 60$. We therefore choose $\Delta\chi^2_{\rm thresh} = 60$, and thus interpret the binary-lens fits with $\Delta\chi^2_{\rm min} > 60$ to be arising from statistical fluctuations or unrecognized low-level systematics, and do not interpret these as detections.

Based on this choice of $\Delta\chi^2_{\rm thresh} = 60$, we tentatively conclude that we have detected planetary deviations in events MACHO 99-BLG-18 and OGLE-1999-BUL-36. We have examined each of these events individually, and find that there are other, more likely, explanations for their anomalous behavior.

The light curve for OGLE-1999-BUL-36 shows an overall asymmetry will respect to the time of maximum magnification. This asymmetry is well fit by the distortion to the overall light curve created by planetary companion to the primary lens with $q = 0.003$. However, such a distortion requires a special geometry, specifically it requires $\alpha \sim 0$ or $180°$, i.e. a source trajectory nearly parallel to the planet-star axis. All other values of α produce either no asymmetry or a planetary "bump." However, such asymmetries are a generic feature of low-amplitude parallax effects Gould, Miralda-Escudé, & Bahcall (1994); indeed OGLE-1999-BUL-36 is equally well-fit by such a model. Since both models fit the data equally well, we conclude that we cannot reliably distinguish between them, although we favor the parallax interpretation based on the fact that the planetary fit requires a special geometry. We therefore choose to explicitly ignore this "detection" with the justification that we simply cannot robustly detect a planet from an asymmetry. This in turn implies that all planetary perturbations consistent with an overall asymmetry should be ignored in the analysis of all events. Although we have not done this, we have performed simulations which demonstrate that by not doing so, we overestimate our efficiencies by only a few percent, which is small compared to our statistical uncertainties. The parallax and planetary fits to OGLE-1999-BUL-36, as well as a detailed account of these simulations are presented in Appendix 4.11.

The light curve of MACHO 99-BLG-18 displays a slight negative deviation with respect to the PSPL model near the peak with an amplitude of $\sim 2\%$ and duration of ~ 2 days. This deviation is reasonably well-fit by a companion with $q \sim 0.01$. When the event was alerted, MACHO reported deviations from the PSPL form near the beginning of the event, and suggested that these may be due to a binary source star. This prompted us to analyze the baseline MACHO data from the previous 5 years (when the source was not magnified). This analysis revealed that the source is an irregular variable that often produces "bumps" and "dips" characteristic of those seen in our data. This is not surprising, as this event has a baseline magnitude of $I_0 \simeq 13.4$; it is common for such bright stars to be variable at the few percent level. We therefore eliminate this event from further analysis.

Thus, out of an original sample of 43 events, we are left with 42 events (rejecting MACHO 99-BLG-18), and no viable planet candidates. Given this lack of detections, we can use the individual event detection efficiencies ϵ_i to determine a statistical upper limit to the fraction of lenses with a companion in the range of d, q parameter space we explore.

4.6.3. Detection Efficiencies

The detection efficiency $\epsilon_i(d,q)$ is the probability that a companions with mass ratio q and projected separation d would produce a detectable deviation (in the sense of $\Delta\chi^2 > \Delta\chi^2_{\rm thresh}$) in the observed light curve of event i. If no detections are made, then a planetary companion to the primary lens in event i can be ruled out with confidence $\epsilon_i(d,q)$. Figure 4.7 shows the $\epsilon(d,q)$ for our fiducial threshold $\Delta\chi^2_{\rm thresh} = 60$ and all our events in the parameter range we searched for companions, $0.1 \leq d \leq 10$ and

$10^{-4} \leq q \leq 10^{-2}$.

We have plotted ϵ as a function of $\log d$, which clearly reveals the $d \to d^{-1}$ symmetry inherent in planetary perturbations (Griest & Safizadeh, 1998; Dominik, 1999b). For low magnification events ($u_0 \geq 0.1$), the efficiency exhibits a "two-pronged" structure as a function of d, such that the efficiency has two distinct maxima, one at $d_{\epsilon,\max} < 1$ and one at $d_{\epsilon,\max}^{-1}$, and then a minima at $d = 1$. The approximate locations of these maxima occur can be found by determining the separations at which the perturbation due to the planetary caustic occurs at the peak of the light curve,

$$d_{\epsilon,\max}^{\pm 1} = \frac{1}{2}u_0 \mp \frac{1}{2}\sqrt{u_0^2 + 4}. \qquad (4.21)$$

For planetary separations $d_{\epsilon,\max} \leq d \leq d_{\epsilon,\max}^{-1}$, the caustics produced by the companion are with a radius u_0 of the primary lens, and are thus not probed by the event. For high magnification events, ϵ is maximized near $d = 1$. This is not only a consequence of equation (4.21), but also because the central caustic is being probed by the event. However, note that for the very highest magnification events, i.e. MACHO 98-BLG-35, OGLE-1999-BUL-05, and OGLE-1999-BUL-35, there is a narrow minimum exactly at $d = 1$. This reason for this result, which is somewhat contrary to current wisdom, is discussed in Appendix C. As expected, the detection efficiency to companions with $d \lesssim 0.2$ and $d \gtrsim 5$ and all q is negligible for nearly all events.

Of the 43 events, about 13 have very little detection efficiency: $\epsilon(d, q)$ is larger than 5% for only the most massive companions, and never gets larger that 25%. About 8 have excellent sensitivity to companions; for these events $\epsilon(d, q) > 95\%$ for some regions in the (d, q) plane. Notably, these are all high-magnification events, as predicted by Griest & Safizadeh (1998). For these events, companions to the primary lenses with parameters in regions with $\epsilon(d, q) > 95\%$ can be ruled out directly at 95% confidence. For some events, MACHO 98-BLG-35 and ob9935 in particular, this region is quite large in extent. Our resultant upper limits on small mass ratio $q \lesssim 10^{-3}$ companions (§ 4.8) are dominated by these 8 events. For the remainder of the events, the efficiency is substantial ($\gtrsim 25\%$) for some region of parameter space, although companions cannot be directly ruled out on an individual basis. These events contribute significantly to the upper limits for mass ratios $q \gtrsim 10^{-3}$.

In Figure 4.8, we show the efficiency averaged over the lensing zone (where the detection efficiency is the highest),

$$\epsilon_{\mathrm{LZ},i}(q) \equiv \int_{0.6}^{1.6} \epsilon_i(d, q)\ \mathrm{d}d\ , \tag{4.22}$$

as a function of the logarithm of the mass ratio. For a model in which companions have projected separations d uniformly distributed in the lensing zone, $\epsilon_{\mathrm{LZ},i}(q)$ is the probability that a planet of mass ratio q would have been detected in light curve i. Also shown is $\epsilon_{\mathrm{LZ},i}$ for a detection threshold of $\Delta\chi^2_{\mathrm{thresh}} = 100$. For this more conservative threshold, the efficiencies are $5 - 40\%$ lower, with the difference being smaller when the efficiency is larger.

4.7. Finite Source Effects

The results in §§ 4.6.2 and 4.6.3 were derived under the implicit assumption that the source stars of the microlensing events could be treated as point-like. In reality, of course, every star has a finite extent, and numerous authors have discussed the effect of the finite size of the source on the deviation from the PSPL curve caused by planetary companions (Bennett & Rhie, 1996; Gaudi & Gould, 1997; Griest & Safizadeh, 1998; Gaudi & Sackett, 2000). Finite sources smooth out the discontinuous jumps in magnification that occur when the source crosses a caustic curve, and in general lower the amplitude but increase the duration of planetary perturbation. Finite sources also increase the area of influence of the planet in the Einstein ring. Thus finite sources have a competing influence on the detection efficiency: previously significant deviations can be suppressed below the detection threshold, while trajectories for which the limb of the source grazes a high-magnification area can give rise to detectable perturbations when none would have occurred for a point-source. Which effect dominates depends on many factors, including the size of the source relative to the regions of significant deviation from the single-lens form, the photometric accuracy, and the sampling rate. For large sources and small mass ratios, finite source effects can significantly alter the detection efficiency (Gaudi & Sackett, 2000). Hence the results presented in §§ 4.6.2 and 4.6.3 could, in principle, be seriously compromised by ignoring these effects. We therefore evaluate the magnitude of the finite source effect explicitly.

The parameter relevant to the evaluation of the magnitude of the finite source effect is the size of the source in units of $\theta_{\rm E}$,

$$\rho_* = \frac{\theta_*}{\theta_{\rm E}} = \frac{\theta_*}{\mu_{\rm rel} t_{\rm E}}, \simeq 0.02 \left(\frac{\theta_*}{6\ \mu{\rm as}}\right) \left(\frac{\mu_{\rm rel}}{12.5\ {\rm km\,s^{-1}kpc^{-1}}}\right)^{-1} \left(\frac{t_{\rm E}}{40\ {\rm days}}\right)^{-1}, \tag{4.23}$$

where $\theta_* = 6\ \mu$as for a clump giant at 8 kpc. For deviations arising from the planetary caustic, finite source effects become important when θ_* is of order or smaller the planetary Einstein ring radius, $\theta_{\rm p}$, i.e, when

$$\rho_* \gtrsim \sqrt{q} \qquad \text{(Planetary Caustics).} \tag{4.24}$$

The size of the central caustic is $u_{\rm c} \sim qd(d-1)^{-2}$ (Griest & Safizadeh, 1998), thus finite sources affect the magnification due to the central caustic when $\rho_* \gtrsim qd(d-1)^{-2}$. However, in order for the central caustic to be probed at all, the event must have an impact parameter $u_0 \lesssim u_{\rm c}$. Thus we have the requirement that,

$$\rho_* \gtrsim u_0 \qquad \text{(Central Caustic),} \tag{4.25}$$

for finite sources to affect deviations arising from the central caustic.

The difficultly in accessing the affect of finite sources on the detection efficiency lies not in evaluating the affect for a given ρ_*, but rather in determining the appropriate ρ_* for a given event. This is clear from equation (4.23): of the three parameters that determine ρ_*, $t_{\rm E}$ is known from the PSPL fit, θ_* can be estimated based on the color and magnitude of the source, but $\mu_{\rm rel}$ is unknown. Gaudi & Sackett (2000) suggested several possible methods of dealing with this difficulty. The simplest is to simply assume a proper motion equal to the mean proper motion $\langle\mu_{\rm rel}\rangle$ for all events, and then adopt the ρ_* given by equation (4.23) with $\mu_{\rm rel} = \langle\mu_{\rm rel}\rangle$. A more accurate, but also more complicated and time-consuming method is to integrate over a distribution of $\mu_{\rm rel}$ given by a Galactic model; this would imply calculation of finite source effects for many different values of ρ_*. Here we adopt the first approach; we determine ρ_* assuming $\mu_{\rm rel} = \langle\mu_{\rm rel}\rangle = 12.5\ {\rm km\,s^{-1}kpc^{-1}}$. This value of $\langle\mu_{\rm rel}\rangle$ is a factor of two lower than the mean relative proper motion for all lenses toward the bulge (Han & Gould, 1995), and reflects the fact that our median $t_{\rm E}$ is a factor of two larger than the median of all microlensing events toward the bulge and we believe that the larger time scales reflect that fact that we are preferentially selecting slower (rather than more massive or closer) lenses. We justify this assertion in § 4.9. In fact, it is likely that the masses and distances of the lenses contribute somewhat to this larger median time scale, and thus our adopted value of $\langle\mu_{\rm rel}\rangle$ is likely an overestimate. Therefore, the resulting values of ρ_* are likely overestimates, and the following can be thought of as upper limits to the effect of the finite source sizes on our conclusions.

4.7.1. Estimating the Source Sizes

The angular size θ_* of a given source can be estimated from its dereddened $(V-I)_0$ color and magnitude I_0. From the PSPL fits to the I and V photometry, we know the I

and V fluxes of the sources in instrumental units (see § 4.4). However, very few of our fields have been calibrated relative to standard stars. Since calibration of all 43 fields in this way is a time consuming and resource-intensive process, we will instead calibrate the fields using the red giant clump. We assume that the dereddened color $(V-I)_{\rm cl,0}$ and magnitude $I_{\rm cl,0}$ of the clump is invariant for all our fields, adopting the determination by Paczyński et al. (1999),

$$(V-I)_{\rm cl,0} = 1.114 \pm 0.003, \qquad I_{\rm cl,0} = 14.37 \pm 0.02, \tag{4.26}$$

We form instrumental color-magnitude diagrams (CMDs) for each of our fields, and determine the position of the clump in instrumental units by finding the local maximum in the density of sources. The difference between this position and the intrinsic position (Eq. 4.26) gives the offsets $\Delta(V-I)$ and ΔI for all the stars in our fields. Note that these offsets include both the calibration from instrumental to true fluxes, and also the correction for the mean reddening of the field. This implies that, in general, we do *not* assume a constant redenning law from field-to-field. We apply these offset to the instrumental $(V-I)$ and I of our source stars, finally arriving at the $(V-I)_0$ and I_0 for all our sources. These are shown in Figure 4.9, and listed in Table 4.4. We show only those errors in $(V-I)_0$ and I_0 derived from modeling uncertainties; we estimate there to be an additional calibration error of $\sim 5\%$ in $(V-I)_0$ and $\sim 2\%$ in I_0 based on the typical dispersion of the clump. Note that the majority ($\sim 70\%$) of our sources are giants.

Using these colors and magnitudes, we find the angular size of the sources using a modified version of the empirical color-surface brightness relation derived by van Belle (1999), and given in Albrow et al. (2000a). The resulting θ_* for all of our sources are shown in Table 4.4. We estimate the average uncertainty in θ_* to be $\mathcal{O}(20\%)$; this reflects the uncertainty in the color and magnitude of the source due to both modeling and calibration errors. We do not determine the errors on θ_* for individual sources because the error in ρ_* (the parameter in which we are primarily interested) is dominated by the uncertainty in $\langle\mu_{\rm rel}\rangle$. For seven of our events, we had insufficient V-band data to determine the instrumental $(V-I)$ of the source. For these events, we assumed the source had the median $(V-I)$ of all sources in the field with similar I magnitudes. For these events, we do not quote errors on $(V-I)_0$. Finally, four of our events had either no V-band data at all, or the position of the clump was impossible to determine from the CMD of the field. Therefore, no estimate of $(V-I)_0$ and I_0 was possible for these events. For these events, we simply adopt the conservative assumption that the sources are clump giants, with $\theta_* = 6$ μas.

We can now use these estimates of θ_* to determine ρ_* using equation (4.23), under the assumption that all events have the same relative proper motion $\langle\mu_{\rm rel}\rangle = 12.5\ {\rm km\,s^{-1}kpc^{-1}}$. The values of ρ_* derived in this manner are listed in Table 4.4. For two of our events, MACHO 98-BLG-35 and OGLE-1999-BUL-35, the value of ρ_* estimated in this way is larger than the fitted u_0 of the event. In both cases, the derived values of ρ_* are ruled out by the fact that, despite dense coverage at the peak, no deviations from the PSPL form are seen, as would be expected if $\rho_* > u_0$ and the lens was resolving the source (Gould, 1994; Nemiroff & Wickramasinghe, 1994; Witt & Mao, 1994). Therefore, for these two events, we simply assume that $\rho_* = u_0$. In Figure 4.10, we plot u_0 versus ρ_* for all our events, along with the boundaries where finite source effects become important for both the planetary and central caustics (Eqs. 4.24 and 4.25). For the majority of our events, finite source effects should not alter the results for companions with $q \gtrsim 10^{-3}$, whereas a large fraction of our events should be affected for $q \sim 10^{-4}$.

4.7.2. Incorporating Finite Sources

In order to incorporate finite sources into the analysis, we repeat the algorithm presented in § 4.6.1 for all events, but fit the events to binary-lens light curves including the effect of the finite size of the source. While we would like to evaluate the finite-source binary-lens magnification for the specific value of ρ_* determined for each event, this is not computationally feasible, as finite source magnifications are quite time consuming to calculate. We therefore adopt a similar procedure as described in § 4.6.1: we create a grid of finite-source binary-lens magnification maps and interpolate in these maps to evaluate the binary-lens light curves. We choose the same grid spacing and size as before for (d, q), namely $10^{-4} \leq q \leq 10^{-2}$ at equal intervals of 0.25 in $\log q$, and $0.1 \leq d \leq 10$ at $d = 0.1, 0.2, ..., 1.0$ and again at the inverses of these values. For each of these (d, q) pairs, we create finite-source magnification maps for $10^{-4} \leq \rho_* \leq 10^{-1}$ at intervals of 1/3 in $\log \rho_*$. These maps have same the extent and sampling in the source plane as the point source maps (see § 4.6.1). We evaluate the finite-source magnification using the method of integrating over the boundary of the images (Kayser & Schramm, 1988; Gould & Gaucherel, 1997). We assume uniform sources; this overestimates the size of the finite source effect relative to limb-darkened sources, and thus is conservative. For each event, we use the value of ρ_* in this grid closest to the actual value estimated for the source, and use this suite of maps to perform the detection efficiency algorithm. In fact, we have repeated this process for the next-closest value of ρ_* in the grid for all events, and find that there is no appreciable difference in the conclusions.

4.7.3. Results

The distribution of $\Delta\chi^2_{\rm min}$ for the finite-source binary-lens fits is shown in Figure 4.6, along with the distribution for the point-source binary-lens fits. For the most part, the two distributions are quite similar. The significance of the best-fit binary-lens model has increased in some cases, i.e. MACHO 98-BLG-35, however all of the events that fall below our detection threshold ($\Delta\chi^2_{\rm min} > -60$) in the point-source case also fall below this threshold in the finite source case. We still only recover two "detections," MACHO 99-BLG-18 and OGLE-1999-BUL-36. As argued in § 4.6.2, these two anomalies have other explanations for their behavior. Thus our conclusions are unchanged: out of a sample of 43 events, we find no viable planet candidates.

The resulting finite source lensing zone detection efficiencies (Eq. 4.22) are shown in Figure 4.7 along with the corresponding point-source efficiencies. We find, in agreement with the expectations in § 4.7.1, that the difference between the point-source and finite-source efficiencies for mass ratios $q \gtrsim 10^{-3}$ is negligible for nearly *all* events, with the exception of a few events with very large sources ($\rho_* \sim 0.1$). Finite source effects begin to become appreciable for $q \lesssim 10^{-3}$ and by $q = 10^{-4}$, the finite source detection efficiency is markedly smaller than the point-source efficiency, at least for large sources. However, as we show in § 4.8, we have very poor constraints on such small mass-ratio companions anyway. In other words, the finite size of the sources have no appreciable effect on the detection efficiencies for those mass ratios where we have significant constraints; while for those mass ratios where finite source effects are appreciable we have no interesting constraints. Therefore we conclude that, for this sample of events, finite source effects are negligible.

4.8. Upper Limits

The fact that a large fraction of our final sample of 42 microlensing events have significant detection efficiencies to planetary companions, in conjunction with the fact that we have detected no viable planetary candidates in these events, implies that the fraction of primary lenses with planetary companions must be considerably smaller than unity. To quantify the exact number implied by our data, we combine the individual event efficiencies $\epsilon_i(d,q)$ to obtain a statistical upper limit to the fraction of lenses with companions as a function of mass ratio q and projected separation d.

Assume that a fraction $f(d,q)$ of primary lenses have planets at (d,q). Averaged over a large number of events, the probability that any single event would harbor such a planet is then also $f(d,q)$. The probability that such a planet would be detected in event i is the detection efficiency, $\epsilon_i(d,q)$. Therefore, the probability that any given event has a planet that is detected is $f(d,q)\epsilon_i(d,q)$. The probability that the event has a planet but is not detected is $1-f(d,q)\epsilon_i(d,q)$. Thus the probability that a sample of N events results in no detections is simply,

$$P(d,q) = \Pi_{i=1}^{N}\left[1-f(d,q)\epsilon_i(d,q)\right]. \tag{4.27}$$

The 95% confidence level (c.l.) upper limit to $f(d,q)$ implied by such a sample of events if found by setting $P(d,q)=0.05$ and solving for $f(d,q)$.

In Figure 4.11 we show the 95% c.l. upper limit to $f(d,q)$ as a function of d,q derived from our final sample of 42 events, assuming $\Delta\chi^2_{\rm thresh}=60$ and point sources. We conclude that $<25\%$ of lenses have a companion of mass ratio $q \gtrsim 10^{-3}$ and projected separation $d \sim 1$. We can exclude the hypothesis that more than one-half of the primary lenses have a companion near $d=1$ for the full range of mass ratios $10^{-4} \le q \le 10^{-2}$. Also shown in Figure 4.11 are cross sections of the (d,q) exclusion diagram (95% c.l. upper limits as a function of d) for three different mass ratios, namely $q=10^{-2}$, 10^{-3}, and 10^{-4}. For these cross sections, we also show the 95% c.l. upper limits derived assuming point sources and $\Delta\chi^2_{\rm thresh}=100$, and assuming finite sources and $\Delta\chi^2_{\rm thresh}=60$. Clearly finite source effects are negligible where we having interesting constraints.

In Figure 4.12 we show the 95% c.l. upper limit as a function of q for companions anywhere in the lensing zone $0.6 \le d \le 1.6$, and anywhere in the "extended" lensing zone,

$0.5 \leq d \leq 2.0$. Less than 20% of primaries can have a $q = 10^{-2}$ mass ratio companion in the lensing zone. For $q = 10^{-3}$ companions in the lensing zone, the upper limit is 45%.

4.9. Interpretation

The upper limits presented in § 4.8 are the most direct, least model dependent inferences we can draw from our data. Unfortunately, they are also not very illuminating, for several reasons. First, we have not specified the nature of primaries around which we limiting planets. Second, we have quoted our results in terms of the two natural binary-lens parameters, the mass ratio of the system q and the instantaneous projected separation d of the companion, rather than the more common (and more interesting) parameterization of planetary mass $m_{\rm p}$ and physical separation a.

Unfortunately, it is not possible to determine the mass of the primaries, and hence their nature, directly. This is because the one observable parameter containing information about the lens, the event time scale $t_{\rm E}$, is a degenerate combination of the mass, distance, and velocity of the lens (c.f. Eqs. 4.1 and 4.4). Thus is it only possible to make model-dependent inferences about the nature of the primary lenses. The majority of the microlensing events in our sample are likely to be due to bulge stars lensing other bulge stars (Kiraga & Paczyński, 1994). Following Gould (2000), we adopt the bulge mass function as measured by Zoccali et al. (2000), and assume a model such that the sources and lenses are distributed as r^{-2}, and have Gaussian velocity distributions with dispersion $\sigma = 100\ {\rm km\,s^{-1}}$. This model gives typical parameters for bulge self-lensing events of $\langle M \rangle \sim 0.3\ M_{\odot}$, $\langle \pi_{\rm rel} \rangle = 40\ \mu{\rm as}$, and thus $\langle \theta_{\rm E} \rangle \sim 320\ \mu{\rm as}$. For the relative proper motion, this model predicts $\langle \mu_{\rm rel} \rangle \sim 25\ {\rm km\,s^{-1}\ kpc^{-1}}$, and thus $\langle t_{\rm E} \rangle \sim 20$ days, which is the median time scale found by OGLE for events toward the Galactic bulge (Udalski et al., 2000), and thus gives us some confidence that the model is approximately correct. If we take this model at face value, the fact that the median time scale of the events in our sample is a factor of 2 times implies that we are selecting a biased subset of lenses. From eqs. 4.1 and 4.4, this bias could be toward higher mass lenses, slower lenses (smaller $\mu_{\rm rel}$) or closer lenses (larger $\pi_{\rm rel}$), or any combination of these three factors. In fact, as demonstrated by Gould (2000), the majority of the dispersion in the expected distribution of time scales arises from the dispersion in $\mu_{\rm rel}$, not the dispersion in $\pi_{\rm rel}$ or M. This implies that we are, for the most part, preferentially selecting slower, rather than more massive or closer lenses, justifying our assumption of $\langle\mu_{\rm rel}\rangle \sim 12.5\ {\rm km\,s^{-1}\ kpc^{-1}}$ for the estimates of ρ_* in § 4.7. Thus the typical mass of the lenses in our sample is likely close to the typical mass for all microlensing events, and the typical relative source-lens parallax is also close to that for all microlensing events. We will therefore adopt $\langle\pi_{\rm rel}\rangle = 40\ \mu$as, which for source stars at $D_{\rm S} \sim 8$ kpc implies lens distances of $D_{\rm L} \sim 6$ kpc. We also adopt $\langle M\rangle = 0.3\ M_\odot$. In other words, our primary lenses are normal M dwarfs in the Galactic bulge.

Some caveats must be noted. Kiraga & Paczyński (1994) estimate that $\sim 20\%$ of events toward the Galactic bulge are due lensing of bulge stars by disk stars, and of the remaining $\sim 80\%$, Gould (2000) estimates that another $\sim 20\%$ are due to remnants (white dwarfs, neutron stars, and black holes). Thus, we would expect $\sim 60\%$ of the events in our sample to be due to normal stars in the Galactic bulge. However, we have no idea which 60% these are. Also, some fraction of the events in our sample are likely members of binary systems with separations that are either too small or too large to be distinguishable from single lenses. We have no way of determining which events these are, or even what fraction of our events are in such systems. Given the rather small sample of events we are concerned with here, and the uncertainties in the magnitude of these contaminations, we feel it is not appropriate at this stage to attempt to correct for these effects, and choose to ignore them.

The estimates of $\langle M\rangle$ and $\langle\pi_{\rm rel}\rangle$ adopted above imply $\langle\theta_{\rm E}\rangle = 320\ \mu$as and thus $\langle r_{\rm E}\rangle = 2$ AU (for $D_{\rm S} = 8$ kpc). We can use the values to convert the upper limits derived in § 4.8 from the dimensionless units to physical units. We first note that these assumptions result in the relations,

$$m_{\rm p} = \left(\frac{q}{0.003}\right) M_{\rm Jup}, \qquad a_{\rm P} = \left(\frac{d}{0.5}\right) {\rm AU}, \tag{4.28}$$

where $a_{\rm P}$ is the analog of d (the instantaneous projected separation) in physical units. To convert from $a_{\rm P}$ to the conventional three-dimensional separation a, we must convolve with the distribution function (Gould & Loeb, 1992),

$$p(a_{\rm P}; a) = \frac{a_{\rm P}}{a}\left(1 - \frac{a_{\rm P}^2}{a^2}\right)^{1/2}, \tag{4.29}$$

which is found by integrating over all random inclinations and orbital phases, assuming circular orbits. Thus the detection efficiency of each event i in the $(a, m_{\rm p})$ plane is,

$$\epsilon_i(a, m_{\rm p}) = \int_0^a {\rm d}a_{\rm P}\, p(a_{\rm P})\epsilon_i(a_{\rm P}, m_{\rm p}) \tag{4.30}$$

These individual efficiencies $\epsilon_i(a, m_{\rm p})$ can now be combined in the same manner as in § 4.8 to derive 95% c.l. upper limits to the fraction $f(a, m_{\rm p})$ of events with companions as a function of the mass $m_{\rm p}$ and separation a of the companion.

In Figure 4.13 we show the 95% c.l. upper limit to $f(a, m_{\rm p})$ as a function of $(a, m_{\rm p})$, assuming $\Delta\chi^2_{\rm thresh} = 60$ and point sources. This figure is analogous to Figure 4.11, except that now our upper limits are in terms of the physical variables of the mass of the companion in $M_{\rm Jup}$ and separation of the companion in AU, and we have identified our primaries as M-dwarfs in the Galactic bulge. In Figure 4.14 we show the 95% c.l. upper limits to the fraction of lenses with planets in two ranges of semi-major axes, $(1.5 - 4)$ AU and $(1 - 7)$ AU. Taking our inference about the nature of the primary lenses literally, we conclude that less than 25% of M-dwarfs in the Galactic bulge have Jupiter mass companions between 1.5 and 4 AU. Less than 45% have Jupiter mass companions between 1 and 7 AU. These are the first significant limits on planetary companions to M-dwarfs, and are the primary result of this work.

4.10. Discussion

The majority of what we know about planetary companions has been gathered from radial velocity surveys of stars in the local neighborhood. However, these surveys have told us very little about planetary companions to M-dwarf primaries, as they have primarily focused on G-dwarf and have only recently begun surveying cooler stars. To date, only one planetary companion has been found to an M-dwarf, the $2.1 M_{\rm Jup}$ companion to Gliese 876 (Marcy et al., 1998). Therefore our results place interesting limits in an entirely new region of parameter space. However, this also means that the comparison between our results and those of radial velocity surveys is not entirely straightforward, as we are probing different primaries, and therefore different regimes of star, disk, and planet formation. Furthermore, our primaries are mostly old stars in the bulge, whereas those studied by radial velocity surveys are likely relatively young. Finally, there is evidence that the host stars of local companions have super-solar metallicity, whereas stars in the Galactic bulge typically have solar to sub-solar metallicity. It is not at all clear clear how these differences between the parent samples we probe will affect the various proposed planet formation mechanisms. Our results likely place interesting constraints on planet formation and migration theories; unfortunately it is not at all clear what these constraints might be.

Rather than attempt to delve into and interpret the various planetary formation theories, we will simply make a direct comparison between our results and those of radial velocity surveys, and let the ambitious theorist attempt to interpret these comparisons. In Figure 4.15, we show our 95% c.l. upper limits on the fraction of primaries with a companion as a function of the mass $m_{\rm p}$ and semi-major axis a of the companion, along with the measured $m_{\mathrm{p}} \sin i$ and a of those companions detected by radial velocity surveys. More the most part, radial velocity surveys are sensitive to companions with smaller a than microlensing, although there is clearly some overlap. Also shown in the radial-velocity detection limit for an accuracy of 20 ms^{-1} and a primary mass of 0.3 $M_{\odot}$ (typical of our primaries), and a survey lifetime of 10 years. It is clear that radial velocity methods are unlikely to place interesting constraints on companions at the larger separations we probe 3 AU $\leq a \leq$ 5 AU anytime in the near future. As we show in Figure 4.15 this is also true for future astrometric surveys such as SIM, whose anticipated lifetime is 5 years.

In Figure 4.15, we also compare the constraints on the fraction of stars with planets derived from the statistical analysis of the Lick radial velocity survey (Cumming, Marcy, & Butler, 1999) with our constraints. In the region of overlap, we find that they are comparable. For small a, approximately $f \sim 5\%$ of local G-dwarfs have companions between $0 \leq a \leq 0.1$ AU. It is interesting to ask how many more events we will need to monitor in order to limit the fraction of primaries with companions to 10% in range of the separations we to which we are sensitive. From equation (4.27), we find that, for small f, $f \propto N^{-1}$. Given that our limits are $f \sim 25\%$, we would require 5 times more events of similar quality. This number could be significantly reduced if the quality of the alerts could be improved, i.e. if a larger fraction of events we monitor in the future where bright, high-magnification events. This will likely be possible with the next generation OGLE campaign (Udalski et al., 2000).

4.11. Summary and Conclusion

We have analyzed 5 years of PLANET photometry of microlensing events toward the Galactic bulge in the context of searching for planets. All of the 125 bulge microlensing events for which PLANET has acquired data over the last five years can be subdivided into four categories: apparently normal point-source point-lens events (PSPL), events due to binary lenses of nearly equal mass, events that deviate from the single lens for in a way not associated with binary lensing (parallax, finite source, binary source, etc.), and events for which the data quality is too poor to determine the nature of the event. We find no events in a hypothetical fifth category: events which have short-durations deviations from the single lens light curve that are indicative of the presence of planetary companions to the primary microlenses. This indicates that Jupiter-mass companions to bulge stars with separation of a few AU are not very common.

In order to justify and quantify this conclusion, we imposed strict event selection criterion, and derived a well-defined subset of 43 intensively monitored events which we carefully analyzed for the presence of companions. Using the method of Gaudi & Sackett (2000), we searched for the signatures of planetary companions in these events over a densely sampled, extensive region of parameter space. Specifically, we searched for companions with mass ratios q from $10^{-2} - 10^{-4}$ and instantaneous projected separations d in units of the angular Einstein ring radius from $0.1 \leq d \leq 10$. We required that the difference in χ^2 between the best-fit binary lens model and the best-fit single lens model be < -60 for a detection. We found two such detections, events MACHO 99-BLG-18 and OGLE-1999-BUL-36. Analysis of MACHO 99-BLG-18 uncovered irregular variability in the baseline, and we thus eliminated it the sample. OGLE-1999-BUL-36 displays an overall asymmetry that is equally-well explained by a low-amplitude parallax signal. We therefore concluded that we cannot reliably detect planets from asymmetries, and we therefore explicitly ignored this "detection." Thus we find no viable planetary candidates out of a sample of 43 events.

We then calculated the detection efficiency for our events in (d, q) space. Out of our sample of 42 events, 30 have substantial ($> 25\%$) efficiency to companions with $q = 10^{-2}$ and separations in the lensing zone $0.6 \leq d \leq 1.6$. This implies that, had the majority of the primary lenses harbored such companions, we should have detected a

~ 7 of them. The fact that we detected no companions implies that this is clearly not the case. Specifically, by combining our efficiencies, we obtain a statistical upper limits on the fraction of lenses with massive planets in the lensing zone. At the 95% confidence level, we find that < 25% of lenses can have a companion of with mass ratio $q = 10^{-2}$ in the lensing zone.

Using a model of the mass function, spatial distribution, and velocity distribution of stars in the Galactic bulge, we infer that the majority of our lenses are likely due to $M \sim 0.3\ M_{\odot}$ stars at 6 kpc, i.e. M dwarfs in the Galactic bulge. Using this assumption, we convert our upper limits from (q, d) space to mass-physical separation space. We conclude that less than than 25% of M-dwarfs in the Galactic bulge have Jupiter mass companions between 1.5 and 4 AU, and less than 45% have Jupiter mass companions between 1 and 7 AU, the first significant limits on planetary companions to M-dwarfs.

We have also tested the robustness of our conclusions to various assumptions. We explicitly included the effect of the finite size of the source stars for each event, estimating the source size using the color and magnitude of the source and assuming a mean relative proper motion of the lens. We find that the finite source effect only becomes important for mass ratios $q \lesssim 10^{-3}$, where our constraints on companions are already weak. Therefore, we conclude that finite source effects have a negligible effect on our results. We also tested the effect of changing our detection criterion from $\Delta\chi^2_{\rm thresh} = 60$ to $\Delta\chi^2_{\rm thresh} = 100$. As expected, this lowers our sensitivity somewhat, but does not change our conclusions substantially. Finally, we have tested the effect of ignoring parallax asymmetries in the calculation of our detection efficiencies, and find that this changes our limits by substantially less than our statistical uncertainties.

In the process of this analysis, we have uncovered a couple of surprises. First, we find that our median event time scale ($t_{\rm E} = 40$ days) is a factor of two larger than the median time scale for all events toward the Galactic bulge. This bias is a selection effect that arises from the manner in which we choose our targets. We argued that this primarily biases our events towards slower, rather than closer or more massive lenses. Therefore, our assertion of a typical lens mass of 0.3 $M_\odot$ is justified. Second, we found that for our very highest magnification events, there is a minimum in the detection efficiency at $d = 1$. This is somewhat contrary to current wisdom, and arises from the fact the single caustic created by planets at $d = 1$ is quite weak, and therefore the deviation from the single-lens form is quite brief, and easy to miss. This implies that, for high-magnification events, the detection probability in the lensing zone, while large, is not 100%.

Our upper limits probe separations that are probably unattainable via astrometric or radial velocity surveys, due to the long orbital time scales involved and the finite survey lifetimes. The smallest separations we are sensitive to overlap with radial velocity surveys, and thus can eventually be used to compare the frequency of companions in the Galactic bulge with that in the solar neighborhood. However, we estimate that an approximately 5 times larger sample than that considered here would be needed to probe fractions as small as those being measured by radial velocity surveys ($\sim 5\%$). This is assuming that future microlensing events are of similar quality to those analyzed here. If the number of alerts is increased substantially, however, more care could be taken to choose higher-quality (brighter, higher maximum magnification) events. This would considerably reduce the number of event needed to probe companion fractions of 5%.

Our results likely have important implications for theories of planet formation, as the separations we constrain may be closer to the sites of planet formation, rather than the small separations at which radial-velocity companions are found, which are likely reached via orbital migration. Regardless, our limits provide fundamental constraints on the frequency and distribution of extra-solar planets in our Galaxy.

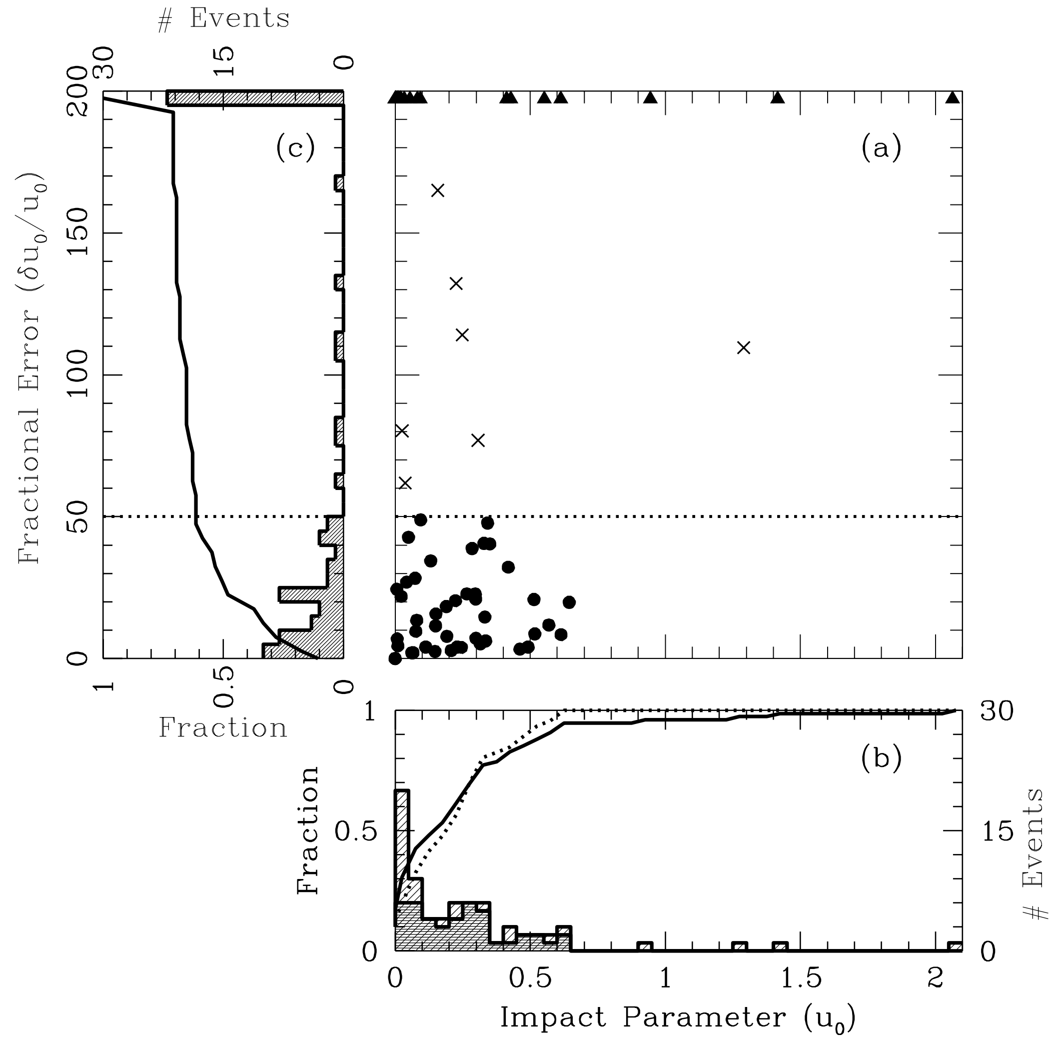

Fig. 4.1.— (a) The fractional error in the impact parameter, $\delta u_0/u_0$ is plotted versus u_0 for all events which pass our data quantity cut. The u_0 for those events with $\delta u_0/u_0 > 200\%$ are plotted as triangles. The dotted line indicates our cut on the fractional error, $\delta u_0/u_0 = 50\%$. Events with $\delta u_0/u_0 \leq 50\%$ are included in the final event sample and are shown as solid circles, while events with $\delta u_0/u_0 > 50\%$ are discarded (crosses and triangles). (b) The lines show the cumulative distribution of u_0 for all events (solid) and those events that pass our cut (dashed). The histograms show the differential distributions of u_0 for all events (unshaded) and those events that pass our cut (shaded). The left axis refers to the cumulated distribution, while the right axis refers to the differential distributions. (c) The line shows the cumulative distribution of $\delta u_0/u_0$ (bottom axis). The histogram shows the differential distribution (top axis).

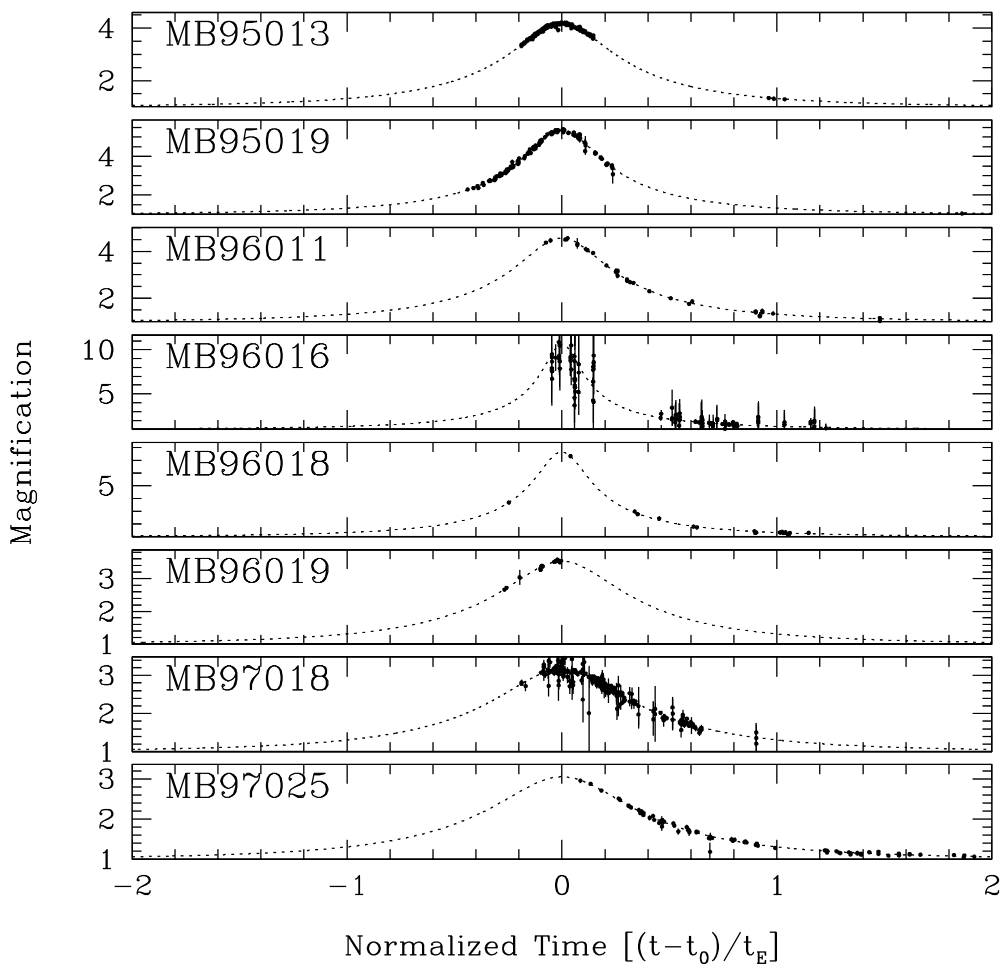

Continued

Fig. 4.2.— The light curves for the events which passed our selection criteria (§ 4.4). The magnification, $(F - F_{\mathrm{S}})/F_{\mathrm{B}}$, is plotted as a function of normalized time, $\tau = (t - t_0)/t_{\mathrm{E}}$, for the "cleaned" light curves, i.e. with seeing systematics removed and errors scaled. See § 4.2.

Fig. 4.2.— Continued

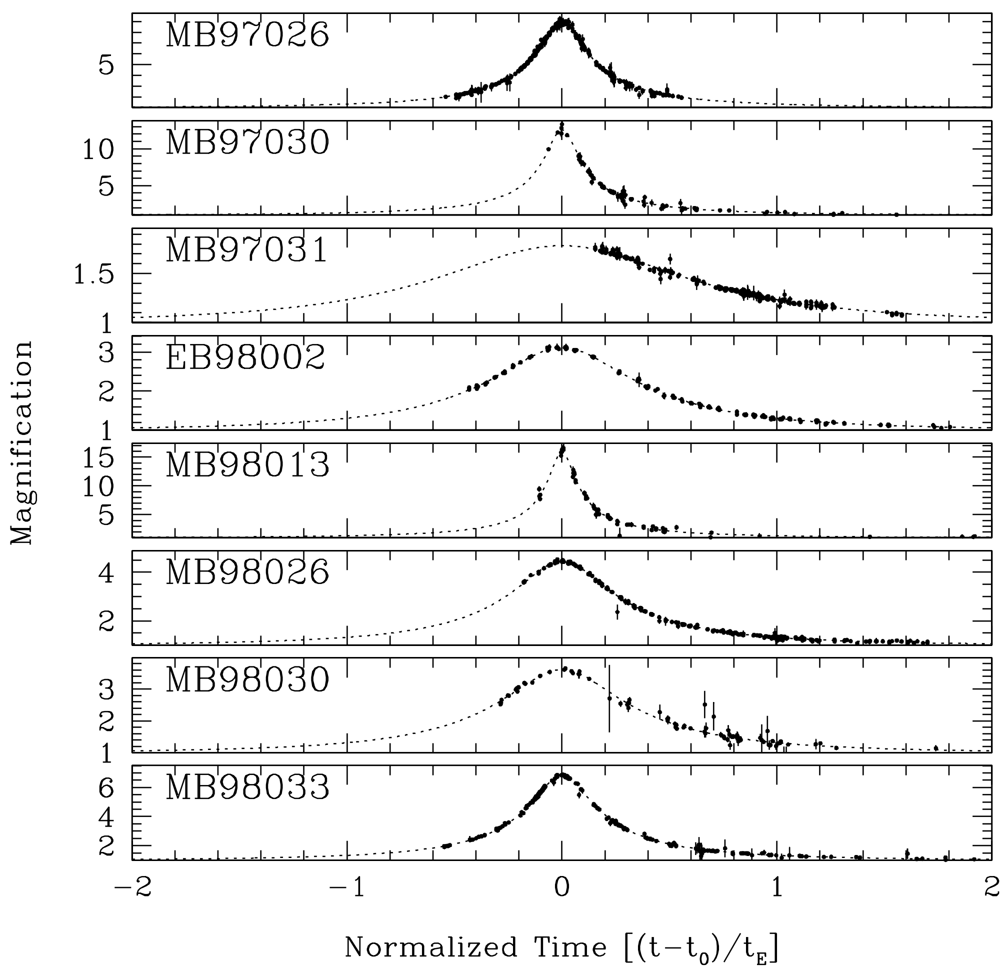

Continued

Fig. 4.2.— Continued

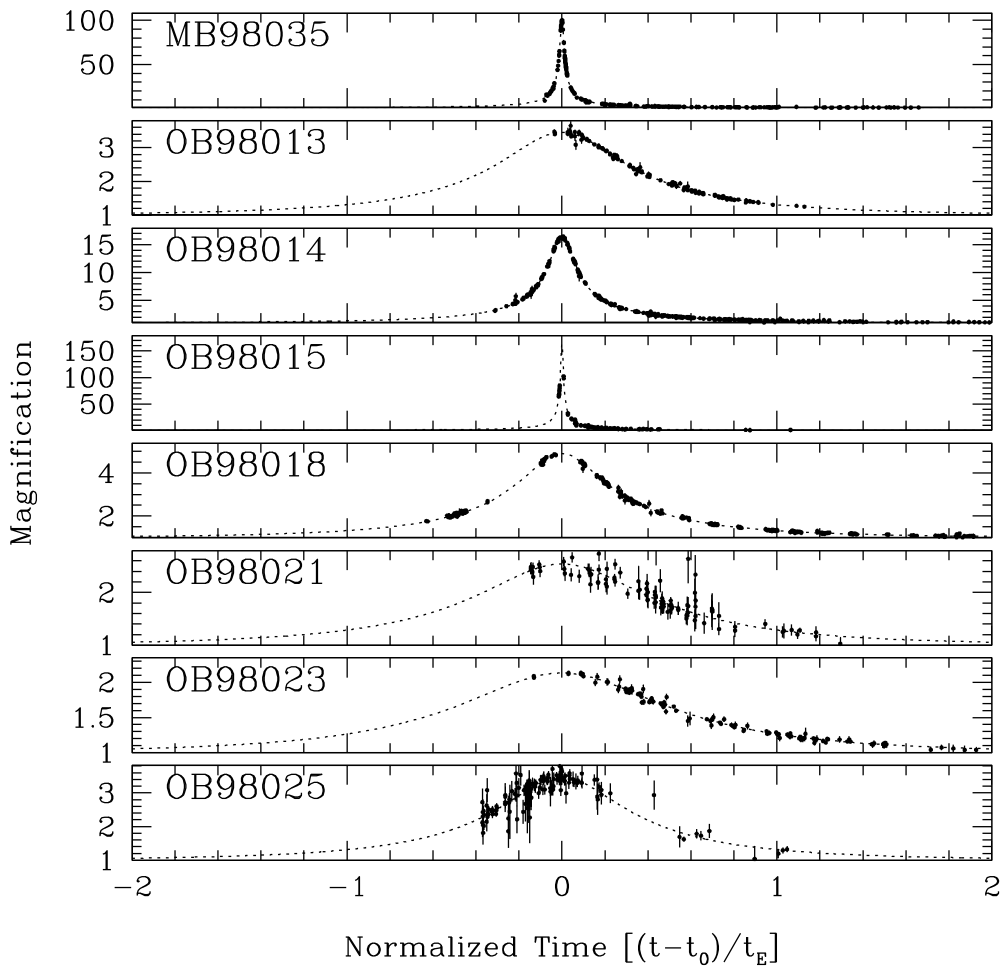

Continued

Fig. 4.2.— Continued

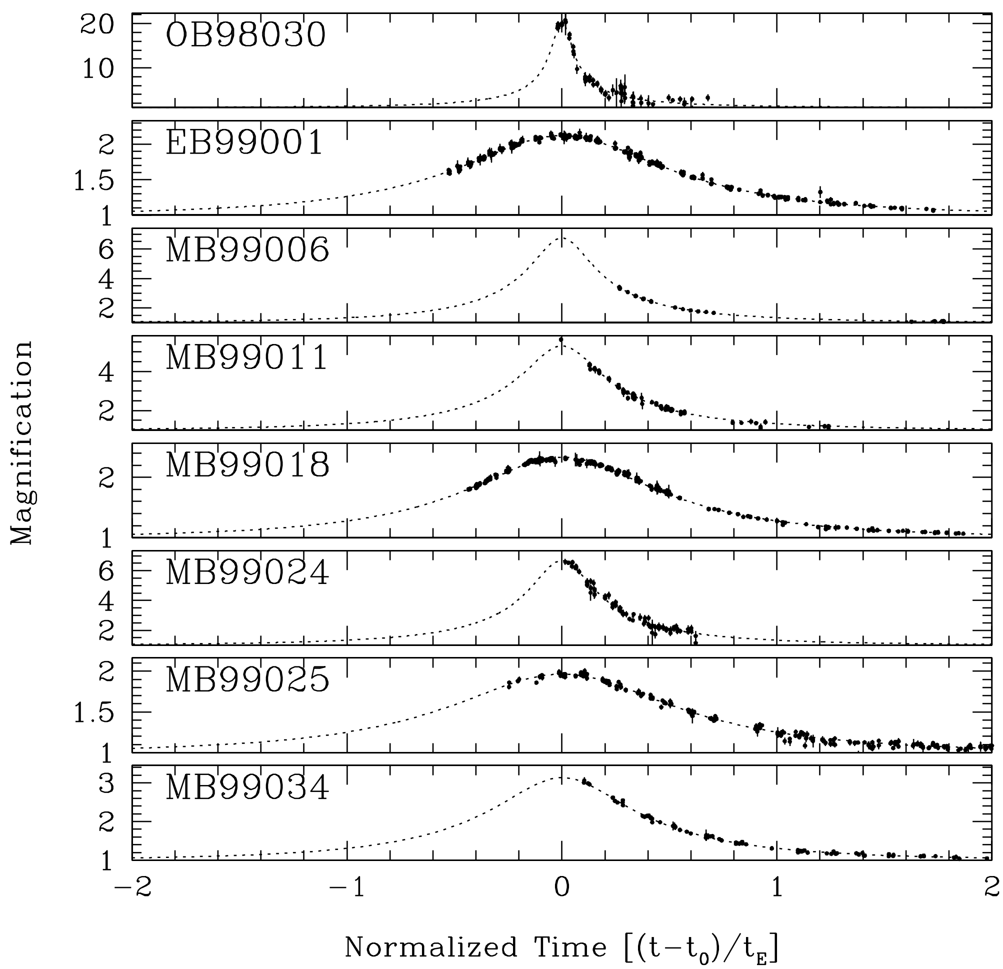

Continued

Fig. 4.2.— Continued

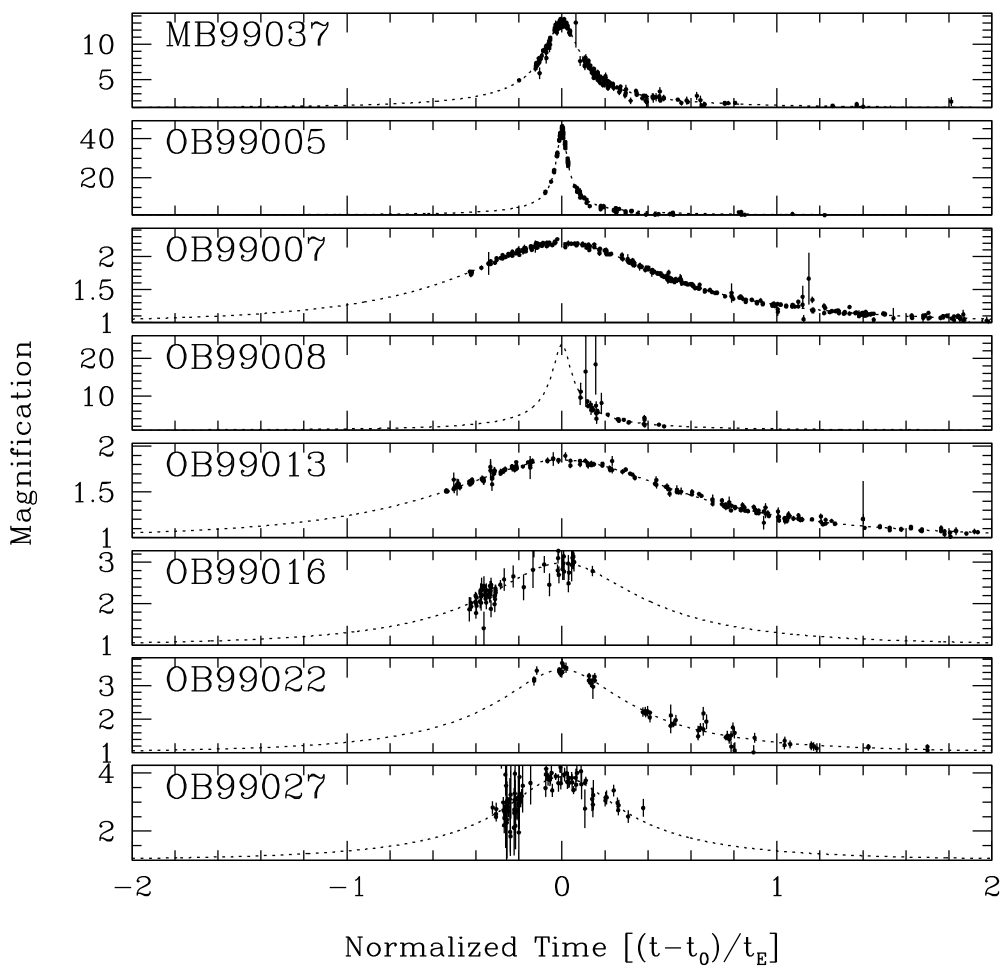

Continued

Fig. 4.2.— Continued

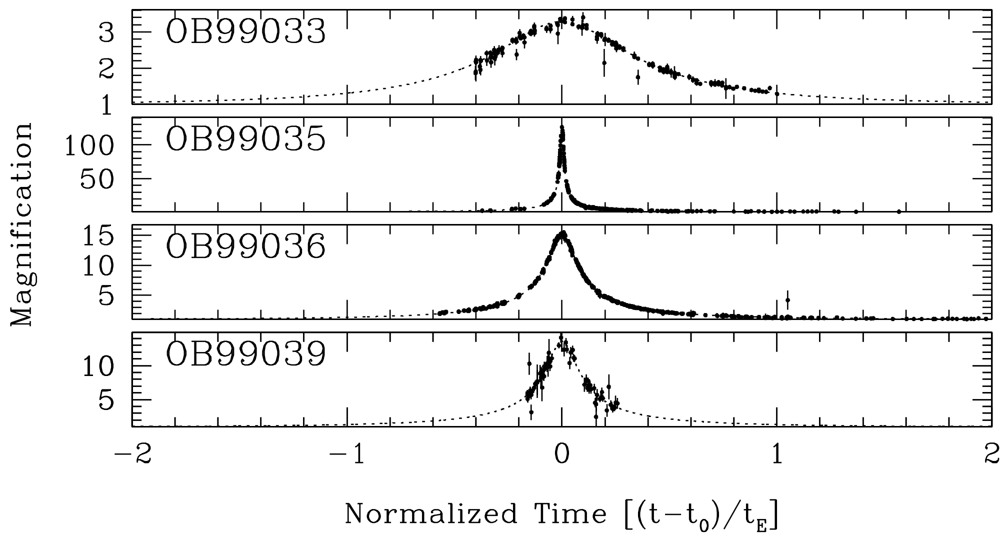

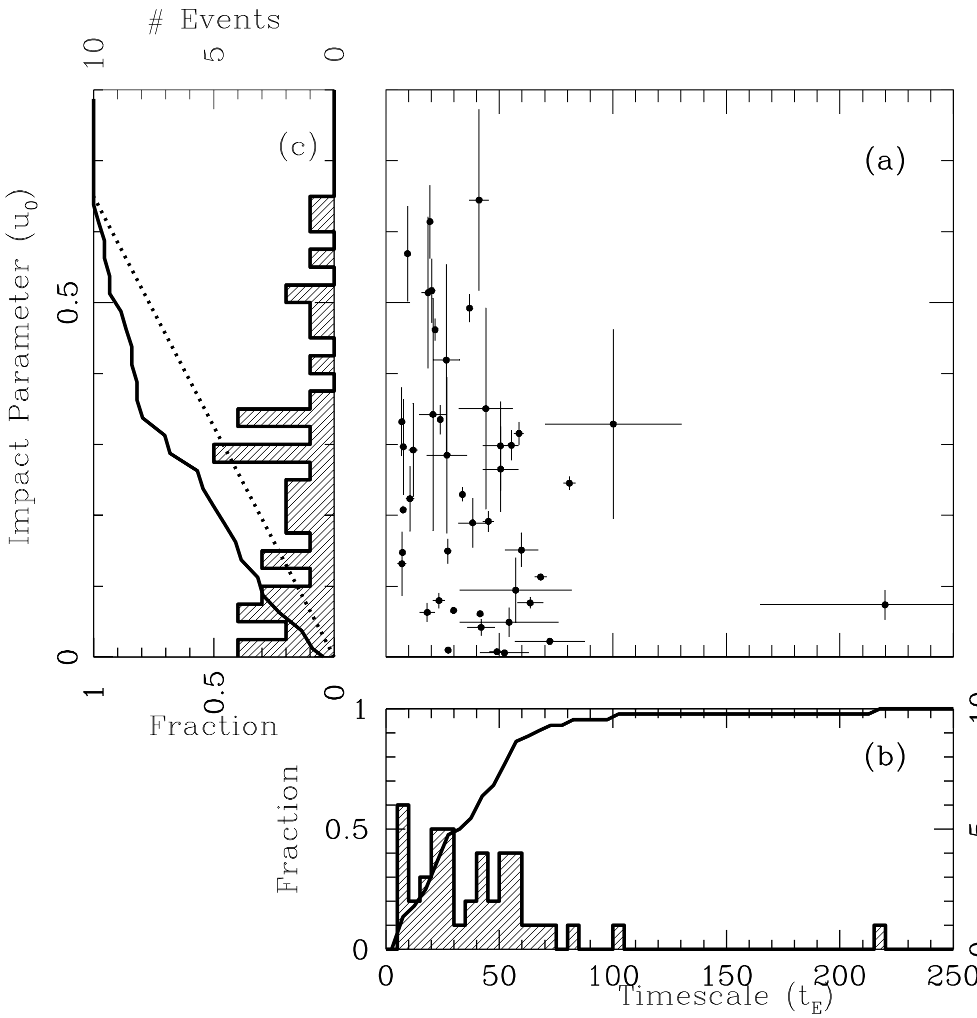

Fig. 4.3.— (a) The impact parameter, $\delta u_0/u_0$, is plotted versus the time scale, t_{E}, for those events which pass all our cuts. (b) The line shows the cumulative distribution of t_{E} (left axis), while the histogram shows the differential distribution (right axis). (c) The line shows the cumulative distribution of u_0 (bottom axis), while histogram shows the differential distribution (top axis).

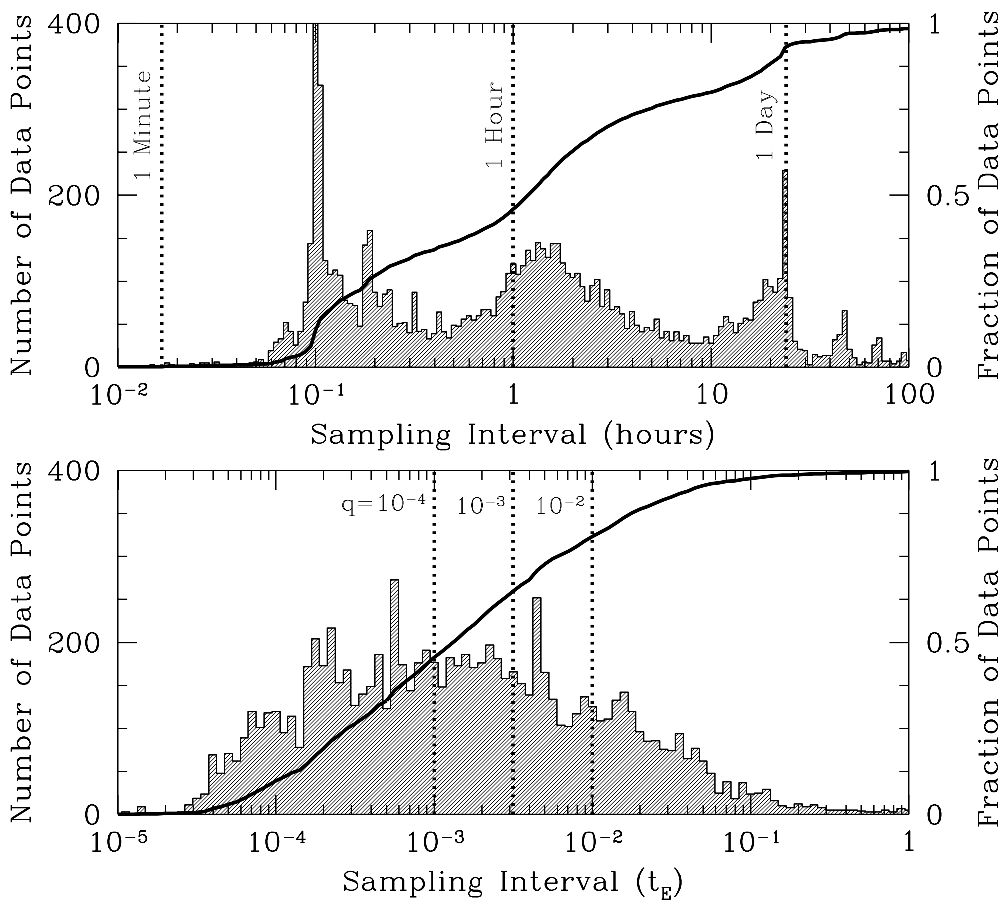

Fig. 4.4.— (a) The histogram shows the differential distribution of sampling intervals (in hours) for our final event sample (left axis). The solid line shows the cumulative distribution (right axis). (b) Same as (a), except in units of $t_{\rm E}$. The vertical dotted lines indicate the approximate minimum sampling rates necessary for detection of companions of the indicated mass ratios.

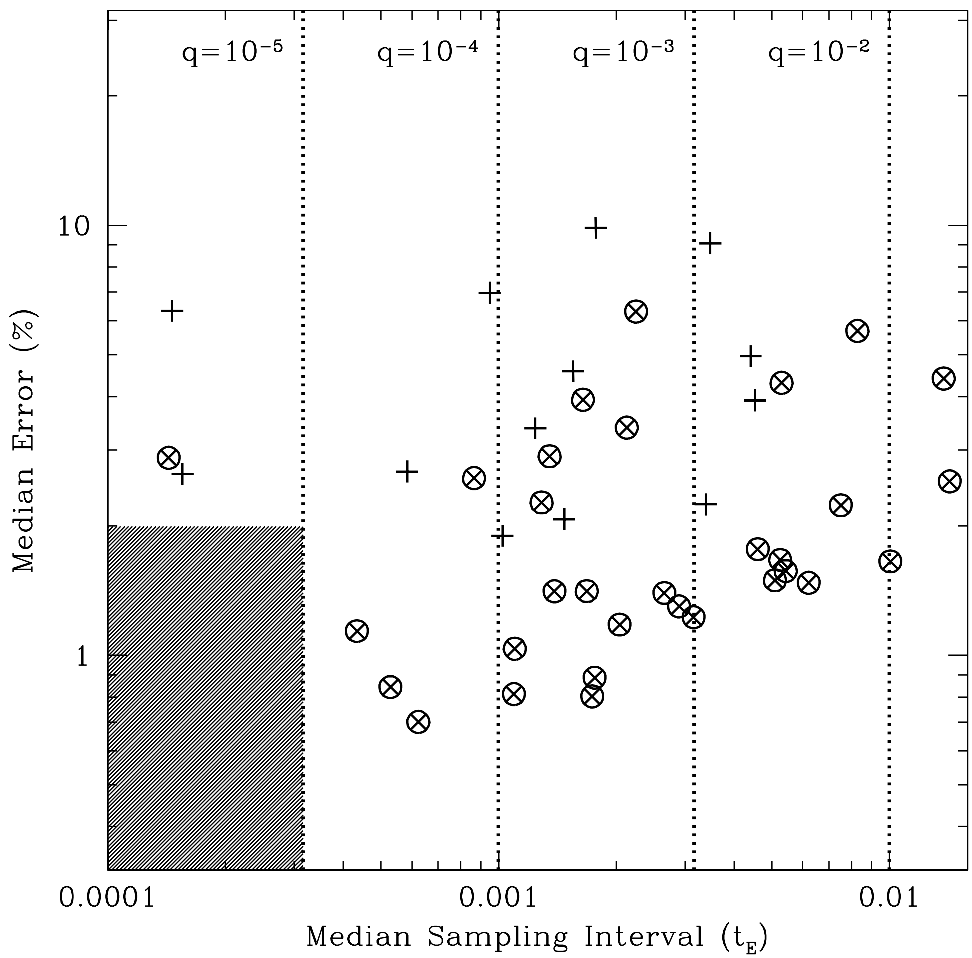

Fig. 4.5.— The median photometric error is plotted versus the median sampling interval in units of $t_{\rm E}$ for our final event sample. The plus signs indicate high-magnification events ($u_0 < 0.1$ or $A_{\rm max} > 10$). The vertical dotted lines indicate the approximate minimum sampling rates necessary for detection of companions of the indicated mass ratios. The shaded box indicates approximately the error and sampling needed to routinely detect 10^{-5} mass ratio companions.

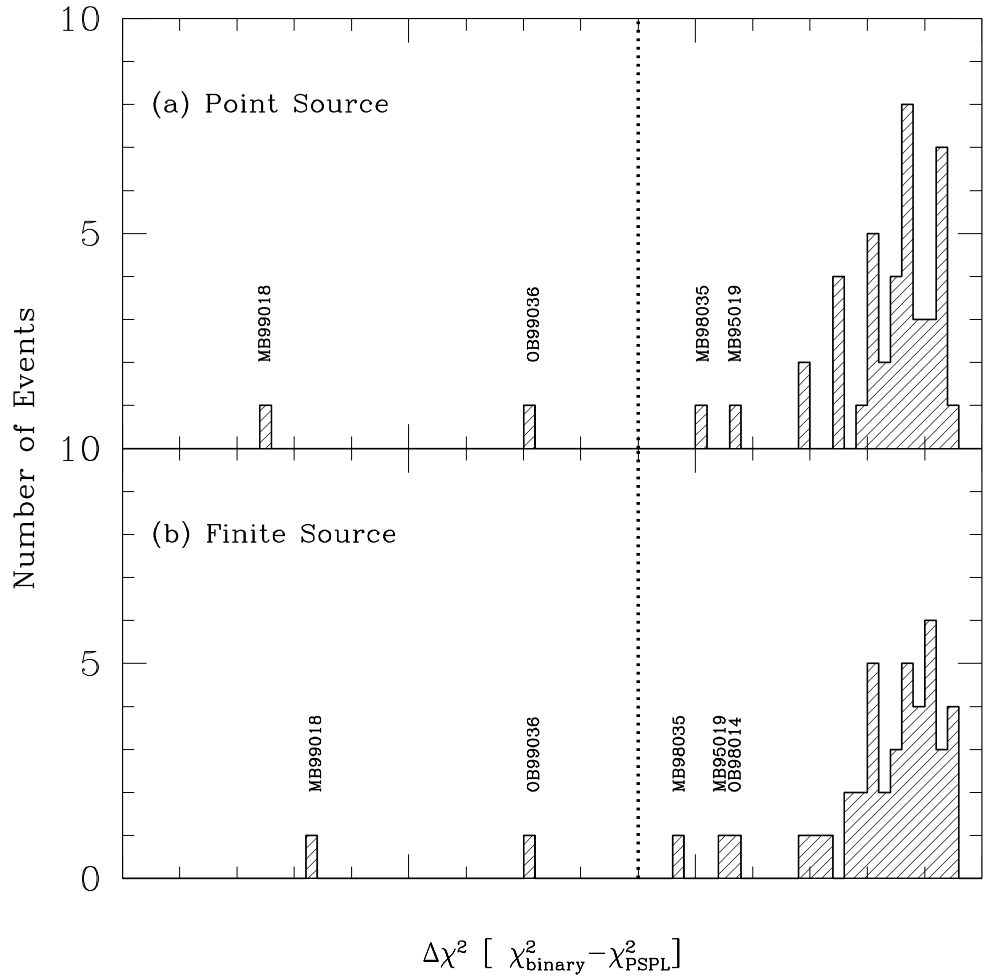

Fig. 4.6.— The histogram shows the distribution of the difference in χ^2 between the best-fit binary lens model in the range $q = 10^{-2} - 10^{-4}$, and the point-source point-lens fit. Events with $\Delta\chi^2 < -30$ are labelled. The dotted line is our adopted detection threshold, $\Delta\chi^2_{\rm thresh} = -60$. (a)Binary-lens models where the source is assumed to be point-like. (b) Binary lens models where the source is assumed to have the dimensionless size ρ_* as given in 4.4.

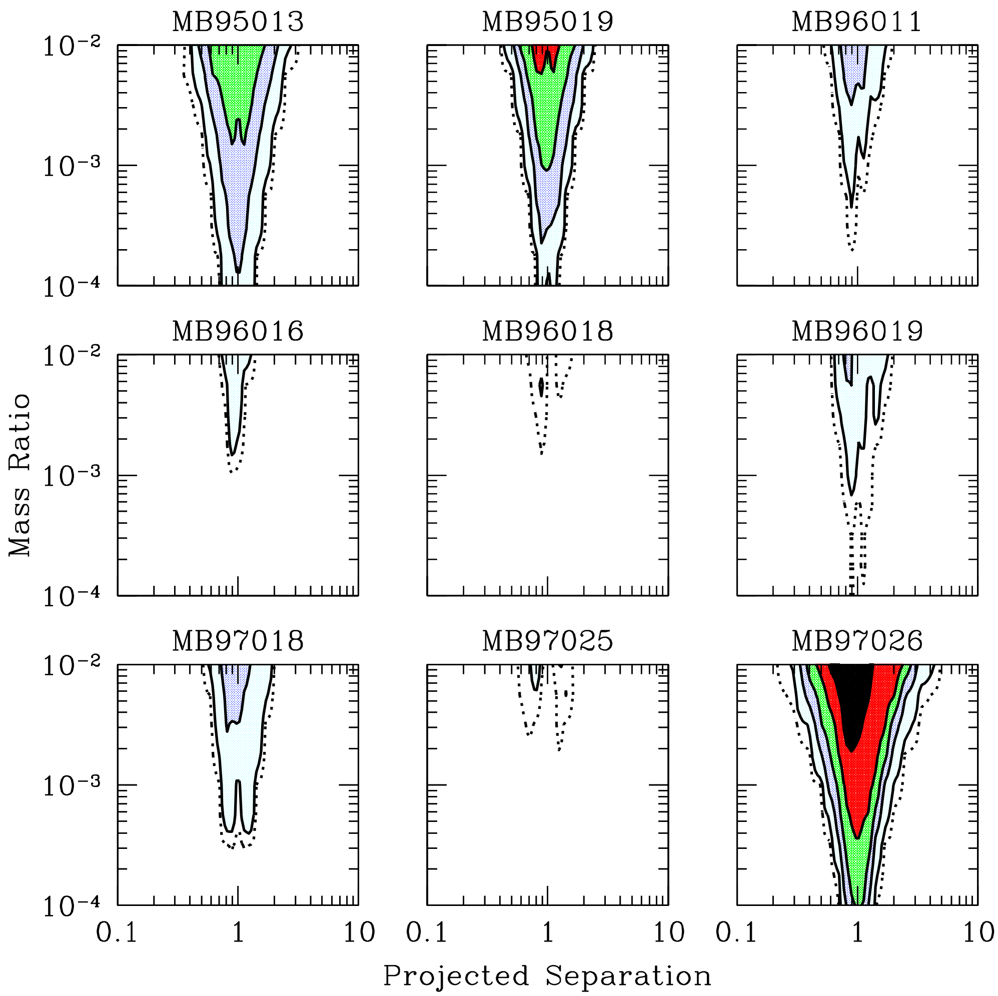

Continued

Fig. 4.7.— The black lines are contours of constant detection efficiency, $\epsilon(d,q)$, shown for projected separations d between the primary and companion in units of the Einstein ring radius, of $-1 < \log d \leq 1$, and mass ratios between the primary and companion, q, of $-2 > \log(q) > -4$. The contours mark $\epsilon = 1\%$(outer contour; dotted), 5%, 25%, 50%, 75%, and 95% (inner contour). Each panel is for a separate event; the abbreviated event name is indicated above the panel. Note that the "wiggly" nature of the outer contours apparent in some events is an artifact of the (d, q) sampling and the plotting routine.

Fig. 4.7.— Continued

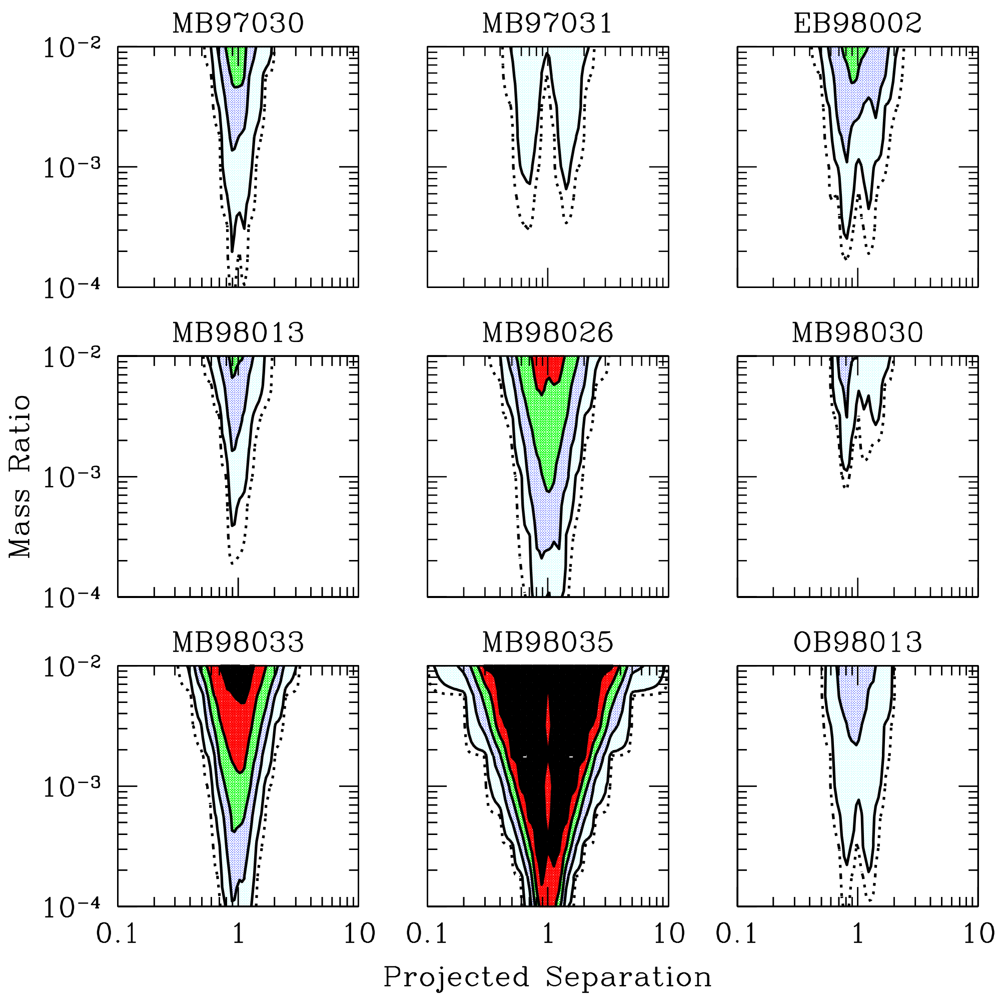

Continued

Fig. 4.7.— Continued

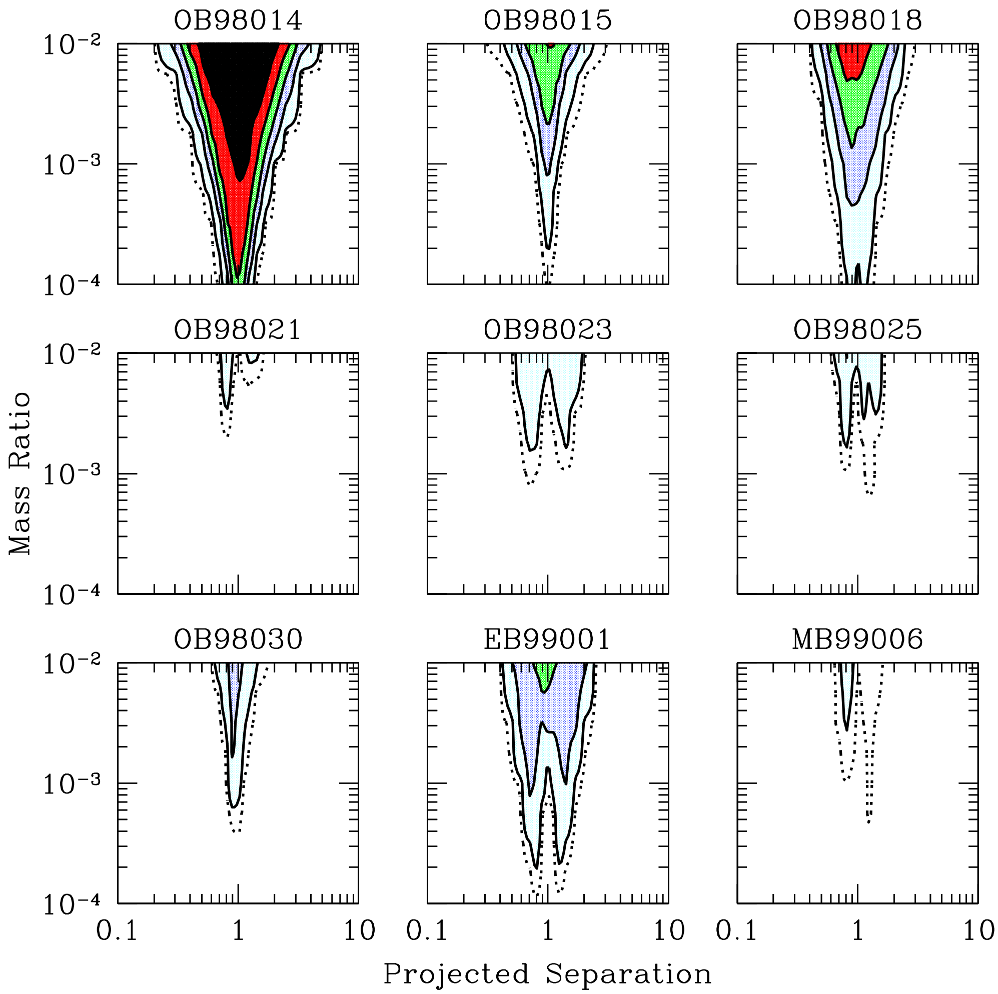

Continued

Fig. 4.7.— Continued

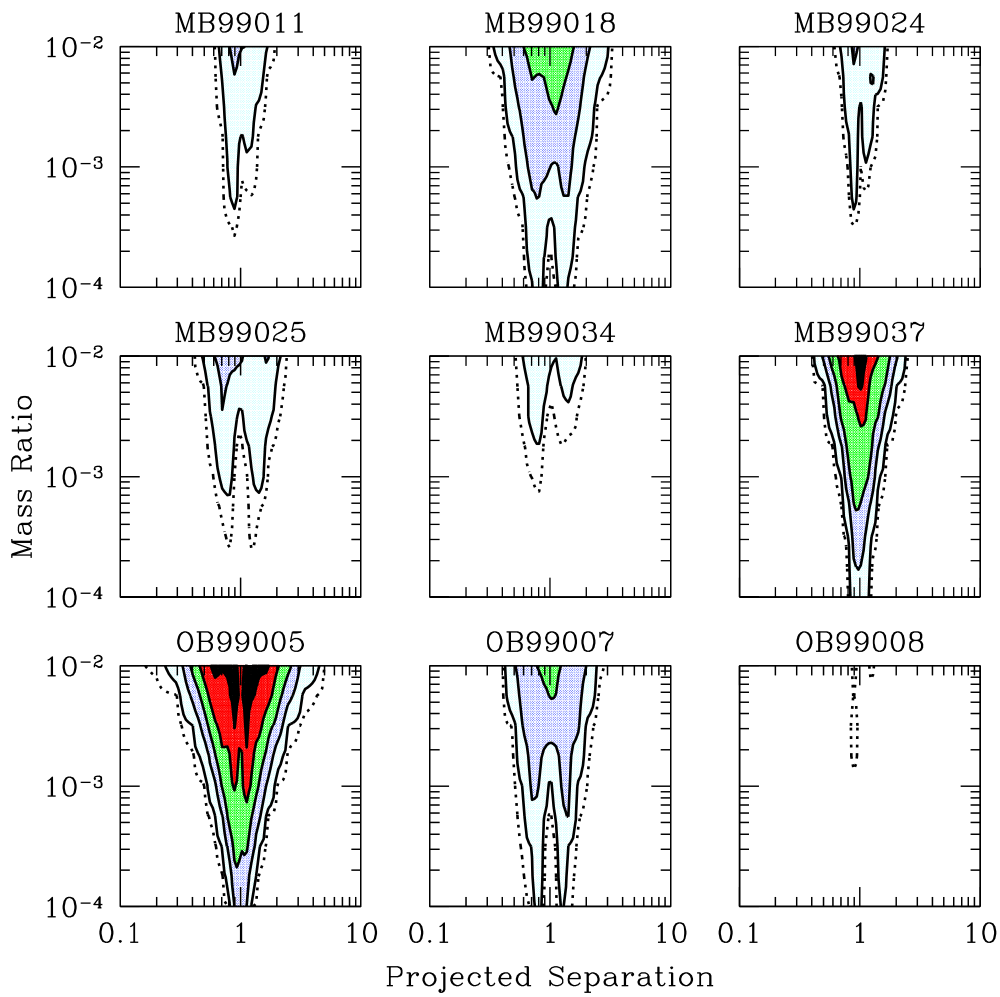

Continued

Fig. 4.7.— Continued

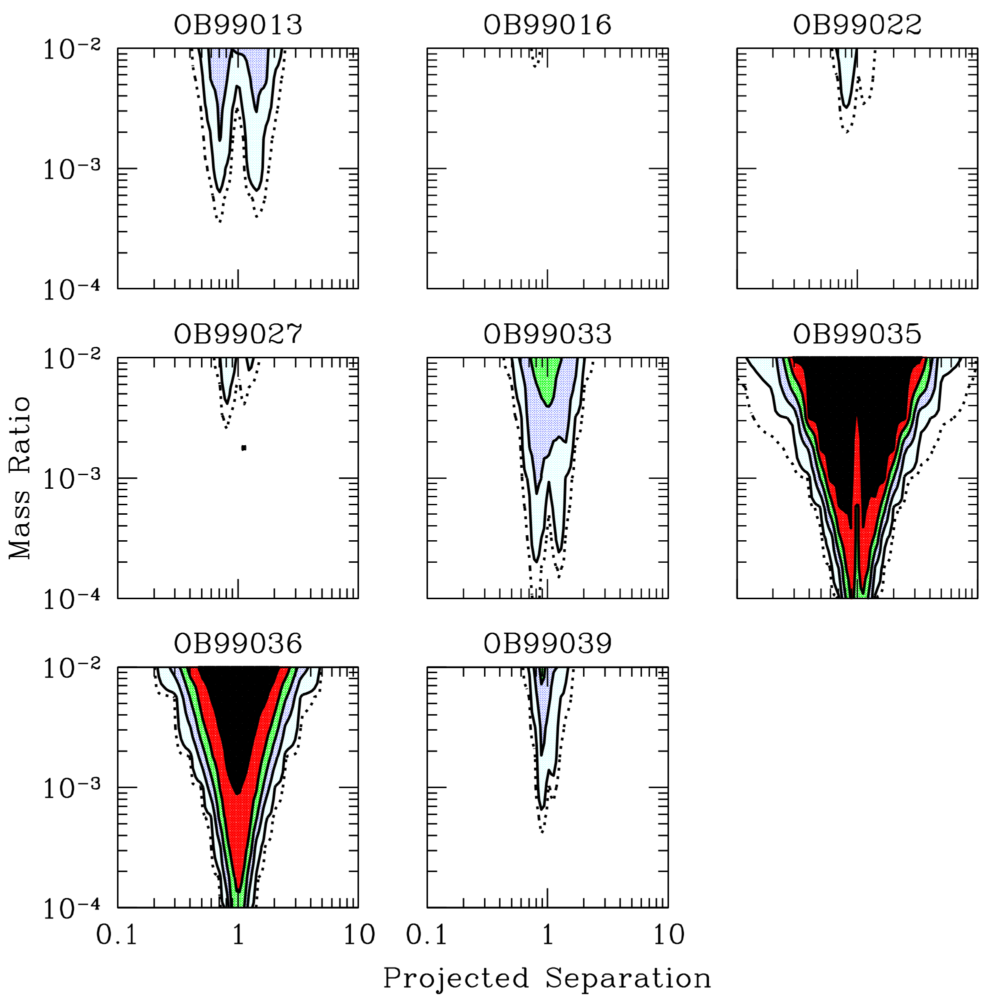

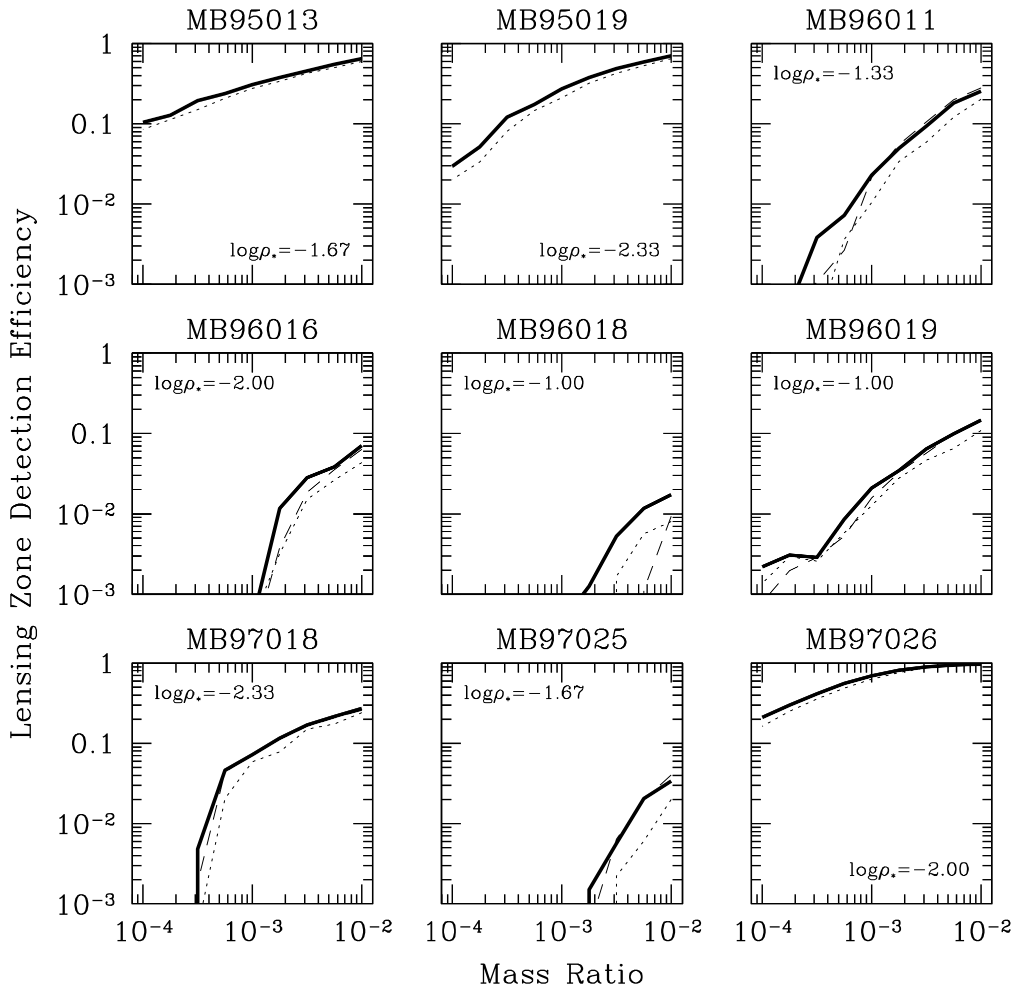

Continued

Fig. 4.8.— The solid heavy lines are the point-source detection efficiencies averaged over the lensing zone ($0.6 \leq d \leq 1.6$) as a function of the mass ratio of the companion for a threshold of $\Delta\chi^2_{\rm thresh} = 60$. The dotted line is for a threshold of $\Delta\chi^2_{\rm thresh} = 100$. The dashed line is the lensing zone detection efficiency for $\Delta\chi^2_{\rm thresh} = 60$ assuming a finite source of size ρ_* Each panel is for a separate event; the abbreviated event name is indicated above the panel and the adopted source size for the finite source efficiencies is also shown.

Fig. 4.8.— Continued

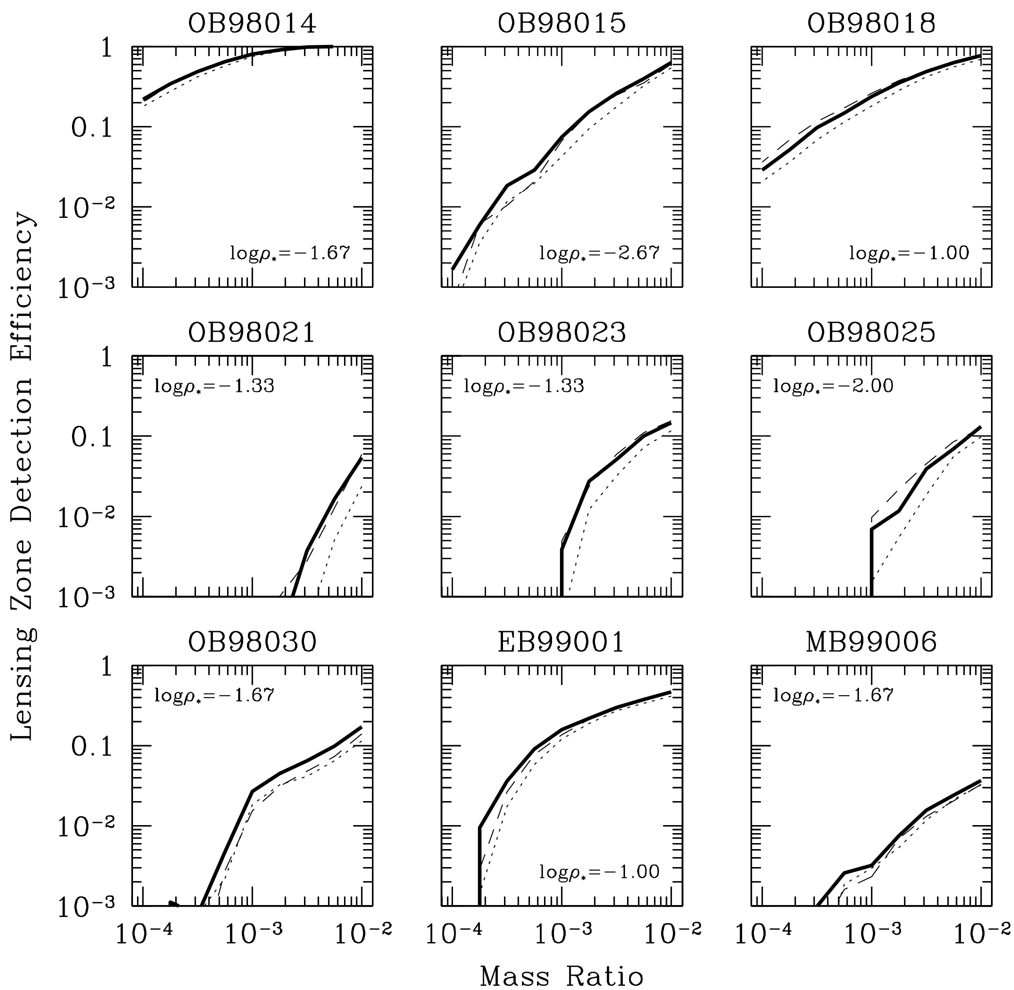

Continued

Fig. 4.8.— Continued

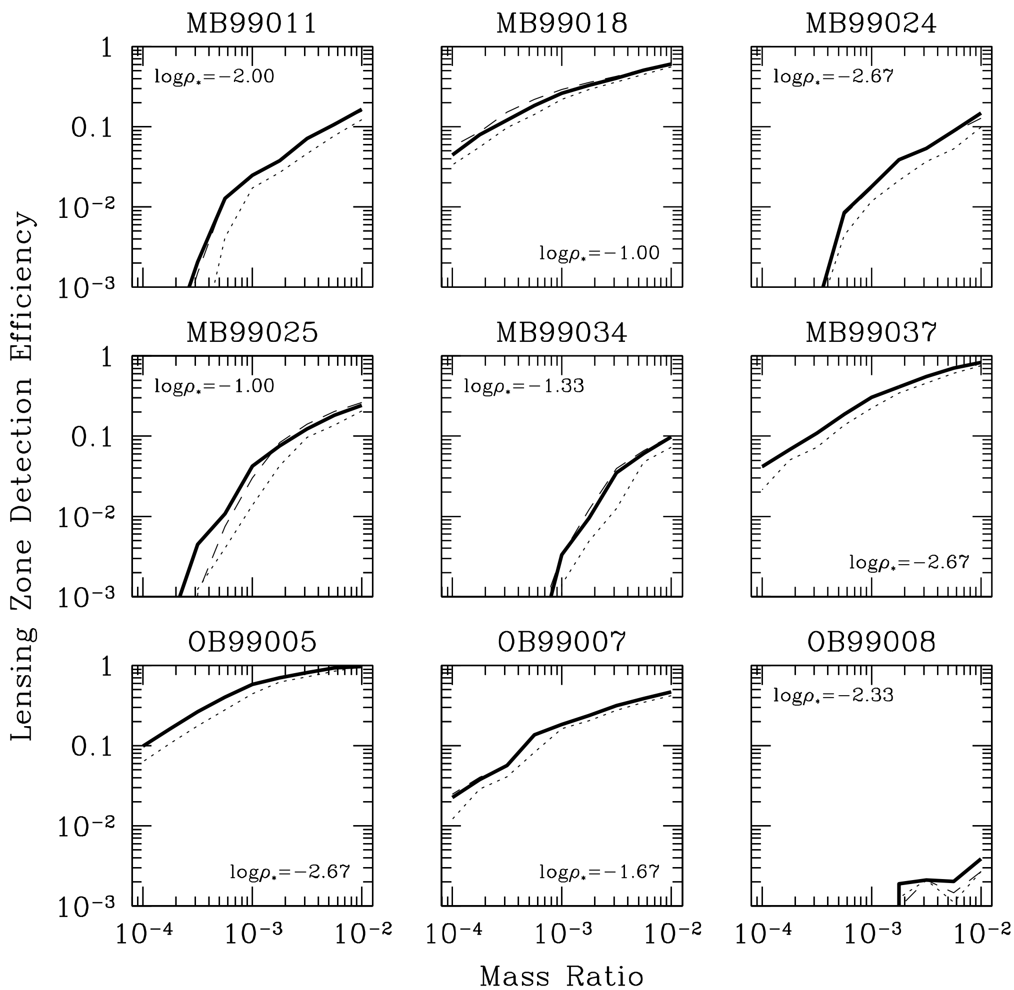

Continued

Fig. 4.8.— Continued

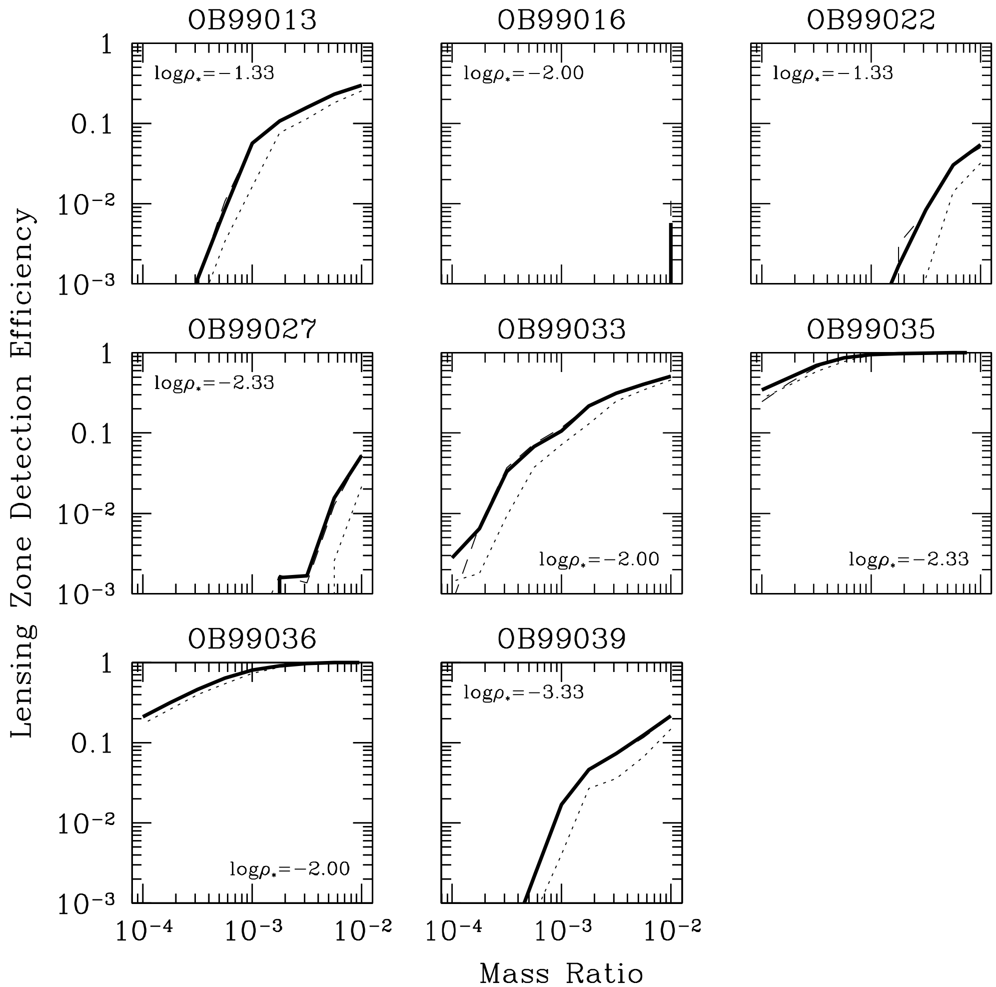

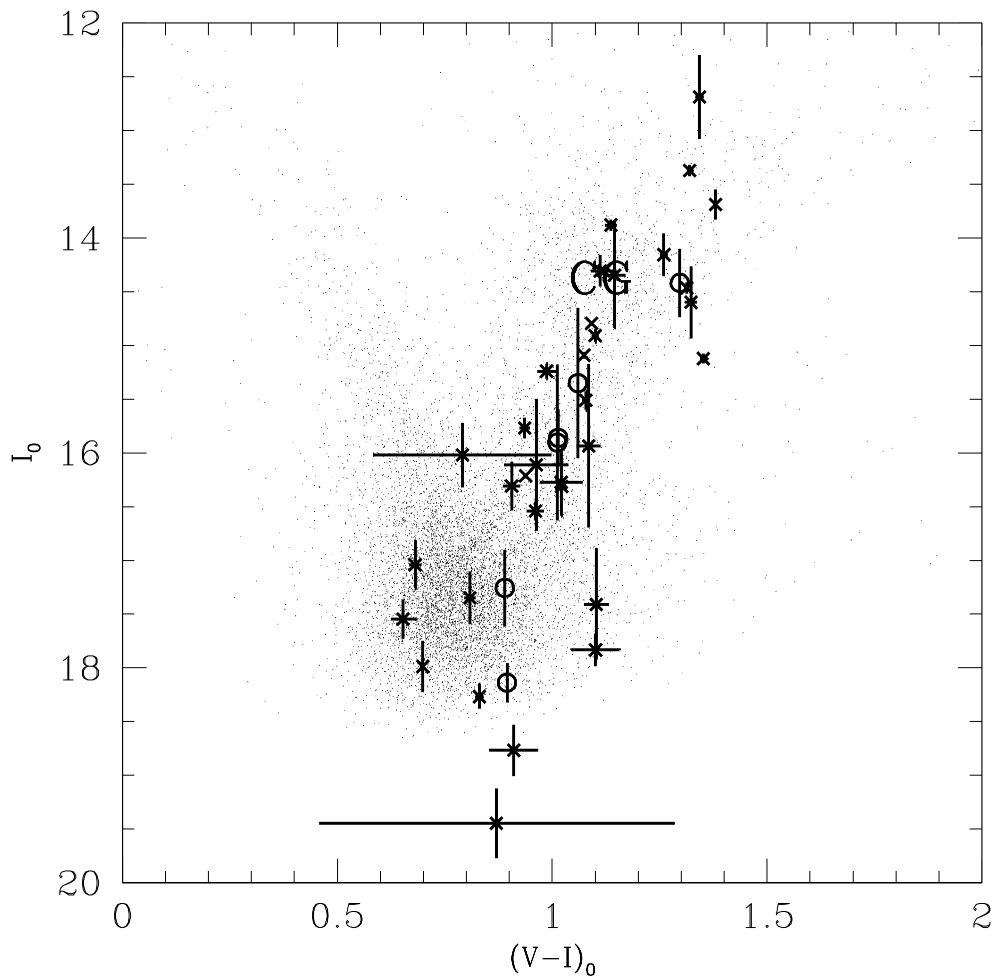

Fig. 4.9.— The dereddened, "clump" calibrated color-magnitude diagram for our sources. Crosses indicate those sources for which separate I_0 and $(V - I)_0$ determination was possible; circles indicate those events for which the $(V - I)_0$ was assumed to be typical of stars with the same I_0 as measured for the event. The center of the clump is indicated with "CG". Also shown is the CMD of a typical field (small dots).

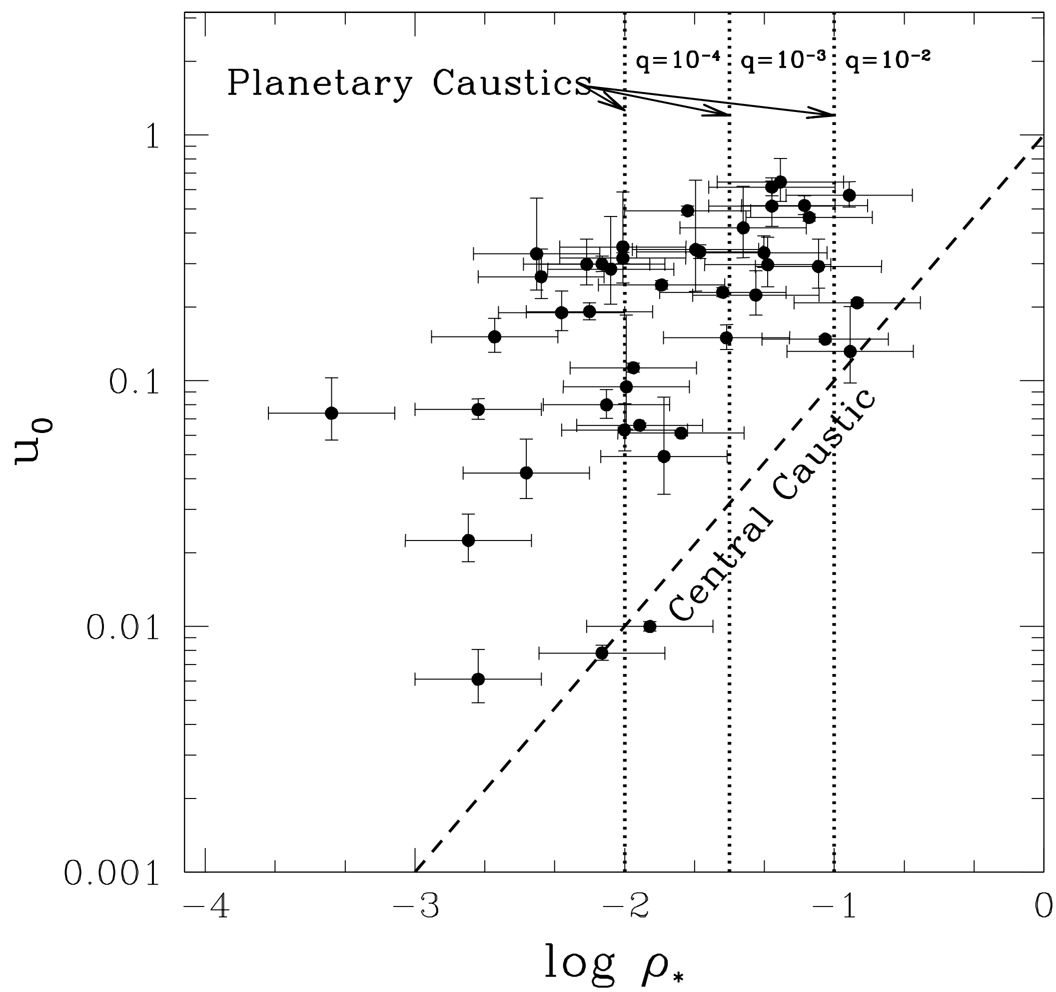

Fig. 4.10.— The impact parameter, u_0, is plotted versus the logarithm of the source size ρ_* in units of the angular Einstein ring radius $\theta_{\rm E}$. The dotted lines indicate the boundaries where finite source effects become important for the detection of the companion via the planetary caustics for the mass ratios indicated; source sizes to the right of these boundaries significantly affect the amplitude and duration of the deviation caused by the planetary caustics. The dashed line indicates the boundary of the region where finite source effects become important for the detection of the companion via the central caustic.

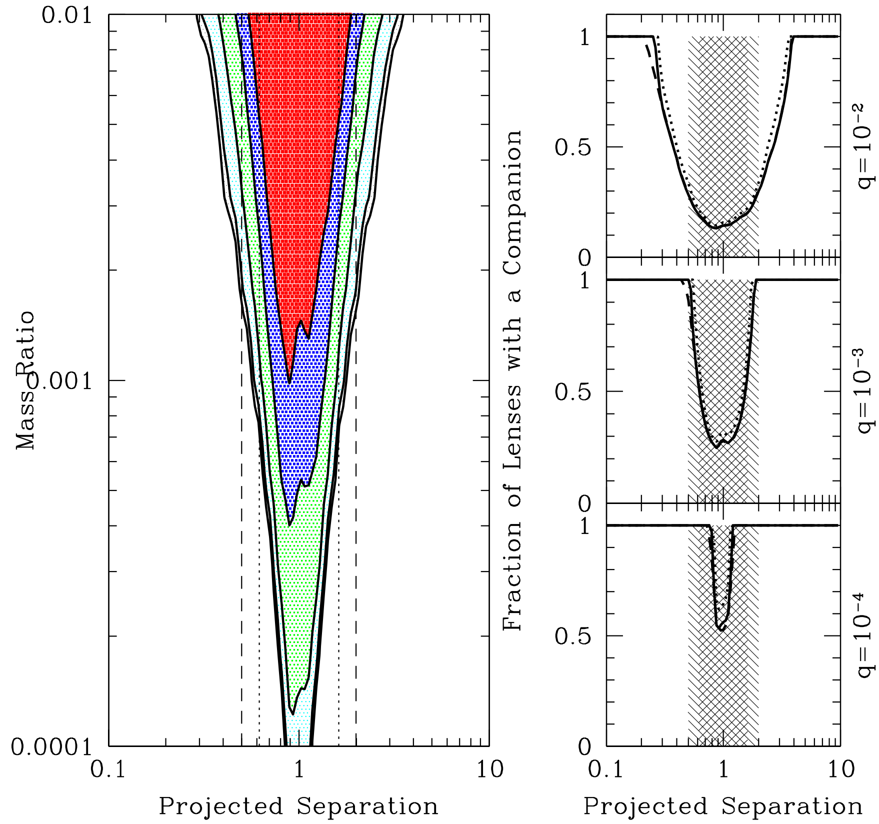

Fig. 4.11.— *Left Panel*: The 95% c.l. upper limit to the fraction of primary lenses with a companion derived from the efficiencies of 42 events, as a function of the mass ratio and projected separation of the companion. The solid black lines show upper limit contours of 75%, 66%, 50%, 33% and 25% (outer to inner), i.e. $< 25\%$ of all primary lenses have companions with any combination of mass ratio and separation within the 25% contour. The dotted (dashed) vertical lines indicate the boundaries of the lensing zone (extended lensing zone). *Right Panels*: Cross sections through the right panel (fraction of lenses with a companion as a function of projected separation) for three different mass ratios. The solid line is derived from the point-source efficiencies with a threshold of $\Delta\chi^2_{\rm thresh} = 60$. The dotted line is derived from the point-source efficiencies with a threshold of $\Delta\chi^2_{\rm thresh} = 100$. The dashed line is finite-source efficiencies with a threshold of $\Delta\chi^2_{\rm thresh} = 60$. The heavy (light) shaded region indicates the extend of the lensing zone (extended lensing zone).

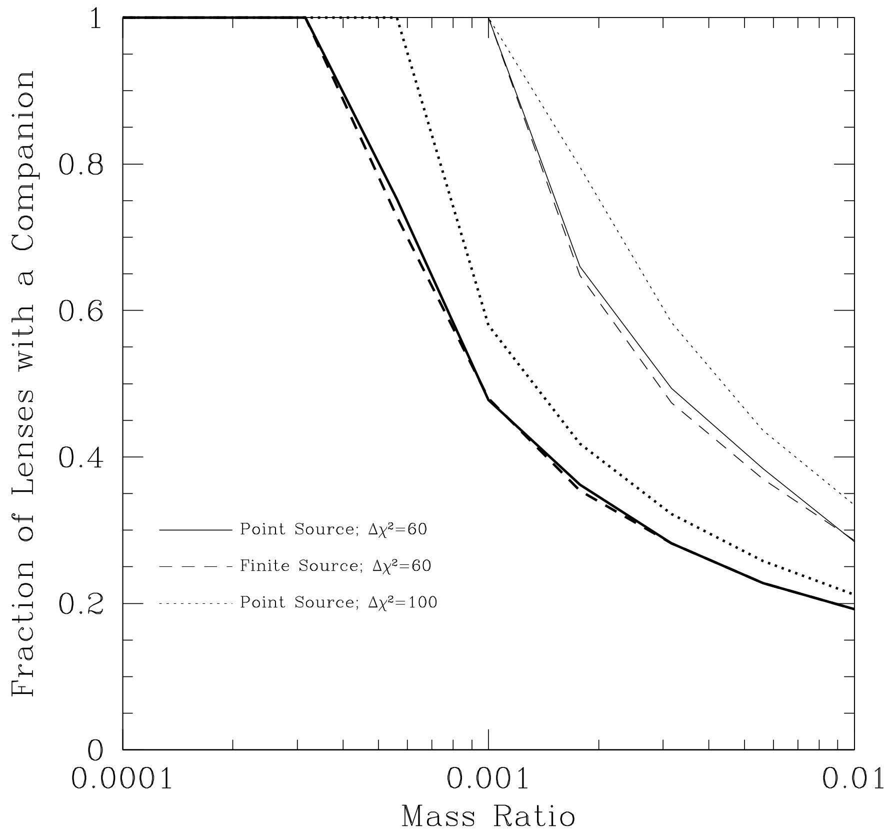

Fig. 4.12.— Upper limits to the fraction of primary lenses with a companion as a function of the mass ratio between the companion and the primary. The bold lines are for companions with projected separations in the lensing zone, $0.6 - 1.6\ r_{\rm E}$. The light lines are for projected separations in the extended lensing zone, $0.5 - 2\ r_{\rm E}$.

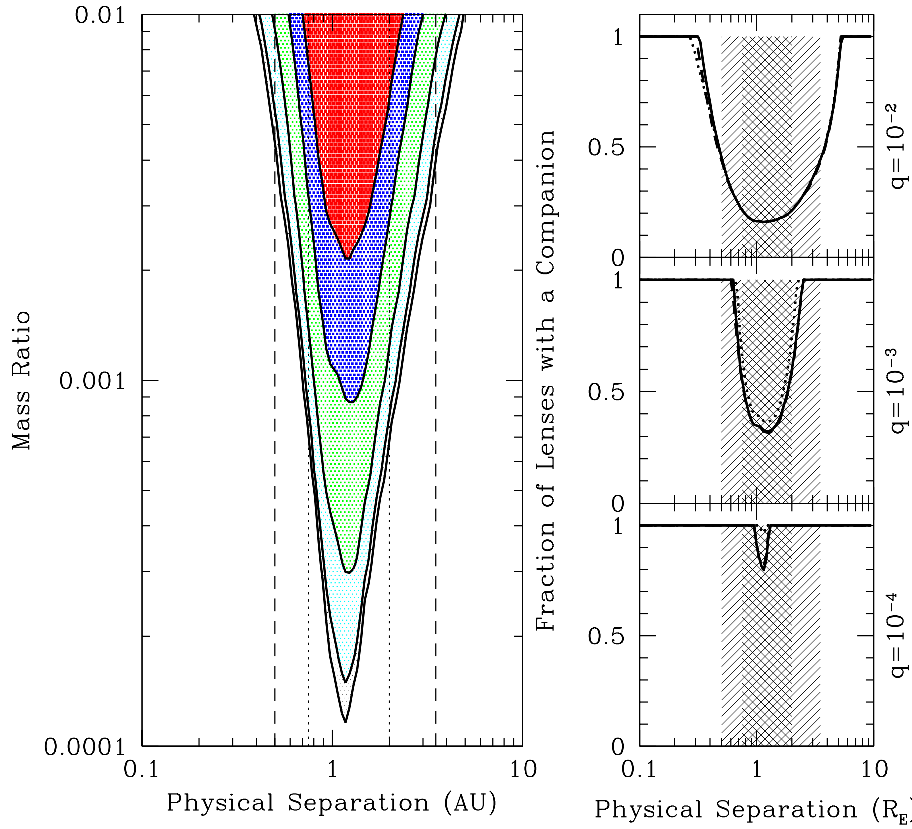

Fig. 4.13.— Same as Fig. 4.11, except we have integrated over all possible orbital inclinations and phases to convert from projected separation to physical separation.

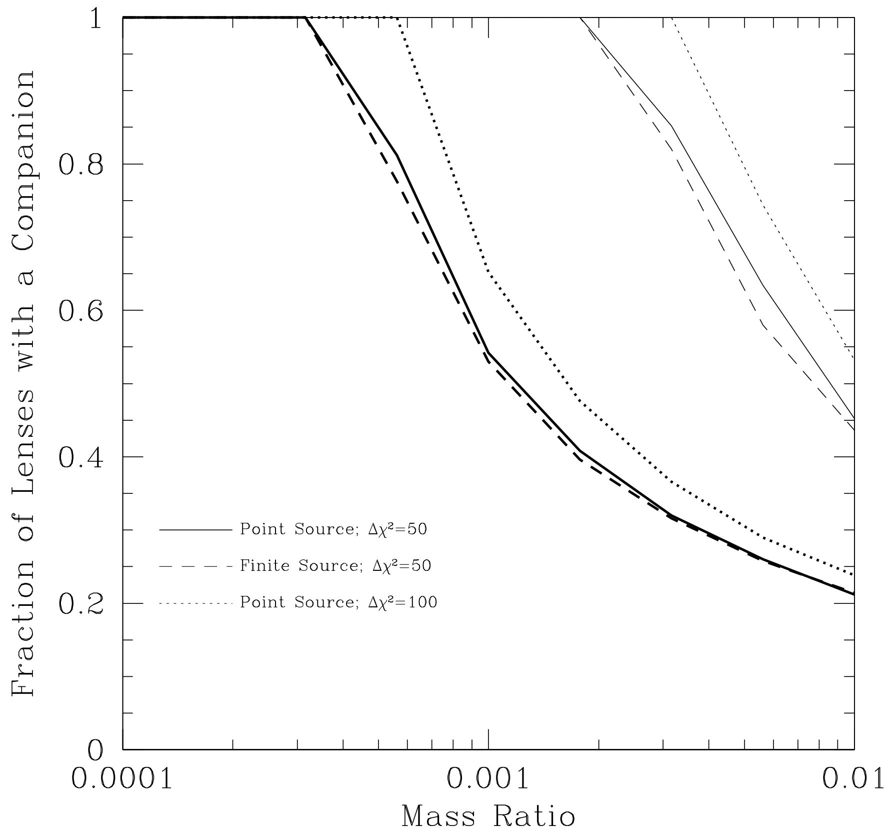

Fig. 4.14.— Upper limits to the fraction of primary lenses with a companion as a function of the mass ratio between the companion and the primary. The bold lines are for companions with physical separations $0.75 - 2\ r_{\rm E}$. The light lines are for physical separations in the extended lensing zone, $0.5 - 3.5\ r_{\rm E}$. This figure is essentially identical to Fig. 4.12, except we have integrated over all possible orbital inclinations and phases to convert from projected separation to physical separation.

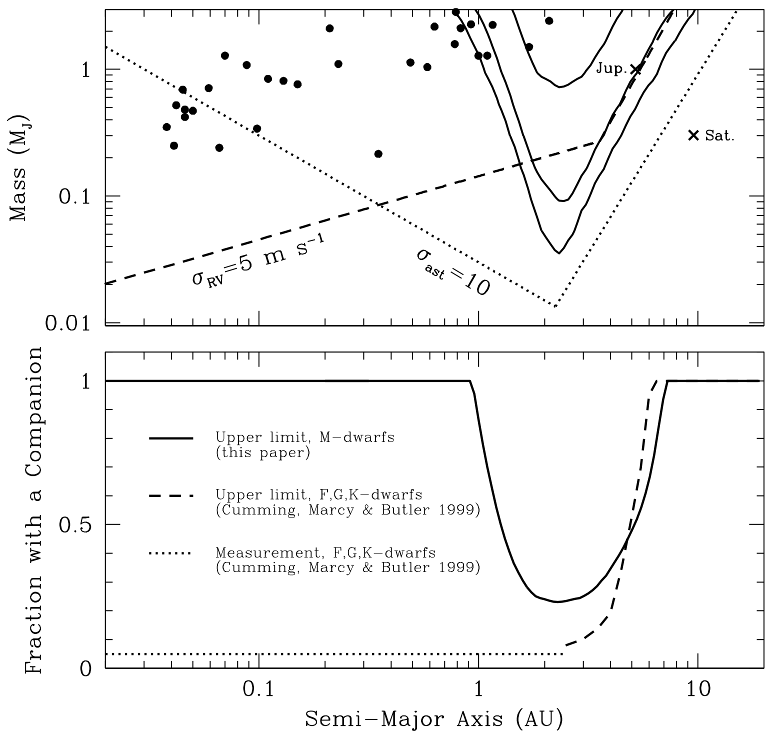

Fig. 4.15.— *Upper Panel* Our 95% c.l. upper limit to the fraction of M-dwarf primaries with a as a function of the mass $m_{\rm p}$ and semi-major axis a of the companion. The solid black lines show upper limit contours of 75%, 50%, and 25%. The points show the $m_{\rm p} \sin i, a$ of companions to stars (mostly G-dwarfs) in the local neighborhood detected by radial velocity surveys. Jupiter and Saturn are marked with crosses. The dotted line shows the radial-velocity detection limit for an accuracy of 5 ms^{-1} and a primary mass of 0.3 $M_{\odot}$, and a survey lifetime of 10 years. The dashed line is the astrometric detection limit for an accuracy of 10 μas, a primary of mass 0.3 $M_{\odot}$ at 10 pc, and a survey lifetime of 5 years. *Bottom Panel*: The solid line is our upper limit to the fraction of stars with a companion of mass $1-3$ $M_{\rm Jup}$ as a function of the semi-major axis a. The dashed line is the upper limit to the fraction of F,G, and K-dwarf primaries with companions of mass >1 $M_{\rm Jup}$ as determined from the Lick radial velocity survey Cumming, Marcy, & Butler (1999). The dotted line is the fraction of local G-stars with extrasolar planets of mass $ga0.5$ $M_{\rm Jup}$ from the Lick survey, $\sim 5\%$.

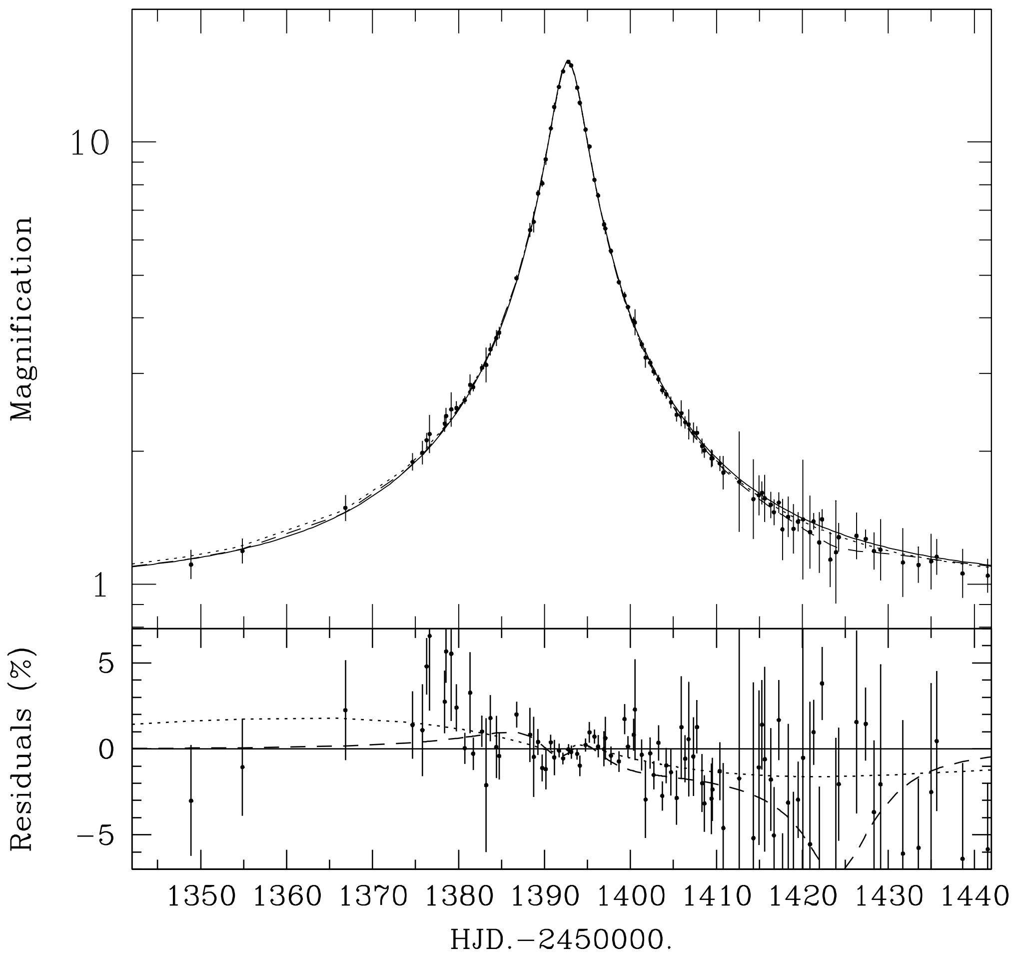

Fig. 4.16.— *Top Panel*: The points with error bars show the magnification as a function of time for PLANET and OGLE data of event OGLE-1999-BUL-36, binned into 1 day intervals. The solid line shows the best-fit point-source point-lens (PSPL) model, while the dotted line shows the best-fit parallax asymmetry model, and the dashed line shows the best-fit binary model. *Bottom Panel*: The residuals from the best-fit PSPL model (in %) as a function of time. The dotted (dashed) line shows the deviation of the parallax asymmetry (binary-lens) model from the PSPL model.

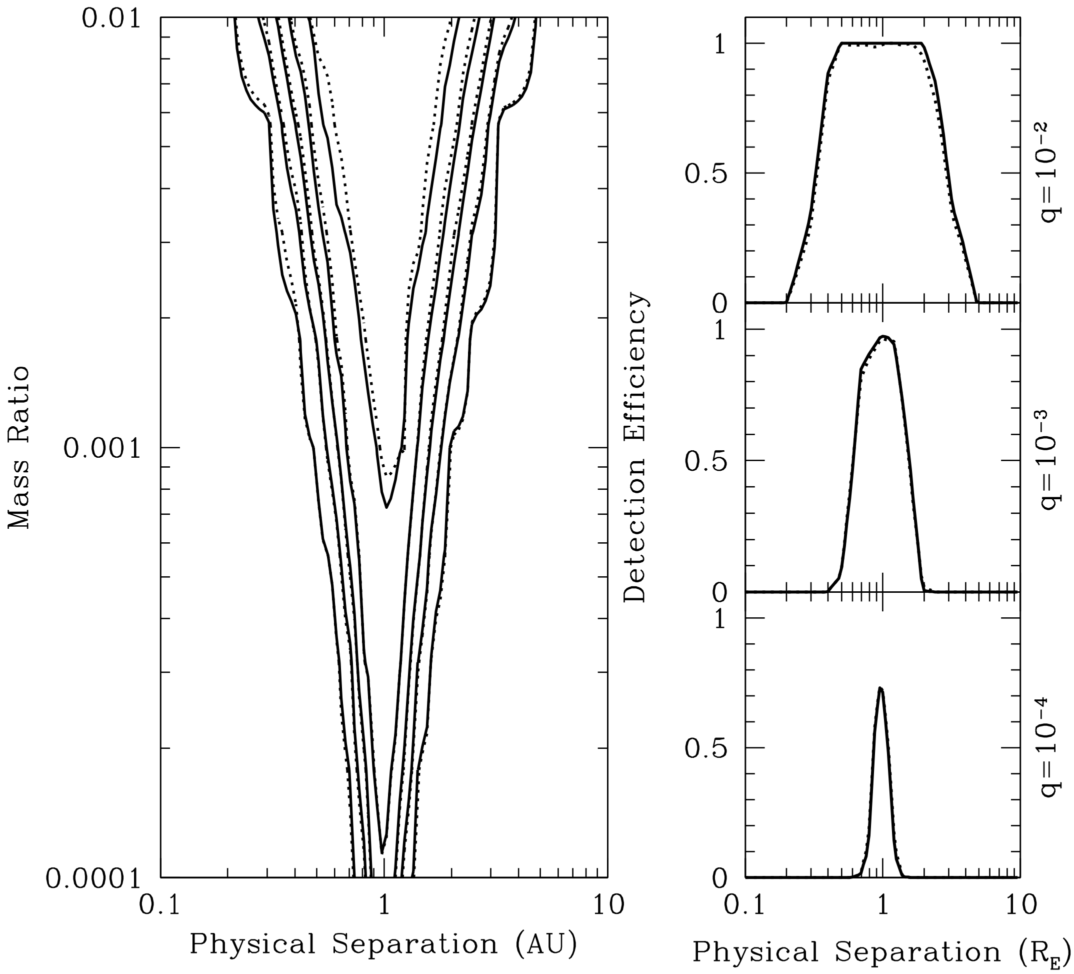

Fig. 4.17.— *Left Panel*: Contours of constant detection efficiency, ϵ, as a function of mass ratio and projected separation for event OB98014. The contours are $\epsilon = 5\%, 25\%, 50\%, 75\%$, and 95% (outer to inner). The solid contours are the efficiencies under the assumption that the parallax asymmetry parameter is zero, while the dotted contours are calculated with the asymmetry as a free parameter. *Right Panels*: Detection efficiencies as a function of projected separation for three mass ratios. The solid lines are for no parallax asymmetry, and the dashed lines are with asymmetry as a free parameter.

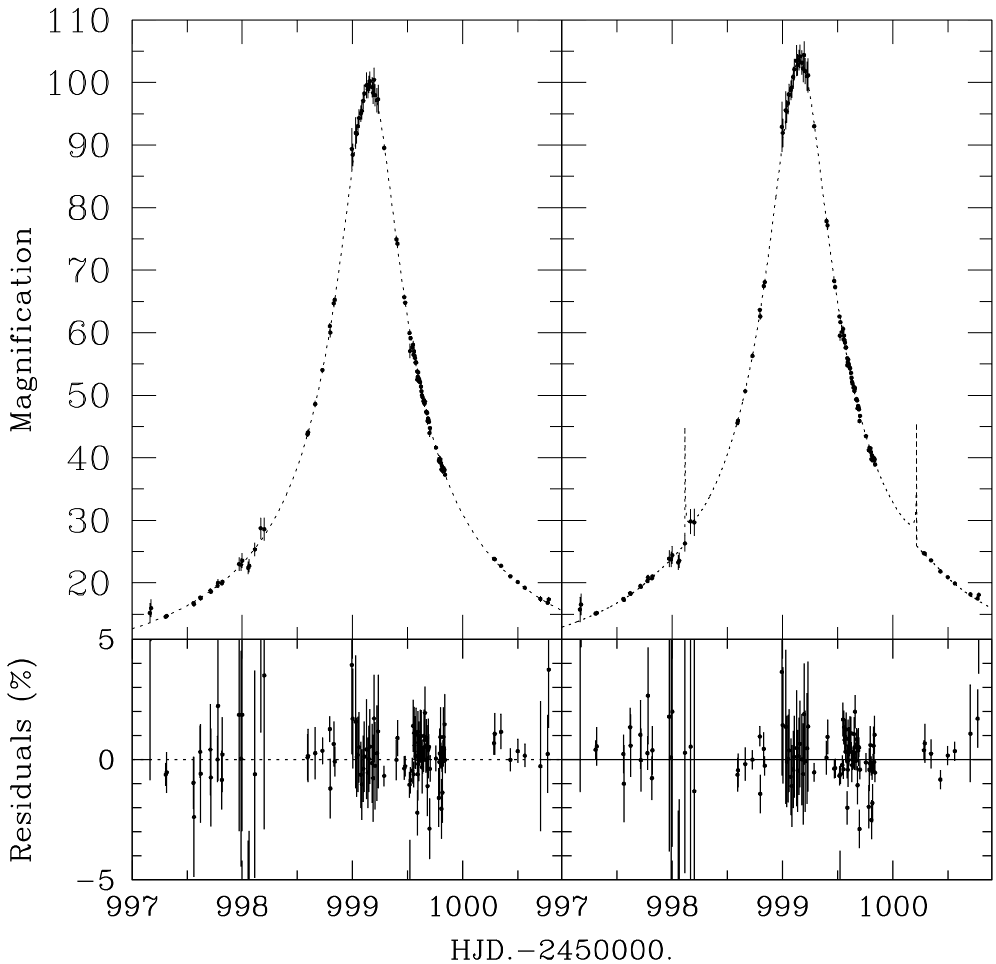

Fig. 4.18.— *Left Panels*: The PLANET data for event MACHO 98-BLG-35, along with the best-fit single-lens model and residuals. *Right Panels*: A binary-lens model fit and residuals with mass ratio $\log(q) = -3.05$ and projected separation $d = 1.00$.

Official Alert Name	Abbreviated Name	Status	Notes
MACHO 95-BLG-10	MB95010	Cut	Error in u_0
MACHO 95-BLG-12	MB95010	Cut	Binary[1,2]
MACHO 95-BLG-13	MB95013	Passed	–
MACHO 95-BLG-17	MB95017	Cut	Error in u_0
MACHO 95-BLG-18	MB95018	Cut	Error in u_0
MACHO 95-BLG-19	MB95019	Passed	–
MACHO 95-BLG-21	MB95021	Cut	Insufficient Data
MACHO 95-BLG-24	MB95024	Cut	Insufficient Data
MACHO 95-BLG-25	MB95025	Cut	Insufficient Data
MACHO 95-BLG-30	MB95030	Cut	Error in u_0
OGLE-1995-BUL-04	OB95004	Cut	Error in u_0
MACHO 96-BLG-1	MB96001	Cut	Insufficient Data
MACHO 96-BLG-4	MB96004	Cut	Binary[2]
MACHO 96-BLG-5	MB96005	Cut	Error in u_0
MACHO 96-BLG-6	MB96006	Cut	Error in u_0
MACHO 96-BLG-7	MB96007	Cut	Error in u_0
MACHO 96-BLG-8	MB96008	Cut	Error in u_0
MACHO 96-BLG-9	MB96009	Cut	Error in u_0
MACHO 96-BLG-10	MB96010	Cut	Error in u_0
MACHO 96-BLG-11	MB96011	Passed	–
MACHO 96-BLG-12	MB96012	Cut	Error in u_0
MACHO 96-BLG-13	MB96013	Cut	Insufficient Data
MACHO 96-BLG-14	MB96014	Cut	Error in u_0
MACHO 96-BLG-15	MB96015	Cut	Insufficient Data
MACHO 96-BLG-16	MB96016	Passed	–
MACHO 96-BLG-17	MB96017	Cut	Insufficient Data
MACHO 96-BLG-18	MB96018	Passed	–
MACHO 96-BLG-19	MB96019	Passed	–
MACHO 96-BLG-20	MB96020	Cut	Error in u_0
MACHO 96-BLG-21	MB96021	Cut	Error in u_0
MACHO 96-BLG-23	MB96023	Cut	Error in u_0
MACHO 96-BLG-24	MB96024	Cut	Insufficient Data
MACHO 96-BLG-25	MB96025	Cut	Error in u_0
MACHO 96-BLG-26	MB96026	Cut	Error in u_0
MACHO 96-BLG-27	MB96027	Cut	Insufficient Data

Continued

Table 4.1: All Events from 1995-1999 with PLANET data.

Table 4.1.— Continued

Official Alert Name	Abbreviated Name	Status	Notes
MACHO 97-BLG-10	MB97010	Cut	Insufficient Data
MACHO 97-BLG-18	MB97018	Passed	–
MACHO 97-BLG-25	MB97025	Passed	–
MACHO 97-BLG-26	MB97026	Passed	–
MACHO 97-BLG-28	MB97028	Cut	Binary[3,2]
MACHO 97-BLG-30	MB97030	Passed	–
MACHO 97-BLG-31	MB97031	Passed	–
MACHO 97-BLG-36	MB97036	Cut	Insufficient Data
MACHO 97-BLG-37	MB97037	Cut	Error in u_0
MACHO 97-BLG-41	MB97041	Cut	Binary[4]
MACHO 97-BLG-49	MB97049	Cut	Insufficient Data
MACHO 97-BLG-50	MB97050	Cut	Error in u_0
MACHO 97-BLG-52	MB97052	Cut	Error in u_0
MACHO 97-BLG-54	MB97054	Cut	Insufficient Data
MACHO 97-BLG-56	MB97056	Cut	Insufficient Data
MACHO 97-BLG-58	MB97058	Cut	Insufficient Data
MACHO 97-BLG-59	MB97059	Cut	Insufficient Data

Continued

Table 4.1.— Continued

Official Alert Name	Abbreviated Name	Status	Notes
EROS BLG-1998-2	EB98002	Passed	–
EROS BLG-1998-4	EB98004	Cut	Insufficient Data
MACHO 98-BLG-1	MB98001	Cut	Insufficient Data
MACHO 98-BLG-5	MB98005	Cut	Insufficient Data
MACHO 98-BLG-6	MB98006	Cut	Parallax
MACHO 98-BLG-12	MB98005	Cut	Binary
MACHO 98-BLG-13	MB98013	Passed	–
MACHO 98-BLG-14	MB98013	Cut	Binary
MACHO 98-BLG-16	MB98016	Cut	Binary
MACHO 98-BLG-17	MB98017	Cut	Error in u_0
MACHO 98-BLG-18	MB98018	Cut	Error in u_0
MACHO 98-BLG-19	MB98019	Cut	Insufficient Data
MACHO 98-BLG-22	MB98022	Cut	Insufficient Data
MACHO 98-BLG-24	MB98024	Cut	Insufficient Data
MACHO 98-BLG-26	MB98026	Passed	–
MACHO 98-BLG-27	MB98027	Cut	Error in u_0[a]
MACHO 98-BLG-28	MB98028	Cut	Insufficient Data
MACHO 98-BLG-30	MB98030	Passed	–
MACHO 98-BLG-31	MB98031	Cut	Insufficient Data
MACHO 98-BLG-33	MB98033	Passed	–
MACHO 98-BLG-35	MB98035	Passed	–
MACHO 98-BLG-37	MB98037	Cut	Error in u_0
MACHO 98-BLG-38	MB98038	Cut	Error in u_0
MACHO 98-BLG-39	MB98039	Cut	Error in u_0
MACHO 98-BLG-40	MB98040	Cut	Error in u_0
MACHO 98-BLG-42	MB98042	Cut	Binary[2]
∗OGLE-1998-BUL-13	OB98013	Passed	–
∗OGLE-1998-BUL-14	OB98014	Passed	–
∗OGLE-1998-BUL-15	OB98015	Passed	–
∗OGLE-1998-BUL-18	OB98018	Passed	–
∗OGLE-1998-BUL-20	OB98020	Cut	Insufficient Data
∗OGLE-1998-BUL-21	OB98021	Passed	–
∗OGLE-1998-BUL-23	OB98023	Passed	–
∗OGLE-1998-BUL-25	OB98025	Passed	–
∗OGLE-1998-BUL-26	OB98026	Cut	Error in u_0
∗OGLE-1998-BUL-27	OB98027	Cut	Error in u_0
∗OGLE-1998-BUL-28	OB98028	Cut	Binary
∗OGLE-1998-BUL-29	OB98029	Cut	Finite Source
∗OGLE-1998-BUL-30	OB98030	Passed	–

Continued

Table 4.1.— Continued

Official Alert Name	Abbreviated Name	Status	Notes
EROS BLG-1999-1	EB99001	Passed	–
EROS BLG-1999-2	EB99002	Cut	Insufficient Data
∗MACHO 99-BLG-6	MB99006	Passed	–
∗MACHO 99-BLG-8	MB99008	Cut	Parallax
∗MACHO 99-BLG-11	MB99011	Passed	–
∗MACHO 99-BLG-18	MB99018	Passed	–
∗MACHO 99-BLG-22	MB99022	Passed	–
∗MACHO 99-BLG-24	MB99024	Passed	–
∗MACHO 99-BLG-25	MB99025	Passed	Binary Source?
∗MACHO 99-BLG-34	MB99034	Passed	–
∗MACHO 99-BLG-37	MB99037	Passed	–
∗MACHO 99-BLG-42	MB99042	Cut	Insufficient Data
∗MACHO 99-BLG-45	MB99045	Cut	Insufficient Data
∗MACHO 99-BLG-47	MB99047	Cut	Binary
∗MACHO 99-BLG-57	MB99057	Cut	Binary Lens/Binary Source?
∗OGLE-1998-BUL-5	OB99005	Passed	–
∗OGLE-1999-BUL-7	OB99007	Passed	–
∗OGLE-1999-BUL-8	OB99008	Passed	–
∗OGLE-1999-BUL-11	OB99011	Cut	Binary
∗OGLE-1999-BUL-13	OB99013	Passed	–
∗OGLE-1999-BUL-14	OB99014	Cut	Error in u_0
∗OGLE-1999-BUL-16	OB99016	Passed	–
∗OGLE-1999-BUL-17	OB99017	Cut	Insufficient Data
∗OGLE-1999-BUL-19	OB99019	Cut	Insufficient Data
∗OGLE-1999-BUL-22	OB99022	Passed	–
∗OGLE-1999-BUL-23	OB99023	Cut	Binary[4]
∗OGLE-1999-BUL-25	OB99025	Cut	Binary?
∗OGLE-1999-BUL-27	OB99027	Passed	–
∗OGLE-1999-BUL-33	OB99033	Passed	–
∗OGLE-1999-BUL-35	OB99035	Passed	–
∗OGLE-1999-BUL-36	OB99036	Passed	–
∗OGLE-1999-BUL-39	OB99039	Passed	–
∗OGLE-1999-BUL-42	OB99042	Cut	Error in u_0
∗OGLE-1999-BUL-43	OB99043	Cut	Insufficient Data

[a] Also shows evidence for binarity

∗MACHO and/or OGLE data included in the PSPL fit.

References. — (1)Albrow et al. (1998); (2) Alcock et al. (2000); (3)Albrow et al. (1999); (4)Albrow et al. (2000); (5)Albrow et al. (2000).

Event Name	t_0[a] (HJD-2450000.)	t_E[a] (days)	u_0[a] (%)	$\delta u_0/u_0$
MB95013	-101.169 ± 0.034	80.85 ± 2.71	0.245 ± 0.010	3
MB95019	-93.573 ± 0.030	38.22 ± 6.41	0.189 ± 0.035	18
MB96011	241.405 ± 0.058	10.59 ± 1.66	0.223 ± 0.046	20
MB96016	259.777 ± 0.265	57.19 ± 24.70	0.094 ± 0.046	48
MB96018	259.391 ± 0.041	7.07 ± 1.98	0.132 ± 0.045	34
MB96019	266.944 ± 0.129	12.03 ± 1.95	0.292 ± 0.065	22
MB97018	609.529 ± 0.497	100.19 ± 30.14	0.329 ± 0.134	40
MB97025	598.011 ± 1.423	20.75 ± 6.18	0.342 ± 0.164	47
MB97026	636.624 ± 0.007	68.17 ± 2.70	0.113 ± 0.005	4
MB97030	601.243 ± 0.050	23.43 ± 2.69	0.080 ± 0.011	13
MB97031	593.439 ± 1.772	41.05 ± 4.33	0.645 ± 0.128	19
EB98002	964.024 ± 0.041	23.97 ± 1.12	0.335 ± 0.021	6
MB98013	930.529 ± 0.027	18.24 ± 3.47	0.063 ± 0.014	21
MB98026	986.377 ± 0.022	33.73 ± 1.15	0.229 ± 0.009	4
MB98030	992.117 ± 0.093	26.95 ± 8.95	0.285 ± 0.111	38
MB98033	990.463 ± 0.002	7.33 ± 0.15	0.148 ± 0.004	2
MB98035	999.157 ± 0.001	27.46 ± 1.17	0.010 ± 0.000	4
OB98013	945.081 ± 0.157	55.30 ± 3.03	0.299 ± 0.022	7
OB98014	956.033 ± 0.005	41.52 ± 0.78	0.061 ± 0.001	2
OB98015	943.840 ± 0.007	52.24 ± 10.72	0.006 ± 0.001	24
OB98018	971.078 ± 0.006	7.64 ± 0.16	0.208 ± 0.006	2
OB98021	992.190 ± 0.410	26.64 ± 5.75	0.419 ± 0.135	32
OB98023	998.735 ± 0.151	18.60 ± 2.92	0.514 ± 0.107	20
OB98025	1041.701 ± 0.250	50.49 ± 7.88	0.298 ± 0.063	21
OB98030	1043.417 ± 0.069	54.26 ± 21.85	0.049 ± 0.021	42
EB99001	1415.023 ± 0.021	20.19 ± 1.39	0.517 ± 0.045	8
MB99006	1247.546 ± 0.130	27.24 ± 1.69	0.150 ± 0.017	11
MB99011	1286.711 ± 0.117	45.17 ± 2.42	0.191 ± 0.015	7
MB99018	1301.897 ± 0.019	21.69 ± 0.52	0.462 ± 0.016	3
MB99024	1304.710 ± 0.192	59.74 ± 7.37	0.151 ± 0.024	15
MB99025	1317.787 ± 0.047	9.55 ± 0.74	0.569 ± 0.067	11
MB99034	1326.699 ± 0.152	7.04 ± 0.59	0.332 ± 0.049	14
MB99037	1354.220 ± 0.031	63.59 ± 5.63	0.076 ± 0.007	9

Continued

Table 4.2: Point-Source Point-Lens Fit Parameters for the Final Event Sample.

Table 4.2: Continued

Event Name	t_0 [a] (HJD-2450000.)	t_E [a] (days)	u_0 [a] (%)	$\delta u_0/u_0$
OB99005	1275.168 ± 0.009	72.24 ± 15.48	0.022 ± 0.005	21
OB99007	1316.100 ± 0.048	36.87 ± 1.05	0.492 ± 0.020	4
OB99008	1287.546 ± 0.154	41.94 ± 6.06	0.042 ± 0.011	26
OB99013	1318.005 ± 0.053	19.43 ± 1.09	0.614 ± 0.052	8
OB99016	1334.421 ± 0.615	44.02 ± 11.91	0.351 ± 0.142	40
OB99022	1323.514 ± 0.066	7.68 ± 1.23	0.297 ± 0.067	22
OB99027	1365.833 ± 0.280	50.59 ± 7.82	0.265 ± 0.060	22
OB99033	1434.789 ± 0.099	58.67 ± 2.18	0.316 ± 0.016	5
OB99035	1392.552 ± 0.001	48.97 ± 3.32	0.008 ± 0.001	6
OB99036	1392.730 ± 0.004	29.84 ± 0.55	0.066 ± 0.001	2
OB99039	1436.605 ± 0.395	219.90 ± 55.16	0.074 ± 0.021	28

[a] t_0=time of maximum magnification; t_E=Einstein ring radius crossing time; u_0=minimum impact parameter.

Event Name	# Points	$\sigma_{\rm med}$[a] (%)	$\Delta t_{\rm med}$[a] (hrs)	$\Delta t_{\rm med}/t_E$
MB95013	266	0.7	1.21	6.23×10^{-4}
MB95019	163	1.4	1.54	1.68×10^{-3}
MB96011	40	2.5	3.62	1.43×10^{-2}
MB96016	169	6.3	0.20	1.46×10^{-4}
MB96018	21	4.4	2.34	1.38×10^{-2}
MB96019	95	1.5	1.47	5.10×10^{-3}
MB97018	257	2.6	2.08	8.66×10^{-4}
MB97025	78	1.5	3.09	6.21×10^{-3}
MB97026	556	1.1	0.71	4.34×10^{-4}
MB97030	106	2.2	1.91	3.39×10^{-3}
MB97031	328	0.8	1.08	1.09×10^{-3}
EB98002	160	1.2	1.81	3.15×10^{-3}
MB98013	80	5.0	1.93	4.42×10^{-3}
MB98026	253	1.3	2.34	2.90×10^{-3}
MB98030	82	2.2	4.86	7.51×10^{-3}
MB98033	278	1.0	0.19	1.10×10^{-3}
MB98035	356	4.6	1.02	1.55×10^{-3}
OB98013	147	1.2	2.71	2.04×10^{-3}
OB98014	619	1.9	1.02	1.02×10^{-3}
OB98015	121	7.0	1.19	9.49×10^{-4}
OB98018	404	1.4	0.25	1.39×10^{-3}
OB98021	115	6.3	1.44	2.25×10^{-3}
OB98023	128	1.7	2.35	5.25×10^{-3}
OB98025	148	3.9	1.99	1.64×10^{-3}
OB98030	65	9.9	2.31	1.77×10^{-3}
EB99001	333	0.8	0.84	1.74×10^{-3}
MB99006	38	0.9	1.15	1.76×10^{-3}
MB99011	118	2.9	0.16	1.43×10^{-4}
MB99018	407	0.8	0.28	5.29×10^{-4}
MB99024	74	4.3	7.59	5.30×10^{-3}
MB99025	243	1.8	1.05	4.60×10^{-3}
MB99034	88	1.7	1.70	1.01×10^{-2}
MB99037	301	2.7	0.89	5.84×10^{-4}

Continued

Table 4.3: Data Characteristics for the Final Event Sample.

Table 4.3: Continued

Event Name	# Points	σ_{med}[a] (%)	Δt_{med}[a] (hrs)	$\Delta t_{\mathrm{med}}/t_E$
OB99005	229	2.6	0.27	1.55×10^{-4}
OB99007	388	1.4	2.35	2.66×10^{-3}
OB99008	31	9.1	3.50	3.48×10^{-3}
OB99013	256	1.6	2.53	5.43×10^{-3}
OB99016	75	2.9	1.43	1.35×10^{-3}
OB99022	59	5.7	1.53	8.28×10^{-3}
OB99027	94	3.4	2.58	2.13×10^{-3}
OB99033	162	2.3	1.81	1.29×10^{-3}
OB99035	316	3.4	1.46	1.24×10^{-3}
OB99036	501	2.1	1.05	1.47×10^{-3}
OB99039	77	3.9	23.89	4.53×10^{-3}

[a] σ_{med}: the median photometric error; Δt_{med}: the median sampling interval.

Event Name	$(V-I)_0$	I_0	θ_*[a] (μas)	ρ_*[a]
MB95013	1.137±0.014	13.88± 0.05	8.71	1.61×10^{-2}
MB95019	0.681±0.014	17.04± 0.22	1.38	5.40×10^{-3}
MB96011[b]	1.014	15.86± 0.27	3.21	4.54×10^{-2}
MB96016[b]	1.060	15.35± 0.70	4.20	1.10×10^{-2}
MB96018[c]	–	–	6.00	1.28×10^{-1}
MB96019[b]	1.297	14.42± 0.32	7.27	9.04×10^{-2}
MB97018	0.963±0.075	16.11± 0.61	2.74	4.09×10^{-3}
MB97025	1.085±0.028	15.94± 0.76	3.27	2.36×10^{-2}
MB97026	1.352±0.008	15.12± 0.05	5.36	1.18×10^{-2}
MB97030	1.101±0.057	17.83± 0.15	1.38	8.79×10^{-3}
MB97031	1.343±0.010	12.69± 0.39	16.38	5.97×10^{-2}
EB98002	1.078±0.008	15.51± 0.09	3.95	2.47×10^{-2}
MB98013	0.809±0.013	17.35± 0.24	1.31	1.07×10^{-2}
MB98026	1.313±0.006	14.47± 0.05	7.15	3.17×10^{-2}
MB98030	1.103±0.029	17.41± 0.51	1.68	9.31×10^{-3}
MB98033	1.074±0.002	15.09± 0.03	4.78	9.76×10^{-2}
MB98035	1.022±0.002	16.31± 0.05	2.62	1.43×10^{-2}
OB98013	0.936±0.012	15.77± 0.10	3.12	8.43×10^{-3}
OB98014	1.092±0.004	14.80± 0.02	5.55	2.00×10^{-2}
OB98015	0.911±0.057	18.77± 0.24	0.76	2.18×10^{-3}
OB98018	1.120±0.030	14.31± 0.04	7.07	1.38×10^{-1}
OB98021	1.145±0.026	14.35± 0.49	7.07	3.97×10^{-2}
OB98023	1.323±0.014	14.60± 0.33	6.75	5.43×10^{-2}
OB98025	0.791±0.208	16.02± 0.30	2.39	7.09×10^{-3}
OB98030[c]	–	–	6.00	1.65×10^{-2}
EB99001	1.380±0.005	13.69± 0.14	10.50	7.78×10^{-2}
MB99006[c]	–	–	6.00	3.30×10^{-2}
MB99011	0.961±0.020	16.54± 0.09	2.24	7.43×10^{-3}
MB99018	1.320±0.006	13.37± 0.05	11.86	8.18×10^{-2}
MB99024	0.653±0.028	17.55± 0.18	1.07	2.68×10^{-3}
MB99025	1.260±0.009	14.16± 0.20	8.10	1.27×10^{-1}
MB99034	0.906±0.020	16.31± 0.23	2.34	4.98×10^{-2}
MB99037	0.831±0.010	18.27± 0.11	0.88	2.06×10^{-3}

Continued

Table 4.4: Source Characteristics for the Final Event Sample.

Table 4.4: Continued

Event Name	$(V-I)_0$	I_0	θ_* [a] (μas)	ρ_* [a]
OB99005	0.699±0.006	17.99± 0.24	0.91	1.87×10^{-3}
OB99007	1.100±0.008	14.91± 0.07	5.29	2.15×10^{-2}
OB99008[b]	0.895	18.14± 0.19	1.00	3.56×10^{-3}
OB99013	1.112±0.012	14.31± 0.15	7.04	5.42×10^{-2}
OB99016[b]	1.012	15.90± 0.73	3.14	1.07×10^{-2}
OB99022	1.021±0.050	16.27± 0.32	2.66	5.19×10^{-2}
OB99027[b]	0.890	17.26± 0.36	1.49	4.40×10^{-3}
OB99033	0.987±0.021	15.24± 0.07	4.17	1.06×10^{-2}
OB99035[c]	–	–	6.00	7.80×10^{-3}
OB99036	0.938±0.005	16.21± 0.02	2.55	1.28×10^{-2}
OB99039	0.870±0.412	19.45± 0.32	0.53	3.62×10^{-4}

[a] θ_*= angular size of the source; ρ_*=angular size of the source in units of the angular Eistein ring radius of the lens.

[b] Insufficient V-band data to determine the color of the source; the source is assumed to have the typical $(V-I)$ for its magnitude.

[c] No CMD available, or CMD inconclusive. The source is assumed to be a clump giant.

BIBLIOGRAPHY

Alard, C., & Lupton, R.H. 1998, ApJ, 503, 325

Albrow, M., et al. 1997, in Variable Stars and the Astrophysical Returns of Microlensing Surveys, ed. R. Ferlet, J.-P. Maillard, & B. Raban (Gif-sur-Yvette:Editions Frontires), 135

Albrow, M., et al. 1998, ApJ, 509, 687

Albrow, M., et al. 1999, ApJ, 522, 1011

Albrow, M., et al. 1999, ApJ, 522, 1022

Albrow, M., et al. 2000, ApJ, 534, 894

Albrow, M., et al. 2000, ApJ, 535, 176

Albrow, M., et al. 2000, ApJ, submitted

Albrow, M., et al. 2001a, in preparation

Albrow, M., et al. 2001b, in preparation

Albrow, M., et al. 2001d, in preparation

Albrow, M., et al. 1999, ApJ, 512, 672

Alcock, C., et al. 1993, Nature, 365, 621

Alcock, C., et al. 1995, ApJ, 454, L125

Alcock, C., et al. 1996, ApJ, 463, L67

Alcock, C., et al. 1997a, ApJ, 479, 119

Alcock, C., et al. 1997, ApJ, 491, 436

Alcock, C., et al. 1997b, ApJ, 486, 697

Alcock, C., et al. 2000, ApJ, 539, 000

Afonso, C., et al. 2000, ApJ, 532, 340

Afonso, C., et al. 2001, in preparation

Angel, R., & Woolf, N. 1997, ApJ, 475, 373

Aubourg, E., et al. 1993, Nature, 365, 623

Bennett, D. & Rhie, S. H. 1996, ApJ, 472, 660

Bennett, D., et al. 1999, Nature, 402, 57

Bertelli, G., et al. 1994, A&AS, 106, 275

Boden, A., et al. 1998a, ApJ, 502, 538

Boden, A., et al. 1998b, ApJ, 504, L39

Bolatto, A., & Falco, E. 1993, ApJ, 436, 112

Borucki, W. J., et al. 1997, in Planets Beyond the Solar System and the Next Generation of Space Missions, ed. D. Soderblom (San Francisco:Astronomical Society of the Pacific), 119

Borucki, W.J., Caldwell, D.A., Koch, D.G., Webster, L.D., Jenkins, J.M., & Ninkov, Z. 1999, BAAS, 195, 24.01

Bozza, V. 1999, A&A, 348, 311

Bozza, V. 1999, A&A, 355, 423

Bozza, V. 1999, A&A, 359, 1

Brown, T.M., & Charbonneau, D. 2000, in ASP Conference Series, Disks, Planetesimals, and Planets, eds. F. Garzon and T. J. Mahoney (San Francisco: ASP), in press (astro-ph/0005009)

Buchalter, A., & Kamionkowski, M. 1996, ApJ, 469, 676

Butler, R., & Marcy, G. 1996, ApJL, 464, L15

Butler, R., et al. 1996, PASP, 108,500

Butler, R., Marcy, G., Fischer, D., Brown, T., Contos, A., Korzennik, S., Nisenson, P., & Noyes, R. 1999, ApJ, 526, 916

Charbonneau, D., Brown, T.M., Latham, D.W., & Mayor, M. 2000, ApJ, 529, L45

Cochran, W.C., et al. 1997, ApJ, 483, 457

Cumming, A., Marcy, G., & Butler, R. 1999, ApJ, in press

Deeg, H.J., et al. 1998, A&A, 338, 479

Deleuil, M., et al. 1997, in Planets Beyond the Solar System and the Next Generation of Space Missions, ed. D. Soderblom (San Francisco:Astronomical Society of the Pacific), 259

Demarque, P., et al. 1996, Yale Isochrones 1996, in http://shemesh.gsfc.nasa.gov/iso.html

Di Stefano, R., & Mao, S. 1996, ApJ, 457, 93

Di Stefano, R., & Perna, R. 1998, ApJ, 000, 000

Di Stefano, R., & Scalzo, R. 1999a, ApJ, 512, 564

Di Stefano, R., & Scalzo, R. 1999b, ApJ, 512, 579

Dominik, M. 1998, A&A, 330, 963

Dominik, M. 1998, A&A, 333, L79

Dominik, M. 1999, A&A, 341, 943

Dominik, M. 1999, A&A, 349, 108

Dominik, M., & Sahu, K. 1999, ApJ, submitted

Gaudi, B. S. 1998, ApJ, 506, 533

Gaudi, B. S., Naber, R. M., & Sackett P. D. 1998, ApJ, 502, L33

Gaudi, B. S., & Sackett, P. D. 2000, ApJ, 528, 000 (astro-ph/9904339)

Gaudi, B., & Gould, A. 1997, ApJ, 477, 152

Gaudi, B. S., & Gould, A. 1997, ApJ, 486, 85

Gilliland, R., et al. 2000, BAAS, 196, 0202

Goldberg, D.M. 1998, ApJ, 498, 156

Goldberg, D.M., & Woźniak, P. 1998, Acta Astron., 48, 19

Gould, A. 1992, ApJ, 392, 442

Gould, A. 1994, ApJ, 421, L71

Gould, A. 1996, ApJ, 470, 201

Gould, A. 2000, ApJ, 535, 928

Gould, A., & Gaucherel, C. 1997, ApJ, 477, 580

Gould, A., & Loeb, A. 1992, ApJ, 396, 104

Gould, A., & Salim, S. 1999, ApJ, submitted

Gould, A., & Welch, D. 1996, ApJ, 464, 212

Gould, A., Miralda-Escudé, J., & Bahcall, J. 1994, ApJ, 423, 105L

Griest, K., & Hu, W. 1992, ApJ, 397, 362

Griest, K., & Safizadeh, N. 1998, ApJ, 500, 37

Han, C. 1997, ApJ, 490, 51

Han, C., Jeong, Y., & Kim, H.-I. 1998, ApJ, 507,102

Han, C., & Gould, A. 1995, ApJ, 447, 53

Hale, A., & Doyle, L. 1994, Ap&SS, 212, 335

Henry, G.W., Marcy, G.W., Butler, R.P., & Vogt, S.S. 2000, ApJ, 529, L41

Jeong, Y., Han, C., & Park, S.-H. 1999, ApJ, 511, 569

Kayser, R., & Schramm, T. 1998, A&A, 191, 39

Kiraga, M., & Paczyńsky, B. 1994, ApJ, 430, L101

Landolt, A. 1992, AJ, 104, 340L

Lindegren, L. & Perryman, M.A.C. 1996, A&AS, 116, 579

Mao, S., & Di Stefano, R. 1995, ApJ, 440, 22

Mao, S., & Paczyński, B. 1991, ApJ, 374, 37

Marcy, G.,& Butler, R. 1998, ARA&A, 36, 57

Marcy, G., Butler, R., & Vogt, S. 2000, ApJ, 536, L43

Marcy, G., Butler, R., Vogt, S., Fischer, D., & Lissauer, J. 1998, ApJ, 505, L147

Marcy, G.W., Cochran, W.D., & Mayor M. 2000, in Protostars and Planets IV, eds. V. Mannings, A.P. Boss and S.S. Russell (Tuscon: Univeristy of Arizona), 1285

Mayor, M., & Queloz, D. 1995, Nature, 378, 355

McMillan, R.S., et al. 1993, ApJ, 403, 801

Nemiroff, R., & Wickramasinghe, W. A. D. T. 1994, ApJ, 424, L21

Noyes, R.W., et al. 1997, ApJ, 483, L111

Paczyński, B. 1986, ApJ, 304, 1

Paczyński, B., & Stanek, K. 1998, ApJ, 494, L219

Paczyński, B., Udalski, A., Szymański, M., Kubiak, M., Pietrzyński, G., Soszynski, I., Woźniak, P., & Zebruń, K. 1999, Acta Astron., 49, 319

Peale, S. J. 1997, Icarus, 127, 269

Press, W. H., Flannery, B. P., Teukolsky, S.A., & Vetterling, W. T. 1992, Numerical Recipes (Cambridge: Cambridge Univ. Press)

Rhie, S. H., et al. 1999a, ApJ, 522, 1037

Rhie, S. H., et al. 1999b, ApJ, 532, 000

Saar, S.H., Butler, R.P., & Marcy, G.W. 1998, ApJ, 403, L153

Sackett, P.D. 1997, Final Report of the ESO Working Group on the Detection of Extrasolar Planets, Appendix C (ESO Document: SPG-VLTI-97/002, and astro-ph/9709269)

Sackett, P.D. 1999a, in Planets outside the Solar System: theory and observations, eds. J.-M. Mariotti & D. Alloin, NATO-ASI Series, Kluwer. (astro-ph/9811269)

Sackett, P.D. 1999b, in preparation

Schechter, P. L., Mateo, M., & Saha, A. 1993, PASP, 105, 1342

Schneider, P., Ehlers, J., & Falco, E.E. 1992, Gravitational Lenses (Berlin, Springer)

Stanek, K. 1995, ApJ, 441, L29

Tomaney, A.B., & Crotts, A.P.S. 1996, AJ, 112, 2872

Udalski, A., et al. 1993, Acta Astron., 43, 289

Udalski, A., et al. 1994, Acta Astron., 44, 165

Udalski, A., et al. 1994, Acta Astron., 44, 227

Udalski, A., et al. 1997, Acta Astron., 47, 169

Udalski, A., et al. 2000, Acta Astron., 50, 1

van Belle, G. T. 1999, PASP, 111, 1515

Vogt, S., Marcy, G., Butler, R., & Apps, K. 2000, ApJ, 536, 902

Walker, M.A. 1995, ApJ, 453, 37

Wambsganss, J. 1997, MNRAS, 284, 172

Witt, H. 1990, A&A, 236, 311

Witt, H. 1995, ApJ, 449, 42

Witt, H., & Mao, S. 1994, ApJ, 430, 505

Woolf, N., & Angel, R. 1998, ARA&A, 36, 507

Woźniak, P., & Paczyński, B. 1997, ApJ, 487, 55

Zoccali, M.S., Cassisi, S., Frogel, J.A., Gould, A., Ortolani, S., Renzini, A., Rich, R.M., & Stephens, A. 2000, ApJ, 530, 418

Appendix A

Excluded Anomalous Events

In § 4.4, we rejected 17 anomalous events from the analysis that we asserted were not caused by planetary (i.e. small mass ratio binary) lenses. Here we list each of these events, and briefly justify why we believe the anomaly to be non-planetary in origin. For those events for which binary-lens fits are available in the literature, we will simply state the fitted mass ratio(s), and refer the reader to the paper; for a large fraction of these events, we will be relying on the analysis and binary-lens fits of Alcock et al. (2000). One caveat should be noted. It is known (Dominik, 1999a; Albrow et al., 1999c) that binary lens events can often have degenerate solutions, even for extremely well sampled events (Afonso et al., 2000). This is due to intrinsic degeneracies in the binary-lens lens equation (Dominik, 1999b). Finding all of these degenerate solutions to an observed light curve is highly non-trivial, due to the extremely sharp variations in χ^2 with respect to the canonical parameters, although several methods have been proposed to deal with this difficulty (Di Stefano & Mao, 1996; Di Stefano & Perna, 1998; Albrow et al., 1999c). However, as Alcock et al. (2000) themselves allow, it is not at all clear that they have found all possible fits to their events. It is therefore possible, in principle, that some of the events they analyze actually have planetary solutions that they missed. We find this extremely unlikely, however, based simply on examination of the data, which typically reveal gross deviations from the PSPL form, in contradiction to what would be expected from a small mass ratio binary.

For caustic-crossing binary-lens events for which the source is resolved, we can use the following argument to place a lower limit on the mass ratio q. The maximum magnification obtained when a source of angular size θ_* crosses a fold caustic is (Schneider, Ehlers, & Falco, 1992)

$$A^{\rm cc}_{\rm max} \sim \left(\frac{u_{\rm r}}{\theta_*}\right)^{1/2}, \tag{4.31}$$

where $u_{\rm r}$ is a factor that describes the "strength" of the caustic. For caustics originating from binary lenses with small q, this scale is of order the planetary Einstein ring radius, $q = \mathcal{O}(\theta_{\rm p})$. Due to possible blending, the observed maximum magnification, $A^{\rm cc}_{\rm max,obs}$ is a lower limit to the true magnification, and by combining eqs. (4.31), (4.1), and (4.23), we obtain an approximate lower limit on q:

$$q_{\rm min} \gtrsim 0.01 \left(\frac{A^{\rm cc}_{\rm max,obs}}{3}\right)^4 \left(\frac{\theta_*}{1\ \mu{\rm as}}\right)^2 \left(\frac{\mu_{\rm rel}}{12.5\ {\rm km\,s^{-1}\ kpc^{-1}}}\right)^{-2} \left(\frac{t_{\rm E,obs}}{40\ {\rm days}}\right)^{-2}, \tag{4.32}$$

where $t_{\rm E,obs}$ is the observed (i.e. blended) timescale of the event, which is always a lower limit to the true timescale. Since $q_{\rm min}$ depends on $t_{\rm E,obs}$ squared, while $q_{\rm min}$ depends on $A^{\rm cc}_{\rm max,obs}$ to the fourth power, the limit in equation (4.32) holds even in the presence of blending. The smallest sources in the Galactic bulge have $\theta_* \sim 1\ \mu$as, and the dispersion in $\mu_{\rm rel}$ for bulge-bulge lensing is a factor of 10. Thus, if a caustic crossing is observed with $A^{\rm cc}_{\rm max,obs} > 10$, it is almost certainly due to binary lens with mass ratio larger than those we consider, $q \leq 0.01$. This is also true for disk-disk lensing, for which $\mu_{\rm rel} \sim xx\ {\rm km\,s^{-1}\ kpc^{-1}}$.

MACHO 95-BLG-12 Both PLANET (Albrow et al., 1998), and MACHO/GMAN (Alcock et al., 2000) data show a smooth double-peaked event, with both peaks having comparable duration. This morphology suggests a weak binary lens or binary source (Griest & Hu, 1992). However, the achromaticity of the event suggests a binary-lens interpretation, and we find that a binary-source model provides a poor fit to the PLANET data. We cannot uniquely constrain a binary-lens fit, but Alcock et al. (2000) find a binary-lens fit with mass ratio $q = 0.47$. The fact that the peaks are of comparable duration precludes a small mass ratio binary-lens (i.e. planetary) model.

MACHO 96-BLG-04 The MACHO/GMAN data show two nearly equal-duration deviations separated by ~ 500 days (Alcock et al., 2000). Both deviations are separately well-fit by a standard PSPL model, suggesting a widely separation binary-source or binary-lens (Di Stefano & Mao, 1996). Alcock et al. (2000) find $q = 0.88$ for their binary-lens fit. Regardless of the interpretation, the PLANET data on this event would not have passed our second cut, due to insufficient data.

MACHO 97-BLG-28 We find only one viable model that fits our data on this event (Albrow et al., 1999), with $q = 0.23$. Alcock et al. (2000) find a similar binary-lens model fit for their dataset, with $q = 0.21$.

MACHO 97-BLG-41 Our data for this peculiar event is well-fit by a rotating binary-lens model with mass ratio $q = 0.34$ (Albrow et al., 2000c). Bennett et al. (1999) favor the interpretation that this event is best explained by a planet orbiting a binary-lens. Our data is clearly inconsistent with their particular fit, although this does not preclude the possibility that some fit of this nature would explain our data. Regardless of the interpretation, this event should be rejected because of the presence of the binary.

MACHO 98-BLG-6 This is a long-timescale (> 100 days) event that shows global deviations from the PSPL form indicative of parallax.

MACHO 98-BLG-12 MACHO/GMAN data indicate that this event likely underwent four caustic crossings, separated by ~ 40 days (Alcock et al., 2000). The MACHO/GMAN coverage of the first set of caustic crossing is poor, but constrain the amount of time that the source was between the second set of crossings to be $\lesssim 3$ days. Due to its short duration, one might suppose that the second crossing was due to a planetary caustic. However, the first set of caustic crossings, combined with the fact that the event exhibits a *rise* toward the second set of crossings, makes this interpretation impossible. Indeed, Alcock et al. (2000) find that the event is well-fit by an intermediate-topology binary lens with $q = 0.68$. PLANET acquired a few data points immediately after the second crossing, and then data immediately after the fourth crossing continuing until the end of the event. Due the the fact that the PLANET data did not probe any of the caustic structures, we find that our dataset is reasonably well-fit by a PSPL model. However, our data by themselves would fail our $\delta u_0/u_0$ cut.

MACHO 98-BLG-14 Both the MACHO/GMAN dataset (Alcock et al., 2000) and the PLANET dataset show a highly asymmetric light curve with a "shoulder" and then a peak. Such a morphology is indicative of a weakly-perturbed binary-lens event, and as such is prone to degeneracies. In fact Alcock et al. (2000) find two fits, one with mass ratio $q = 0.09$ and the other with $q = 0.22$. However, the event deviates from the PSPL form for a large fraction ($\sim 40\%$) of its apparent duration, making a planetary interpretation unlikely. We performed a systematic search of binary-lens fits to this event, using our data and the MACHO data. We recover the fits reported by (Alcock et al., 2000), along with a few other fits of similar significance. The best-fit binary with $q < 0.01$ is ruled out at the $> 7\sigma$ level.

MACHO 98-BLG-16 The MACHO/GMAN data show a short time scale peak, followed by an abrupt rise and a plateau at magnification ~ 10 that lasts ~ 8 days. Following the plateau, the event returned to magnification ~ 2 (Alcock et al., 2000). Although the coverage is poorer, PLANET data qualitatively confirm this behavior. This morphology is consistent with a caustic-crossing binary lens, with the short-time scale peak being due to a cusp approach. MACHO/GMAN data near the peak of the first caustic crossing have $A^{\rm cc}_{\rm max,obs} \sim 20$, and thus constrain the event to be non-planetary by equation (4.32). Indeed, Alcock et al. (2000) find a binary-lens fit with $q = 0.68$.

MACHO 98-BLG-28 This event displays a double-peaked structure indicative of a weak binary-lens or binary source. This is seen in both OGLE and PLANET data for the event. Using the combined dataset, we find the best-fit binary-lens model has $q = 0.34$ and $b = 0.42$. Normalizing the errors to this model, the best model in the range $q = 10^{-4} - 10^{-2}$ has $\Delta\chi^2 \sim 19$, and thus is excluded at the $\sim 4\sigma$ level.

MACHO 98-BLG-42 Alcock et al. (2000) find $q = 0.33$. The PLANET data cover the second half of the event, including the falling side of a second caustic crossing. The data near the peak of the second caustic-crossing have $A^{\rm cc}_{\rm max,obs} \sim 40$; therefore the event must be non-planetary in origin [Eq.(4.32)].

OGLE-1998-BUL-29 The PLANET data for this high-magnification ($A_{\rm max} \sim 50$) event show deviations near the peak that are indicative of source resolution effects.q

MACHO 99-BLG-8 Similar to MACHO 98-BLG-6, this long-time scale event shows severe parallax effects. We also find shorter time scale variability in the source.

MACHO 99-BLG-22 Although the PLANET, MACHO, and OGLE data show no obvious anomalous behavior, our PSPL fit to the combined datasets yielded a time scale of $t_{\rm E} \sim 900$ days, leading us to suspect parallax effects might be present. In fact, we find that a fit with parallax improves χ^2 significantly, and results in a much more reasonable time scale.

MACHO 99-BLG-25 MACHO data for MACHO 99-BLG-25 show a clear deviation from PSPL at early times, in the form a smaller amplitude, but nearly equal duration peak occurring before PLANET began monitoring the event. The fact that both peaks are of similar duration suggests that this event is likely to be due to a binary source, and exclude the possibility that it is due to a planet. Our data only cover the rise and fall of the second peak and are perfectly consistent with a PSPL model. In fact, we find that this event does not have a significant planetary signal, nor does it have a large detection efficiency to planetary companions. Therefore excluding this event has no significant impact on our conclusions.

MACHO 99-BLG-47 PLANET data show a departure from the PSPL form lasting ~ 3 days near the peak. Detailed analysis of this event shows that the deviation is caused by a small separation binary with $q \sim 0.4$ (Albrow et al., 2001a).

MACHO 99-BLG-57 MACHO data show a large, long time scale deviation from the PSPL form that is likely due to a binary-source or binary-lens. PLANET has very little data on this event, and so cannot confirm or clarify the nature of this anomaly.

OGLE-1999-BUL-11 A caustic-crossing binary lens; PLANET data resolve the second crossing. Data near the of the second crossing have $A^{\rm cc}_{\rm max,obs} \sim 10$, and thus the event must be non-planetary in origin [Eq.(4.32)].

OGLE-1999-BUL-23 We find only one viable fit to this event, with $q = 0.39$ (Albrow et al., 2000c).

OGLE-1999-BUL-25 PLANET data show a large positive deviation lasting < 1 day superposed atop an extremely noisy light curve. As we see a "break" in the light curve immediately after this deviation, we conclude that it is due a caustic crossing of some kind. The magnification at the peak of this deviation is $A^{\rm cc}_{\rm max,obs} \sim 40$, and thus the deviation cannot be due to planet.

Appendix B

OGLE-1999-BUL-36 and Parallax Contamination

Figure 4.16 shows the PLANET and OGLE data for OGLE-1999-BUL-36, binned into 1 day intervals, along with the best-fit single lens, planetary, and parallax asymmetry models to the unbinned data. The difference in χ^2 between the binary-lens and parallax models is 4 (with the binary-lens model giving the worse fit); both models are favored over the PSPL model by $\Delta\chi^2 \sim 80$. The best-fit binary lens model has $q \simeq 0.003$, $d \simeq 0.6$, and $\alpha \simeq 360°$. We also find fits for other mass ratios and separations that are nearly as good. The parallax asymmetry fit (see Gould, Miralda-Escudé, & Bahcall (1994) for the exact form) yields a measurement of the asymmetry factor, κ, given by,

$$\kappa = \Omega_{\oplus} \frac{v_{\oplus}}{\tilde{v}} \sin\lambda \sin\phi, \tag{4.33}$$

where $\tilde{v} = v(D_{\mathrm{S}}/D_{\mathrm{LS}})$ is the transverse velocity of the lens projected on the observer plane, $\Omega_{\oplus} = 2\pi\ \mathrm{yr}^{-1}$, $v_{\oplus} \simeq 30\ \mathrm{km\,s}^{-1}$ is the speed of the Earth, and λ is the angle between the source and Sun at the time of maximum magnification. In the case of OGLE-1999-BUL-36, $\sin\lambda \sim 0.6$. We find $\kappa = 0.002 \pm 0.0001$, which implies,

$$\frac{\tilde{v}}{\sin\phi} = 80 \pm 10\ \mathrm{km\,s}^{-1}. \tag{4.34}$$

Combining this constraint with $t_{\rm E}$, we find an upper limits to the mass of the lens as a function of the distance of lens,

$$M \leq 0.06\ M_{\odot}\frac{1-x}{x}, \tag{4.35}$$

where $x = D_{\rm L}/D_{\rm S}$. Thus, if the parallax interpretation is correct, the lens must be closer than ~ 3.5 kpc to be above the hydrogen burning limit.

The primary lesson learned from the analysis of OGLE-1999-BUL-36 is that we cannot robustly detect planetary companions based on asymmetries, as such asymmetries cannot be distinguished from low-level parallax. However, when calculating our detection efficiencies (§ 4.6.3), we excluded all deviations that produced $\Delta\chi^2 > 60$, including asymmetries. Therefore, our efficiencies are overestimated. To estimate by how much, we choose a well sampled, high-quality event that contains data on both rising and falling sides, OGLE-1998-BUL-14. We repeat the algorithm in § 4.6.1 to calculate the efficiency of this event, except that we simultaneously fit for both the binary-lens magnification and parallax asymmetry. This procedure removes all detections based on asymmetry alone. In Figure 4.17 we show the detection efficiency both with and without excluding such detections. The difference is quite small, a few percent. This is because a very small range of angles produce deviations consistent with asymmetries. The majority of events have converge and photometric accuracy that is poorer than OGLE-1998-BUL-14, and we therefore conclude that this effect is negligible.

Appendix C

The Efficiency of High-Magnification Events Near d=1

Griest & Safizadeh (1998) found that the detection probability for $q \gtrsim 10^{-3}$ companions with the separations in the lensing zone is nearly 100% for high-magnification events $A_{\max} > 10$. This was confirmed empirically for the light curve of the high-magnification event MACHO 98-BLG-35 by the MPS collaboration (Rhie et al., 1999b). Griest & Safizadeh (1998) also found that the higher the maximum magnification, the higher the detection probability, at least for small sources, and the detection probability is *always* maximized at $d = 1$ (see their Figure 7). The results for our events are in contradiction to these results. In particular, we find that for two of our highest magnification events (MACHO 98-BLG-35, $A_{\max} \sim 100$; OGLE-1999-BUL-35, $A_{\max} \sim 130$), the point-source detection efficiency has a minimum a $d = 1$, whereas other events with somewhat smaller, but still large, maximum magnifications (i.e. OGLE-1998-BUL-14, $A_{\max} \sim 16$; OGLE-1999-BUL-36, $A_{\max} \sim 15$), do not display this minimum, and in fact have higher detection efficiencies at $d = 1$ for some mass ratios (see Fig. 4.7). In fact, inspection of the caustic topologies in the two cases reveals that the highest magnification events like MACHO 98-BLG-35 and OGLE-1999-BUL-35 have source trajectories that always cross caustics, whereas the source trajectories for OGLE-1998-BUL-14 and OGLE-1999-BUL-36 typically do not. Yet the efficiency for the former is smaller than the latter. This paradoxical result can be understood in term of the caustic structure. For planetary companions with $d = 1$, there is one caustic centered at the position of the primary. This caustic is quite large (relative to the planetary Einstein ring) and thus quite weak (Wambsganss, 1997). Therefore, the caustic crossings create only very short time scale deviations to the PSPL form, at least for some trajectories. Given incomplete sampling of the light curve, these caustic crossings can fall into gaps in the data. This is illustrated in Figure 4.18, where we show an example binary lens fit with $q \sim 10^{-3}$ and $d = 1$ to the light curve of MACHO 98-BLG-35.

We suspect that the reason Griest & Safizadeh (1998) and Rhie et al. (1999b) did not discover this effect was that they did not explicitly fit for the impact parameter u_0 in both the single and binary-lens fits. As can be seen in Figure 4.18, the binary-lens and single lens fits require slightly different values of u_0 to match the data, although with this adjustment, the two fits are nearly indistinguishable. We conclude that, even for very high-magnification events, the detection probability for companions in the lensing zone, while large, is not 100%, and higher magnification does not necessarily imply higher detection probability.